Dynamics and materials physics of fault rupture and glacial processes

A dissertation presented
by
John Daniel Platt
to
The School of Engineering and Applied Sciences

in partial fulfillment of the requirements
for the degree of
Doctor of Philosophy
in the subject of
Applied Mathematics

Harvard University
Cambridge, Massachusetts
November 2014

Thesis advisor: Professor James R. Rice John Daniel Platt

Dynamics and materials physics of fault rupture and glacial processes

Abstract

This thesis focuses on two main topics, the physics governing how faults rapidly weaken during an earthquake and the thermal and mechanical structure of ice stream shear margins. The common theme linking these two projects is the desire to understand how the complicated interactions between stress and temperature control deformation and failure. All of the problems in this thesis are attacked using a combination of analytic and numerical methods, and the interplay between these two approaches provides a powerful way to understand the different physical balances that dominate in different regimes. We also use aspects of materials science to understand how the often complicated rheologies are controlled by underlying physical phenomena such as melting, phase transitions, diffusion, and dislocation motion. With regards to fault mechanics, we begin by showing how co-seismic weakening mechanisms driven by elevated pore fluid pressures lead to micron-scale strain localization during an earthquake. We solve for the localized zone thickness for a range of fault temperatures, test these predictions using numerical simulations, and show how the onset of localization accelerates fault weakening. Next we present the first solutions to account for thermal decomposition reactions during a dynamic rupture, showing that the activation of thermal decomposition may lead to a larger slip duration and total slip. Finally we present a new set of experiments studying flash heating of serpentinite, highlighting the dependence of friction on normal stress and the presence of gouge, and producing the first model to explain the hysteresis commonly observed in flash heating experiments. With regards to ice stream shear margins, we begin by extending the work of *Perol and Rice* [2011][161] to study the formation of temperate ice in shear margins, and quantify the total melt that may be generated within the shear margins. We conclude by investigating how the presence of such a channel alters the stress on and strength of the undeforming bed in the shear margin, showing that the transition from a deforming to an undeforming bed across a channel is stable when the water flux in the channel exceeds a critical value.

Contents

Listing of figures

Acknowledgments

First and foremost I would like to thank Jim for his thoughtful guidance over the past five years. His encouragement and help has been immensely valuable, and without him the work presented in this thesis would not have been possible. In addition I would like to thank Renata for her constant care and attention during my time at Harvard.

The coursework component of my PhD was extremely valuable due to the efforts of a large number of Harvard faculty. In particular I would like to thank Professors Suo, Hutchinson, Bertoldi, Spaepen, Mahadevan, Brenner, O'Connell, Mitrovica, and Ishii. In addition I would like to thank my committee members Jerry Mitrovica, Alan Rempel, and Chris Rycroft for taking the time to read my thesis.

My time as a PhD student has been greatly enriched by interactions with other researchers working on a range of different problems. In particular I would like to thank Thibaut Perol, Jenny Suckale, Robert Viesca, Dmitry Garagash, Nicolas Brantut, John Rudnicki, Brooks Proctor, Tom Mitchell, Greg Hirth, Giuilio Di Toro, David Goldsby, Terry Tullis, Nick Beeler, and Federico Zorzi for thoughtful and rewarding collaborations.

Finally I would like to thank my wife Meghan and my parents for their constant love and support.

1

Introduction

1.1 Structure of thesis

The work presented in this thesis focuses on two main projects, the physics governing how faults rapidly weaken during an earthquake and the thermal and mechanical structure of ice stream shear margins. The common theme linking these two projects is the desire to understand how the complicated interactions between stress and temperature and sometimes

chemistry control deformation and failure. The thesis is structured such that all fault mechanics chapters are grouped together, followed by the work on ice stream shear margins. One additional paper is included as an appendix rather than a chapter because I played a limited role in preparing the manuscript. Each chapter begins with a short note detailing my role in the project and a citation is included at the start of all chapters that are already published.

1.2 Rapid co-seismic fault weakening

Geophysical observations suggest that mature faults weaken significantly at seismic slip rates. Several mechanisms have been proposed to explain this dynamic weakening, though this thesis will largely focus on just two of these mechanisms: thermal pressurization and thermal decomposition. Both mechanisms rely on elevated pore fluid pressures in a fluid-saturated gouge layer, with thermal pressurization achieving this through thermal expansion of native pore fluid and thermal decomposition by releasing additional pore fluid – for example H_2O or CO_2 – during devolatilization reactions that are ubiquitous among common fault materials. In this thesis we will begin by studying how thermal pressurization and thermal decomposition drive seismic strain localization, move on to study how these two weakening mechanisms combine to propagate a rupture, and end by showing how modeling and experiments can be combined to understand the underlying physics of co-seismic weakening.

In chapters 2 and 3 we use a one-dimensional model for a fluid-saturated gouge layer sheared between two undeforming half-spaces to show how thermal pressurization can drive shear strain localization during an earthquake. To begin we use a linear stability anal-

ysis to predict the localized zone thickness as a function of the gouge properties and slip rate. Inserting typical values for these material properties we predict that most of the deformation occurs in a zone just a few tens of microns wide, which is in good agreement with field and laboratory observations of localized zone thicknesses. This prediction is then tested using numerical simulations that account for nonlinear effects, and we find excellent agreement between the analytic and numerical methods. The numerical simulations also show that the onset of localization accelerates fault weakening, which demonstrates that coseismic strain localization is an important consideration neglected in all current models for earthquake rupture. This work was done in collaboration with James R. Rice and John W. Rudnicki and led to two papers published in the Journal of Geophysical Research[189,166].

In chapter 4 we extend the analysis in chapters 2 and 3 to account for thermal decomposition. As before we begin by using a linear stability analysis to predict the localized zone thickness as a function of the gouge properties for a range of fault temperatures. We show that thermal decomposition is the dominant weakening mechanism at high temperatures and that the onset of thermal decomposition drives additional strain localization. Next we use numerical simulations to test these predictions, investigate how thermal decomposition may control the peak temperature attained during an earthquake, and show how the strength drop associated with the onset of thermal decomposition is controlled by the reaction properties. This work was done in collaboration with Nicolas Brantut and James R. Rice and a paper was submitted to the Journal of Geophysical Research[167].

In chapter 5 we present the first dynamic rupture simulations to account for thermal decomposition. To do this we solve for steady slip pulses propagating at a constant rupture velocity, building on the work of *Garagash* [2012][86] that solved for steady slip pulses driven

by thermal pressurization alone. We show that there is a distinct signature associated with the triggering of thermal decomposition, with thermal decomposition leading to a longer slip duration, a larger total slip, and a lower rupture velocity. Furthermore we show that there can be multiple ways to balance thermal pressurization and thermal decomposition during a rupture, leading to the existence of multiple steady slip pulses for a single set of fault properties. Finally, we investigate how the bulk rupture properties such as slip duration and rupture velocity depend on the properties of the fault, focussing in particular on the reaction parameters and the balance between hydraulic and thermal diffusion. This work was performed in collaboration with Robert C. Viesca and Dmitry I. Garagash and will be submitted to the Journal of Geophysical Research soon.

Flash heating is another commonly studied dynamic weakening mechanism that relies on the breakdown of highly stressed frictional contacts at a critical weakening temperature. *Rice* [1999][185] presented a model of flash heating for bare rock surfaces sliding against each other, showing that flash heating occurs when the slip rate exceeds a critical slip rate $V_w \sim$0.1 – 0.2 m/s and also predicting how the friction coefficient depends on slip rate when $V > V_w$. This prediction was later validated experimentally by *Goldsby and Tullis* [2011][93] and *Kohli et al.* [2011][125] for normal stresses of ~ 5 MPa, slip rates of ≤ 0.5 m/s, and total slips of ≤ 50 mm. Appendix F presents a new set of experiments that extends this work to much higher normal stresses, slip rates and total slips, while also studying the role a gouge layer may play in limiting the efficiency of flash heating. This experimental work is complemented by simple thermal models for the evolution of sliding surface temperature and frictional contact temperature. Combining the experiments and models we study the dependence of key frictional properties such as weakening velocity and friction

coefficient on normal stress, show that the presence of a gouge layer dramatically reduces the efficiency of flash heating, and produce the first model that is able to explain some of the hysteresis commonly observed in flash heating experiments. The lead researcher on this project was Brooks P. Proctor – a PhD student at Brown University – and other collaborators included Tom M. Mitchell, Greg Hirth, David L. Goldsby, Federico Zorzi, and Giulio Di Toro. Based on this work we recently published a paper in the Journal of Geophysical Research[171].

1.3 The structure of ice stream shear margins

The mass loss from the West Antarctic ice sheet is dominated by numerous rapidly flowing ice streams, which are separated from the stagnant ice in the adjacent ridge by zones of concentrated deformation known as shear margins. Since the discharge from a single ice stream is thought to depend sensitively on the ice stream width, determining the physical processes that control the shear margin location is crucial to understanding how ice streams may respond to a changing climate. Building on the work of *Perol and Rice* [2011][161] and *Perol et al.* (in preparation)[163], I was involved in a project looking at the mechanical and thermal structure of ice stream shear margins in collaboration with Thibaut Perol, Jenny Suckale, and James R. Rice.

My involvement with this project began with the work presented in chapter 6. In this chapter we investigate when the concentrated deformation present at the shear margin leads to the formation of temperate ice, where the ice is at the melting temperature and all additional heating is turned into melt. We showed that surface velocity observations of a specific shear margin in West Antarctica can only be explained by the presence of a large

body of temperate ice within the shear margin. Following this we studied how the advection associated with the movement of cold ice could limit the formation of temperate ice and showed that the shear margins could be a significant source of melt, as previously noted in *Schoof* [2004][198] and *Perol and Rice* [2011][161]. This project was performed in collaboration with Jenny Suckale, Thibaut Perol and James R. Rice, and resulted in a paper published in the Journal of Geophysical Research[216].

Perol and Rice [2011][161] argued that a subglacial drainage channel should form at the base of the shear margin due to the melt produced in the temperate ice, and used the classic theories for subglacial drainage channels to quantify the size of such a channel[191,204,238]. Furthermore, *Perol and Rice* (in preparation)[163] showed that such a drainage channel would raise the basal strength within the shear margin, and possibly select the location of the shear margin. In chapter 7 we focus on how the presence of a channel could alter the stress field if the channel is located at the transition from a deforming to an undeforming bed. The presence of a channel limits the maximum stress on the bed to a finite value, which is solved for as a function of all of the parameters in the model. In addition we show that the presence of a channel alters the till strength in the immediate vicinity of the channel by changing the normal stress applied on the ice-till interface. Comparing the maximum stress on the bed with the yield strength of the bed we determine the conditions that must be satisfied for the transition from a deforming to an undeforming bed at a channel to be stable. This is shown to be controlled by a critical water flux within the channel, though the exact value of this critical flux is uncertain due to uncertainties in the ice rheology.

This project was a collaboration with James R. Rice and John W. Rudnicki, who together performed the linear stability analysis before I arrived at Harvard. My role in the project was to use numerical simulations to test the linear stability predictions, further explore the dependence on different key parameters, and assist in the preparation of the final manuscript. The work in this chapter has already been published and the relevant citation is: Rice, J.R, J.W. Rudnicki, and J. D. Platt (2014), Stability and localization of rapid shear in fluid-saturated gouge, 1. Linearized stability analysis, Journal of Geophysical Research, 119, 4311-4333.

2

Stability and Localization of Rapid Shear in Fluid-Saturated Fault Gouge, 1. Linearized stability analysis

2.0 Abstract

Field observations of major earthquake fault zones show that shear deformation is often confined to principal slipping zones that may be of order $1 - 100$ μm wide, located within a broader gouge layer of order $10 - 100$ mm wide. This paper examines the possibility that the extreme strain localization observed may be due to the coupling of shear heating, thermal pressurization and diffusion. In the absence of a stabilizing mechanism shear deformation in a continuum analysis will collapse to an infinitesimally thin zone[186]. Two possible stabilizing mechanisms, studied in this paper, are rate-strengthening friction and dilatancy. For rate-strengthening friction alone, a linear stability analysis shows that uniform shear of a gouge layer is unstable for perturbations exceeding a critical wavelength. Using this critical wavelength we predict a width for the localized zone as a function of the gouge properties. Taking representative parameters for fault gouge at typical centroidal depths of crustal seismogenic zones, we predict localized zones of order $5 - 40$ μm wide, roughly consistent with field and experimental observations. For dilatancy alone, linearized strain

rate perturbations with a sufficiently large wavelength will undergo transient exponential growth before decaying back to uniform shear. The total perturbation strain accumulated during this transient strain rate localization is shown to be largely controlled by a single dimensionless parameter E, which is a measure of the dilatancy of the gouge material due to an increase in strain rate.

2.1 Introduction

Detailed examinations of fault zones have shown a hierarchical structure, with a fault core composed of ultracataclasite and fault gouge sitting within a broader damage zone. Further investigation reveals a zone of highly localized shear on the order of $10 - 300$ μm wide nested within the fault core[101,43,55]. This localized shear zone is interpreted as the principal slip surface of the fault. What determines the width of this zone? Extreme localization is readily understandable in a fluid-saturated fault gouge undergoing thermal pressurization during shear. In this paper and the companion paper *Platt et al.* [2014][166] we study how two localization limiting mechanisms could combine with thermal pressurization and hydrothermal diffusion to set the width of the localized shear zone during rapid shear. The first limiting mechanism is frictional rate-strengthening. The friction coefficient varies with the rate of shearing in a manner suggested by laboratory experiments, with strengthening observed at higher temperatures or higher clay fractions. Such rate-strengthening friction is appropriate in stable regions of faults where rupture cannot nucleate but can propagate through, or in initially unstable regions that have been driven to high temperatures by shear heating. The second limiting mechanism is dilatancy. The gouge porosity, and hence pore fluid volume, increases with shear strain rate, reducing the pore pressure. When this oc-

curs faster than fluid diffusion into the newly expanded pore space, dilatancy will have a strengthening effect. In the absence of a limiting mechanism the shearing will collapse to a zone of zero width in a continuum model, as noted in *Rice* [2006][186]. In this paper we present a linear stability analysis of these two mechanisms separately. For frictional rate-strengthening alone the solution for homogeneous deformation of the gouge presented in *Lachenbruch* [1980][127] is unstable for gouge layer thicknesses exceeding a critical value. This critical thickness is interpreted as the localization thickness during rapid shear. For dilatancy alone the linear stability analysis predicts intense transient strain rate localization, followed by a return to uniform shear of the gouge layer at large slips. We show that, except for very small wavelengths, the total accumulated strain during this transient localization is controlled by a single dimensionless parameter representing the efficiency of dilatant strengthening.

The companion paper *Platt et al.* [2014][166] presents full numerical simulations that complement the linear stability predictions of this paper. These simulations show that for both stabilizing mechanisms the final localized zone thickness is almost independent of the initial thickness of the gouge layer, and is controlled by the physical properties of the gouge. The influence of strain rate localization on shear strength evolution is also studied, and we observe dramatic weakening associated with the onset of localization caused by the focusing of frictional heating into a narrower zone.

2.1.1 Field observations of strain localization

Chester and Chester [1998][42] studied the structure of the Punchbowl Fault, an inactive branch of the San Andreas fault system thought to have accommodated 44 km of slip[44], at

a depth of $\sim 3 - 4$ km[169]. They observed a continuous ultracataclasite layer $0.15 - 0.55$ m wide, surrounded by a much broader damage zone ~15 m wide. Within this ultracataclasite layer there runs a single continuous fracture surface, which *Chester and Chester* [1998][42] called the principal fracture surface, parallel to the direction of shear. Other fracture surfaces exist but are <1 m in length, and are truncated by the principal fracture surface. These fracture surfaces are thought to represent strain localization within the ultracataclasite layer, and the principal fracture surface is identified as the principal slip surface for the Punchbowl Fault. Subsequent studies of a thin section sample under cross-polarized light showed that the majority of the shearing had been accommodated within in a zone just $100 - 300$ μm wide[43] (see the thin section from their work reproduced as Figure 1b in *Rice* [2006][186]). The concurrent work of *Heermance et al.* [2003][101] also showed 100 micron-scale strain localization, and will be discussed further below.

In another study *De Paola et al.* [2008][55] analyzed a series of normal faults in the Northern Apennines, hosted in dolostone and anhydrite rocks. On small displacement faults, with a slip of < 10 m, they observed a cataclasite fault core a few centimeters thick. Within this gouge layer zones of intense shear strain localization are observed, ranging in width from a few to tens of microns, running parallel to the fault core boundary. *De Paola et al.* [2008][55] also studied a larger displacement fault, with a slip of > 100 m. In this case the fault core was much broader, $5 - 6$ m wide, and contained multiple principal slip surfaces. Associated with each principal slip surface was a layer of very-fine grained cataclasites $2 - 3$ mm wide, and within each of these layers they observed a zone of localized shear ~ 10 μm wide. These observations appear to show that, in the region studied in *De Paola et al.* [2008][55], although the width of the fault core and surrounding damage zone increases

with fault displacement, the localized shear zones observed are consistently $\sim 1 - 10\ \mu$m wide.

Not all field observations showed micron-scale strain localization. *Boullier et al.* [2009][27] analyzed the microstructural distribution in two borehole samples taken from depths of 1111 m and 1136 m on the Chelunqpu fault after the Mw 7.6 Chi-Chi earthquake in 1999. In both samples they interpreted the principal slip surface to be an isotropic gouge layer $3 - 20$ mm wide with no evidence of sub-millimeter scale localized shear structures. *Heermance et al.* [2003][101] also analyzed the principal slip surface of the Chelungpu fault using a combination of borehole drilling and outcrops. They found evidence of extreme strain localization in the northern region of the fault, down to a width of approximately $50 - 300\ \mu$m, and much more diffuse deformation in the southern region. Noting that the location of distributed shear in *Boullier et al.* [2009][27] is near the location of micron-scale localization in *Heermance et al.* [2003][101] it appears that extreme strain localization does not occur in every seismic event, and there may be significant spatial variation in the localized zone thickness. For completeness we also mention one final observation of millimeter-scale localization to supplement the centimeter-scale and micron-scale structures discussed above. *Wibberley and Shimamoto* [2003][243] identified a "central slip zone" on the Median Tectonic Line fault with a nominal thickness of 3 mm (C. A. Wibberley, private communication, 2003), although no measurements were made to look for finer scale structures within this zone.

It should be noted that there is no definitive proof that the shear zones described in this subsection are formed coseismically, though highly localized shear is commonly used as an indicator of seismic deformation.

2.1.2 Localization in high-velocity friction experiments

Velocity stepping experiments first presented in *Dieterich* [1979][57] have led to a much clearer understanding of friction, and the frictional response to velocity changes, at slip rates of $\sim 1 - 10\ \mu$m/s. However, the picture at seismic slip rates is much less clear with complicated thermal and hydraulic processes obscuring the purely frictional response. Rotary shear devices have been used in recent years to investigate this high-velocity regime for rock-rock friction and gouge materials[223]. In a typical experiment, for example *Brantut et al.* [2008][29], *Kitajima et al.* [2010][124], *Reches et al.* [2012][177], *Smith et al.* [2013][211] and many additional studies, a gouge layer around 1 mm wide is confined between two cylindrical blocks, one rotating and one stationary, leading to rapid shearing of the gouge.

Kitajima et al. [2010][124] performed rotary shear experiments on a fluid-saturated gouge composed of disaggregated ultracataclasite from the Punchbowl fault. The resulting microstructures were analyzed under plane-polarized and cross-polarized light by cutting thin sections through the axis of the cylinder, creating a radial cross-section of the gouge material. Four distinct microstructural units were identified, and the formation of the different units was correlated with different slip and slip rate conditions. At slip rates of $\sim$ 1 m/s they observed two distinct microstructural units, one a less compacted gouge with a random fabric, the other a zone of extremely fine grained material with a very strong foliation that is interpreted as a region of intense strain localization. The width of this localized zone is typically $\sim$100 μm. However, the distinct banded nature of the zone of highly localized shear may indicate multiple slipping zones each much thinner than the total width of the localized zone. *Kitajima et al.* [2010][124] linked the onset of strain localization with the observed dynamic weakening, an observation in agreement with the results presented in the

companion paper *Platt et al.* [2014][166].

A similar set of rotary shear experiments was presented in *Brantut et al.* [2008][29] using gouge taken from the Median Tectonic Line, Southwest Japan. Optical microscopy showed a thin, darker zone $\sim 1 - 10$ μm wide, which due to a lack of other indications of deformation in the gouge layer was identified as the main slipping zone of the experiment. Other high-velocity friction experiments[28,150] have also shown evidence of micron-scale strain localization.

It should be noted that micron-scale strain localization also occurs in rotary shear experiments performed at slip rates of ~ 10 μm/s[24,4,7], and the model presented here cannot explain these observations.

2.1.3 Influence on rupture properties

Previous studies of thermally-driven weakening mechanisms have shown that the width of the deforming zone is a key parameter. Narrow deforming zones concentrate the frictional heating leading to large temperature rises, and thus more rapid weakening. This can be seen in the solution of *Lachenbruch* [1980][127] for uniform shear of a gouge layer undergoing thermal pressurization, where the slip-weakening distance scales linearly with the width of the deforming zone. Very thin zones require only small slips to cause dynamic weakening. This may explain why the gouge layer width plays a significant role in determining the rupture propagation mode in the calculations performed in *Noda et al.* [2009][155], which showed a transition from crack-like ruptures through growing slip pulses to arresting slip pulses as the gouge layer thickness was increased. Thinner layers will experience more weakening and thus are more likely to propagate as an accelerating crack-like rupture. Extending

the thermal pressurization model in a different direction, *Rempel and Rice* [2006][180] studied the temperature rise expected for a uniformly sheared, fluid-saturated gouge layer. They found that, for a fixed amount of slip, thinner shear zones will experience larger temperature rises. Thus the deforming zone thickness may determine if melting occurs, or if other temperature controlled dynamic weakening mechanisms such as thermal decomposition are activated. A final example of the importance of the deforming zone thickness can be seen in the solutions for a steadily propagating slip pulse presented in *Garagash* [2012][86]. In these results the total slip in the event scales linearly with the deforming zone thickness, and the slip duration scales as the square of the deforming zone thickness.

2.2 Model Derivation

Figure 2.1 shows an idealized one-dimensional model for deformation of a fluid-saturated gouge material. The layer represents a gouge zone inherited from previous stable or seismic slip. In this model the only non-zero velocity component, $u(y,t)$, is parallel to the fault zone and depends only on the time since the onset of shear, t, and the coordinate perpendicular to the direction of slip, y. The stresses in the deforming zone are the shear stress τ, a constant compressive normal stress σ_n in the y direction, and whatever other normal stresses are required to meet the constraints of zero straining in the other directions.

We do not intend to model a specific fault, and our results are valid for any fluid-saturated gouge material with a rate-strengthening friction law. Seismic shear in rate-strengthening materials is expected to occur when a rupture that nucleated elsewhere propagates into a stably creeping region of a fault, or when a fault that can nucleate earthquakes is heated to temperatures associated with rate-strengthening friction[24,25].

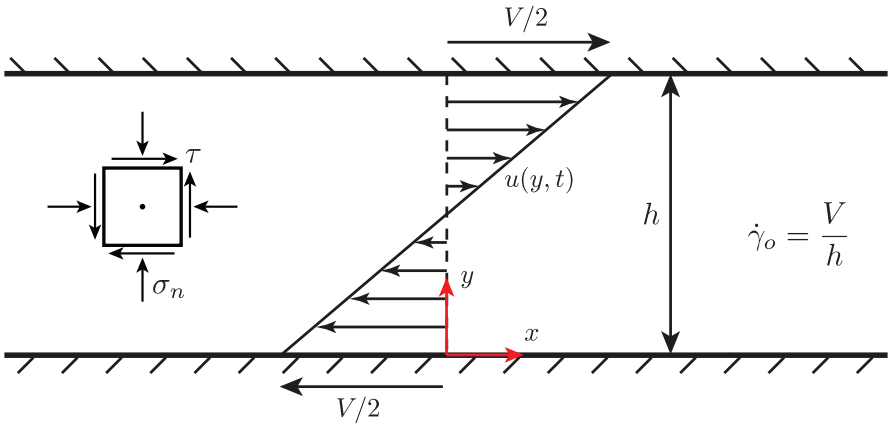

Figure 2.1: A fault zone idealized as a gouge layer of thickness h subjected to homogeneous shear strain rate $\dot{\gamma}_o$. The stresses in the layer are a constant normal stress σ_n, a shear stress τ and whatever other normal stresses in the x and z directions needed to maintain zero normal strain in these directions.

2.2.1 Mechanical equilibrium

Rice [2006][186] hypothesized that inertial effects within the gouge will be negligible since even very large accelerations contribute a small amount to the change of stress over the small distances, on the order of a few 10's mm, over which thermal and fluid diffusion is important. This means that the deformation process can be approximated as quasi-static, and the stresses within the layer satisfy

$$\frac{\partial \tau}{\partial y} = 0 \quad , \quad \frac{\partial \sigma_n}{\partial y} = 0. \tag{2.1}$$

The quasi-static approximation means that the shear and normal stress do not depend on y, and are at most a function of t. In the companion paper to this study we further analyze the small inertial effects and investigate under what conditions they may become impor-

tant[166].

2.2.2 Gouge friction

The shear stress is taken to be the product of a friction coefficient f and the Terzaghi effective stress

$$\tau = f(\sigma_n - p), \tag{2.2}$$

where $p = p(y,t)$ is the pore pressure. Many studies of thermally driven weakening mechanisms assume that the friction coefficient is constant. When constant friction and mechanical equilibrium are assumed, and dilatancy is neglected, only two forms of deformation are possible, homogeneous shear in the gouge material or slip on the plane of maximum pore pressure[186]. However, when the friction coefficient is allowed to vary a finite thickness shear zone can exist, with regions of large pore pressure balanced by larger friction coefficients. In this paper we consider a friction coefficient that is a function of the strain rate alone,

$$f = f(\dot{\gamma}) \quad , \quad \dot{\gamma} = \frac{\partial u}{\partial y}. \tag{2.3}$$

The analysis in this paper requires only the linearization of the friction law around the uniform strain rate $\dot{\gamma}_o$,

$$f(\dot{\gamma}) = f_o + \frac{a-b}{\dot{\gamma}_o}\left(\dot{\gamma} - \dot{\gamma}_o\right), \tag{2.4}$$

where we have defined,

$$f_o = f(\dot{\gamma}_o) \quad , \quad (a-b) = \dot{\gamma}_o \frac{df}{d\dot{\gamma}}\bigg|_{\dot{\gamma}=\dot{\gamma}_o}. \tag{2.5}$$

We consider a rate-strengthening material so $(a - b) > 0$. The form of these coefficients is chosen so that $(a - b)$ is equivalent to the typical rate-and-state friction parameter when one writes

$$f = f_o + (a - b) \log(\dot{\gamma}/\dot{\gamma}_o) \tag{2.6}$$

for shearing at steady state. This standard logarithmic form is used in the companion paper *Platt et al.* [2014][166]. However, the results in this paper are valid for any friction law that depends on strain rate alone. We ignore the state evolution effects accompanying changes in shear rate, not least because there is no presently accepted way of describing these effects of distributed shear in gouge. For regions of rate-weakening friction a fuller description that includes a dependence on state and a procedure to limit localization would be needed. The inclusion of the direct effect, meaning that any increase in strain rate leads to a transient increase in the friction coefficient, may prevent localization from evolving to an infinitesimally narrow zone.

2.2.3 Conservation of energy

Conservation of energy can be expressed as

$$\tau\dot{\gamma} = \rho c \frac{\partial T}{\partial t} + \frac{\partial q_h}{\partial y}, \tag{2.7}$$

where T is the temperature, c is the specific heat, ρ is the density in the reference state and q_h is the heat flux. This expression neglects generally small additional terms due to the work of the normal stress and pore pressure, and internal energy transfer due to flow of the fluid, a common assumption justified in *Mase and Smith* [1985,1987][144,145] for representative per-

meabilities of fault gouges. The heat flux is related to the temperature gradient by Fourier's law

$$q_h = -K\frac{\partial T}{\partial y}, \tag{2.8}$$

where K is the thermal conductivity. Substituting (2.8) into (2.7) and simplifying we arrive at

$$\frac{\partial T}{\partial t} = \frac{\tau\dot{\gamma}}{\rho c} + \alpha_{th}\frac{\partial^2 T}{\partial y^2}, \tag{2.9}$$

where $\alpha_{th} = K/\rho c$ is the thermal diffusivity. When combining equations (2.8) and (2.9) we have assumed that the thermal conductivity is insensitive to temperature and porosity changes.

2.2.4 Conservation of pore fluid mass

Conservation of pore fluid mass can be expressed as

$$\frac{\partial m}{\partial t} + \frac{\partial q_f}{\partial y} = 0, \tag{2.10}$$

where m is the fluid mass per unit volume of porous medium with that volume as measured in a reference state, and q_f is the pore fluid mass flux. According to Darcy's Law, this mass flux is proportional to the negative of the pore pressure gradient

$$q_f = -\frac{\rho_f k}{\eta_f}\frac{\partial p}{\partial y}, \tag{2.11}$$

where k is the intrinsic permeability, and ρ_f and η_f are the density and viscosity of pore fluid respectively. Writing $m = \rho_f n$, where n is the porosity, and differentiating this prod-

uct yields

$$\frac{\partial m}{\partial t} = n\frac{\partial \rho_f}{\partial t} + \rho_f \left(\frac{\partial n^{el}}{\partial t} + \frac{\partial n^{pl}}{\partial t} \right). \tag{2.12}$$

Here the rate of change of the porosity has been written as the sum of elastic and inelastic or plastic contributions from dilatancy, as in the *Segall and Rice* [1995][201] formulation. We later explain a possible reinterpretation of the symbols n^{el} and n^{pl} in a manner consistent with critical state soil mechanics[196,152] which may be more appropriate for sustained shearing (rather than nucleation of instability as considered in *Segall and Rice* [1995][201]). Variations in the elastic porosity with pore pressure and temperature can be accounted for by setting

$$\frac{1}{n}\frac{\partial n^{el}}{\partial t} = \beta_n \frac{\partial p}{\partial t} + \lambda_n \frac{\partial T}{\partial t}, \tag{2.13}$$

where β_n and λ_n are the compressibility and the thermal expansivity of the pore volume respectively. These can be expressed in terms of coefficients for poro-thermo-elasticity[147,51] evaluated for constant normal stress perpendicular to the fault zone ($\sigma_n = \text{const}$) and zero normal strains in the plane of the fault zone (see *Rice* [2006][186]). In a similar fashion the rate of change of the fluid density ρ_f can be expressed as

$$\frac{1}{\rho_f}\frac{\partial \rho_f}{\partial t} = \beta_f \frac{\partial p}{\partial t} - \lambda_f \frac{\partial T}{\partial t}, \tag{2.14}$$

where β_f and λ_f are the compressibility and thermal expansivity of the pore fluid respectively. Combining equations (2.10)-(2.14) we arrive at

$$\frac{\partial p}{\partial t} = \Lambda \frac{\partial T}{\partial t} - \frac{1}{\beta}\frac{\partial n^{pl}}{\partial t} + \alpha_{hy}\frac{\partial^2 p}{\partial y^2}, \tag{2.15}$$

where

$$\beta \equiv n(\beta_f + \beta_n) \quad , \quad \Lambda \equiv \frac{\lambda_f - \lambda_n}{\beta_f + \beta_n}. \tag{2.16}$$

Here β is an elastic storage coefficient and Λ is the ratio of pore pressure change to temperature change during undrained, adiabatic elastic deformation. The hydraulic diffusivity is defined as

$$\alpha_{hy} = k/[\eta_f n(\beta_f + \beta_n)] \tag{2.17}$$

and is assumed to be constant. The first term on the right hand side of equation (2.15) models thermal pressurization, the second term models pore pressure drops due to inelastic porosity increases, and the final term represents hydraulic diffusion.

Equations equivalent to (2.9) and (2.15) have been used by *Garagash and Rudnicki* [2003][85] and *Segall and Rice* [1995][201] with $\partial^2 p/\partial y^2$ and $\partial^2 T/\partial y^2$ approximated by the difference between local and remote values of p and T divided by a characteristic length squared. This form is appropriate for the single degree-of-freedom (spring-slider) model considered in those papers, but is too severe an idealization for continuum deformation.

2.2.5 Gouge dilatancy

In this paper we assume that all of the inelastic porosity change is due to dilatancy, although other mechanisms also exist, with one possible example being thermal decomposition[217]. We assume that the gouge is sufficiently sheared that all porosity changes are due to changes in strain rate, allowing us to write $n^{pl} = n^{pl}(\dot{\gamma})$. As with the friction law, the analysis in this

paper requires only the linearized form

$$n^{pl}(\dot{\gamma}) = n_o^{pl} + \varepsilon \frac{\dot{\gamma} - \dot{\gamma}_o}{\dot{\gamma}_o}, \tag{2.18}$$

where we define

$$n_o^{pl} = n^{pl}(\dot{\gamma}_o) \quad , \quad \varepsilon = \dot{\gamma}_o \frac{dn^{pl}}{d\dot{\gamma}}\bigg|_{\dot{\gamma}=\dot{\gamma}_o}. \tag{2.19}$$

Here n_o^{pl} is the plastic porosity at the uniform strain rate $\dot{\gamma}_o$, and ε is a measure of the strength of dilatancy in the gouge material, with a larger value of ε leading to more dilation. The forms of the coefficients are chosen to agree with the steady state form for shear dilatancy at low strain rates introduced by *Segall and Rice* [1995][201], and based on experiments in *Marone et al.* [1990][143]. Note that the dilatancy rate vanishes for constant strain rate.

2.2.6 Critical state reinterpretation

In the classical critical state formulation for sustained shear, rate effects are ignored and the porosity is taken to be a function of effective normal stress (which we may generalize to be a function of effective stress and, weakly, temperature). We reinterpret the symbol n^{el} as

$$n^{el} = n^{cs}(\sigma_n - p, T), \tag{2.20}$$

where the superscript cs denotes critical state and, in our case, σ_n is constant. That is, we represent the porosity as the sum of the rate-independent critical state form (2.20), and take n^{pl} as above in equations (2.18) and (2.19) to represent the actual rate effects neglected in the standard critical state formulations. Thus β_n and λ_n are redefined by equation (2.13) above,

now with n^{el} replaced by n^{cs}, with σ_n constant. They are now interpreted as coefficients expressing rate-independent changes of porosity linearized about the critical state.

We expect the (small) thermal expansion effect to be little changed, although now β_n is expected to be larger because the change of porosity n with effective stress at the critical state (defining $-\beta_n$) is comparable in magnitude to the change of n with effective stress during one-dimensional consolidation. The latter compressibility is typically several times larger than the compressibility for elastic response (say by unloading from one-dimensional consolidation), which is the basis for estimates of β_n in *Segall and Rice* [1995][201] and *Rice* [2006][186].

2.3 Parameter Values

The hydraulic parameters of the problem are poorly constrained, and depend strongly on the stress state, pore pressure, temperature, and amount of damage that develops during initial shear of the fault gouge. To account approximately for these complications we use the parameters in Table 1 of *Rempel and Rice* [2006][180], which are based on Tables 1-3 of *Rice* [2006][186] and the procedures in *Rice* [2006][186] to take account for damage and variations of properties with pressure and temperature.

The large stresses near the tip of a dynamically propagating rupture may alter the gouge through processes such as comminution and opening of cemented micro-cracks. To model this damage *Rice* [2006][186] made the somewhat arbitrary choices to increase the permeability by a factor of ten and the drained compressibility by a factor of two relative to their laboratory values at a given stress, pore pressure, and temperature. This leads to parameter sets modeling an intact and damaged material.

Parameter	Intact material, nominal values	Intact material, path-averaged values	Damaged material, nominal values	Damaged material, path-averaged values
α_{th}, mm^2/s	0.7	0.66	0.7	0.54
ρc, MPa/K	2.7	2.7	2.7	2.7
Λ, MPa/K	0.93	0.89	0.31	0.30
α_{hy}, mm^2/s	0.86	2.05	3.52	6.71
β, $\times 10^{-10}$ Pa^{-1}	0.52	0.55	1.26	2.97
ε	1.7×10^{-4}	1.7×10^{-4}	1.7×10^{-4}	1.7×10^{-4}
$\sigma_n - p_a$, MPa	126	126	126	126
ρ, kg/m^3	2800	2800	2800	2800

Table 2.1: Representative parameters modeling a centroidal depth of 7 km. Thermal and hydraulic properties are taken from Table 1 of *Rempel and Rice* [2006][180], which are based on Tables 1-3 of *Rice* [2006][186] and the procedures in *Rice* [2006][186] to take account of (1) damage to the fault zone material at the onset of shearing, due to concentrated stresses near the tip of a propagating rupture front, and (2) variations of properties with pressure and temperature (for the path-averaged values). To model the damaged gouge, permeability is increased by a factor of ten, and the drained compressibility by a factor of two. The path-averaged values roughly account for parameter variations with pore pressure p and temperature T; a p-T path is calculated based on the nominal parameters, and new parameter values are chosen as averages of parameter values along that path. The ambient effective stress is calculated using an effective stress gradient of 18 MPa/km. The value of ε is taken from *Segall and Rice* [1995][201], and is found by fitting to the low strain rate experiments performed by *Marone et al.* [1990][143].

Pore fluid properties, and thus parameters such as α_{hy} and Λ that depend on the fluid properties, will change with pore pressure and temperature. The simplest choice to account for these changes is to evaluate all properties at the ambient pore pressure and temperature conditions. We call parameter sets created using this choice the nominal parameters. Another approach suggested in *Rice* [2006][186] is to average the parameters over the p-T path anticipated from calculations based on the nominal parameter values. Parameter sets that use this method are called path-averaged parameters.

These methods lead to the four parameter sets, nominal and path-averaged parameters for an intact and damaged material, summarized in Table 2.1. All four parameter sets are intended to model a depth of 7 km, a typical centroidal depth for a crustal seismogenic zone.

The final parameter in the pore pressure equation is ε, which models the inelastic porosity change associated with a change in strain rate. We choose $\varepsilon = 1.7 \times 10^{-4}$, which is the value *Segall and Rice* [1995][201] found by fitting to the experimental data in *Marone et al.* [1990][143]. As with the frictional parameters, ε is inferred from experiments performed at strain rates much lower than those considered here. The value of ε appropriate for high strain rates is uncertain.

Some observations of strain localization come from borehole drilling, which typically intersects the fault at a depth much shallower than 7 km[101,27]. To allow comparisons with these observations we also select an additional set of parameters intended to model the uppermost region of the crust, assuming ambient conditions appropriate for a depth of 1 km. These are listed in Table 2.2, and a full discussion on how these parameters are chosen is included in the companion paper *Platt et al.* [2014][166]. As with the parameters modeling a depth of 7 km, we account for damage to the material using the method in *Rice* [2006][186]. However, we do not use the path-averaging technique to account for parameter variations due to changes in temperature and pressure, and all parameters are evaluated at the ambient conditions.

The thermal parameters of the problem are more tightly constrained than the hydraulic parameters. We choose the specific heat $\rho c = 2.7$ MPa/K[127,145]. *Rice* [2006][186] notes a range of 0.5-0.7 mm^2/s for α_{th}, and based on this we choose $\alpha_{th} = 0.7$ mm^2/s for the nominal parameter sets, and take the values from *Rempel and Rice* [2006][180] for the path-averaged parameter sets.

Current experiments are unable to provide a friction law of the form $f(\dot{\gamma})$ at the high strain rates considered in this study due to the difficulty of isolating the pure frictional

Parameter	Intact material,	Damaged material,
α_{th}, mm^2/s	0.7	0.7
ρc, MPa/K	2.7	2.7
Λ, MPa/K	0.22	0.068
α_{hy}, mm^2/s	2.34	7.15
β, $\times 10^{-10}$ Pa^{-1}	1.34	4.39
ε	1.7×10^{-4}	1.7×10^{-4}
$\sigma_n - p_a$, MPa	18	18
ρ, kg/m^3	2800	2800

Table 2.2: Representative parameters modeling a depth of 1 km, taken from *Platt et al.* [2014][166]. A fuller discussion on the origin of the parameters is included in *Platt et al.* [2014][166].

response from other temperature and pore fluid related effects, and problems confining gouge materials at high slip rates. Lacking data in the ideal strain rate range we instead use steady state friction values from low slip rate friction experiments[57,193,227,134]. We implicitly ignore dynamic weakening mechanisms such as flash heating[186,93] or the as yet poorly understood weakening that seems to be associated with gouge particles in the nanometer size range[61]. One ad hoc way to account for such a mechanism may be to choose a lower value of f_o. Even when we have accepted the compromise of using the low strain rate friction law to describe seismic deformation there is still a wide range of possible values for f_o and $(a - b)$. Data from low strain rate experiments on granite under hydrothermal conditions show that both f_o and $(a - b)$ vary with temperature[41,23,24,25]; another study shows how fault mineralogy can alter the steady state friction coefficient f_o[110]. For the sake of simplicity we will neglect these complications and choose the fixed values $f_o = 0.6$ and $(a - b) = 0.025$. A strong argument could be made for different values. Predicted thicknesses of shear zones will be shown to be proportional to approximately $(a - b)/{f_o}^2$, making it straightforward to reinterpret numbers and plots for other choices of the frictional

parameters. If a different friction law that depends on strain rate alone is assumed then effective values of f_o and $(a-b)$ can be found by linearizing about the uniform strain rate $\dot{\gamma}_o$, as shown in equation (2.5).

2.4 Spatially uniform solution

In this section we model a homogeneous medium that is uniformly sheared at a constant strain rate $\dot{\gamma} = \dot{\gamma}_o$ under locally undrained and adiabatic conditions, writing the corresponding solutions to equations (2.9) and (2.15). The assumption of undrained and adiabatic conditions is valid when the boundaries of the gouge layer are impermeable and thermally insulating. These conditions are also asymptotically valid for the earliest stage of deformation when diffusion has had very limited time to act. In this scenario the stress, pore pressure and temperature are independent of y, meaning that

$$\{\tau(y,t), p(y,t), T(y,t)\} = \{\tau_0(t), p_0(t), T_0(t)\}\,. \tag{2.21}$$

For a gouge layer with a thickness h accommodating a slip rate V, the geometry sketched in Figure 2.1, *Lachenbruch* [1980][127] developed an exact solution for this system. The shear stress and pore pressure are related by

$$\tau_0(t) = f_o \bar{\sigma}_0(t), \tag{2.22}$$

where

$$\bar{\sigma}_0(t) = \sigma_n - p_0(t) = (\sigma_n - p_a)\exp\left[-\frac{f_o \Lambda}{\rho c}\dot{\gamma}_o t\right] \tag{2.23}$$

and p_a is the ambient pore pressure present before shear begins. This means that

$$\gamma_w = \frac{\rho c}{f_o \Lambda} \tag{2.24}$$

is the characteristic weakening shear strain for thermal pressurization under undrained and adiabatic conditions. This can be converted to a slip weakening distance for a gouge layer with a finite thickness h, leading to

$$D_{ud,ad} = h \frac{\rho c}{f_o \Lambda}. \tag{2.25}$$

Note that the slip weakening distance scales with the width of the deforming gouge, making strain localization crucial in the evolution of strength during shear. This will be investigated further in the companion paper *Platt et al.* [2014][166]. *Lachenbruch* [1980][127] also solved for the temperature evolution

$$T_0(t) = T_0(0) + \frac{\bar{\sigma}_a}{\Lambda} \left[1 - \exp\left(-\frac{f_o \Lambda}{\rho c} \dot{\gamma}_o t \right) \right], \tag{2.26}$$

where $\bar{\sigma}_a = \sigma_n - p_a$ is the ambient effective stress. Note that our formulation of dilatancy, which accounts only for porosity changes due to changes in strain rate, does not alter the solution from *Lachenbruch* [1980][127]. *Lachenbruch* [1980][127] also considered a constant dilation rate, and in this case the shear strength (2.22) decays exponentially to a finite value rather than zero. However, if dilation is confined to the early stages of deformation, as is consistent with our formulation of dilatancy, then the effect is essentially to increase $\bar{\sigma}_0(0)$ (see *Rice* [2006][186]).

For a constant friction coefficient this uniform shear solution is the only possible solution in which the deforming zone has a finite width. The alternative is slip on the plane of maximum pore pressure, with no deformation in the rest of the system. If the rate-dependence of the friction law is accounted for then the straining can localize to a thin zone with a small, but finite, width. In the following section we show what selects this critical width for the deforming zone.

2.5 Linear stability of uniform shear

In this section we study the stability of small spatial perturbations away from the uniform shear solution. The velocity, pore pressure and temperature are written as the sum of the spatially uniform solution from the previous section and a small spatially dependent perturbation,

$$\tau(y,t) = f_o\bar{\sigma}_0(t) + \tau_1(y,t) \tag{2.27a}$$

$$\dot{\gamma}(y,t) = \dot{\gamma}_0 + \dot{\gamma}_1(y,t) \tag{2.27b}$$

$$p(y,t) = p_0(t) + p_1(y,t) \tag{2.27c}$$

$$T(y,t) = T_0(t) + T_1(y,t) \tag{2.27d}$$

where the unperturbed strain rate $\dot{\gamma}_0$ is chosen as the reference strain rate $\dot{\gamma}_o$ in the previous section. Substituting these forms for τ, $\dot{\gamma}$, p and T into our model from Section 2.2 (Equa-

tions (2.1)-(2.4), (2.9) and (2.15)) and linearizing we arrive at,

$$\frac{\partial \tau_1}{\partial y} = 0 \quad , \quad \tau_1 = (\sigma_n - p_0)\,\frac{(a-b)}{\dot{\gamma}_o}\dot{\gamma}_1 - f_o p_1 \tag{2.28a}$$

$$\frac{\partial T_1}{\partial t} = \frac{\dot{\gamma}_o \tau_1 + f_o \bar{\sigma}_0(t)\dot{\gamma}_1}{\rho c} + \alpha_{th}\frac{\partial^2 T_1}{\partial y^2} \tag{2.28b}$$

$$\frac{\partial p_1}{\partial t} = \Lambda\frac{\partial T_1}{\partial t} - \frac{\varepsilon}{\beta\dot{\gamma}_o}\frac{\partial \dot{\gamma}_1}{\partial t} + \alpha_{hy}\frac{\partial^2 p_1}{\partial y^2} \tag{2.28c}$$

Next the spatial dependence of the perturbations is decomposed into Fourier modes with wavelength λ,

$$\{p_1, T_1, \dot{\gamma}_1\} = \Re\left[\{p_1, T_1, \dot{\gamma}_1\}(t)\exp\left(\frac{2\pi i y}{\lambda}\right)\right], \tag{2.29}$$

where the new functions p_1, T_1 and $\dot{\gamma}_1$ now denote complex functions of t alone, and $\Re(F)$ indicates the real part of a complex function F. Equations (2.28) then become

$$\bar{\sigma}_0(t)\frac{(a-b)}{\dot{\gamma}_o}\dot{\gamma}_1 - f_o p_1 = 0 \tag{2.30a}$$

$$\frac{dT_1}{dt} = \frac{f_o \bar{\sigma}_0(t)\dot{\gamma}_1}{\rho c} - \frac{4\pi^2\alpha_{th}}{\lambda^2}T_1 \tag{2.30b}$$

$$\frac{dp_1}{dt} = \Lambda\frac{dT_1}{dt} - \frac{\varepsilon}{\beta\dot{\gamma}_o}\frac{d\dot{\gamma}_1}{dt} - \frac{4\pi^2\alpha_{hy}}{\lambda^2}p_1 \tag{2.30c}$$

The above equations, a linear but non-autonomous system due to the exponentially decaying $\bar{\sigma}_0(t)$, describe the stability of an unbounded gouge material being sheared uniformly with a strain rate of $\dot{\gamma}_o$. This can be specialized for a gouge layer of thickness h sheared between rigid, impermeable and thermally insulating blocks moving relative to each other

with a slip rate V using the boundary conditions

$$\frac{\partial T}{\partial y} = \frac{\partial p}{\partial y} = 0 \quad \text{at} \quad y = 0, h. \tag{2.31}$$

These can be satisfied by perturbations that are proportional to the Fourier mode

$$\cos\left(\frac{\pi N y}{h}\right), \tag{2.32}$$

where N is any positive integer and the wavelength is defined by $\lambda = 2h/N$. We see that N corresponds to the number of half-wavelength oscillations in the gouge layer. Once we have determined the allowed values of λ corresponding to growth or decay of strain rate perturbations, and calling λ_{shr} the longest stable wavelength for which strain rate perturbations do not grow, only shear zones with

$$h < \lambda_{shr}/2 \tag{2.33}$$

will support stable homogeneous shear.

2.6 Stabilization by Frictional Rate-Strengthening Only

First we consider only the effects of frictional rate-strengthening, neglecting dilatancy by setting $\varepsilon = 0$. Using equation (2.30a) we can relate the perturbations in pore pressure and strain rate through

$$\dot{\gamma}_1 = \frac{f_o \dot{\gamma}_o}{(a-b)\bar{\sigma}_0(t)} p_1, \tag{2.34}$$

allowing us to eliminate $\dot{\gamma}_1$ from equations (2.30). We arrive at the pair of equations for p_1 and T_1,

$$\frac{dT_1}{dt} = \frac{f_o^2 \dot{\gamma}_o}{(a-b)\rho c} p_1 - \frac{4\pi^2 \alpha_{th}}{\lambda^2} T_1 \tag{2.35a}$$

$$\frac{dp_1}{dt} = \Lambda \frac{dT_1}{dt} - \frac{4\pi^2 \alpha_{hy}}{\lambda^2} p_1 \tag{2.35b}$$

Remarkably, this sub-system does not explicitly depend on time. It can be solved by perturbations of pressure and temperature of the form

$$\left\{ \begin{array}{c} p_1(t) \\ T_1(t) \end{array} \right\} = \left\{ \begin{array}{c} p_1(0) \\ T_1(0) \end{array} \right\} \exp(st) \tag{2.36}$$

and equation (2.34) then provides the solution for the strain rate perturbation,

$$\dot{\gamma}_1(t) = \frac{f_o \dot{\gamma}_o p_1(0)}{(a-b)(\sigma_n - p_a)} \exp\left[\left(s + \frac{f_o \Lambda}{\rho c} \dot{\gamma}_o \right) t \right]. \tag{2.37}$$

This is a rare case where a system of linear differential equations with some time-dependent coefficients has exact solutions in exponential form, albeit with coefficients of t in the exponentials that are different for $\dot{\gamma}_1$ than for p_1 and T_1. Substituting (2.36) into (2.35) yields two linear equations for $p_1(0)$ and $T_1(0)$. Since the equations are homogeneous, a nonzero solution is possible only if the determinant of the coefficients vanishes. This requires that s satisfy

$$\frac{f_o^2 \Lambda}{(a-b)\rho c} \dot{\gamma}_o s = \left(s + \frac{4\pi^2 \alpha_{th}}{\lambda^2} \right) \left(s + \frac{4\pi^2 \alpha_{hy}}{\lambda^2} \right). \tag{2.38}$$

We can use this equation to determine the stability of uniform shear of a fluid-saturated

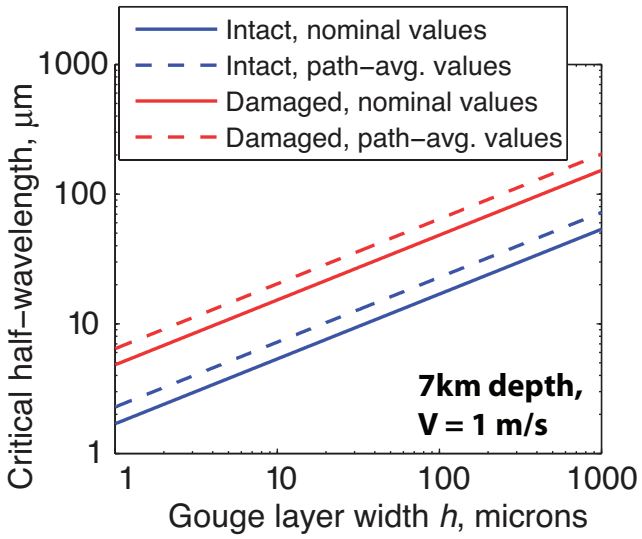

Figure 2.2: Rate-strengthening friction: A plot showing how the critical half-wavelength $\lambda_{shr}/2$ varies with gouge layer thickness for parameters modeling a depth of 7 km and a slip rate $V = 1$ m/s. Since $\dot{\gamma}_o = V/h$ thicker gouge layers experience lower strain rates, leading to a wider critical half-wavelength. Modeling damage as in *Rice* [2006] [186] we find that damaged material is less susceptible to localization due to larger hydraulic diffusion and less efficient thermal pressurization. When we use the path-averaging method from *Rice* [2006] [186] to account for parameter variations with pressure and temperature the predictions increase by about a factor of two.

gouge material. If the real part of the exponential coefficient $s + f_o \Lambda \dot{\gamma}_o / \rho c$ is positive, then the perturbation away from uniform straining grows exponentially in time. This exponential growth is interpreted as strain rate localization. Consequently, the condition that uniform shear be linearly stable is

$$\Re\left(s + \frac{f_o \Lambda}{\rho c}\dot{\gamma}_o\right) < 0. \tag{2.39}$$

As shown in Appendix A.1, this condition is equivalent to wavelengths satisfying

$$\lambda < \lambda_{shr} \equiv 2\pi \sqrt{\frac{(a-b)\rho c}{f_o \Lambda} \frac{\alpha_{th} + \alpha_{hy}}{(f_o + 2(a-b))\dot{\gamma}_o}}. \tag{2.40}$$

Spatial perturbations with wavelengths shorter than the critical value will decay exponentially, and those greater than the critical value will grow exponentially. We highlight (2.40) as the key result of the linear stability analysis. Interested readers can find a much fuller discussion of the possible behaviors associated with different values of s in Appendix A.1.

2.6.1 Width of the localized zone

We now evaluate the critical wavelength using the nominal parameter set for intact material at a depth of 7 km. For a representative seismic slip rate $V = 1$ m/s accommodated over a gouge thickness $h = 10$ mm, leading to a nominal strain rate $\dot{\gamma}_o = 100\ \mathrm{s}^{-1}$, the critical wavelength is $\lambda_{shr} = 0.34$ mm. Recall that for a layer of thickness h the largest possible half-wavelength satisfying insulating and impermeable boundary conditions at the edge of the gouge layer is $\lambda/2 = h$. If the strain rate is $\dot{\gamma}_o = 100\ \mathrm{s}^{-1}$ then the critical half-wavelength is much less than the layer thickness, and thus homogeneous shearing is unstable. Straining will not be distributed over the gouge thickness but, as more fully studied in the companion paper *Platt et al.* [2014][166], will localize to a thinner zone within the gouge comparable to the critical half-wavelength.

Figure 2.2 shows the critical half-wavelength as a function of the gouge layer width h for each of the four parameter sets and a fixed slip rate of $V = 1$ m/s, representative of the time-averaged slip rate in tectonic earthquakes. This value of V can be compared with

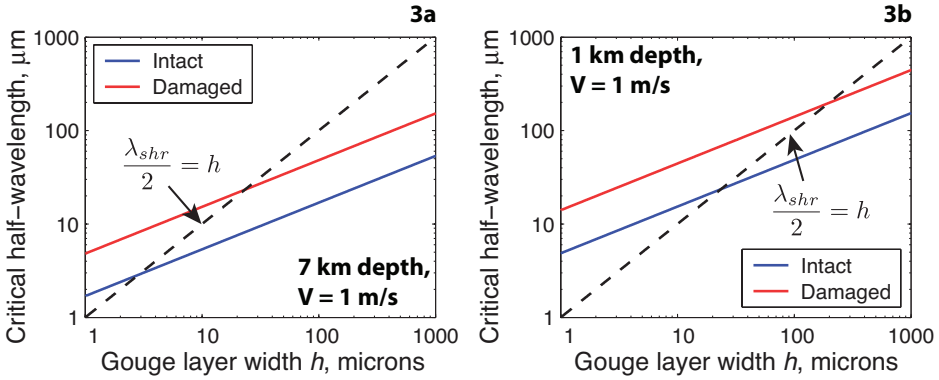

Figure 2.3: Rate-strengthening friction: A pair of plots showing how the critical width W_{rsf} can be calculated graphically for depths of 1 km and 7 km. Both plots use the nominal parameter sets and a slip rate $V = 1$ m/s. To find the self-consistent width for the shear zone we look for points at which the critical half wavelength is equal to the gouge layer thickness. This condition is indicated by the black line, and the intersection points indicated give the localized zone thickness for the different parameter sets. Localization is expected when the gouge layer thickness is greater than this critical width, and uniform shear is expected when the gouge layer thickness is thinner than this critical width. Using the nominal parameter sets for a depth of 7 km we predict a width of 3 μm for the intact material, and a width of 23 μm for the damaged material. Accounting for changes in the parameters with pressure and temperature using the path-averaging technique of *Rice* [2006][186] increases both of these predictions by a factor of two. At a depth of 1 km we predict a width of 24 μm for the intact material and 197 μm for the damaged material. We do not have access to path-averaged parameter sets for a depth of 1 km but we tentatively assume that the change in localized zone width due to changes in parameters with pore pressure and temperature will be the same at 1 km and 7 km.

the slip rate range $0.48 - 1.5$ m/s found as the ratio of the slips to slip durations inferred for seven earthquakes analyzed in *Heaton* [1990][100]. The average slip rate for this range of values is 0.95 m/s. As h increases the strain rate $\dot{\gamma}_o$ decreases leading to wider critical half-wavelengths. We note that parameters modeling damaged material predict larger values of $\lambda_{shr}/2$ than the parameter sets modeling an intact material, due to larger values of α_{hy} and lower values of Λ in the damaged parameter sets. The path-averaged parameters predict

larger values of $\lambda_{shr}/2$ than the nominal parameter sets, possibly suggesting that $\lambda_{shr}/2$ will increase during shearing.

To turn the critical half-wavelength into a consistent estimate for the localized zone thickness W_{rsf}, based on rate-strengthening friction, we search for solutions where the critical half-wavelength is equal to the gouge layer thickness by setting

$$\frac{\lambda_{shr}}{2} = W_{rsf} \quad , \quad \dot{\gamma}_o = \frac{V}{W_{rsf}}, \tag{2.41}$$

leading to the formula

$$W_{rsf} = \pi^2 \frac{(a-b)\rho c}{f_o \Lambda} \frac{\alpha_{hy} + \alpha_{th}}{V(f_o + 2(a-b))}. \tag{2.42}$$

Figure 2.3 shows a graphical solution for this problem. Typical friction data from low strain rate experiments show $f_o \gg (a-b)$, which allows us to simplify the formula to

$$W_{rsf} = \pi^2 \frac{a-b}{f_o^2} \frac{\rho c}{\Lambda} \frac{\alpha_{hy} + \alpha_{th}}{V}. \tag{2.43}$$

We see that the critical thickness is a balance between competing processes. Fluid and thermal diffusion and rate-dependent frictional strengthening tend to expand the zone, while thermal pressurization tends to narrow it.

Our predictions for the localized zone thickness are equivalent to the widest gouge layer that can be sheared uniformly. Localization is expected to occur when the initial width of the deforming zone is thicker than this critical width, and numerical simulations in *Platt et al.* [2014][166] show that straining localizes until it reaches a width very similar to the thick-

ness predicted by equation (2.43). This allows us to compare the predictions from equation (2.43) with field and laboratory observations of localized shear zones sitting within a broader gouge layer without having to make any assumptions about the initial thickness of the deforming zone.

We now evaluate equation (2.42) for the different parameter sets. For a depth of 7 km, using the superscript int to represent intact material, dam to represent damaged material, n for nominal parameter sets, and pa for path-averaged parameter sets,

$$\begin{aligned} W_{rsf}^{int,n} &= 3\,\mu\text{m} \quad , \quad W_{rsf}^{int,pa} = 5\,\mu\text{m}, \\ W_{rsf}^{dam,n} &= 23\,\mu\text{m} \quad , \quad W_{rsf}^{dam,pa} = 41\,\mu\text{m}. \end{aligned} \tag{2.44}$$

Comparison of the nominal and path-averaged parameters demonstrates that variations with pressure and temperature do not strongly influence the results, changing W_{rsf} by about a factor of two. More important in controlling the width is the amount of damage. Damaged material has a larger value of α_{hy} and a smaller value of Λ, leading to predictions for W_{rsf} that are an order of magnitude wider than those for intact material. Caution must be used in applying this result, since the model for damage used in *Rice* [2006][186] is somewhat arbitrary.

Next we compare the predictions for a depths of 7 km and 1 km. Using the parameters from *Platt et al.* [2014][166] for an ambient effective stress $(\sigma_n - p_a) = 18$ MPa, summarized in Table 2.2, in (2.42) we find

$$W_{rsf}^{1km,int} = 24\,\mu\text{m} \quad , \quad W_{rsf}^{1km,dam} = 197\,\mu\text{m}. \tag{2.45}$$

The localized zone is predicted to be wider at shallower depths. When considering the parameters modeling a depth of 7 km, the path-averaged values approximately doubled W_{rsf} for both intact and damaged material. Although we do not have calculations of path-averaged parameters for a depth of 1 km, we tentatively assume they will also increase W_{rsf} by $70 - 80\%$, suggesting widths of ~ 40 μm for intact material, and ~ 350 μm for damaged material.

We note that *Benallal and Comi* [2003][11] have addressed the possible instability of spatially homogeneous elastic-plastic deformation, and onset of localized straining, in fluid-saturated porous media. That was studied initially without consideration of the effects of frictional heating and thermal pressurization, with those effects being added to their analysis subsequently by *Benallal* [2005][12]. Their model did not include a non-zero viscoplastic, or rate-dependence, of friction, which is represented here by the $(a - b)$ term and is seen in the expressions above, and in the accompanying paper *Platt et al.* [2014][166], to be critical to our results for a non-zero thickness of the localized zone, which thickness vanishes when $(a - b) \to 0$.

2.7 Stabilization by Dilatancy Only

2.7.1 Transient growth of perturbations

Neglecting frictional rate-strengthening corresponds to taking $(a - b) \to 0$ in (2.30a), which requires that the perturbation in pore fluid pressure vanish. Setting $p_1 = 0$ in equation (2.30c) we find,

$$-\Lambda T_1(t) + (\varepsilon/\beta\dot{\gamma}_o)\,\dot{\gamma}_1(t) = (\varepsilon/\beta\dot{\gamma}_o)\,C, \tag{2.46}$$

where C is the constant

$$C = \dot{\gamma}_1(0) - (\Lambda\beta\dot{\gamma}_o/\varepsilon)\, T_1(0). \tag{2.47}$$

We can use (2.46) to eliminate T_1 from (2.30b) leading to an equation for $\dot{\gamma}_1$ alone. To have a more compact notation in the formulae which follow we redefine the strain rate perturbation $\dot{\gamma}_1$ as a function of the nondimensional time $\hat{t} = t/t_w$, where $t_w = \rho c/f_o\Lambda\dot{\gamma}_o (= \gamma_w/\dot{\gamma}_o)$ is the characteristic weakening time for the homogeneous solution from *Lachenbruch* [1980][127] given in equation (2.23). We arrive at the following equation for $\dot{\gamma}_1(\hat{t})$

$$\frac{d\dot{\gamma}_1}{d\hat{t}} = \left(\frac{1}{E}\exp(-\hat{t}) - \frac{1}{\hat{\lambda}^2}\right)\dot{\gamma}_1 + \frac{C}{\hat{\lambda}^2}, \tag{2.48}$$

where E is a dimensionless parameter measuring the strength of the gouge dilatancy

$$E = \frac{\varepsilon}{(\sigma_n - p_a)\beta}, \tag{2.49}$$

and $\hat{\lambda}$ is the nondimensionalized wavelength,

$$\hat{\lambda} = \lambda/L_{thd} \quad , \quad L_{thd} = 2\pi\sqrt{\alpha_{th}t_w}. \tag{2.50}$$

Here L_{thd} is the lengthscale over which thermal diffusion acts on a timescale comparable to the weakening timescale t_w. The long time solution of equation (2.48) is $\dot{\gamma}_1(\hat{t} \to \infty) = C$, where C is the constant defined in equation (2.47), and is on the order of the initial perturbations in strain rate and temperature. While strain rate perturbations will always decay, for small values of E the solution can experience rapid initial growth.

If $\dot{\gamma}_1$ is to experience large transient growth before decaying back to C there must be a

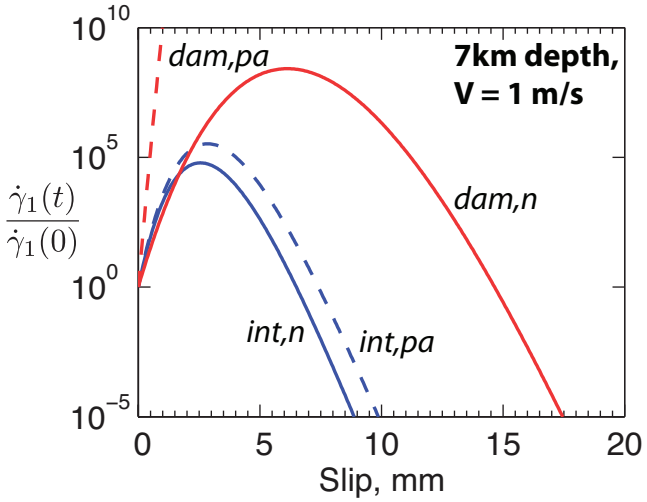

Figure 2.4: Gouge dilatancy: A plot showing the evolution of the strain rate perturbation $\dot{\gamma}_1$, normalized by the initial value $\dot{\gamma}_1(0)$, for a slip rate of $V = 1$ m/s accommodated across a 1 mm wide gouge layer, a wavelength $\lambda = 100\,\mu$m, and the parameter sets modeling a depth of 7 km (see Table 2.1). We see dramatic initial growth, followed by a decay back to zero. In our model a damaged material has a higher storage capacity, leading to a smaller value of $E = \varepsilon/\beta\sigma_a$, and larger excursions away from homogeneous shearing.

point satisfying

$$\frac{d\dot{\gamma}_1}{d\hat{t}} = 0 \quad , \quad \dot{\gamma}_1 \gg C. \tag{2.51}$$

Equation (2.48) allows us to calculate that such a turning point must occur at

$$t_{max} = t_w \log\left(\frac{\hat{\lambda}^2}{E}\right). \tag{2.52}$$

From this we conclude that transient growth of $\dot{\gamma}_1$ will only be possible when $t_{max} > 0$, and thus

$$\lambda > L_{thd}\sqrt{E}. \tag{2.53}$$

Recalling that L_{thd} depends on the nominal strain rate $\dot{\gamma}_o$ this inequality can be converted into a critical gouge layer thickness W_{dil} that must be exceeded for transient localization to be possible. As with the frictional rate-strengthening only case, this is done by setting

$$W_{dil} = \frac{L_{thd}\sqrt{E}}{2} \quad , \quad \dot{\gamma}_o = \frac{V}{W_{dil}}, \tag{2.54}$$

leading to

$$W_{dil} = \pi^2 \frac{\rho c \alpha_{th}}{f_o \Lambda V} \frac{\varepsilon}{\beta \bar{\sigma}_a}. \tag{2.55}$$

For gouge layers with thicknesses greater than W_{dil} uniform shear will be initially unstable and $\dot{\gamma}_1$ will undergo transient growth.

We now calculate the values of W_{dil} for the different parameter sets modeling a depth of 7 km. We find,

$$\begin{aligned} W_{dil}^{int,n} &= 0.87\ \mu\text{m} \quad , \quad W_{dil}^{int,pa} = 0.81\ \mu\text{m}, \\ W_{dil}^{dam,n} &= 1.08\ \mu\text{m} \quad , \quad W_{dil}^{dam,pa} = 0.35\ \mu\text{m}. \end{aligned} \tag{2.56}$$

Here we have used the previous superscript definitions to indicate intact or damaged material, and nominal or path-averaged parameters. All four parameter sets predict widths that are on the order of a micron or less. For a given parameter set the values of W_{dil} are at least a factor of two, and up to a factor of forty, less than the predictions for W_{rsf}. This means that dilatancy, as modeled by *Segall and Rice* [1995][201], is less effective than frictional rate-strengthening at limiting localization for the parameters chosen here. The values of W_{dil} cover a narrower range than the predictions for W_{rsf}.

Next we make a comparison with the parameters for a depth of 1 km. Using the parame-

ters in Table 2.2 we find

$$W_{dil}^{1km,int} = 1.42\,\mu\text{m} \quad , \quad W_{dil}^{1km,dam} = 1.41\,\mu\text{m}. \tag{2.57}$$

We see that the shallower parameters predict larger values of W_{dil}, but the predictions for W_{dil} at 1 km are still thinner than the smallest prediction for W_{rsf} at 7 km.

While W_{dil} tells us when transient strain rate localization is expected, it does not predict how intense this localization will be when the gouge layer is wider than W_{dil}. To investigate the intensity of localization we solve equation (2.48) to find the full solution for $\dot{\gamma}_1$,

$$\begin{aligned}\dot{\gamma}_1(\hat{t}) = \exp\left[\frac{1}{E}\Big(1-\exp(-\hat{t})\Big) - \frac{\hat{t}}{\hat{\lambda}^2}\right] \times \\ \left\{\dot{\gamma}_1(0) + \frac{C}{\hat{\lambda}^2}\int_0^{\hat{t}} \exp\left[\frac{1}{E}\Big(\exp(-\xi)-1\Big) + \frac{\xi}{\hat{\lambda}^2}\right] d\xi\right\}.\end{aligned} \tag{2.58}$$

For the case $C = 0$ this has the simple solution

$$\frac{\dot{\gamma}_1}{\dot{\gamma}_1(0)} = \exp\left[\frac{1}{E}\Big(1-\exp(-\hat{t})\Big) - \frac{\hat{t}}{\hat{\lambda}^2}\right]. \tag{2.59}$$

Figure 2.4 shows the normalized strain rate perturbation predicted by equation (2.59) as a function of slip. We observe large initial growth of the perturbations, followed by a return to uniform shearing as the perturbations decay. For a small enough initial perturbation $\dot{\gamma}_1(0)$, the remarkably large $\dot{\gamma}_1(t)/\dot{\gamma}_1(0)$ need not be at conflict with a linearized perturbation approach. However, unless the initial perturbation $\dot{\gamma}_1(0)$ is taken to be unrealistically small, the size of the perturbations far exceeds the region in which the linearized model can be applied. The linearized behavior observed is in qualitative agreement with the numerical

simulations for the fully nonlinear system presented in *Platt et al.* [2014][166], so we use these linearized results to predict which parameters are most important in controlling the severity of localization.

Using the solution for $C = 0$, given in equation (2.59), we can determine the maximum value of $\dot{\gamma}_1$

$$\left(\frac{\dot{\gamma}_1(\hat{t})}{\dot{\gamma}_1(0)}\right)_{max} = \exp\left[\frac{1}{E}\left(1 - \frac{E}{\hat{\lambda}^2}\right) - \frac{1}{\hat{\lambda}^2}\ln\left(\frac{\hat{\lambda}^2}{E}\right)\right], \tag{2.60}$$

which occurs at $t_{max} = t_w \log(\hat{\lambda}^2/E)$. As shown in Figure 2.4 smaller values of E lead to larger peak strain rates, which can be interpreted as more intense localization. Recalling that for $E = 0$ the solution collapses to slip on a plane, we see that as the strength of dilatancy increases the straining is distributed over a wider zone. This fits well with the idea of stabilization by dilatancy.

When calculating this maximum value of $\dot{\gamma}_1$ the assumption that $C = 0$ is valid provided that

$$\dot{\gamma}_1(0) \gg \frac{C}{\hat{\lambda}_2}\int_0^{\log(\hat{\lambda}^2/E)} \exp\left[\frac{1}{E}\Big(\exp(-\xi) - 1\Big) + \frac{\xi}{\hat{\lambda}^2}\right] d\xi. \tag{2.61}$$

For small values of E the integrand decays rapidly and thus the largest contribution to the integral comes from around $\xi = 0$. This leads us to approximate the integrand as

$$\exp\left[\frac{1}{E}\Big(\exp(-\xi) - 1\Big) + \frac{\xi}{\hat{\lambda}^2}\right] \approx \exp\left[\left(\frac{1}{\hat{\lambda}^2} - \frac{1}{E}\right)\xi\right], \tag{2.62}$$

allowing the integral to be evaluated as

$$\int_0^{t_{max}} \exp\left[\frac{1}{E}\Big(\exp(-\xi)-1\Big)+\frac{\xi}{\hat{\lambda}^2}\right] d\xi \approx \frac{\hat{\lambda}^2 E}{\hat{\lambda}^2 - E}. \tag{2.63}$$

This approximation is valid to within a few percent when $E < 0.05$. Inequality (2.61) then simplifies to

$$\dot{\gamma}_1(0) \gg \frac{CE}{\hat{\lambda}^2 - E}. \tag{2.64}$$

If this condition is not satisfied then the maximum value of $\dot{\gamma}_1$ given in equation (2.60) will have an additional contribution which can be calculated using the approximation for the integral developed above. This does not change the conclusion that smaller values of E will lead to larger peak strain rates.

Since the maximum value of $\dot{\gamma}_1$ depends most sensitively on E we calculate values for the different parameter sets. For a the parameter sets modeling a depth of 7 km we find

$$\begin{aligned} E_{int,n} = 0.0259 \quad &, \quad E_{int,pa} = 0.0245, \\ E_{dam,n} = 0.0107 \quad &, \quad E_{dam,pa} = 0.0045. \end{aligned} \tag{2.65}$$

Here we have used the previous superscript definitions to indicate intact or damaged material, and nominal or path-averaged parameters. For a depth of 1 km we find

$$E_{1km,int} = 0.0705 \quad , \quad E_{1km,dam} = 0.0215. \tag{2.66}$$

We see that the shallower parameters have larger values of E, leading us to expect more stabilization from dilatancy at shallower depths, and thus wider localized zones.

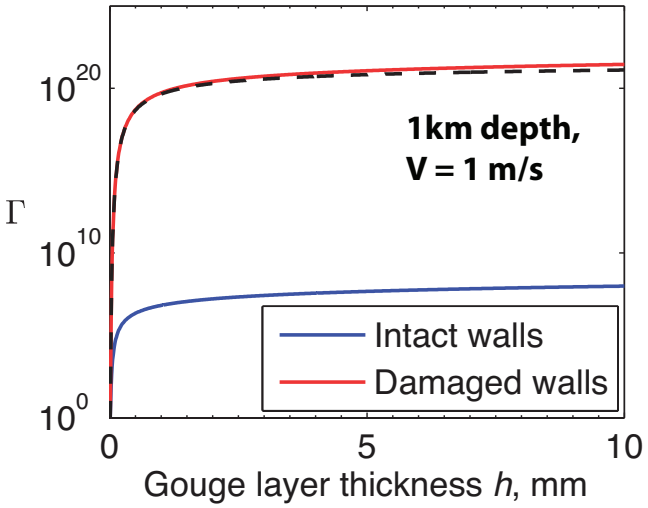

Figure 2.5: Gouge dilatancy: A plot of the total perturbation strain parameter Γ versus gouge layer thickness for the parameters modeling a depth of 1 km (see Table 2.2). Damaged material experiences more intense strain localization, in contrast with the results for stabilization by frictional-strengthening alone. The dashed line shows the asymptotic approximation from equation (2.69), which agrees well with the values of Γ found by integrating equation (2.67) numerically. This linearized analysis is only valid while the perturbations are small compared to the uniform shear solution. For the largest values of Γ this will only be true for unrealistically small values of $\dot{\gamma}_1(0)$. However, we still argue that localization stabilized by dilatancy alone is highly sensitive to changes in E, and insensitive to changes in other parameters.

2.7.2 Total strain accumulated

Field observations are unable to observe in-situ strain rates, and can only, at best, observe the final strain distribution. Motivated by this we integrate the strain rate perturbation $\dot{\gamma}_1$ to find the total perturbation strain

$$\gamma_1(t) = \frac{\gamma_w}{\dot{\gamma}_o} \int_0^{\hat{t}} \dot{\gamma}_1(s) \mathrm{d}s. \tag{2.67}$$

Taking $\hat{t} \to \infty$ we capture all of the transient localization, allowing us to define a measure of the total perturbation strain

$$\Gamma = \frac{\dot{\gamma}_o \gamma_1(t \to \infty)}{\gamma_w \dot{\gamma}_1(0)}. \tag{2.68}$$

For $E \ll 1$ the integral in equation (2.67) can be approximated using Laplace's method[13] to find

$$\Gamma \sim \hat{\lambda}\sqrt{2\pi} \exp\left[\frac{1}{E}\left(1 - \frac{E}{\hat{\lambda}^2}\right) - \frac{1}{\hat{\lambda}^2} \ln\left(\frac{\hat{\lambda}^2}{E}\right)\right], \tag{2.69}$$

which for large values of $\hat{\lambda}$ simplifies to,

$$\Gamma \sim \hat{\lambda}\sqrt{2\pi} \exp\left(\frac{1}{E}\right). \tag{2.70}$$

The exponential function means that Γ depends sensitively on E, and is relatively insensitive to changes in $\hat{\lambda}$. Setting $\lambda/2 = h$, corresponding to a single localized straining peak located at the boundary of the gouge layer, we now plot Γ as a function of gouge layer thickness for the different parameter sets. As predicted Γ reaches a value relatively independent of h, with this final value largely controlled by the value of E. Larger values of E lead to smaller values of Γ showing that stronger dilatancy will lead to a wider localized zone. The asymptotic approximation (2.69) is plotted in Figure 2.5 alongside the actual values of Γ, showing that the asymptotic approximation provides a good prediction for Γ.

As before the assumption that $C = 0$ is valid provided that inequality (2.64) is satisfied. If this is not true then there will be an additional pre-factor in equation (2.69), but this does not change the conclusion that Γ depends most sensitively on E.

2.8 Discussion

2.8.1 Frictional rate-strengthening only

Equation (2.43) predicts a localized zone thickness W_{rsf} as a function of the gouge properties and the slip rate V. The shear zone thickness is set by a balance between thermal pressurization, diffusion and frictional rate-strengthening. Using the parameters from Section 2.3, this formula was used to predict localized zone thicknesses in the range $3 - 41$ μm for a depth of 7 km and a slip rate $V = 1$ m/s. We now discuss how various factors could alter these predictions.

While the analysis above considered a fixed slip rate applied across the gouge layer, in reality the slip rate will vary dramatically during seismic slip. Previous dynamic rupture simulations accounting for thermal pressurization showed that slip rates within the slipping patch of the fault vary by at least an order of magnitude, with the largest slip rates near the rupture tip[155,86]. The linear stability analysis predicts $W_{rsf} \propto 1/V$, suggesting that the localized zone thickness will evolve with V during seismic shear. For the slip rate profiles in *Noda et al.* [2009][155] and *Garagash* [2012][86] the zone of localized zone shear will be thinnest at the rupture tip and will gradually widen as shear continues. Large changes in localized zone thickness during rupture may make it hard to compare our prediction for localized zone thickness with field observations of final strain profiles. We intend to address the variable slip rate scenario in future work.

Next we discuss the influence of the frictional parameters on W_{rsf}. We recall that the linear stability analysis is valid for any rate-strengthening friction law that depends on $\dot{\gamma}$

alone, and for a general friction law the parameter $(a-b)$ is defined as

$$(a-b) = \dot{\gamma}_o \frac{\partial f(\dot{\gamma})}{\partial \dot{\gamma}}\Big|_{\dot{\gamma}_o}. \tag{2.71}$$

Equation (2.43) provides the framework to discuss how our predictions would change for different friction laws. We see that W_{rsf} scales linearly with $(a-b)$, meaning that a friction law that exhibits stronger rate-strengthening will more effectively limit localization leading to wider localized shear zones. Also $W_{rsf} \propto f_o^{-2}$, the most sensitive dependence of W_{rsf} on any parameter. If other dynamic weakening mechanisms such as flash heating or nanoscale effects are active, and these mechanisms can be modeled in an ad hoc fashion by reducing f_o without altering $(a-b)$, then we expect dynamic weakening to lead to wider localized zones. A drop from $f_o = 0.6$ to $f_o = 0.2$, a typical friction value from *Goldsby and Tullis* [2011][93] and *Di Toro et al.* [2011][61], would increase the localized zone width by a factor of nine. Precise predictions are hard until laboratory experiments are able to separate strain rate, temperature and pore fluid effects at high strain rates to provide a function $f(\dot{\gamma})$.

The parameter sets used in this paper use the model for damage proposed in *Rice* [2006][186]. In this model the permeability is increased by an order of magnitude and the drained compressibility by a factor of two. The parameter sets modeling a damaged material predict a localized zone width approximately five times wider than those for an intact material. This is because the increased permeability leads to more efficient hydraulic transport, while the increased pore volume compressibility leads to less efficient thermal pressurization, as shown by the values of Λ in Table 2.1. Other damage models will predict different parameter values, but the generality of the formula for W_{rsf} allows other damage models to be

used to predict a localized zone thickness. Any damage that increases the permeability or makes thermal pressurization less efficient will lead to a wider shear zone.

Since the linear stability analysis only has a simple exponential solution when the gouge properties are constant, we accounted for parameter changes due to changes in pore fluid state using the path-averaging approach suggested in *Rice* [2006][186]. A better approach is to solve numerically using the full equation of state for the pore fluid and allowing the hydraulic properties of the gouge to vary with effective stress, as done by *Rempel and Rice* [2006][180] for a uniformly sheared gouge layer. They found that the most significant parameter variation was the change in permeability due to changes in pore pressure. Using the data from *Wibberley and Shimamoto* [2003][243] we see that the gouge may experience an order of magnitude increase in permeability, or possibly more, as the pore pressure goes from the ambient conditions to a pore pressure that is a significant fraction of the compressive stress. Assuming that, as observed by *Rempel and Rice* [2006][180], the dependence of permeability on pore pressure is the most important change, this suggests that our estimates for W_{rsf} may be an order of magnitude too low. Since the loading and unloading paths differ for the permeability data in *Wibberley and Shimamoto* [2003][243], the exact value of the permeability for a given effective stress will also depend on the maximum effective stress the gouge has previously experienced, possibly making the exhumation history of the gouge an important variable to consider when comparing with field observations.

2.8.2 Dilatancy only

Our analysis in Section 2.7 showed that for the dilatancy only system strain rate perturbations always decay as $t \rightarrow \infty$. However, strain rate perturbations can experience initial

transient growth whenever the gouge layer thickness exceeds the critical value W_{dil}. This critical thickness is a balance between thermal pressurization, thermal diffusion and dilatancy. For the parameter sets modeling a depth of 7 km (see table 2.1) we predict values of W_{dil} between 0.35 μm and 1.08 μm. In contrast with the predictions for W_{rsf}, the predictions for W_{dil} do not change dramatically when we change from modeling an intact gouge to a damaged gouge. This is because, for the parameterization for damage given in *Rice* [2006][186], the decrease in Λ is balanced by an increase in the storage capacity β. For a given parameter set these values of W_{dil} are at least a factor of two thinner than the localized zone thickness predictions for stabilization by frictional rate-strengthening alone, implying that dilatancy is less efficient at limiting strain rate localization.

When the gouge layer thickness exceeds W_{dil} the strain rate perturbation will experience transient growth. The scaling developed for Γ, the total strain accumulated by the strain rate perturbation, shows the strongest dependence on the parameter $E = \varepsilon/\beta\bar{\sigma}_a$. This means that the parameter ε plays a crucial role in limiting localization. The value of ε used in Section 2.7 is taken from *Segall and Rice* [1995][201], which fitted to the low strain rate experiments in *Marone et al.* [1990][143]. However, for the high strain rates considered here this value of ε may not be appropriate. The sensitive dependence of Γ on ε means that even a modest increases in ε should lead to a significant increase in localization limiting due to dilatancy.

If we neglect the significant grain size reduction or even amorphization that may be associated with seismic strain rates then the localized zone thicknesses predicted for the dilatancy only model – and the thinnest predictions for the frictional rate-strengthening only model – are comparable to a typical grain size in the gouge. This means that our model may

not be valid for the very thinnest localized shear zones when the size of individual grains may be an important localization limiter.

One prediction for the localized zone thickness when the size of individual grains is important can be found in *Sulem et al.* [2011][219], which studied localization in a fluid-saturated material accounting for the motion of individual grains using a Cosserat microstructure. Another prediction that comes from a wide body of research on localization in granular systems suggests setting the localized zone thickness equal to $10 - 20 d_{50}$, where d_{50} is the grain size such that 50% by weight of the particles have larger size. A discussion of the many experiments and numerical simulations that lead to this prediction can be found in *Rice* [2006][186]. Using the grain size distribution for ultracataclasite from the Punchbowl fault presented in *Chester et al.* [2005][45], *Rice* [2006][186] estimated d_{50} fault gouge to be ~ 1 μm, which leads to a localized zone thickness of $10 - 20$ μm. We emphasize that care must be taken when extrapolating the results of numerical simulations of granular flows to natural fault gouges because of the narrow range of grain sizes, uniform grain shapes, and two-dimensional geometry used in typical simulations.

2.8.3 Comparison with observations

Several field studies have shown evidence of 100 micron-scale strain localization, as discussed in the introduction[43,101,55]. Our predictions for localized zone thickness are in good agreement with the lower end of these observations. Elsewhere in this section we have highlighted mechanisms that could increase the localized zone thickness, for example a reduction in f_o due to flash heating or nanoparticle effects or an increase in permeability due to elevated pore pressures. If one or more of these mechanisms is activated then our predic-

tions would be in the middle, or even above, the range of observed localized zone thicknesses.

Not all observations of faults show such extreme strain localization. For example *Boullier et al.* [2009][27] presented a study of two boreholes drilled in the Chelungpu Fault, which hosted the Mw 7.6 Chi-Chi earthquake in 1999, at depths of 1111m and 1136m. Since fault drilling programs typically intersect the rupture surface near the top of the seismogenic zone we compare these observations with our prediction for localized zone thickness at a depth of 1 km, where we predict a range for W_{rsf} of $24 - 350$ μm. The gouge layer that *Boullier et al.* [2009][27] interpreted to be the principal slip zone was observed to be 0.3 cm and 2 cm, considerably wider than our estimates. The discrepancy between our predictions and the observations of centimeter wide shear zones could be due to poor constraints in our parameters, or evidence of another localization limiting mechanism that is active at shallow depths.

Interestingly the study by *Heermance et al.* [2003][101] sampled the Chelungpu fault in a region near to the observations of *Boullier et al.* [2009][27], though at a depth of approximately 330m, which is 800m shallower than the observation in *Boullier et al.* [2009][27]. They observed a diffuse shear zone in some locations on the fault and evidence of $50 - 300$ micron wide localization in others. This suggests that there may be significant along strike variability in localized zone thickness. The widths observed by *Heermance et al.* [2003][101] for the highly localized shear zones are in excellent with our predictions for W_{rsf} at a depth of 1 km.

Current laboratory experiments studying the frictional behavior of gouge materials at high deformation rates use a rotary shear configuration. We compare our results with the

microstructures in *Kitajima et al.* [2010][124], which are taken from high-velocity friction experiments on fluid-saturated ultracataclasite from the Punchbowl fault. Figure 9 in *Kitajima et al.* [2010][124] shows typical microstructural arrangements in a cross-section taken perpendicular to the direction of deformation. At the highest slip rates, present at the exterior of the cylindrical sample, a region of highly localized slip forms. They show the highly localized zone in red. We estimate this zone to have a width of approximately $100\ \mu$m.

However, the distinct banded structure of the localized zone noted in *Kitajima et al.* [2010][124] may indicate that the width of the shear zone at any given moment may be much less than $100\ \mu$m. This is in general agreement with other observations of strain localization from laboratory, which were discussed in more detail in the introduction. *Brantut et al.* [2008][29] identified a primary slipping zone $1 - 10\ \mu$m wide, while other studies also reported extreme localization at seismic slip rates[28,150].

While these observations of localized zone thickness are in good agreement with our predictions from the frictional rate-strengthening only system, care must be taken when making this comparison. Due to difficulties confining gouge at high slip rates most current experiments are performed at modest normal stress of 1 MPa. Since the critical point for water is at $p = 22.06$ MPa and $T = 374\ ^\circ$C, this modest normal stress means that the pore water may boil at laboratory conditions even though this will not happen at typical seismogenic conditions. The onset of localization in high-velocity friction experiments has been linked to this phase transition[28,124]. Choosing parameter values to model the experiment is also difficult, and it is unlikely that any of our parameter sets modeling depths of 1 and 7 km will accurately represent the hydraulic properties of the gouge used in high-velocity friction experiments. The phase transition and poorly constrained parameters make com-

paring our predictions with such experimental observations of localization difficult. Recent advances in gouge confinement[177,211] now make it possible to do experiments at supercritical pore pressure, eliminating the complications associated with the phase transition.

It should be noted that the geometry assumed in our model is different from the typical rotary shear experiment. Though we hope that far from the concentric cylinders that form the lateral boundaries of the sample the deformation can be well approximated by one-dimensional shearing, we cannot rule out the possibility that the localization is largely controlled by the teflon sleeve used to confine the gouge.

2.9 Conclusions

In this paper we analyzed the stability of uniform shear in a fluid-saturated gouge material. To prevent the collapsing of the straining region to a mathematical plane, we considered two separate stabilizing mechanisms, frictional rate-strengthening and dilatancy. For both mechanisms we used a linear stability analysis to determine if small perturbations away from uniform shear will grow or decay. We interpret growing perturbations as a sign of strain localization.

For frictional rate strengthening alone we solved for the critical wavelength λ_{shr} separating growing and decaying strain rate perturbations. Localization is expected for perturbations with wavelengths exceeding the critical wavelength λ_{shr}. The critical wavelength depends on the uniform strain rate, but was converted into a prediction for the localized zone thickness W_{rsf} that depends only on the slip rate V. This localized zone thickness is found to be a balance between frictional rate-strengthening, thermal pressurization and diffusion. Constraining the parameters is difficult, but using the parameters from *Rempel*

and Rice [2006][180] and *Rice* [2006][186] modeling a depth of 7 km and frictional data from *Blanpied et al.* [1998][24] we predict localized zone thicknesses between 3 μm and 41 μm.

In the system stabilized by dilatancy alone strain rate perturbations will always decay, making uniform straining stable as $t \to \infty$. However, perturbations may experience dramatic transient growth, and this transient growth is interpreted as strain localization. The system has a critical gouge layer thickness above which straining will localize. For the parameters modeling a depth of 7 km we predict critical thicknesses between 0.35 μm and 1.08 μm. When transient strain rate localization does occur the peak strain rate perturbation is largely controlled by a single dimensionless parameter modeling the efficiency of dilatancy, making ε a crucial parameter in our model.

This analysis only determines the initial stability of infinitesimally small perturbations away from uniform shear, but neglects nonlinear effects that become important as the perturbations grow. The companion paper *Platt et al.* [2014][166] extends this work using numerical solutions for the full set of equations to determine the width of the localized zone at peak localization, and the impact that strain rate localization has on the shear strength evolution and maximum temperature rise.

This project was a collaboration with John W. Rudnicki and James R. Rice. I was the lead researcher on this project and primary author of the final manuscript. The work in this chapter has already been published and the relevant citation is: Platt, J. D., J.W. Rudnicki, and J. R. Rice (2014), Stability and localization of rapid shear in fluid-saturated fault gouge, 2. Localized zone width and strength evolution, Journal of Geophysical Research, 119, 4334-4359.

3

Stability and Localization of Rapid Shear in Fluid-Saturated Fault Gouge, 2. Localized zone width and strength evolution

3.0 Abstract

Field and laboratory observations indicate that at seismic slip rates most shearing is confined to a very narrow zone, just a few tens to hundreds of microns wide, and sometimes as small as a few microns. *Rice et al.* [2014][189] analyzed the stability of uniform shear in a fluid-saturated gouge material. They considered two distinct mechanisms to limit localization to a finite thickness zone, rate-strengthening friction and dilatancy. In this paper we use numerical simulations to extend beyond the linearized perturbation context in *Rice et al.* [2014][189], and study the behavior after the loss of stability. Neglecting dilatancy we find that straining localizes to a width that is almost independent of the gouge layer width, suggesting that the localized zone width is set by the physical properties of the gouge material. Choosing parameters thought to be representative of a crustal depth of 7 km, this predicts that deformation should be confined to a zone between 4 and 44 μm wide. Next, considering dilatancy alone we again find a localized zone thickness that is independent of gouge layer thickness. For dilatancy alone we predict localized zone thicknesses between 1

and 2 μm wide for a depth of 7 km. Finally we study the impact of localization on the shear strength and temperature evolution of the gouge material. Strain rate localization focuses frictional heating into a narrower zone, leading to a much faster temperature rise than that predicted when localization is not accounted for. Since the dynamic weakening mechanism considered here is thermally driven, this leads to accelerated dynamic weakening.

3.1 Introduction

Field and laboratory observations show evidence for micron-scale strain rate localization in fluid-saturated gouge materials sheared at seismic slip rates, as discussed in the introduction to the companion paper *Rice et al.* [2014][189]. Such extreme localization focuses the frictional heating into a narrow zone, making thermally driven dynamic weakening mechanisms such as thermal pressurization and thermal decomposition very efficient. This sensitive dependence of shear strength evolution on the width of the deforming zone can be seen in the calculations of *Rempel and Rice* [2006][180], *Noda et al.* [2009][155], *Sulem and Famin* [2009][217], and *Garagash* [2012][86].

The companion paper *Rice et al.* [2014][189] used a thermo-poro-mechanical model for deformation of a fluid-saturated gouge material to investigate the width of the deforming zone during rapid shear. In the absence of a stabilizing mechanism the deformation will collapse into a zone with zero width, as noted in *Rice* [2006][186]. Two stabilizing mechanisms were considered in *Rice et al.* [2014][189], frictional rate-strengthening and dilatancy. For each mechanism a linear stability analysis was used to determine when small deviations away from uniform straining of the gouge material will grow, and thus uniform straining will be unstable. For frictional rate-strengthening alone this led to a prediction for the localized

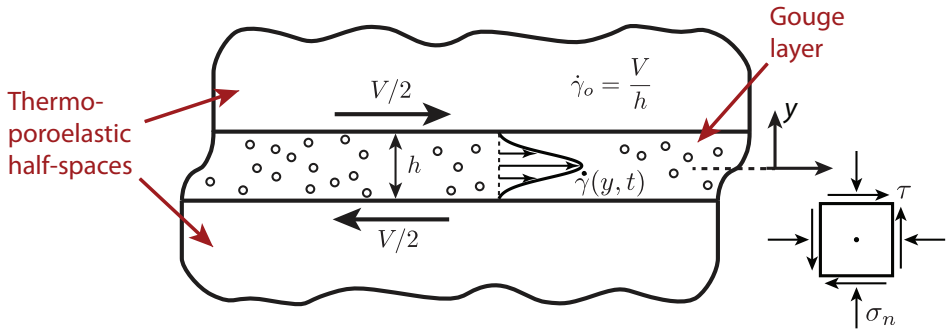

Figure 3.1: A sketch showing the system we are modeling. A gouge layer with a finite thickness h is sheared between two rigid poroelastic half-spaces that are moved relative to each other at a slip rate V. This leads to a nominal strain rate within the gouge layer $\dot{\gamma}_o = V/h$. The strain rate $\dot{\gamma}(y,t)$ will localize within the gouge layer, as shown by the Gaussian strain rate profile sketched within the gouge layer. The width W of the zone of localized straining is then estimated as twice the root mean square width of the Gaussian.

zone thickness as a function of the gouge properties. When localization is stabilized by dilatancy alone *Rice et al.* [2014][189] found a critical gouge layer thickness above which intense transient localization occurs at the onset of shear, although the strain rate perturbations eventually decay and shear is uniform at large slip.

In this paper we use numerical simulations to test the predictions of *Rice et al.* [2014][189]. We study how the properties of the gouge combine to set the localized zone thickness when nonlinear effects are accounted for, and compare this with the formula predicted in *Rice et al.* [2014][189]. We also study how the development of a localized shear zone influences the maximum temperature rise and shear strength evolution, showing that the development of a localized zone corresponds to a sudden strength drop.

3.2 Model formulation

In this section we outline the model for deformation of a fluid-saturated gouge material. A more detailed development of the model can be found in the companion paper, *Rice et al.* [2014][189]. We consider a gouge layer with a finite thickness h confined between two poroelastic half-spaces being moved relative to each other at a slip rate V. The model is one-dimensional and we only account for spatial variations that depend on the coordinate perpendicular to the slip direction, y. All values of y are measured relative to the line $y = 0$ at the center of the gouge layer. A sketch of this system is shown in Figure 3.1.

3.2.1 Mechanical equilibrium

Rice [2006][186] hypothesized that, due to the small lengths that diffusion of heat and pore fluid act over, unrealistically high accelerations are required to make inertial effects important within the gouge layer. Motivated by this we neglect inertia within the gouge layer, leaving us with the conditions for mechanical equilibrium

$$\frac{\partial \tau}{\partial y} = 0 \quad , \quad \frac{\partial \sigma_n}{\partial y} = 0, \tag{3.1}$$

where τ is the shear stress in the layer, σ_n is the compressive stress normal to the fault. This means that the stresses in the layer are at most a function of time, t. We assume that the normal stress does not evolve with time, and thus σ_n is constant. Later in this paper we determine when inertial effects will significantly alter our results. The shear stress is taken to

be the product of the effective stress and a friction coefficient f

$$\tau = f(\sigma_n - p), \tag{3.2}$$

where p is the local pore pressure.

3.2.2 Gouge friction

Constructing friction laws appropriate for the high deformation rates considered here is difficult due to the complex interplay between purely frictional, temperature and pore fluid effects. In the absence of such a friction law we use

$$f(\dot{\gamma}) = (a-b)\sinh^{-1}\left[\frac{\dot{\gamma}}{2\dot{\gamma}_o}\exp\left(\frac{f_o}{a-b}\right)\right], \tag{3.3}$$

which for $(a-b) \ll f_o$ is asymptotically the same as the friction law for steady state shearing inferred from low strain rate velocity-stepping experiments such as those in *Dieterich* [1979][57],

$$f = f_o + (a-b)\log\left(\frac{\dot{\gamma}}{\dot{\gamma}_o}\right). \tag{3.4}$$

Here f_o is the friction coefficient at the reference strain rate $\dot{\gamma}_o$, and $(a-b)$ quantifies the change in friction with strain rate. We will assume that the gouge is rate-strengthening, and thus $(a-b) > 0$. We use the regularized friction law in equation (3.3) instead of the logarithmic friction law in equation (3.4) to avoid difficulties when $\dot{\gamma} \to 0$.

Since the shear stress is at most a function of t, combining equations (3.2) and (3.3) we can see high pore pressures will correspond to high values of $\dot{\gamma}$. Equation (3.3) is a simpli-

fication of reality, and neglects temperature, state evolution and mineralogical effects. An expanded discussion of the assumptions implicit in using steady state friction laws that depend on strain rate alone can be found in *Rice et al.* [2014][189].

3.2.3 Conservation of energy

Following[189] the conservation of energy is written as

$$\frac{\partial T}{\partial t} = \frac{\tau \dot{\gamma}}{\rho c} + \alpha_{th} \frac{\partial^2 T}{\partial y^2}, \tag{3.5}$$

where T is temperature, α_{th} is the thermal diffusivity, and ρc is the effective heat capacity per unit volume in the reference state. Both ρc and α_{th} are taken to be constant. Since the shear stress τ is constant throughout the gouge layer, frictional heating will be focused in regions of high strain rate. Diffusion will then transport this heat into the adjacent material.

3.2.4 Conservation of pore fluid

As shown in *Rice et al.* [2014][189], conservation of pore fluid mass leads to,

$$\frac{\partial p}{\partial t} = \Lambda \frac{\partial T}{\partial t} - \frac{\varepsilon}{\beta \dot{\gamma}} \frac{\partial \dot{\gamma}}{\partial t} + \alpha_{hy} \frac{\partial^2 p}{\partial y^2}. \tag{3.6}$$

The first term on the right hand side of equation (3.6) represents thermal pressurization. As the pore fluid is heated it will expand, and if the gouge is undrained or partially drained this thermal expansion will lead to a pore pressure increase. The parameter Λ is defined as

$$\Lambda = \frac{\lambda_f - \lambda_n}{\beta_f + \beta_n}, \tag{3.7}$$

where β_n and λ_n are the compressibility and the thermal expansivity of the pore volume, β_f and λ_f are the compressibility and the thermal expansivity of the pore fluid, and the instantaneous pore pressure change accompanying a temperature change ΔT is $\Delta p = \Lambda \Delta T$. The second term in equation (3.6) models pore pressure decreases due to gouge dilatancy. Our model for dilatancy is based on the work of *Segall and Rice* [1995][201], which assumes that changes of inelastic porosity are a result of changes in strain rate. ε quantifies the magnitude of dilatancy and β is the storage capacity of the gouge. The final term in equation (3.6) represents hydraulic diffusion and, for simplicity, we have assumed that the hydraulic diffusivity α_{hy} is constant.

3.2.5 Nondimensional parameters

Now we determine the dimensionless parameters for this system of equations. The scalings used are based upon the geometry of the gouge layer and the solution for a uniformly sheared gouge layer developed by *Lachenbruch* [1980][127], discussed in more detail in Section 3.4 and in *Rice et al.* [2014][189].

First, the gouge layer width h is used to scale y. The gouge layer of thickness h can then be combined with slip rate V to find the nominal strain rate $\dot{\gamma}_o = V/h$ for the gouge layer. This nominal strain rate is used to scale $\dot{\gamma}$. The nominal strain rate is combined with the critical weakening strain for thermal pressurization $\gamma_w = \rho c / f_o \Lambda$ to get the characteristic weakening timescale $t_w = \gamma_w / \dot{\gamma}_o$ for thermal pressurization, which is used to scale t. Finally, we use the ambient effective stress $\bar{\sigma}_a$ to scale the pore pressure variations, and the total temperature rise from the uniform solution $\bar{\sigma}_a / \Lambda$ to scale the temperature variations.

To summarize

$$y = hy' \quad , \quad t = \frac{\rho c h}{f_o \Lambda V} t' \quad , \quad \dot{\gamma} = \dot{\gamma}_o \dot{\gamma}' \tag{3.8}$$
$$p = p_a + (\sigma_n - p_a) p' \quad , \quad T = T_a + \frac{\sigma_n - p_a}{\Lambda} T',$$

where p_a and T_a are the ambient pore pressure and temperature of the material, and the primed variables are dimensionless.

The above scalings leads to the set of dimensionless equations,

$$\frac{\partial T'}{\partial t'} = \tau' \dot{\gamma}' + D_{th} \frac{\partial^2 T'}{\partial y'^2}, \tag{3.9a}$$
$$\frac{\partial p'}{\partial t'} = \frac{\partial T'}{\partial t'} - \frac{E}{\dot{\gamma}'} \frac{\partial \dot{\gamma}'}{\partial t'} + D_{hy} \frac{\partial^2 p'}{\partial y'^2}, \tag{3.9b}$$
$$\frac{\partial \tau'}{\partial y'} = 0, \tag{3.9c}$$
$$\tau = f(\dot{\gamma}')(1 - p'), \tag{3.9d}$$
$$f(\dot{\gamma}') = z^{-1} \sinh^{-1}\left(\frac{\dot{\gamma}'}{2} \mathrm{e}^z\right). \tag{3.9e}$$

Despite the large number of parameters in our model, there are only four dimensionless parameters,

$$D_{th} = \frac{\alpha_{th} \rho c}{f_o \Lambda V h} \quad , \quad D_{hy} = \frac{\alpha_{hy} \rho c}{f_o \Lambda V h}, \tag{3.10}$$
$$z = \frac{f_o}{a - b} \quad , \quad E = \frac{\varepsilon}{\beta \bar{\sigma}_a}.$$

All of the parameters in our problem affect the response only in so far they affect these four

dimensionless parameters. D_{th} and D_{hy} measure the strength of thermal and hydraulic diffusion respectively, z measures the rate-strengthening component of friction, and E quantifies the strength of dilatancy.

The parameters D_{th} and D_{hy} can be better understood by rewriting them as

$$D_{th} = \left(\frac{L_{thd}}{4\pi^2 h}\right)^2 \quad , \quad D_{hy} = \left(\frac{L_{hyd}}{4\pi^2 h}\right)^2 , \tag{3.11}$$

where L_{thd} and L_{hyd} are the distances over which diffusion acts for a timescale comparable to the characteristic weakening timescale for thermal pressurization

$$L_{thd} = 2\pi\sqrt{\alpha_{th} t_w} \quad , \quad L_{hyd} = 2\pi\sqrt{\alpha_{hy} t_w}. \tag{3.12}$$

This means that small values of D_{th} and D_{hy} correspond to diffusion distances much smaller than the gouge layer thickness, allowing for the possibility of steep gradients in p and T across the gouge layer.

3.3 Parameter values

The hydraulic parameters α_{hy}, Λ and β are the least constrained in the model, and are expected to vary with temperature, pore pressure and damage to the gouge and surrounding material. In this paper we will consider one class of hydraulic parameters modeling a depth of 7 km, a typical centroidal depth for crustal earthquakes, and another class of hydraulic parameters modeling a depth of 1 km, a typical depth for boreholes drilled through active fault zones. Within each class of parameters we use the methods outlined in *Rice* [2006][186] to account for parameters variations due to damage, as well as pore pressure and tempera-

Parameter	Intact material, nominal values	Intact material, path-averaged values	Damaged material, nominal values	Damaged material, path-averaged values
α_{th}, mm^2/s	0.7	0.66	0.7	0.54
ρc, MPa/K	2.7	2.7	2.7	2.7
Λ, MPa/K	0.93	0.89	0.31	0.30
α_{hy}, mm^2/s	0.86	2.05	3.52	6.71
β, $\times 10^{-10}$ Pa^{-1}	0.52	0.55	1.26	2.97
ε	1.7×10^{-4}	1.7×10^{-4}	1.7×10^{-4}	1.7×10^{-4}
$\sigma_n - p_a$, MPa	126	126	126	126
ρ, kg/m^3	2800	2800	2800	2800

Table 3.1: Representative parameters modeling a depth of 7 km. A fuller discussion on the origin of the parameters is included in *Rice et al.* [2014][189].

ture changes.

To model a depth of 7 km we use the four parameter sets from *Rempel and Rice* [2006][180], which are based on Tables 1-3 in *Rice* [2006][186] and the procedures in *Rice* [2006][186]. Damage of the gouge by inelastic shear and fresh micro-cracking may occur in the concentrated stress field at the tip of a propagating rupture. This damage is modeled, somewhat arbitrarily, by increasing the permeability by an order of magnitude and the drained compressibility by a factor of two, as suggested in *Rice* [2006][186]. Parameter variations due to temperature and pore pressure changes are either neglected by evaluating the parameters at the ambient conditions, leading to the nominal parameter sets, or accounted for by averaging along an expected $p-T$ path, leading to the path-averaged parameter sets. The four parameter sets are summarized in Table 3.1 and are discussed in more detail in *Rice et al.* [2014][189].

Next we develop parameters modeling a depth of 1 km. No attempt is made to account for the effects of pore pressure and temperature changes and all parameters are evaluated at the ambient conditions $p_a = 10$ MPa, $\sigma_n = 28$ MPa and $T_a = 30\,^\circ$C. As before damage is accounted for using the procedure from *Rice* [2006][186]. The gouge properties are determined using the data from *Wibberley and Shimamoto* [2003][243]. We infer a porosity

of $n = 0.068$, and a pore volume thermal expansion coefficient $\lambda_n = -1.36 \times 10^{-4}$ °C^{-1}. For an intact material the pore volume compressibility is $\beta_n = 1.53 \times 10^{-9}$ Pa^{-1}, and for a damaged material $\beta_n = 6.01 \times 10^{-9}$ Pa^{-1}. To estimate the permeability we assume a maximum burial depth of $4 - 5$ km, we find a permeability of $\sim 2.5 \times 10^{-19}$ m^2 for intact material. As suggested in *Rice* [2006][186] this value is increased by a factor of ten to model a damaged material. Next we consider the pore fluid properties. *Fine and Millero* [1973][74] used sound speed data to calculate the compressibility and thermal expansion coefficient of pure water as a function of pressure and temperature, leading to $\beta_f = 0.44 \times 10^{-9}$ Pa^{-1} and $\lambda_f = 3.11 \times 10^{-4}$ °C^{-1}. Finally *Likhachev* [2003][132] provides a formula for the viscosity of water for a temperature range of $273 - 463$ K and a pressure range of $1 - 250$ bar. Using this we calculate $\eta_f = 7.97 \times 10^{-4}$ Pa s. These parameter sets are summarized in Table 3.2.

The parameter sets in Tables 3.1 and 3.2 show that damaged material, when modeled as in *Rice* [2006][186], is characterized by higher values of α_{hy} and β, and lower values of Λ. This means that thermal pressurization and dilatancy will be less efficient in a damaged material, while hydraulic diffusion will be more efficient. Comparing the nominal parameter sets modeling a depth of 1 km and 7 km we see the same pattern, with more efficient thermal pressurization and dilatancy expected at 7 km than at 1 km and less efficient hydraulic diffusion.

Compared with the hydraulic parameters, the thermal parameters are well constrained. The effective heat capacity per unit volume is $\rho c = 2.7$ MPa °C^{-1} [127,145], and *Rice* [2006][186] quotes a range for α_{th} of 0.5 to 0.7 mm^2/s. We choose a value of 0.7 mm^2/s for the nominal parameter sets, and use the values for α_{th} given in *Rempel and Rice* [2006][180] for the path-

Parameter	Intact material	Damaged material
n	0.068	0.068
β_f, $\times 10^{-9}$ Pa^{-1}	0.44	0.44
β_n, $\times 10^{-9}$ Pa^{-1}	1.53	6.01
λ_f, $\times 10^{-4}$K^{-1}	3.11	3.11
λ_n, $\times 10^{-4}$K^{-1}	-1.36	-1.36
η_f, $\times 10^{-4}$ Pa s	7.97	7.97
k, $\times 10^{-19}$ m^2	2.5	25
α_{th}, mm^2/s	0.7	0.7
ρc, MPa/K	2.7	2.7
Λ, MPa/K	0.22	0.068
α_{hy}, mm^2/s	2.34	7.15
β, $\times 10^{-10}$ Pa^{-1}	1.34	4.39
ε	1.7×10^{-4}	1.7×10^{-4}
$\sigma_n - p_a$, MPa	18	18
ρ, kg/m^3	2800	2800

Table 3.2: Two parameters sets intended to model a depth of 1 km, a typical intersection depth for boreholes drilled through active faults. Parameter variations due to pore pressure and temperature changes are neglected, so all parameters are evaluated at the ambient conditions $p_a = 10$ MPa, $\sigma_n = 28$ MPa and $T_a = 30\,^\circ$C. Damage is modeled by increasing the permeability by a factor of ten and the drained compressibility by a factor of two, as suggested in *Rice* [2006][186]. Sources for the parameter values are outlined in the text and include *Fine and Millero* [1973][74], *Wibberley and Shimamoto* [2003][243], and *Likhachev* [2003][132].

averaged parameter sets. The thermal parameters are assumed to not change with depth. In reality there will be some variation with depth, but we implicitly assume that changes in the thermal parameters are negligible when compared with the depth variation of the hydraulic parameters.

The logarithmic friction law used in this paper is taken from experiments performed at slip rates on the order of $1 - 10$ μm/s, and thus equation (3.3) may not accurately describe gouge friction at the seismic slip rates considered in this paper. However, current high-velocity friction experiments are unable to separate the frictional response from tem-

perature and pore fluid effects to provide a formula for the friction coefficient valid at the deformation rates considered here. As in *Rice et al.* [2014][189] we choose $f_o = 0.6$ and $(a - b) = 0.025$ motivated by the measurements for granite under hydrothermal conditions in *Blanpied et al.* [1998][24], though the results are presented in a form that allows predictions for a range of f_o and $(a - b)$. A larger discussion of the simplifications associated with equation (3.3) can be found in the companion paper *Rice et al.* [2014][189].

3.4 End-member solutions

In this section we discuss two end-member solutions for dynamic weakening driven by thermal pressurization. To do this we compare the hydrothermal diffusion distance $\sqrt{4\alpha t}$ with the gouge layer width h, where we define the lump hydrothermal diffusivity as

$$\alpha = \left(\sqrt{\alpha_{th}} + \sqrt{\alpha_{hy}}\right)^2 . \tag{3.13}$$

During the initial stages of deformation the hydrothermal diffusion distance will be much smaller than the width of the gouge layer, $\sqrt{4\alpha t} \ll h$. This means that deformation is effectively undrained and adiabatic, the limit studied in *Lachenbruch* [1980][127] when the constant dilatational strain rate assumed in *Lachenbruch* [1980][127] is zero. *Lachenbruch* [1980][127] solved for the strength evolution

$$\tau = f_o \bar{\sigma}_a \exp\left(-\frac{f_o \Lambda}{\rho c}\dot{\gamma}_o t\right) . \tag{3.14}$$

Thermal pressurization leads to an exponentially decaying shear stress, and the weakening

shear strain associated with thermal pressurization is

$$\gamma_w = \frac{\rho c}{f_o \Lambda}. \tag{3.15}$$

The weakening timescale, which was used earlier to nondimensionalize t, is then the ratio of the weakening strain and strain rate, $t_w = \gamma_w / \dot{\gamma}_o$. Since the system is controlled by a critical strain, the slip-weakening distance $h\gamma_w$ scales linearly with the width of the deforming zone. *Lachenbruch* [1980][127] also solved for T in the undrained and adiabatic limit, finding

$$T - T_a = \frac{\bar{\sigma}_a}{\Lambda} \left[1 - \exp\left(-\frac{\dot{\gamma}_o t}{\gamma_w} \right) \right], \tag{3.16}$$

where T_a is the ambient temperature. The dynamic weakening associated with thermal pressurization leads to a finite temperature rise of $\bar{\sigma}_a / \Lambda$ and the critical weakening strain γ_w also controls the approach of T to the maximum temperature.

At very large displacements the diffusion distance will be much larger than the gouge layer width, $\sqrt{4\alpha t} \gg h$. In this limit the finite thickness of the gouge layer will be negligible, and deformation can be approximated by slip on a mathematical plane. This problem was solved for a uniform slip rate V by *Mase and Smith* [1985,1987][144,145] for the special case of an immobile pore fluid (i.e $\alpha_{hy} = 0$). The more general solution was found by *Rice* [2006][186], for the case of non-zero α_{hy}, which in the end involved no more than replacing α_{th} in their result for $\tau(t)$ with the lump hydrothermal diffusivity α defined above in equation (3.13), leading to the shear strength evolution

$$\tau = f_o \bar{\sigma}_a \exp\left(\frac{Vt}{L^*} \right) \operatorname{erfc}\left(\sqrt{\frac{Vt}{L^*}} \right), \tag{3.17}$$

where

$$L^* = \frac{4\alpha}{V}\left(\frac{\rho c}{f_o \Lambda}\right)^2 . \tag{3.18}$$

This solution had been recognized by *Mase and Smith* [1987][145], in the case of thermal diffusion only, as a limiting result for a narrow shear zone. The weakening slip distance L^* is set by the weakening strain γ_w and the lengthscale defined by the hydrothermal diffusivity α and the slip rate V. The corresponding solution for slip surface temperature is

$$T - T_a = \frac{\bar{\sigma}_a}{\Lambda}\left(1 + \sqrt{\frac{\alpha_{hy}}{\alpha_{th}}}\right)\left[1 - \exp\left(\frac{Vt}{L^*}\right)\operatorname{erfc}\left(\sqrt{\frac{Vt}{L^*}}\right)\right] . \tag{3.19}$$

Again we see that thermal pressurization leads to a finite temperature rise, and the lengthscale that controls the temperature evolution is the same length that controls the shear strength evolution. We shall refer to the *Rice* [2006][186] solution in equations (3.17)-(3.19) as the Mase-Smith-Rice slip on a plane solution.

Rempel and Rice [2006][180] showed that the two limits considered above are the end-member solutions for a gouge layer sheared uniformly between two conducting half-spaces. We will investigate how strain rate localization alters the results of *Rempel and Rice* [2006][180], and how the solutions with localization relate to these two end-member solutions.

3.5 Frictional rate-strengthening only

3.5.1 Linear stability results

Initially we consider a system in which dilatancy is neglected, and thus $\varepsilon = 0$. *Rice et al.* [2014][189] determined the stability of the uniform shearing solution presented in *Lachen-*

bruch [1980][127]. Linearizing about this solution led to a relationship between the wavelength λ of a perturbation in p and T and the growth rate s, in an $\exp(st)$ form, given by

$$\frac{z\dot{\gamma}_o}{\gamma_w}s = \left(s + \frac{4\pi^2\alpha_{th}}{\lambda^2}\right)\left(s + \frac{4\pi^2\alpha_{hy}}{\lambda^2}\right). \tag{3.20}$$

Separating the growth rate into real and imaginary components, $s = s_R(\lambda) + s_I(\lambda)$, we determine the critical wavelength λ_{pT} that separates growing and decaying perturbations in p and T is

$$\lambda_{pT} = 2\pi\sqrt{\frac{\alpha_{th} + \alpha_{hy}}{z(\dot{\gamma}_o/\gamma_w)}}. \tag{3.21}$$

For $\lambda > \lambda_{pT}$ perturbations in p and T will grow unstably, while for $\lambda < \lambda_{pT}$ they will decay. Perturbations in strain rate are proportional to $\exp((s + \dot{\gamma}_o/\gamma_w)t)$ so we can define a similar critical wavelength

$$\lambda_{shr} = 2\pi\sqrt{\frac{\alpha_{th} + \alpha_{hy}}{(z+2)(\dot{\gamma}_o/\gamma_w)}}, \tag{3.22}$$

which separates growing and decaying perturbations in strain rate. For $\lambda > \lambda_{shr}$ strain rate perturbations will grow, leading to strain localization.

The critical wavelengths outlined above depend on the nominal strain rate $\dot{\gamma}_o$, which depends on the width of the deforming zone. *Rice et al.* [2014][189] turned the critical wavelength (3.22) into an approximate prediction for the localized zone thickness W_{rsf}, as controlled by rate-strengthening friction, by setting

$$W_{rsf} = \frac{\lambda_{shr}}{2} \quad \text{with} \quad \dot{\gamma}_o = \frac{V}{W_{rsf}}. \tag{3.23}$$

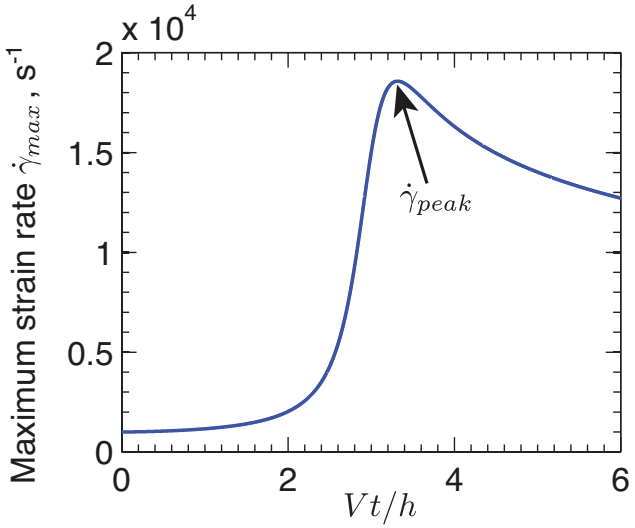

Figure 3.2: Rate-strengthening friction: The blue curve shows the evolution of the maximum strain rate $\dot{\gamma}_{max}$ within the gouge layer for the path-averaged parameters modeling a damaged material, $V = 1$ m/s and $h = 1$ mm. The maximum strain rate grows indicating that straining is localizing within the gouge layer. After a finite amount of slip the peak strain rate begins to decay indicating that the localized zone is thickening. This thickening occurs whenever both α_{th} and α_{hy} are non-zero. We define the peak strain rate $\dot{\gamma}_{peak}$ to be the largest value of $\dot{\gamma}_{max}$.

This leads to a prediction for the localized zone thickness that depends only on the gouge properties and the slip rate V,

$$W_{rsf} = \frac{\pi^2 \rho c}{f_o \Lambda (z+2)} \frac{\alpha_{hy} + \alpha_{th}}{V}. \tag{3.24}$$

The localized thickness is set by a balance between frictional rate-strengthening, thermal pressurization and hydrothermal diffusion.

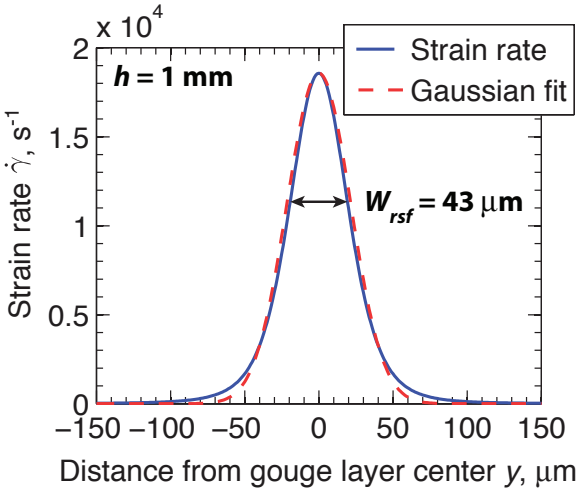

Figure 3.3: Rate-strengthening friction: A plot showing the strain rate profile at peak localization for the path-averaged parameters modeling a damaged material, $V = 1$ m/s and $h = 1$ mm. The numerical solution is shown in blue with the Gaussian fit defined by equation (3.27) shown by the red dashed line. The width W_{rsf} of the localized zone is estimated as twice the root mean square width of the Gaussian, and we find $W_{rsf} = 43$ μm.

3.5.2 Localized zone thickness

Now we solve numerically for a finite thickness gouge layer sheared between two poroelastic half-spaces, the geometry shown in Figure 3.1, to see how the linear stability prediction matches the behavior of the full nonlinear system. The poroelastic half-spaces do not deform and conduct heat and pore fluid away from the gouge layer. We assume that the transport properties of the half-spaces are the same as those of the gouge material. For initial conditions we set pressure and temperature to the ambient values $p_a = 70$ MPa and $T_a = 210\,^{\circ}$C, and assume that the gouge begins shearing uniformly with $\dot{\gamma} = \dot{\gamma}_o$. Interestingly the three dimensionless parameters that control this system are independent of the ambient pore pressure and temperature. The additional constraint imposed to solve for τ is

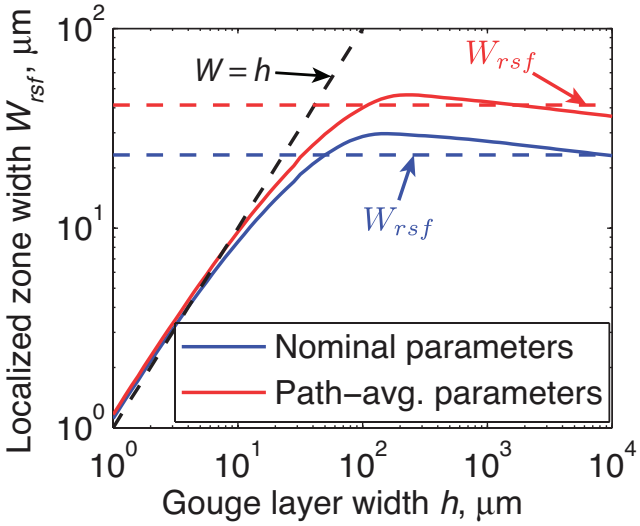

Figure 3.4: Rate-strengthening friction: Figure showing how the localized zone thickness W_{rsf} at peak localization depends on gouge layer thickness h. Numerical results for the path-averaged and nominal parameters for a damaged material and a slip rate of $V = 1$ m/s are shown by solid colored lines, with the accompanying linear stability predictions for these parameters shown by dashed colored line. For thin gouge layers we see that the localized zone thickness is equal to the gouge layer thickness, with the line $W = h$ shown by dashed black line for guidance. When the gouge layer thickness is large the straining localizes to a width that is only weakly dependent on the gouge layer thickness. This width is in good agreement with the predictions for W_{rsf} from the linear stability analysis in *Rice et al.* [2014][189].

$$\int_{-h/2}^{h/2} \dot{\gamma}(y,t)\mathrm{d}y = V, \tag{3.25}$$

and assures that the total straining within the gouge layer is equal to the slip rate V imposed across the gouge layer, as shown in Figure 3.1. This means that the average strain rate within the layer is equal to the nominal strain rate $\dot{\gamma}_o = V/h$.

Using the path-averaged parameters for a damaged material (see Table 3.1) we now solve for a gouge layer thickness $h = 1$ mm and a slip rate $V = 1$ m/s, justified as an average

earthquake slip rate in *Rice et al.* [2014][189]. For this parameter set the linear stability prediction for the localized zone thickness is $W = 41$ μm, over an order of magnitude smaller than the gouge layer thickness. This leads us to expect significant strain rate localization to occur.

To visualize the evolution of strain rate localization we plot the maximum strain rate in the gouge layer

$$\dot{\gamma}_{max}(t) = \max_{y}[\dot{\gamma}(y,t)] \tag{3.26}$$

as a function of time. Since the total straining accommodated across the gouge layer is fixed at $\dot{\gamma}_o$ a larger value of $\dot{\gamma}_{max}$ corresponds to a narrower deforming zone. Figure 3.2 shows how the maximum strain rate within the gouge layer evolves with time. Initially the maximum strain rate grows to values over an order of magnitude greater than the nominal strain rate $\dot{\gamma}_o$ showing that, as expected, straining is localizing within the gouge layer. Eventually $\dot{\gamma}_{max}$ reaches a peak value and begins to decay. This means that the thickness of the deforming zone, which initially will be the width of the gouge layer, gradually decreases to a narrowest value before widening again. Two additional instabilities exist that lead to movement of the localized straining zone across the gouge layer and these prevent the maximum strain rate decaying all the way back to uniform straining. These instabilities are not discussed here but will be the focus of future work.

Having described the temporal evolution of the maximum strain rate within the layer we next look at the spatial distribution of straining. The blue curve in Figure 3.3 shows the strain rate profile at peak localization, where peak localization is the point at which $\dot{\gamma}_{max}$ reaches its maximum value. The shape of the strain rate curve leads us to try to fit $\dot{\gamma}$ using

the Gaussian function

$$\dot{\gamma}_{fit} = A + B \exp\left(-\frac{2y^2}{W_{rsf}^2}\right). \tag{3.27}$$

This provides an excellent fit to the numerical solution as shown by the dashed red curve in Figure 3.3. To determine the three constants A, B and W_{rsf} we impose three conditions; $\dot{\gamma}_{fit}$ matches the numerical solution for $\dot{\gamma}$ at the centre of the gouge layer, the edge of the gouge layer, and accommodates the right amount of straining,

$$\int_{-h/2}^{h/2} \dot{\gamma}_{fit}(y,t)\mathrm{d}y = V. \tag{3.28}$$

This fitting formula gives us an objective way to measure the width of the zone of localized straining, allowing a comparison with the linear stability predictions. The constant A is included to allow us to fit straining profiles that have a width comparable to the gouge layer thickness. When straining is localized A becomes negligible and our fitting function becomes equivalent to the Gaussian straining profile previously used in models of thermal pressurization, for example *Andrews* [2002][4], *Rempel and Rice* [2006][180], *Noda et al.* [2009][155], and *Garagash* [2012][86]. For this limit where A is negligible we can calculate W_{rsf} using the formula

$$W_{rsf} = \sqrt{\frac{2}{\pi}}\frac{V}{\dot{\gamma}_{peak}}, \tag{3.29}$$

where we have defined the peak strain rate

$$\dot{\gamma}_{peak} = \max_{t,y}\left[\dot{\gamma}(y,t)\right]. \tag{3.30}$$

For the rate-strengthening friction simulation shown in Figure 3.3 we find $W_{rsf} = 43\ \mu$m,

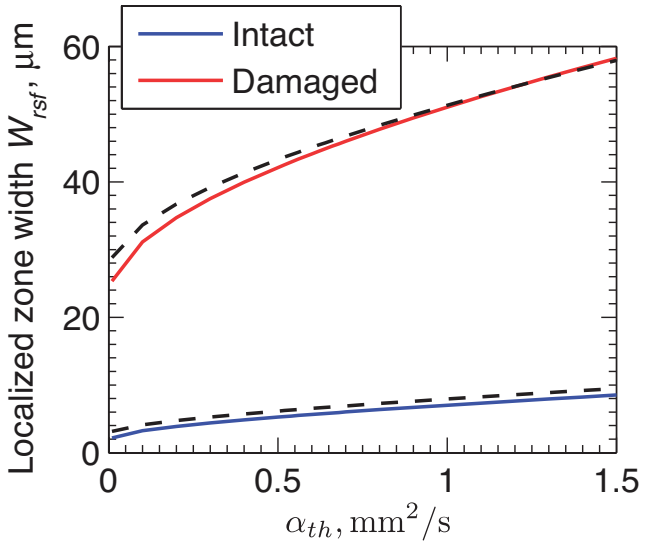

Figure 3.5: Rate-strengthening friction: A plot showing how the localized zone thickness W_{rsf} changes with α_{th} for the path-averaged parameters modeling an intact material and a damaged material given in Table 3.1, a slip rate $V = 1$ m/s and gouge layer thickness $h = 1$ mm. This parameter sweep allows us to vary the dimensionless parameter D_{th} while the other two dimensionless parameters D_{hy} and z remain unchanged. The black dashed lines show the fitting formula given in equation (3.31). Larger values of α_{th} lead to wider localized zones.

in good agreement with the linear stability prediction of 41 μm. While Figure 3.3 only shows a snapshot of the strain rate profile, the Gaussian function above provides an excellent fit to the numerical solutions throughout the evolution of the localized zone.

Next we see how the width of the gouge layer influences the width of the localized zone. Figure 3.4 shows the localized zone thickness at peak localization found using the Gaussian fit versus gouge layer thickness for the nominal and path-averaged parameters modeling a damaged material, $h = 1$ mm and $V = 1$ m/s. We see two distinct regimes. For thin gouge layers $W_{rsf} \approx h$, corresponding to a gouge layer that is too narrow to allow straining to localize. However, once the gouge layer width exceeds a critical value the straining

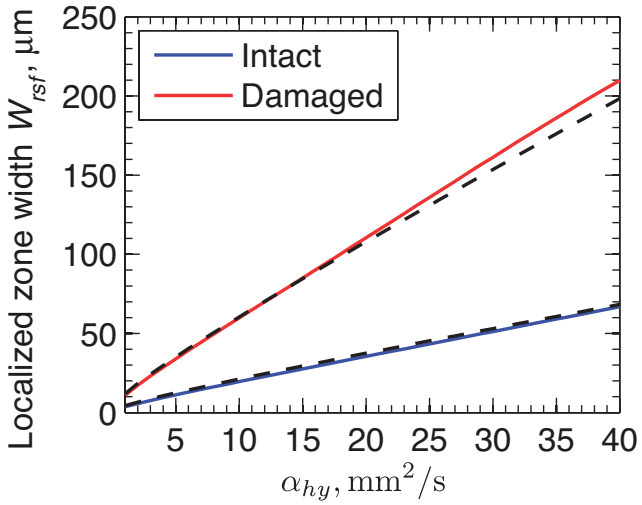

Figure 3.6: Rate-strengthening friction: A plot showing how the localized zone thickness W_{rsf} changes with α_{hy} for the path-averaged parameters modeling an intact material and a damaged material given in Table 3.1, a slip rate $V = 1$ m/s and gouge layer thickness $h = 1$ mm. This parameter sweep allows us to vary the dimensionless parameter D_{hy} while the other two dimensionless parameters D_{th} and z remain unchanged. The black dashed lines show the fitting formula given in equation (3.31). Larger values of α_{hy} lead to wider localized zones. The deviation at large values of α_{hy} for the damaged parameter set is due to W_{rsf} becoming comparable to h.

begins to localize, shown by the two curves falling beneath the line $W = h$. Once h exceeds this critical width the localized zone thickness is almost independent of h, changing by just twenty percent while h changes by three orders of magnitude. The linear stability predictions, shown by the colored dashed lines in Figure 3.4, provide reasonable agreement with the widths observed in the numerical simulations. It is encouraging that the linear stability prediction, which is taken infinitesimally close to uniform shearing, agrees so well with the localized zone thickness inferred at peak localization.

Next we perform a parameter sweep to determine how W_{rsf} depends on the gouge properties, implicitly assuming that the weak dependence of h is unimportant and the lo-

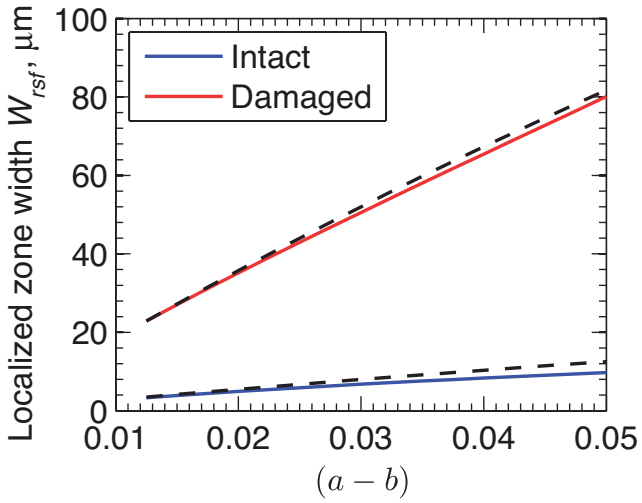

Figure 3.7: Rate-strengthening friction: A plot showing how the localized zone thickness W_{rsf} changes with $(a-b)$ for the path-averaged parameters modeling an intact material and a damaged material given in Table 3.1, a slip rate $V = 1$ m/s and gouge layer thickness $h = 1$ mm. This parameter sweep allows us to vary the dimensionless parameter z while the other two dimensionless parameters D_{hy} and D_{th} remain unchanged. The black dashed lines show the fitting formula given in equation (3.31). Larger values of $(a-b)$ lead to wider localized zones.

calized zone thickness is set by the gouge properties. As shown in Subsection 3.2.5, when dilatancy is neglected, there are just three dimensionless parameters that can be varied independently. This means it is sufficient to vary just α_{th}, α_{hy} and $(a-b)$, which corresponds to varying D_{th}, D_{hy} and z respectively. The parameters not being varied are fixed to the base parameters shown in Table 1. The results of this are shown in Figures 3.5, 3.6 and 3.7.

The numerical results agree well with the formula

$$W_{rsf} \approx \frac{C(a-b)\rho c}{f_o \Lambda} \frac{(\sqrt{\alpha_{hy}} + \sqrt{\alpha_{th}})^2}{V(f_o + 2(a-b))}. \tag{3.31}$$

This equation is shown by the dashed black lines in Figures 3.5, 3.6 and 3.7 for $C = 6.9$.

While we have only shown a narrow range of values for α_{th}, slightly larger than the range quoted in *Rice* [2006][186], further simulations show that equation (3.31) provides a good fit across nearly three orders of magnitude. In the limit $f_o \gg (a-b)$, which is valid for almost all values of f_o and $(a-b)$ found in laboratory experiments, we can neglect $(a-b)$ in the denominator of equation (3.31) and W_{rsf} becomes linear in $(a-b)$. The localized zone thickness is a balance between thermal pressurization, frictional rate-strengthening and hydrothermal diffusion, with hydrothermal diffusion entering through the lump diffusivity α of *Rice* [2006][186].

Using equation (3.31) we now make predictions for the localized zone thickness using the four parameter sets modeling a depth of 7 km. Using the superscript int to represent intact material, dam to represent damaged material, n for nominal parameter sets, and pa for path-averaged parameter sets, we find

$$W_{rsf}^{int,n} = 4\,\mu\text{m} \quad , \quad W_{rsf}^{int,pa} = 7\,\mu\text{m}, \tag{3.32a}$$

$$W_{rsf}^{dam,n} = 28\,\mu\text{m} \quad , \quad W_{rsf}^{dam,pa} = 44\,\mu\text{m}. \tag{3.32b}$$

These predictions are close to the predicted values in *Rice et al.* [2014][189], and in good agreement with some field and laboratory observations, for example *De Paola et al.* [2008][55], *Brantut et al.* [2008][29], and *Kitajima et al.* [2010][124]. These observations are discussed in detail in the introduction to *Rice et al.* [2014][189]. Due to more efficient hydraulic diffusion and less efficient thermal pressurization, we predict a wider localized zone for the damaged parameter sets. Parameter variations due to changes in pore pressure and temperature, which are accounted for using the path-averaging method from *Rice* [2006][186], increase the

localized zone thickness by $60 - 75\%$.

Next we evaluate (3.31) for the parameter sets modeling a depth of 1 km from Table 3.2, finding,

$$W_{rsf}^{1km,int} = 30\ \mu\text{m} \quad , \quad W_{rsf}^{1km,dam} = 216\ \mu\text{m}. \tag{3.33}$$

Wider localized zones are predicted at shallower depths, as predicted in *Rice et al.* [2014][189]. Changes in gouge properties due to changes in pore fluid pressure and temperature were not accounted for when making these predictions. Tentatively assuming that the percentage increase in thickness is the same as the values for a depth of 7 km we predict a width of $\sim 55\ \mu$m for an intact material and $\sim 340\ \mu$m for a damaged material.

3.5.3 Impact of localization on shear strength evolution

During our calculations we also track the shear strength. Figure 3.8 shows the shear strength evolution when we use the path-averaged parameters for a damaged material, $h = 1$ mm and $V = 1$ m/s, the same calculation used to produce the localized straining profile in Figure 3.3. For comparison we also show the shear strength evolution when the gouge layer is forced to deform uniformly, with the uniform solution calculated by setting $\dot{\gamma} = \dot{\gamma}_o$ throughout the gouge layer and approximating the shear stress using the pore pressure in the center of the gouge layer

$$\tau(t) = f_o[\sigma_n - p(0,t)]. \tag{3.34}$$

This calculation is very similar to those performed in *Rempel and Rice* [2006][180]. Henceforth, the solution where the gouge layer is forced to deform uniformly is referred to as the

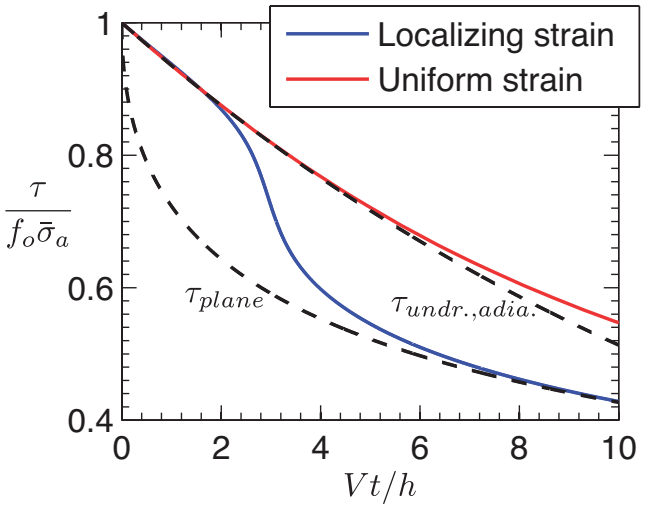

Figure 3.8: Rate-strengthening friction: A plot showing how the strength of the gouge layer evolves, normalized by the initial strength, for localizing shear and uniform shear. These simulations were produced using the path-averaged parameters modeling a damaged material, $V = 1$ m/s and $h = 1$ mm. We see that a sudden drop in strength coincides with the onset of localization. The initial deformation, before diffusion and localization have had time to act, is well described by the solution for uniform shear under undrained and adiabatic conditions [127] . At large slips the solution is no longer influenced by the small yet finite width of the shearing zone and the strength is well approximated by the solution for slip on a plane [145,186]. The two limits for undrained adiabatic deformation and slip on a plane are shown above by the dashed black lines. Note that the undrained adiabatic solution from *Lachenbruch* [1980] [127] differs from our simulation of a uniformly sheared layer because our numerical simulations allow for diffusion of heat and fluid into the surroundings.

uniform shear solution, and the solution where the straining is allowed to localize within the gouge layer is referred to as the localized shear solution.

Initially the shear strength evolution is the same for the uniform shear solution and the localized shear solution. This corresponds to the early stages of deformation when straining has not had time to localize. As expected both the uniform shear and localized shear solutions also agree with the solution for uniform shear under undrained and adiabatic conditions from *Lachenbruch* [1980] [127]. At the onset of localization we see a dramatic drop

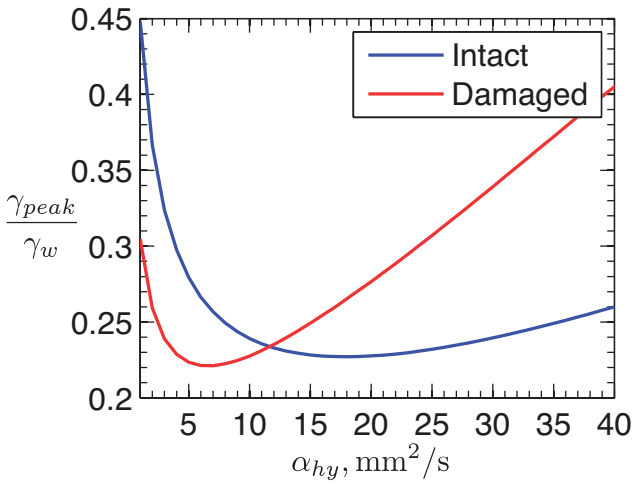

Figure 3.9: Rate-strengthening friction: A plot showing how the nominal strain at which peak localization occurs varies with α_{hy}. These simulations were produced using the path-averaged parameters for an intact and a damaged material, $V = 1$ m/s and $h = 1$ mm. For low values of α_{hy}, corresponding to localized zone thicknesses that are much smaller than the gouge layer thickness, the critical strain is a decreasing function of α_{hy}. For both parameter sets γ_{peak} reaches a minimum before increasing at large values of α_{hy}.

in strength, typically $20 - 40\%$ of the initial strength $\tau_0 = f_o(\sigma_n - p_a)$. The exact strength drop at the onset of localization depends on the gouge layer width h, with more dramatic strength drops for larger values of h. These observation can be explained by recalling that thinner deforming zones lead to more rapid dynamic weakening. As the straining localizes the deforming zone thins leading to accelerated weakening. Larger values of h lead to larger strength drops at the onset of localization due to the larger contrast between the initial gouge layer width and final localized zone thickness. After straining has strongly localized the shear strength evolution is in excellent agreement with the Mase-Smith-Rice solution for slip on a plane.

Since the most rapid dynamic weakening is linked to strain rate localization, our results

predict that the slip at which the most rapid dynamic weakening occurs is controlled by the gouge parameters. Motivated by this we now track γ_{peak} as a function of the gouge properties. Figures 3.9 and 3.10 shows the strain at which $\dot{\gamma}_{max}$ reaches its peak value divided by the weakening strain γ_w for thermal pressurization as a function of α_{hy}, and $(a-b)$. We see that smaller values of $(a-b)$, and thus larger values of z, lead to smaller value of γ_{peak}/γ_w. This means that not only does frictional rate-strengthening limit localization, it also slows the rate at which a localized zone develops. The dependence of γ_{peak} on α_{hy} is the reverse of that observed for $(a-b)$. Whenever the localized zone thickness is over an order of magnitude thinner than the gouge layer thickness, smaller values of α_{hy} lead to larger values of γ_{peak}/γ_w. The increase in γ_{peak} for larger values of α_{hy} occurs when the localized zone thickness becomes comparable to the gouge layer thickness. Since the thermal diffusivity is relatively well constrained we do not show the dependence of γ_{peak} on α_{th}, but the results are qualitatively very similar to those observed for α_{hy}.

It should be emphasized that this dependence of γ_{peak} on α_{hy} may not transfer to other geometries. In our system the localization is initiated by hydrothermal diffusion from the gouge layer into the half-spaces, leading to larger pore pressures and strain rates in the center of the gouge layer, and thus the formation of a localized zone. Lower values of the bulk hydrothermal diffusivity α defined in equation (3.13) limit diffusion into the half-spaces leading to larger values of γ_{peak}. If localization is instead initiated by heterogeneities within the gouge layer then the dependence of γ_{peak} on α_{hy} could be very different. This link between localization and heterogeneities within the gouge layer is the subject of ongoing work.

If the gouge layer is sufficiently thick, or the slip is sufficiently small it may be possible

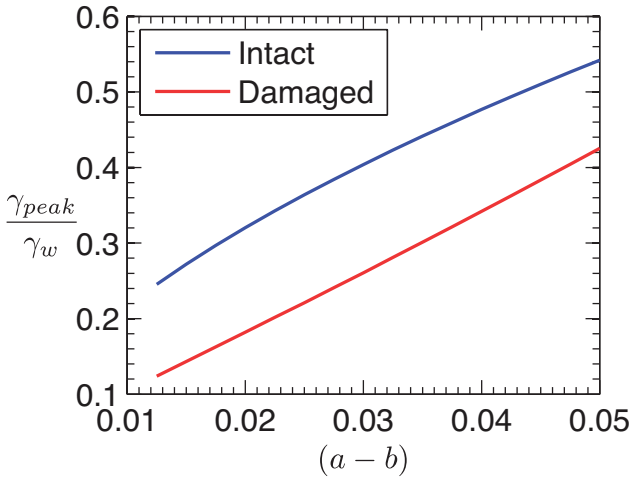

Figure 3.10: Rate-strengthening friction: A plot showing how the nominal strain at which peak localization occurs varies with $(a-b)$. These simulations were produced using the path-averaged parameters for an intact and a damaged material, $V = 1$ m/s and $h = 1$ mm. We see that small values of $(a-b)$ lead to small values of γ_{peak}, and so the more intense localized zones also develop the fastest.

that a fully developed localized zone will not occur during a seismic event. To estimate when this will happen we assume that for a wide gouge layer $\gamma_{peak}/\gamma_w = 1$, which leads to a critical slip that must be reached for localization to fully develop

$$D_{loc.} = \frac{\rho c h}{f_o \Lambda}. \tag{3.35}$$

Using a typical slip of 1 meter and the range of γ_w implied by the parameters in Table 3.1 we predict the critical gouge layer thickness above which localization does not have sufficient time to fully develop to be $6.6 - 20$ cm. If the gouge layer thickness is only slightly less than the critical thickness then the majority of shear will have occurred with an underdeveloped localized zone, with full localization occurring just before deformation ceases.

An underdeveloped localized zone will have three important consequences. First, even though strain rate localization is occurring, there may be little evidence of highly localized shear in the final strain profile. Second, since the most rapid dynamic weakening occurs during the most rapid localization, we would expect a much smoother strength evolution profile than the one shown in Figure 3.8. Finally, since the straining is never focused into a narrow zone we would expect a significantly lower temperature rise.

3.5.4 Influence on maximum temperature rise

Rempel and Rice [2006][180] showed that the undrained and adiabatic solution of *Lachenbruch* [1980][127] and the Mase-Smith-Rice slip on a plane solution, equations (3.16) and (3.19) respectively, are the end-member solutions for the maximum temperature rise in the uniform shear solution. However, the maximum temperature rise for the uniform shear solution will approach the Mase-Smith-Rice slip on a plane solution only at very large slips that may be larger than typical seismic slips.

We now compare the maximum temperature rise

$$\Delta T_{max}(t) = \max_{y} \left[T(y,t)\right] - T_a \tag{3.36}$$

predicted by our new localized shear solution with these two end-members, as well as the uniform shear solution. This is done using the path-averaged parameters for a damaged material, gouge layer width $h = 1$mm, and slip rate of $V = 1$ m/s, the same parameter set used to generate Figures 3.2, 3.3 and 3.8. The blue curve in Figure 3.11 shows the maximum temperature for the localized shear solution as a function of time. The symmetry of the system means that this maximum temperature occurs in the middle of the gouge layer,

which in our coordinate system is $y = 0$. Alongside this is plotted the maximum temperature rise for the uniform shear solution in red, as well as the two end-member solutions for undrained and adiabatic conditions, and the Mase-Smith-Rice slip on a plane solution. The onset of localization is accompanied by a large increase in the maximum temperature as frictional heating is focused into a narrow zone in the center of the gouge layer. After a slip of 10 mm the temperature rise for the localized shear solution is over three times larger than the temperature rise for the uniform shear solution. For the parameters used in this simulation this corresponds to a difference of $\sim 580\,^{\circ}\mathrm{C}$.

Initially the uniform shear solution and localized shear solution are in excellent agreement with equation (3.16), which describes the temperature evolution under undrained and adiabatic conditions. After localization the solution mirrors the solution for slip on a plane, as would be expected when all of the deformation is accommodated in a very narrow zone, though the slip on a plane solution still does not give an accurate prediction of the maximum temperature since it neglects the initial stages of shear when deformation is distributed throughout the gouge layer. The maximum temperature rise for the localized shear solution will never approach the slip on a plane solution due to a pair of instabilities that cause the zone of localized straining to move across the gouge layer, thus distributing the frictional heating across a wider zone.

Finally we investigate how the magnitude of the temperature rise associated with localization depends on the gouge parameters. To quantify this we study the maximum heating rate

$$\left(\frac{\partial T}{\partial t}\right)_{peak} = \max_{t,y}\left(\frac{\partial T}{\partial t}\right). \tag{3.37}$$

This is found to be a decreasing function of α_{hy}, α_{th} and $(a - b)$. This is easily understood

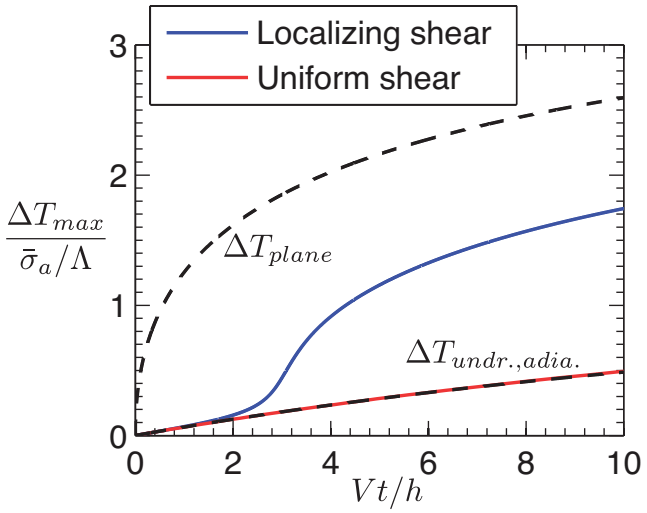

Figure 3.11: Rate-strengthening friction: A plot showing how the maximum temperature rise, $\Delta T_{max} = T_{max} - T_a$, in the gouge layer evolves for localized and uniform shear using the path-averaged parameters for a damaged material, $h = 1$ mm and $V = 1$ m/s. The initial behavior, before localization and diffusion become important, is well described by the undrained adiabatic solution of *Lachenbruch* [1980][127] (marked $\Delta T_{undr.,adia.}$). As straining localizes the frictional heating is focused into a zone much narrower than the gouge layer thickness, leading to a sharp temperature rise. After localization the localized shear solution mirrors the Mase-Smith-Rice slip on a plane solution (marked ΔT_{plane}), but the slip on a plane solution never provides a good approximation for maximum temperature rise.

by noticing that the localized zone thickness W_{rsf} is an increasing function of α_{hy}, α_{th} and $(a - b)$. Parameters that predict a narrower localized zone will lead to a larger maximum heating rate as straining is focused more intensely.

3.6 Stabilization by Dilatancy Only

Having considered the case where the localized zone is stabilized by frictional strengthening alone, we now consider a system with constant (i.e. rate-independent) friction where

stabilization is provided by dilatancy only. For this case the model simplifies to

$$\frac{\partial T}{\partial t} = \frac{\tau \dot{\gamma}}{\rho c} + \alpha_{th} \frac{\partial^2 T}{\partial y^2}, \tag{3.38a}$$

$$\frac{\partial p}{\partial t} = \Lambda \frac{\partial T}{\partial t} - \frac{\varepsilon}{\beta \dot{\gamma}} \frac{\partial \dot{\gamma}}{\partial t}. \tag{3.38b}$$

Mechanical equilibrium combined with constant friction requires that p be a function of t alone, and the shear strength is given by $\tau = f_o[\sigma_n - p(t)]$.

3.6.1 Linear stability predictions

As with the frictional strengthening only case, *Rice et al.* [2014][189] analyzed small perturbations away from this uniform shear solution, finding the linearized equation for a strain rate perturbation $\dot{\gamma}_1$ with a wavelength λ

$$\frac{d\dot{\gamma}_1}{dt'} = \left(\frac{1}{E} \exp\left(-t'\right) - \frac{1}{\hat{\lambda}^2} \right) \dot{\gamma}_1 + \frac{C}{\hat{\lambda}^2}. \tag{3.39}$$

Here we have defined the dimensionless time $t' = (\dot{\gamma}_o / \gamma_w) t$, E is defined as in equation (3.10), $\hat{\lambda}$ is a dimensionless wavelength defined by

$$\hat{\lambda} = \frac{\lambda}{L_{thd}} \quad , \quad L_{thd} = 2\pi \sqrt{\alpha_{th} t_w} \tag{3.40}$$

and C is a constant set by the initial perturbations in strain rate and temperature

$$C = \dot{\gamma}_1(0) - (\Lambda \beta \dot{\gamma}_o \varepsilon) T_1(0). \tag{3.41}$$

Rice et al. [2014][189] showed that the large slip solution to (3.39) is $\dot{\gamma}_1 \rightarrow C$ as $t \rightarrow \infty$. However, for gouge layer thicknesses exceeding a critical width W_{dil} the strain rate perturbation will undergo transient growth. This transient growth is interpreted as strain rate localization. By determining the maximum values of $\dot{\gamma}_1$ it was shown that small values of E correspond to more extreme growth. This can be understood in the stabilization framework since small values of E correspond to small dilatant suctions, less stabilization, and thus more intense localization.

3.6.2 Localized zone thickness

The solution to the linearized equation (3.39) predicts very large strain rate perturbations, far beyond the magnitudes at which the linearization is valid, unless the initial strain rate perturbations are unrealistically small, on the order of 10^{-10} to 10^{-20} of $\dot{\gamma}_o$ or less (see *Rice et al.* [2014][189]). To account for nonlinear effects we now solve the full system numerically for a slip rate $V = 1$ m/s, and a gouge layer thickness $h = 0.5$ mm. In all that follows the strain localization develops from an initial perturbation away from uniform straining

$$\dot{\gamma} = \dot{\gamma}_o \left[1 + \delta \cos \left(\frac{2\pi y}{h} \right) \right], \tag{3.42}$$

where $\delta = 10^{-3}$. Since $y = 0$ is located at the center of the gouge layer this initial perturbation is symmetric about the center of the gouge layer. The initial pore pressure and temperature are assumed to be the ambient values $p = p_a$ and $T = T_a$. Other values of δ were tested, as were initial conditions with a temperature perturbation, but the results are qualitatively the same. Slightly larger peak strain rates are observed for larger initial perturbations.

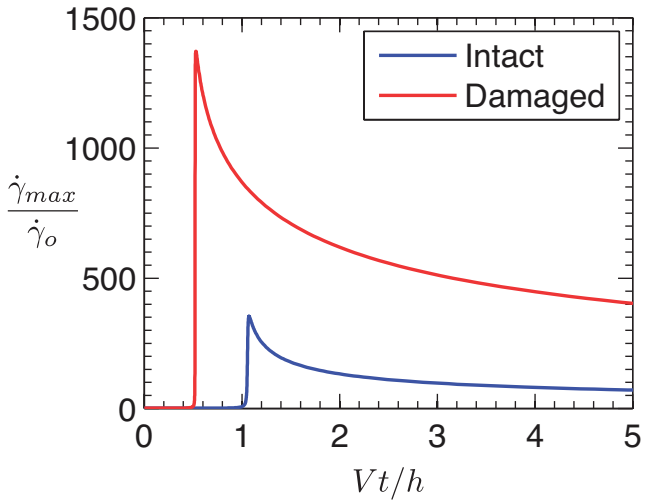

Figure 3.12: Gouge dilatancy: A plot showing how the maximum strain rate $\dot{\gamma}_{max}$ evolves for the path-averaged parameters modeling an intact and a damaged material, for $V = 1$ m/s and $h = 0.5$ mm. As predicted by the linear stability analysis there is an initial transient of intense strain rate localization followed by decay to homogeneous straining. In contrast with the frictional strengthening case, the damaged material shows more intense localization.

For strain rate localization stabilized by dilatancy alone we assume that the half-spaces adjacent to the gouge layer are thermally and hydraulically insulating. This is in contrast to the results for stabilization by frictional rate-strengthening alone presented in the previous section that accounted for transport of heat and pore fluid into the half-spaces. We assume the half-spaces are thermally and hydraulically insulating to match the requirement that p is independent of y within the gouge layer. The symmetry of the no-flux boundary conditions at the edge of the gouge layer means that our simulations for a finite thickness gouge layer are equivalent to the periodic domain considered in the companion paper *Rice et al.* [2014][189].

As before the maximum strain rate $\dot{\gamma}_{max}$ in the gouge layer is used as a proxy for localization, recalling that a higher maximum strain rate indicates more intense localization. The

maximum strain rate is defined in equation (3.26). Figure 3.12 shows how $\dot{\gamma}_{max}$ evolves for the path-averaged parameters modeling intact and damaged material. As predicted by the linear stability analysis straining localizes within the gouge layer. Even when nonlinear effects are accounted for the strain rate localization is transient. As in the system where strain rate localization is stabilized by frictional rate-strengthening alone the maximum temperature within the gouge layer increases rapidly as straining localizes, and this is accompanied by a sudden reduction in the shear strength. The spatial distribution of straining is well described by a Gaussian function throughout the simulations.

We can understand the transient nature of localization by rewriting (3.38a) and (3.38b) as

$$\frac{\varepsilon}{\beta\dot{\gamma}}\frac{\partial\dot{\gamma}}{\partial t} = \Lambda\left(\frac{\tau\dot{\gamma}}{\rho c} + \alpha_{th}\frac{\partial^2 T}{\partial y^2}\right) - \frac{\partial p}{\partial t}. \tag{3.43}$$

The high strain rates associated with localization lead to increased thermal pressurization and a sudden drop in strength, leading us to look at the large slip limit in which the pore pressure approaches the normal stress

$$p \to \sigma_n \quad , \quad \frac{\partial p}{\partial t} \to 0. \tag{3.44}$$

This leads to

$$\frac{1}{\dot{\gamma}}\frac{\partial\dot{\gamma}}{\partial t} = \frac{\alpha_{th}\Lambda\beta}{\varepsilon}\frac{\partial^2 T}{\partial y^2}. \tag{3.45}$$

The zero flux boundary conditions at the end of the gouge layer and the symmetry about the center of the gouge layer allow us to deduce that T has its maximum value at $y = 0$ and minimum values at $y = \pm h/2$ for the initial perturbation given in equation (3.42).

Integrating equation (3.38b) we can also show that the maximum and minimum values of T coincide with the maximum and minimum values of $\dot{\gamma}$. Thus, using equation (3.45) we conclude that at large slips the maximum strain rate will decay and the minimum strain rate will grow. As the maximum and minimum values of $\dot{\gamma}$ approach each other the straining profile in the layer must return to uniform shear, meaning that strain rate localization will always be transient. If we had attempted to model transport of pore fluid and heat into the adjoining half-spaces it may have taken much longer for the limit described in equation (3.44) to be reached, possibly allowing straining to remain at peak localization for longer than is observed in Figure 3.12.

Next we quantify the intensity of localization by tracking the peak strain rate as a function of the two controlling dimensionless parameters

$$E = \frac{\varepsilon}{\beta \bar{\sigma}_a} \quad , \quad L_{thd} = 2\pi\sqrt{\alpha_{th} t_w}. \tag{3.46}$$

By considering the dimensionless parameters we can reduce the number of parameters we must vary dramatically. Note that when setting $\lambda = h$ the parameter $\hat{\lambda} = \lambda/(2\pi\sqrt{\alpha_{th} t_w})$ from *Rice et al.* [2014][189] becomes the ratio of the gouge layer thickness and the diffusional lengthscale L_{thd}. Having discussed how we can use the maximum strain rate as a proxy for intensity of localization, we next use the peak strain rate $\dot{\gamma}_{peak}$ defined in equation (3.30) to quantify the width of localized zone at peak localization. Since for stabilization by dilatancy alone our initial perturbation has a maximum value on $y = 0$ the peak strain rate $\dot{\gamma}_{peak}$ will always occur at $y = 0$. $\dot{\gamma}_{peak}$ can be thought of as the maximum value ever achieved by $\dot{\gamma}_{max}(t)$. Figures 3.13 and 3.14 show how $\dot{\gamma}_{peak}$ varies with the two dimensionless parameters E and L_{thd}. In agreement with the linear stability predictions, we observe that smaller

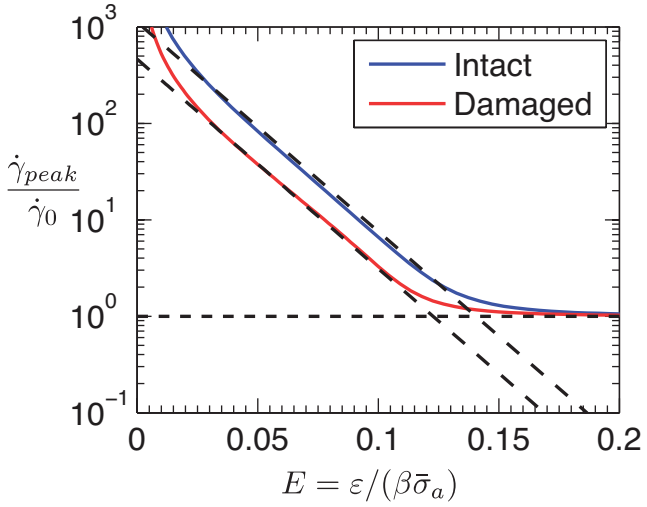

Figure 3.13: Gouge dilatancy: A plot showing how the peak strain rate $\dot{\gamma}_{peak}$ depends on the dimensionless parameter $E = \varepsilon/(\beta\bar{\sigma}_a)$ for the dilatancy only system using the path-averaged parameters modeling an intact and a damaged material, $V = 1$ m/s and $h = 0.5$ mm. For both parameter sets we observe larger peak strain rates for smaller values of E, corresponding to narrower localized shear zones. For all but the smallest values of E our results are well described by equation (3.47), and for each parameter set this formula is shown by the dashed black line.

values of E lead to larger values of $\dot{\gamma}_{peak}$ and thus more intense localization.

Except for the very lowest values of E, the simulations can be well fit using the equation

$$\frac{\dot{\gamma}_{peak}}{\dot{\gamma}_o} = 30\pi^2 \frac{h^2}{L_{thd}^2} \mathrm{e}^{-50E}, \tag{3.47}$$

as shown by the black dashed lines in Figures 3.13 and 3.14. As E gets very small the peak strain rate starts to increase more rapidly than predicted by equation (3.47), and as $E \to 0$ the peak strain rate must go to infinity. A fitting curve is not shown for the damaged parameters in Figure 3.14 since the value of E for this parameter set is in the range of values where (3.47) does not accurately describe our results. For this parameter set the peak strain

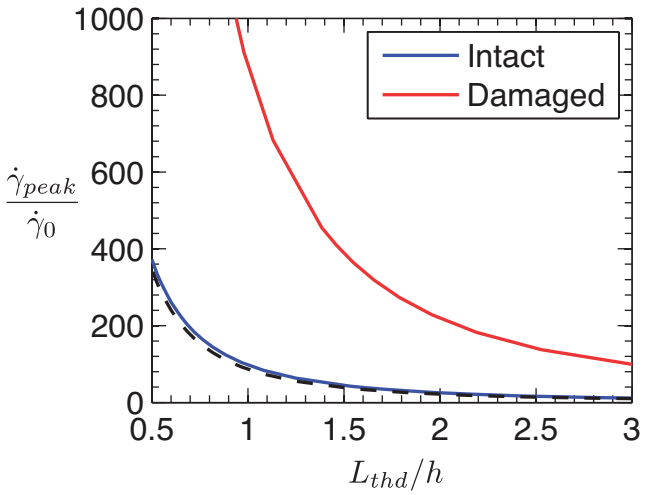

Figure 3.14: Gouge dilatancy: A plot showing how the peak strain rate $\dot{\gamma}_{peak}$ depends on the ratio of the thermal diffusion distance $L_{thd} = 2\pi\sqrt{\alpha_{th} t_w}$, where t_w is the characteristic weakening time for thermal pressurization, and the gouge layer thickness h. These simulations were produced using the path-averaged parameters modeling an intact and a damaged material, $V = 1$ m/s and $h = 0.5$ mm. Larger values of L_{thd}, corresponding to more efficient thermal diffusion, lead to lower peak strain rates and thus wider localized zones. The simulations are well fit by the formula given in equation (3.47), and this curve is shown by the dashed black line. No line is shown for the damaged parameters since the value of E is sufficiently small that equation (3.47) is no longer accurate.

rate is still proportional to $\hat{\lambda}^2$. In theory the exponential in equation (3.47) could be replaced by a more complicated function of E that diverges as $E \to 0$, though we did not attempt to do this due to the computational expense of simulations for very low values of E, and the fact that the localized zone thicknesses in this limit will approach the size of individual grains within the gouge. We emphasize that the exact numerical values in (3.47) depend on the size of the initial perturbations, though the qualitative picture is the same for a wide range of initial perturbations.

Equation (3.47) can be rearranged to give the peak strain rate in dimensional variables

$$\dot{\gamma}_{peak} = \frac{15V^2}{2\alpha_{th}\gamma_w} \exp\left(-\frac{50\varepsilon}{\beta\bar{\sigma}_a}\right). \tag{3.48}$$

As in the frictional strengthening only scenario, this formula is independent of the gouge layer width h, and the peak strain rate is controlled solely by the internal properties of the gouge material. We can relate this to a localized zone width W_{dil} using the relation

$$W_{dil} = \sqrt{\frac{2}{\pi}} \frac{V}{\dot{\gamma}_{peak}}, \tag{3.49}$$

which implies that

$$W_{dil} = \sqrt{\frac{2}{\pi}} \frac{2\alpha_{th}\rho c}{15V f_o \Lambda} \exp\left(\frac{50\varepsilon}{\beta\bar{\sigma}_a}\right). \tag{3.50}$$

The localized zone thickness is set by a balance between thermal pressurization, thermal diffusion, and dilatant strengthening.

The formula in equation (3.50) is now used to predict the localized zone width for the different parameter sets. First for the four parameter sets modeling a depth of 7 km we find

$$W_{int,n} = 1.32\ \mu\text{m} \quad , \quad W_{int,pa} = 1.21\ \mu\text{m}, \tag{3.51a}$$

$$W_{dam,n} = 1.85\ \mu\text{m} \quad , \quad W_{dam,pa} = 1.08\ \mu\text{m}. \tag{3.51b}$$

All four parameter sets predict a localized zone between 1 μm and 2 μm wide. The range of values is much more compact than for the frictional rate-strengthening only analysis. Damaged and intact parameters predict comparable thicknesses.

Next we look at the parameters modeling a depth of 1 km, predicting the localized zone

thicknesses

$$W_{1km,int} = 52\,\mu\text{m} \quad , \quad W_{1km,dam} = 14\,\mu\text{m}. \tag{3.52}$$

The predicted localized zone thicknesses are an order of magnitude larger than our predictions for a depth of 7 km, but still on the micron-scale. This is largely due to the sensitive dependence of W_{dil} on the ambient effective stress $\bar{\sigma}_a$.

The damaged parameters predict a thinner zone than the intact material, the exact opposite of the dependence predicted in the strengthening-only system. These predictions for W_{dil} must be used with caution due to the sensitive dependence on ε. We have used a parameter extracted from a single set of low strain rate experiments, but ε may be different at higher strain rates. An order of magnitude increase in ε leads to localized zone predictions on the tens of centimeters wide.

The formula for W_{dil} given in equation (3.50) is very different than the linear stability prediction from *Rice et al.* [2014][189] for the critical gouge layer thickness above which transient strain rate localization is expected. This means that the linear stability analysis cannot be used to make quantitative predictions for the localized zone thickness when localization is stabilized by dilatancy alone.

Since the shear strength evolution is linked to the onset of localization we also track the strain γ_{peak} at which the peak strain rate is achieved, where the peak strain rate is defined in equation (3.30). Figures 3.15 and 3.16 show γ_{peak}/γ_w as a function of E and L_{thd}. The critical strain γ_{peak} increases with ε but is relatively insensitive to changes in L_{thd} provided that straining localizes to a zone much thinner than the gouge layer thickness. Comparing this dependence on ε with the results from the previous section we see that, for both frictional rate-strengthening and dilatancy, a thicker localized zone corresponds to a larger value of

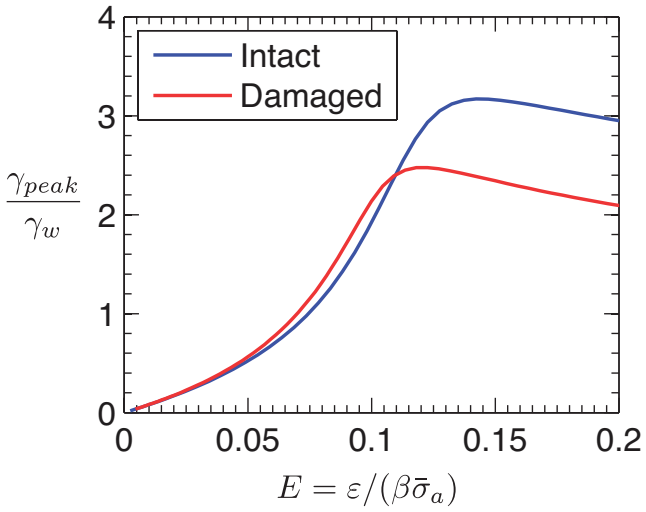

Figure 3.15: Gouge dilatancy: A plot showing how γ_{peak}, the strain at which peak localization occurs, depends on E. These simulations were done using the path-averaged parameters for an intact and damaged material, $V = 1$ m/s and $h = 0.5$ mm. Our results show that when E is small enough that transient strain rate localization occurs γ_{peak} is an increasing function of E, with small values of E leading to small values of γ_{peak}. This means that the most intense localized zones develop very rapidly. Very little difference is observed between the two parameter sets, which can be explained by noting that γ_{peak} is relatively insensitive to changes in L_{thd}, as shown in Figure 3.16.

γ_{peak}; a weaker localization limiting mechanism not only allows a narrower localized zone to form, it also allows this zone to develop faster.

3.6.3 Strain vs. strain rate localization

It is virtually impossible to observe in-situ strain rate profiles from seismic events or high-velocity friction experiments, with at best only the final strain pattern being observable. We now study the final strain profiles by integrating $\dot{\gamma}(y,t)$ to find the total strain $\gamma(y)$. Due to the transient nature of the localization for the dilatancy only system the final strain profile will be controlled by the amount of time spent straining in a localized fashion versus

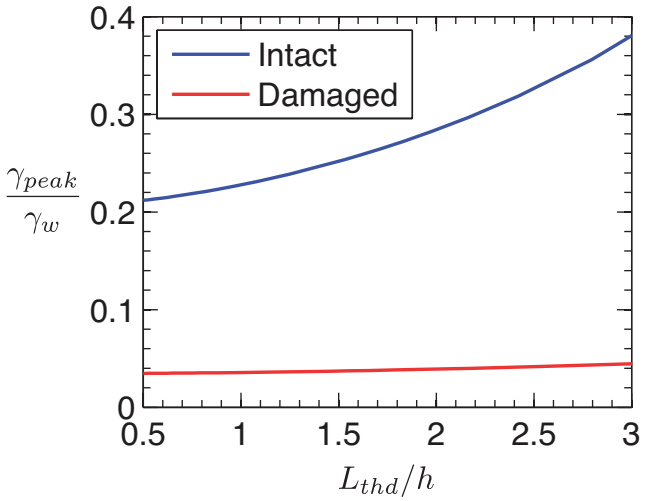

Figure 3.16: Gouge dilatancy: A plot showing how γ_{peak}, the strain at which peak localization occurs, depends on the ratio of the thermal diffusion distance $L_{thd} = 2\pi\sqrt{\alpha_{th} t_w}$, where t_w is the characteristic weakening time for thermal pressurization, and the gouge layer thickness h. These simulations were done using the path-averaged parameters for an intact and damaged material, $V = 1$ m/s and $h = 0.5$ mm. Our results show that γ_{peak} is an increasing function of L_{thd}, though when the localized zone width is much smaller than the gouge layer thickness γ_{peak}/γ_w does not depend strongly on L_{thd}.

the amount of time spent straining in a more uniform state.

Figure 3.17 shows the final strain profile for three total slips of 1 cm, 10 cm, and 100 cm. These results were produced using the path-averaged parameters for a damaged material, $V = 1$ m/s and $h = 0.5$ mm. We observe a reduction in strain localization with increasing slip. This is because, for $Vt \gg h$, the transient strain rate localization lasts for a small fraction of the event and the gouge spends the majority of the simulation shearing uniformly. This leads to final strain profiles with very little strain localization. Thus, even when uniform straining is initially unstable, localization may not be observed in final strain profiles if a large quantity of deformation occurring at the end of the event is approximately uniform.

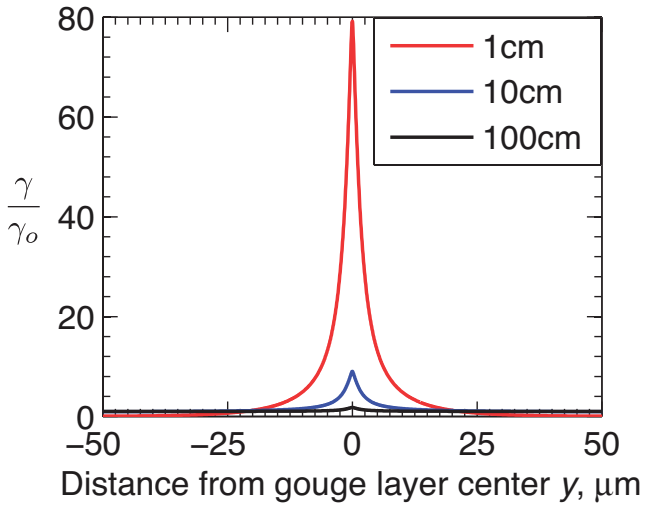

Figure 3.17: Gouge dilatancy: A plot of the final strain normalized by the average strain in the layer γ_o, for slips of 1 cm, 10 cm and 100 cm. These results were generated using the path-averaged parameters for a damaged material, $V = 1$ m/s, and $h = 0.5$ mm. We observe a decrease in strain localization with increasing slip. This can be understood by considering the transient nature of the localization; longer events will spend more time straining uniformly, and thus the effects of the transient strain rate localization will be less pronounced in the final strain profile.

3.7 Inertial effects in the gouge layer

3.7.1 Model including inertia

In this section we study inertial effects within the gouge layer. *Rice* [2006][186] argued that inertial effects across the gouge layer are negligible due to the short distances over which hydraulic and thermal diffusion act. Following this we assumed that deformation within the gouge layer could be regarded as quasi-static, an assumption we now test in this section.

The inertial effects considered here are different from the inertial effects in the bulk material on either side of a fault associated with dynamic rupture. Since we consider kinematically applied slip, in which the motion of the two half-spaces is fixed to a uniform slip rate

at $\pm V/2$, we have implicitly neglected unloading waves that would propagate into an elastic solid adjacent to the gouge layer.

Accounting for inertial effects within the gouge layer the equation for conservation of linear momentum becomes

$$\rho \frac{\partial u}{\partial t} = \frac{\partial \tau}{\partial y}, \tag{3.53}$$

where ρ is the density of the gouge material, and u is the local slip rate. This replaces equation (3.1), which modeled quasi-static deformation within the gouge layer. Differentiating equation (3.53) with respect to y we can express this in terms of the strain rate $\dot{\gamma}$

$$\rho \frac{\partial \dot{\gamma}}{\partial t} = \frac{\partial^2 \tau}{\partial y^2}, \tag{3.54}$$

recalling that the strain rate is defined as,

$$\dot{\gamma} = \frac{\partial u}{\partial y}. \tag{3.55}$$

Using the same scalings as before, given in equation (3.8), the nondimensional form of equation (3.54) is

$$I^2 \frac{\partial \dot{\gamma}'}{\partial t'} = \frac{\partial^2 \tau'}{\partial y'^2} \quad , \quad I = \sqrt{\frac{\rho V^2}{(\sigma_n - p_a)}}, \tag{3.56}$$

where primes indicate dimensionless variables. The dimensionless parameter I quantifies the effect of inertia in the gouge material. Interestingly the definition of I does not depend on the thickness of the gouge layer or the two diffusivities, and is a balance between an inertial stress and the ambient compressive effective stress. For the parameters in Table 3.1 and the slip rate $V = 1$ m/s we find $I = 0.0047$.

This inertial formulation of the problem is compatible with the kinematically applied slip condition (3.25), and thus the gouge material accommodates the correct amount of straining. To show this we integrate equation (3.54) with respect to y to find

$$\frac{\partial}{\partial t}\left(\int_{-h/2}^{h/2}\dot{\gamma}\,\mathrm{d}y\right)=\left[\frac{\partial\tau}{\partial y}\right]_{-h/2}^{h/2}. \tag{3.57}$$

If the half-spaces adjacent to the gouge layer are in uniform motion, and thus have no change in strain, then the right hand side of this equation will vanish and the total strain rate accommodated by the gouge layer will not change with time. Assuming that the initial state of shearing is uniform, $\dot{\gamma}=\dot{\gamma}_o$ for $|y|<h/2$, we recover condition (3.25)

$$\int_{-h/2}^{h/2}\dot{\gamma}\,\mathrm{d}y=V. \tag{3.58}$$

This means that the results from the model accounting for inertial effects can be directly compared with the results that assumed mechanical equilibrium, allowing us to quantify the effects of inertia. For small values of I we expect inertial effects to be negligible and the two models to agree very well.

We now solve the frictional rate-strengthening only system for a range of values of I and compare with the results generated by the model that assumed mechanical equilibrium. As in previous sections we use the maximum strain rate $\dot{\gamma}_{max}$ in the layer as a function of time as a proxy for localization, with larger values of $\dot{\gamma}_{max}$ indicating a thinner deforming zone. Figure 3.18 shows $\dot{\gamma}_{max}$ as a function of time for the nominal parameters describing a damaged material, a gouge layer width $h=0.5$ mm, $V=1$ m/s, and $I=10^{-1.5}$, $I=10^{-1}$, and $I=10^{-0.5}$. For $I=10^{-1.5}$ the inertial and mechanical equilibrium

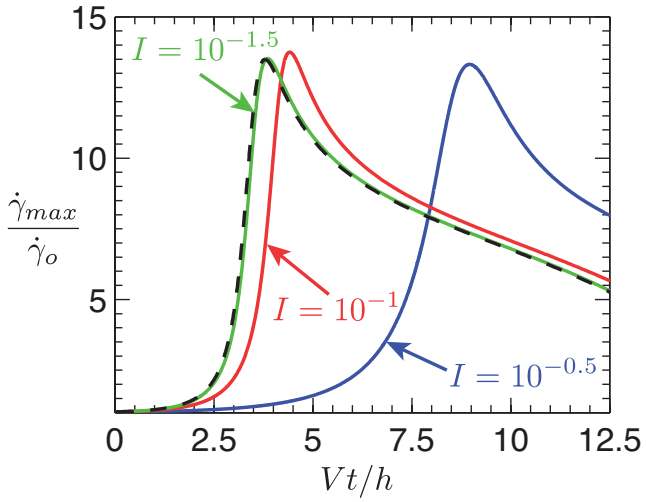

Figure 3.18: Rate-strengthening friction: A plot showing how maximum strain rate evolves in the inertial model for $I = 10^{-0.5}, 10^{-1}$ and $10^{-1.5}$. This plot was created using the nominal parameters modeling a damaged material, $h = 0.5$ mm and $V = 1$ m/s. For comparison the solution when mechanical equilibrium is assumed is shown by the dashed black line. For the lowest value of I the inertial and equilibrium solutions agree almost exactly, while for the larger values we see deviation away from the equilibrium solution.

models agree very well, but for $I = 10^{-1}$ and $I = 10^{-0.5}$ the inertial results begin to differ from the mechanical equilibrium solutions. More noticeable differences are observed for the largest value of I.

To quantify these inertial effects we now track the peak strain rate $\dot{\gamma}_{peak}$ and the time t_{peak} at which this peak strain rate occurs as a function of I. This is shown in Figure 3.19 for the nominal parameters modeling intact and damaged material, $h = 0.5$ mm, and $V = 1$ m/s. To allow easy comparison between the two parameter sets the results are normalized by the value from the mechanical equilibrium model; a value of unity means that the results from the mechanical equilibrium and inertial models agree exactly. As seen in the simulations shown in Figure 3.18, for very small values of I the two models agree almost

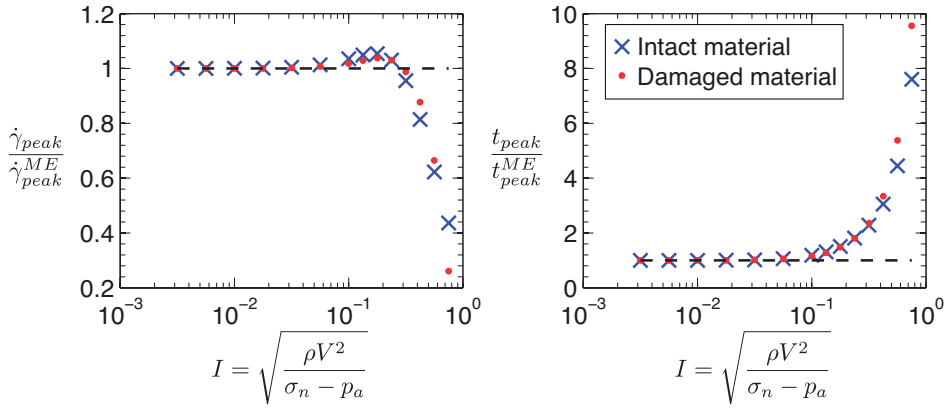

Figure 3.19: Rate-strengthening friction: A plot showing how the peak strain rate $\dot{\gamma}_{peak}$ and time t_{peak} at which this peak strain occurs vary with I for the nominal parameters modeling intact and damaged material, a gouge layer thickness $h = 0.5$ mm, and a slip rate $V = 1$ m/s. To allow easy comparison between the two parameter sets all values of $\dot{\gamma}_{peak}$ and t_{peak} are normalized by the values found when mechanical equilibrium is assumed. These mechanical equilibrium values are indicated by a superscript ME. Above $I = 10^{-1}$ inertial effects become important and the two models diverge. Inertial effects lead to two key differences. The value of $\dot{\gamma}_{peak}$ is decreased, which corresponds to a wider localized zone; the time t_{peak} at which peak localization occurs is larger indicating that the localized zone takes longer to develop.

exactly, but as I increases inertia becomes important and the two models diverge. Inertial effects within the gouge layer lead to lower values of $\dot{\gamma}_{peak}$ and larger values of t_{peak}, indicating that inertial effects lead to wider localized zones that take longer to develop.

Using the results shown in Figures 3.18 and 3.19 we choose a value of $I = 0.1$ as a cutoff above which inertial effects become important. An argument could be made for a slightly larger or smaller critical value of I but this appears to be the correct order of magnitude. This critical value allows us to define a critical slip rate

$$V_c = \sqrt{\frac{\bar{\sigma}_a}{100\rho}}. \tag{3.59}$$

Inertial effects will become important when slip rates exceed this critical value, and will act to limit localization.

Here we chose $I = 0.1$ as an estimate of the critical value based on simulations performed using two different parameter sets. A fuller analysis would find the critical value of I for a much wider range of parameters, showing how it varies as the intensity of strain rate localization varies.

3.7.2 Implications for high-velocity friction experiments

We now use the critical slip rate V_c to comment on the role of inertia during high-velocity friction experiments. These experiments are typically performed using a rotary shear configuration and allow experiments to be performed at seismic slip rates, albeit at compressive stresses much lower than those present during seismic events[29,124,177,211]. Highly localized shear zones are commonly observed in high-velocity friction experiments. A fuller discussion of these observations can be found in the introduction to *Rice et al.* [2014][189].

To estimate V_c for conditions typical in high-velocity friction experiments we use $\sigma_n = 0.6$ MPa and assume that the initial pore pressure is negligible compared with this normal stress. The gouge density appropriate for laboratory conditions is assumed to be the same as that given in Tables 3.1 and 3.2. Combining these values leads to a critical slip rate of $V_c = 1.46$ m/s. This value of V_c is higher than the ~ 1 m/s slip rates normally used in high-velocity shear experiments, and thus we conclude that inertial effects within the gouge layer are not playing a significant role in limiting localization in high-velocity friction experiments.

Additional simulations in which the half-spaces are undrained and adiabatic show that

when pore pressures have risen to a significant fraction of the normal stress the appropriate definition of I may be based on the current effective stress not the ambient effective stress. Motivated by this we make an estimate for V_c based on a much lower effective stress $\bar{\sigma}_a = 0.15$ MPa, which is intended to model a gouge with a compressive stress $\sigma_n = 0.6$ MPa and a pore pressure that has risen to seventy-five percent of the normal stress. In this case we find $V_c = 0.73$ m/s. Thus, for this scenario we would predict that inertial effects within the gouge are not negligible when the applied slip rate is 1 m/s. However, since the critical slip rate V_c is only exceeded by a small amount the actual limiting of localization by inertia would probably not be dramatic. Figure 3.19 shows that significant localization limiting only occurs once $I > 0.3$.

3.7.3 Implications for natural faults

Next we discuss the importance of inertial effects during earthquakes. Consider a fault at a depth D where the depth is measured in kilometers. The effective overburden stress is $(\rho - \rho_w)gD$, assuming hydrostatic fluid pressure. Typically $\rho = 2.8\rho_w$ so the gradient in overburden effective stress is 18 MPa/km and $\bar{\sigma} = 18D$ MPa. This is consistent with the values of $\bar{\sigma}_a$ we chose in the parameter sets given in Tables 3.1 and 3.2. For a depth of 1 km we set $\bar{\sigma}_a = 18$ MPa, and for a depth of 7 km we set $\bar{\sigma}_a = 126$ MPa.

Taking the values in Table 1 we can calculate a critical slip rate $V_c = 21.2$ m/s for a depth of 7 km. Since the hydraulic parameters do not enter the formula for V_c this value is the same for all four parameter sets. This is compared with a typical coseismic slip rates of 1 m/s, justified as an average earthquake slip rate in *Rice et al.* [2014][189]. Since V_c is much larger than typical coseismic slip rates we conclude that, as predicted in *Rice* [2006][186], iner-

tial effects within the gouge layer are negligible at seismic depths. Using our formula for V_c we can calculate what depth D must be exceeded for inertial effects to be negligible. Setting $V_c = 1$ m/s we find that this critical depth is just 15 meters, and thus inertial effects will be negligible throughout the seismogenic zone.

So far the analysis in this section has compared V_c to a typical coseismic slip rate of 1 m/s. However, near the tip of a dynamically propagating fracture the slip rates will be significantly larger. The peak slip velocity $V = 300$ m/s from *Noda et al.* [2009][155], which is taken as a typical peak slip rate during dynamic rupture, is far in excess of our prediction for V_c. This may mean that shear localization is initially limited by inertial effects even though they are unimportant throughout the vast majority of the rupture. Using our formula for $\bar{\sigma}_a$ as a function of depth we find that this picture, in which inertial effects are important near the crack tip yet unimportant for the majority of a rupture, is valid for all depths spanning the seismogenic zone.

Interestingly *Noda et al.* [2009][155] noted that the slip rates above ~ 100 m/s persist for only 1 μs, which corresponds to a slip of just 100 μm. Comparing this small slip with the results in Section 3.5, which showed that a finite strain is required for the localized zone to develop, we conclude that near the tip localization may not have time to fully develop.

A better description of localization near the tip of a dynamically propagating fracture that balances the high slip rates, small slips and inertial effects is still required. It may be possible to use an analysis near the crack tip to predict a thickness of the deforming zone when inertial effects become unimportant and shear of the gouge material is well described by the model in Section 3.2. This could then be used as an input for the model in Section 3.2, and the gouge layer thickness h would be reinterpreted as the thickness of the deform-

ing zone when inertial effects become unimportant. Of course there may be some scenarios in which negligible localization occurs near the tip and the initial width of the deforming zone will be equal to the gouge layer thickness.

As mentioned in the previous subsection, when pore pressures have risen to a significant fraction of the normal stress the appropriate definition of I may be based on the current effective stress not the ambient effective stress. We highlight two scenarios when this distinction may be important.

Simulations that account for thermal decomposition show that the onset of the reaction is accompanied by a large pore pressure increase that can drive the gouge layer into a regime where the pore pressure exceeds the normal stress[217]. As the pore pressure approaches the normal stress inertial effects will become important within the gouge layer and will act to widen the deforming zone. Since this widening will spread frictional heating over a wider zone, which will lead to slower pore pressure rises at the location of peak pore pressure, delocalization driven by inertial effects may be one mechanism to stop the maximum pore pressure exceeding the normal stress.

The other scenario in which inertial effects may become important as pore pressures approach the normal stress is near the trailing edge of a dynamically propagating rupture. We can estimate the minimum effective stress $\bar{\sigma}_{min}(t)$ in the late stages of rupture using the Mase-Smith-Rice slip on a plane solution. Using the asymptotic expansion for the complementary error function valid at large slips this leads to

$$\frac{\bar{\sigma}_{min}}{\bar{\sigma}_a} = \sqrt{\frac{L^*}{\pi\delta}}, \tag{3.60}$$

where $\delta = Vt$ is the total slip accommodated across the gouge layer. Defining $I_{cur.}$ in a

similar fashion to the definition of I but using the current minimum effective stress $\bar{\sigma}_{min}$ we find,

$$I_{cur.} = \left(\frac{\pi\delta}{L^*}\right)^{1/4} I. \tag{3.61}$$

The four parameter sets in Table 3.1 predict values of L^* between 1.69 mm and 57.7 mm. Using a typical seismic slip of one meter this predicts values of $I_{cur.}$ between a factor of 2.71 and a factor of 6.57 larger than I. For a larger slip of ten meters this range of values increases to 4.83 and 11.68. These values of $I_{cur.}/I$ mean that inertial effects may become important near the trailing edge of a rupture for small values of $\bar{\sigma}_a$, which correspond to shallow events, and small values of L^*. However, the range of values for L^* means that this behavior should not be expected for all earthquakes. Since inertial effects act to limit localization, and having shown the link between localization and dynamic weakening, we hypothesize that the gradual onset of inertial effects at the trailing edge of a rupture may lead to a slowdown in dynamic weakening. Without further work it is hard to quantify how much strengthening this mechanism could lead to at the trailing edge, and if this would be a viable mechanism to promote ruptures that propagate as self-healing pulses (as opposed to crack-like ruptures).

3.7.4 Links with granular flow

Discrete simulations of granular flows commonly quantify the effects of particle inertia using a dimensionless parameter known as the inertia number[54,77], which is defined as

$$I_{gran.} = \dot{\gamma} d \sqrt{\frac{\rho_g}{P}}. \tag{3.62}$$

Here ρ_g is the density of the grains, P is the applied pressure, $\dot{\gamma}$ is the applied shear rate, and d is the grain size. Assuming that the density of the grains is equal to the density of the porous material per unit reference volume, an assumption that is justified for a gouge material with a low porosity, and that the pressure is equivalent to the ambient compressive stress $\bar{\sigma}_a$ we can write our dimensionless parameter I as

$$I = \frac{d}{h} I_{gran.}. \tag{3.63}$$

Our parameter I is equal to the inertia number multiplied by the ratio of the grain diameter and the gouge layer thickness. When shear is highly localized it may be more appropriate to use the current width of the deforming zone, W_{rsf} when localization is stabilized by frictional rate-strengthening alone, instead of the initial gouge layer thickness h. This corresponds to setting $\dot{\gamma} = V/W_{rsf}$ instead of $\dot{\gamma} = V/h$ in the definition of $I_{gran.}$. For either choice we expect $I_{gran.}$ to be at least an order of magnitude greater than I.

We now compare the point at which inertial effects across the gouge layer, as described by equation (3.54), become important with the point at which the inertia of individual grains becomes important. *Da Cruz et al.* [2005][54] cites the critical value $I_{gran.} = 0.1$ as the point at which the inertia of individual grains becomes important. Our simulations show that inertial effects across the gouge layer become important when $I > 0.1$. Since $I_{gran.}$ is at least an order of magnitude larger than I we deduce that the inertia of individual particles should become important before the inertial effects across the gouge layer become important. However, without determining how the critical value of I inferred from Figure (3.19) varies with the gouge properties we cannot be sure that this conclusion is valid for all parameter choices.

There are some drawbacks with the granular simulations used to find the critical value of $I_{gran.}$. First the granular simulations typically use particles that are roughly equal in size. This in stark contrast with the particle size distribution for the Punchbowl fault found in *Chester et al.* [2005][45], which showed that in a thin section the particle density was proportional to d^{-2}, where d is the grain size, for a d between 30 nm and 70 μm. This may mean that in a three-dimensional packing the particle density is proportional to d^{-3}. Another problem is the shape of the particles. Granular simulations frequently use discs in two-dimensional simulations, and sometimes spherical particles, while real fault gouge can have a much more diverse set of particle shapes. It is unclear if these considerations will dramatically alter the critical value of $I_{gran.} = 0.1$ at which the inertia of individual particles becomes important.

Our predictions for the localized zone thickness are not valid when the inertia of individual grains becomes important, though several options exist to create a new prediction. The first option is to linearize the friction laws in *Da Cruz et al.* [2005][54] that account for the inertia of individual grains to find effective values of f_o and $(a - b)$, as suggested in equation (5) of *Rice et al.* [2014][189]. These effective values can then be used in the formulae for the localized zone thickness provided in this paper. Another option is to use a higher order continua or gradient theory that models the inertia of individual grains, and examples of how these models interact with thermal and pore fluid effects can be found in *Vardoulakis* [2002][230] and *Sulem et al.* [2011][219].

3.8 Discussion

3.8.1 Frictional rate-strengthening only

Our simulations predict micron-scale strain rate localization in a fluid-saturated gouge material. The strain rate profile has a Gaussian shape throughout the simulation, the same form assumed in previous models for thermal pressurization [4,180,155,86]. The excellent fit between the Gaussian function and our numerical simulations allows us to infer a width for the localized straining zone, which is taken to be twice the root mean square width of the Gaussian. Tracking this width as a function of the gouge layer thickness h we find that straining localizes to a zone that has a very weak dependence on the gouge layer thickness h. This means that the thickness of the localized zone is controlled by the gouge properties not the initial width of the gouge layer.

The nondimensionalization in subsection 3.2.5 shows that for localization stabilized by frictional rate-strengthening alone there are only three dimensionless parameters. One parameter quantifies the rate-strengthening component of the friction law and the other two compare the diffusion distances for thermal and hydraulic diffusion on timescales comparable to the characteristic weakening timescale for thermal pressurization with the gouge layer thickness. A parameter sweep over these three parameters allows us to determine the localized zone thickness at peak localization as a function of the gouge properties. The results are shown in Figures 3.5, 3.6 and 3.7, and our simulations are well fit by

$$W_{rsf} \approx \frac{6.9(a-b)\gamma_w}{f_o + 2(a-b)} \frac{(\sqrt{\alpha_{hy}} + \sqrt{\alpha_{th}})^2}{V}. \tag{3.64}$$

The localized zone thickness is set by a balance between frictional rate-strengthening, ther-

mal pressurization and hydrothermal diffusion. Comparing this formula with the linear stability prediction from *Rice et al.* [2014][189] we see one crucial difference. In the linear stability prediction hydrothermal diffusion enters through the sum of the diffusivities $\alpha_{hy} + \alpha_{th}$, while the results of our simulations are better fit by the *Rice* [2006][186] lump hydrothermal diffusivity $\alpha = \left(\sqrt{\alpha_{hy}} + \sqrt{\alpha_{th}}\right)^2$ from the Mase-Smith-Rice slip on a plane solution. Since nonlinear terms are properly accounted for and the localized zone thickness is tracked from the initial instability all the way to peak localization, we consider the formula in this paper to be a better predictor for localized zone thickness than the formula given in *Rice et al.* [2014][189], which was based on a linear stability analysis. However, the two formulae produce very similar predictions, and in the limit where one diffusivity is much greater than the other the two formulae differ only in the constant fore-factor (π^2 in the linear stability analysis and 6.9 in the nonlinear simulations).

Using the parameters from *Rempel and Rice* [2006][180] modeling a depth of 7 km and frictional data from *Blanpied et al.* [1998][24] our formula for W_{rsf} predicts localized zone thicknesses between 4 μm and 44 μm. We also developed a set of hydraulic parameters intended to model a depth of 1 km, a typical intersection depth for boreholes drilled into active faults. At shallower depths thermal pressurization is less efficient and hydraulic diffusion is more efficient, leading us to predict wider localized zones. For an intact material we predict a localized zone thickness of 31 μm, and for a damaged material, where damage is modeled as in *Rice* [2006][186], we predict a thickness of 217 μm. These values are very similar to those predicted in *Rice et al.* [2014][189]. A comparison between our predictions and observations from laboratory and field studies, and a discussion of other factors that that could alter our predictions, can be found in *Rice et al.* [2014][189].

The discussion above assumes that peak localization is achieved during a seismic event. However, this may not always be the case. Figures 3.9 and 3.10 show γ_{peak}, the nominal strain at which peak localization occurs, as a function of the gouge properties. A typical value for γ_{peak}/γ_w is 0.5. If the nominal strain is less than γ_{peak}, as will be the case for small slips or wide gouge layers, then the localized zone will not have time to fully develop. This will mean that final strain profiles will be thicker than the predictions from our formula for W_{rsf}.

3.8.2 Dilatancy only

For localization limited by dilatancy alone we see rapid strain rate localization, followed by a decay back to uniform shear. As for strain rate localization stabilized by frictional rate-strengthening alone, the localized zone has a Gaussian shape throughout the simulation. The system is controlled by just two dimensionless parameters, one modeling the strength of dilatancy and the other modeling the strength of thermal diffusion. Varying these parameters independently we find a formula for the localized zone thickness W_{dil} at peak localization

$$W_{dil} = \sqrt{\frac{2}{\pi}} \frac{2\alpha_{th}\rho c}{15 V f_o \Lambda} \exp\left(\frac{50\varepsilon}{\beta\bar{\sigma}_a}\right). \tag{3.65}$$

As before the width of the localized zone is independent of the gouge layer thickness, and W_{dil} is set by the gouge properties. Using this formula and the parameters modeling a depth of 7 km (see Table 3.1) we predict localized zone thicknesses between 1 and 2 μm. This range of values is lower than those predicted for frictional rate-strengthening alone, suggesting that dilatancy is less effective at limiting strain rate localization (if a wider localized zone is equivalent to more effective localization limiting). Our predictions fall into

a more compact interval than our predictions for W_{rsf}. This is because the localized zone thickness is less sensitive to changes in hydraulic parameters than the frictional rate-strengthening system, and the hydraulic parameters are among the least constrained parameters in the system. We also predicted localized zone thicknesses at a depth of 1 km, with this depth intended to model a typical intersection depth for boreholes drilled in active faults. We predict $W_{dil} = 54$ μm for an intact material, and $W_{dil} = 15$ μm for a damaged material. Damaged parameters lead to thinner localized zones due to the increase in the storage capacity β. A larger storage capacity leads to less efficient limiting of localization by dilatant suctions. This is in contrast to the frictional rate-strengthening results that predicted wider localized zones for the damaged parameters.

The linear stability analysis in *Rice et al.* [2014][189] predicts transient growth followed by decay back to uniform shearing. However, the transient growth quickly leads to strain rate perturbations that violate the linearization assumptions. Our simulations properly account for nonlinear terms and qualitatively reproduce the transient growth predicted by the linear stability analysis. However, the quantitative predictions from the linear stability analysis do not agree with the widths inferred from our numerical simulations, and the formulae for W_{dil} predicted by the two methods have a very different structure. The linear stability predictions from *Rice et al.* [2014][189] provide a poor prediction of the localized zone thickness because the linearized model is applied beyond the point at which the linearization becomes invalid.

Finally we studied how the transient strain rate localization is expressed in final strain profiles. Figure 3.17 shows the final strain profile for three different slips for the path-averaged parameters modeling a damaged material, $V = 1$ m/s and $h = 0.5$ mm. For slips that are

large compared to the gouge layer thickness the majority of time will be spent shearing the gouge uniformly, leading to final strain profiles with little noticeable strain localization. As with the previous discussion of a localized shear zone that does not fully develop, this is another example of how final strain profiles can look like shearing was uniform even when uniform shearing is unstable. This difference between strain localization and strain rate localization must be considered when interpreting final strain profiles.

3.8.3 Localization and dynamic weakening

Rempel and Rice [2006][180] studied the shear strength evolution for a uniformly sheared gouge layer undergoing thermal pressurization. They verified that the initial stages of deformation are well described by the solution of *Lachenbruch* [1980][127] for uniform shear under undrained and adiabatic conditions, and the later stages of deformation are described by the Mase-Smith-Rice slip on a plane solution. Using this framework we studied the impact of strain rate localization on shear strength evolution.

Figure 3.8 shows that, for localization stabilized by frictional rate-strengthening alone, the onset of strain rate localization is accompanied by an acceleration in dynamic weakening, with the most rapid dynamic weakening coinciding with the most rapid thinning of the localized zone. As straining localizes the frictional heating is focused into a narrow zone leading to more efficient thermal pressurization. The early stages of deformation are still in good agreement with the uniform shear solution from *Lachenbruch* [1980][127]. During this period straining is localizing but is far from peak localization. After peak localization the shear strength is well described by the Mase-Smith-Rice slip on a plane solution. Our solutions are all for a fixed slip rate V. The results for strain rate localization stabilized by dila-

tancy alone also show this link between the onset of localization and accelerated dynamic weakening.

We found that the most rapid weakening corresponds to the time when the localized zone is thinning most rapidly. This means that the strain until peak localization, γ_{peak}, controls the slip at which the most rapid weakening occurs. For strain rate localization stabilized by frictional rate-strengthening alone γ_{peak} is an increasing function of $(a - b)$ and a decreasing function of α_{hy} and α_{th}. Values of γ_{peak}/γ_w are typically around 0.5.

For strain rate localization stabilized by dilatancy alone γ_{peak} is relatively insensitive to changes in the thermal diffusion lengthscale L_{thd}, provided that the gouge layer thickness is not comparable to the localized zone thickness. The critical strain γ_{peak} is an increasing function of ε so, as for the frictional rate-strengthening only system, a more effective localization limiting mechanism not only leads to wider localized shear zones, but also slows the rate at which strain localization occurs.

Since the most rapid dynamic weakening occurs at strains comparable to γ_{peak}, if the gouge layer is sufficiently thick or the slip in an event is sufficiently small then the localized zone may not fully develop. If this occurs then we expect the strength evolution to be far smoother than the example shown in Figure 3.8. One caveat is that it may not be possible for slip to cease during the accelerating dynamic weakening that occurs just before a fully developed localized zone is generated.

3.8.4 Maximum temperature rise

Strain rate localization also has a pronounced effect on the maximum temperature. Figure 3.11 shows the maximum temperature rise for the localized shear solution and uniform shear

solution when localization is stabilized by frictional rate-strengthening alone. For the initial stages of deformation the maximum temperature rise is well described the undrained and adiabatic solution from *Lachenbruch* [1980][127]. However, as the strain rate localizes the frictional heating is focused into a narrow zone, leading to a large increase in the maximum temperature rise. After straining has localized the maximum temperature rise mirrors the solution for slip on a plane, but will never converge to this solution. For the simulation shown in Figure 3.11 the maximum temperature rise for the localized shear solution is about three times larger than that of the uniform shear solution after a slip of 10 mm, a difference of $\sim$ 580 °C. Such a dramatic increase temperature rise has obvious implications for the onset of melting and the triggering of other temperature controlled dynamic weakening mechanisms such as thermal decomposition. Varying the gouge properties we find that the most rapid rises in the maximum temperature correspond to the lowest values of W_{rsf}, as would be expected since lower values of W_{rsf} means straining is confined to a narrower zone.

While the maximum temperature rise for the localized shear solution is much larger than that of the uniform shear solution, the temperature anomaly that might be observed in fault drilling studies would be smaller. This is because the temperature rise observed during drilling is controlled by the total dissipation

$$\int_0^D \tau(\delta)\mathrm{d}\delta, \tag{3.66}$$

where δ is slip and D is the total slip in an event. The rapid weakening that accompanies localization means that the total dissipation for the localized shear solution will be less than the total dissipation for the uniform shear solution, leading to a lower temperature

anomaly.

We can understand the apparent contradiction between a higher maximum temperature rise and a lower temperature anomaly by realizing that the extremely small width of the localized zone means that the maximum temperature rise will rapidly decay after the cessation of slip. The timescale for decay of the localized peak in temperature can be estimated by W_{rsf}^2/α_{th}. Using our predictions of localized zone thickness we predict decay timescales between 0.022 and 3.6 milliseconds. The very short decay time may be important when estimating the maximum temperature rise on a fault using the thermal maturity methods described in*Polissar et al.* [2011][169], with narrower localized zones corresponding to a larger estimate for the temperature rise.

3.9 Conclusions

In this paper we have used numerical simulations to study strain rate localization in a fluid-saturated gouge material undergoing thermal pressurization. Two stabilizing mechanisms were considered to prevent the deformation collapsing onto a mathematical plane, frictional rate-strengthening and dilatancy. We predict a localized zone thickness, which is compared with the predictions for localized zone thickness from the companion paper *Rice et al.* [2014][189], and show the impact localization has on the maximum temperature rise and shear strength evolution.

For frictional rate-strengthening alone the strain rate profile has a Gaussian shape throughout the deformation allowing us to infer the width of the localized zone W_{rsf}. The peak localized zone thickness is found to be almost independent of the gouge layer thickness. A parameter sweep leads to a formula for the localized zone thickness as a function of the

gouge properties, and the thickness is set by a balance between thermal pressurization, hydrothermal diffusion and rate-strengthening friction. For parameters modeling a depth of 7 km we predict localized zone thicknesses between 4 μm and 44 μm.

For dilatancy alone we also predict a localized zone thickness that is independent of the gouge layer thickness. A parameter sweep leads to a formula for the localized zone thickness W_{dil} as a function of the gouge parameters, with the formula given in equation (3.50). Using this formula we predict localized zone thicknesses between 1 μm and 2 μm at a depth of 7 km. The most sensitive dependence of W_{dil} is on ε, which models the magnitude of dilatancy.

Strain rate localization has a dramatic effect on the strength and temperature evolution of the gouge layer. As straining localizes the frictional heating is focused into a narrower zone, leading to a much larger temperature rise than that predicted if localization is neglected. This focusing of frictional heating also leads to rapid thermal pressurization and the development of a localized shear zone coincides with a significant strength drop.

Finally, we tested the hypothesis in *Rice* [2006][186] that inertial effects across the gouge layer will be unimportant during shear. We found that in general inertial effects across the gouge layer will be unimportant in both real earthquakes and high-velocity friction experiments, but may play a role very close to the tip of a dynamically propagating rupture or when the pore pressure approaches the normal stress on the fault.

This project was a collaboration with Nicolas Brantut and James R. Rice. I was the lead researcher on this project and primary author of the final manuscript. The work in this chapter has been submitted to the Journal of Geophysical Research.

4

Strain localization driven by thermal decomposition during seismic shear

4.0 Abstract

Field and laboratory observations show that at seismic slip rates shear deformation is often extremely localized, with a typical deforming zone width on the order of a few tens of

microns. This extreme localization can be easily understood in terms of thermally driven weakening mechanisms such as thermal pressurization and thermal decomposition. A zone of initially high strain rate will experience more shear heating and thus weaken faster, making it more likely to accommodate future deformation. *Rice et al.* [2014][189] and *Platt et al.* [2014][166] showed how a combination of analytic and numerical methods could be used to predict the localized zone thickness when dynamic weakening is controlled by thermal pressurization, finding localized zone thicknesses between 4 and 44 μm for representative fault gouge parameters. In this paper we extend that work to account for thermal decomposition. A linear stability analysis predicts a localized zone thickness that is tested using numerical simulations. We investigate how the onset of thermal decomposition drives additional strain localization, how the endothermic thermal decomposition reaction and thermal diffusion combine to limit the maximum temperature, and how the pore fluid released by the reaction accelerates dynamic weakening.

4.1 Introduction

Field studies of fault zones show a hierarchical structure, with a fault core composed of ultracataclasite and fault gouge sitting within a broader damage zone. Further investigation reveals a zone of highly localized shear on the order of $10 - 300$ μm wide nested within the fault core[101,43,55]. These field observations are consistent with laboratory observations from high-velocity rotary shear experiments, which reveal micron-scale strain localization at seismic slip rates of order 1 m/s. In experimental deformation tests performed at a slip rate of 1 m/s on a dry, natural clay-bearing fault gouge, *Brantut et al.* [2008][29] identified a zone of darker material $\sim 1 - 10$ μm wide that, due to the lack of other indicators of deformation

elsewhere in the sample, was interpreted as the main slipping zone in the experiment. In similar deformation experiments performed under wet conditions on similar natural fault zone materials, *Kitajima et al.* [2010][124] showed that a 100 μm thick zone of extremely fine grained material with a strong foliation forms at seismic slip rates. This zone is thought to have accommodated the majority of deformation in the experiment, and the foliation may indicate that the width of a single localized shear zone is much smaller than 100 μm. A more detailed discussion of these observations and further examples of micron-scale strain localization can be found in the introduction to *Rice et al.* [2014][189].

In general, strain localization should be expected in gouge undergoing thermally driven dynamic weakening. If a region is straining faster then it will experience more shear heating; more shear heating leads to faster weakening; weaker regions of the gouge layer will be more likely accommodate future deformation. In fluid-saturated fault rocks, two distinct thermally driven dynamic weakening mechanisms can be considered: thermal pressurization of native pore fluid and thermal decomposition. Thermal pressurization is due to thermal expansion of the pore fluid and pore volume as the fluid-saturated gouge material is heated. If the heating occurs faster than the pore fluid can drain from the gouge then the pore pressure will increase leading to dynamic weakening[127,144,145]. Thermal decomposition corresponds to the chemical breakdown and devolatilisation of hydrated or carbonated minerals, such as clays or calcite, which are often present in faults. Laboratory experiments have revealed that several devolatilisation reactions can occur within timescales of a few seconds during friction experiments performed at seismic slip rates ($\sim$ 1 m/s); this was shown for the decomposition reaction of calcite[97], siderite[96], antigorite[106], kaolinite[29], dolomite[56] and gypsum[32]. In the crustal seismogenic zone these decomposition reactions are typically

endothermic and at a fixed pressure the reaction products occupy a larger volume than the reactants. The combination of these two effects implies that the onset of rapid thermal decomposition leads to an increase in the pore pressure and a plateau in the maximum temperature, as shown theoretically in *Sulem and Famin* [2009][217], *Sulem et al.* [2009][218] and *Brantut et al.* [2010][30], and experimentally in *Brantut et al.* [2011][32].

For thermal pressurization alone, *Rice et al.* [2014][189] used a linear stability analysis to predict how the localized zone thickness depends on the gouge properties. This analysis was complemented by the numerical simulations, which went well beyond the linear regime, presented in *Platt et al.* [2014][166]. For strain rate localization stabilized by frictional rate-strengthening alone the localized zone thickness is set by a balance between thermal pressurization, hydrothermal diffusion and frictional strengthening. Using hydraulic and thermal parameters from *Rempel and Rice* [2006][180], which model a depth of 7 km as a typical centroidal depth for a crustal seismogenic zone, and friction data from *Blanpied et al.* [1998][24], they predicted that the localized zone is between 4 and 44 μm wide, with the smaller number assuming parameters based on experiments on undamaged gouge and the larger number representing an estimate of the effect of damage at the onset of rapid shear (e.g. microcracking). *Platt et al.* [2014][166] also showed that strain localization has a dramatic effect on the temperature and strength evolution of the gouge. As straining localizes the frictional heating is focused into a very narrow zone leading to an acceleration in dynamic weakening and a temperature rise much larger than that predicted when strain rate localization is not accounted for. In this paper we extend the work in *Rice et al.* [2014][189] and *Platt et al.* [2014][166] to account for thermal decomposition. A linear stability analysis leads to a prediction for the localized zone thickness as a function of fault temperature, and

these predictions are tested using numerical simulations. We also study how thermal decomposition combines with thermal diffusion to limit the maximum temperature rise, and show that the onset of thermal decomposition leads to an acceleration in dynamic weakening.

The width of the deforming zone during seismic shear, which this paper attempts to constrain, is of crucial importance in theoretical models of thermally driven dynamic weakening. *Lachenbruch* [1980][127] showed that for undrained and adiabatic conditions dynamic weakening by thermal pressurization is controlled by a critical weakening strain, so the slip weakening distance for thermal pressurization is proportional to the deforming zone thickness. This may explain why the gouge layer thickness plays a role in determining if a rupture propagates as a crack-like rupture or slip pulse in the results of *Noda et al.* [2009][155]. Another example can be found in *Garagash* [2012][86], which showed that for steadily propagating slip pulses thinner deforming zones lead to smaller slips and faster rupture velocities.

4.2 Model derivation

Here we derive a model for a fluid-saturated gouge material sheared between two undeforming thermo-poroelastic half-spaces that allow diffusion of heat and pore fluid, the same boundary conditions used in *Platt et al.* [2014][166]. In this one-dimensional model the only non-zero velocity component, $u(y,t)$, is parallel to the fault zone and depends only on the coordinate perpendicular to the direction of slip y, and the time since shear commenced t. A sketch of this geometry is shown in Figure 4.1. Our derivation extends the model of *Rice et al.* [2014][189] to account for thermal decomposition, which is modeled using the ideas in *Sulem and Famin* [2009][217], *Sulem et al.* [2009][218] and *Brantut et al.*

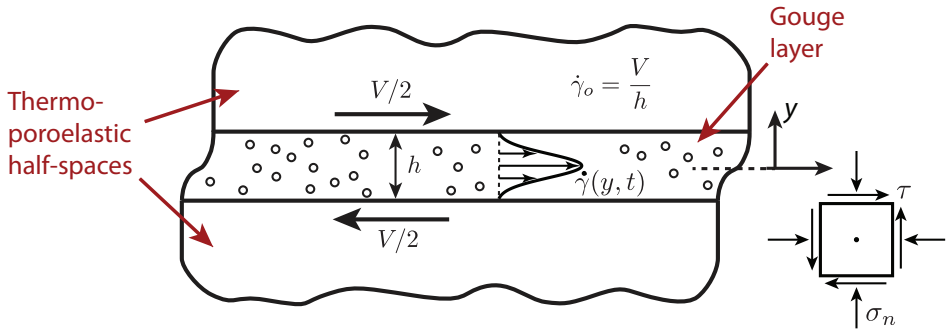

Figure 4.1: A sketch showing the geometry used in our numerical simulations. A gouge layer with a finite thickness h is sheared between two undeforming thermo-poroelastic half-spaces moving relative to each other at a slip rate V leading to a nominal strain rate of $\dot{\gamma}_0 = V/h$ within the gouge layer. In this one-dimensional model we only account for variations in the across-fault direction y. The straining is allowed to localize within the gouge layer, as shown by the Gaussian strain rate profile sketched within the gouge layer. The width W of the zone of localized straining is then estimated as twice the root mean square width of the Gaussian.

[2010][30].

For clarity while deriving the model we specify a single reaction to be modeled, the breakdown of calcite into calcium oxide and carbon dioxide,

$$\mathrm{CaCO_3} \rightarrow \mathrm{CaO} + \mathrm{CO_2}. \tag{4.1}$$

However, the framework used here is general and some results are given for other devolatilization reactions.

4.2.1 Mechanical equilibrium

Rice [2006][186] hypothesized that the short distances associated with hydrothermal diffusion make inertial effects within the gouge layer unimportant. This hypothesis was then tested

in *Platt et al.* [2014][166] and found to be true for typical seismogenic conditions. Based on this we use the equations for mechanical equilibrium to model the stresses within the gouge layer

$$\frac{\partial \tau}{\partial y} = 0 \quad , \quad \frac{\partial \sigma_n}{\partial y} = 0, \tag{4.2}$$

where τ is the shear stress in the gouge material, and σ_n is the normal stress on the gouge layer. As in *Rice et al.* [2014][189] and *Platt et al.* [2014][166] we assume that the normal stress on the gouge layer is constant throughout shear. The assumed quasi-static behavior forces the shear stress to be constant throughout the layer, and thus τ is at most a function of t.

4.2.2 Gouge friction

The shear stress is linked to the normal stress using a friction coefficient f and the Terzaghi effective stress through

$$\tau = f \times (\sigma_n - p)\,, \tag{4.3}$$

where $p = p(y,t)$ is the local pore pressure. For a constant friction coefficient, and neglecting dilatancy, uniform shear of the gouge layer or shear on the plane of maximum pore pressure are the only two forms of deformation that satisfy mechanical equilibrium[186]. Small perturbations away from uniform shearing will be unstable and the deformation will collapse to a plane. However, when the friction coefficient varies across the gouge layer a finite thickness shear zone can exist.

Current high-velocity friction experiments are unable to separate out the complicated temperature and pore fluid effects to provide a friction law as a function of strain rate alone at seismic strain rates. Lacking such a friction law we assume that the friction law is the

steady state friction law

$$f(\dot{\gamma}) = (a-b)\sinh^{-1}\left[\frac{\dot{\gamma}}{\dot{\gamma}_0}\exp\left(\frac{f_0}{a-b}\right)\right], \tag{4.4}$$

which for $(a-b) \ll f_0$ is asymptotically the same as the well-known logarithmic friction law for steady state shearing inferred from low strain rate velocity-stepping experiments such as those in *Dieterich* [1979][57]. Here $\dot{\gamma}$ is the strain rate, f_0 is the friction coefficient at a nominal strain rate $\dot{\gamma}_0$, and $(a-b)$ is the rate-dependent component of the friction law. We will only consider rate-strengthening materials where $(a-b) > 0$.

It is important to note that equations (4.2)-(4.4) link the pore pressure and strain rate profiles within the gouge layer. Locations with high pore pressures will have smaller effective stresses, corresponding to a higher strain rate for a rate-strengthening material.

As discussed in *Rice et al.* [2014][189], the friction law in equation (4.4) neglects important effects of temperature, mineralogy and state evolution, and is unlikely to accurately describe the frictional response of gouge at the seismic slip rates considered here. However, *Rice et al.* [2014][189] shows how effective values of f_0 and $(a-b)$ could be interpreted from other friction laws of the form $f(\dot{\gamma})$, and the results in this paper can easily be recalculated for different values of f_0 and $(a-b)$.

4.2.3 Conservation of pore fluid mass

Defining m to be the mass of pore fluid per unit reference volume of porous material we can write the conservation of pore fluid mass as

$$\frac{\partial m}{\partial t} + \frac{\partial q_f}{\partial y} = \frac{\partial m_d}{\partial t}, \tag{4.5}$$

where q_f is pore fluid flux, and m_d is the mass of pore fluid released by the thermal decomposition reaction per unit reference volume. For a saturated gouge $m = n\rho_f$ where ρ_f is the pore fluid density and n is the pore volume fraction. It follows that

$$\frac{\partial m}{\partial t} = n\frac{\partial \rho_f}{\partial t} + \rho_f \left(\frac{\partial n^{el}}{\partial t} + \frac{\partial n^{in}}{\partial t} \right), \tag{4.6}$$

where we have split the porosity change into an elastic component n^{el} and an inelastic component n^{in}. The new derivatives for ρ_f and the elastic porosity n^{el} can be linked to changes in pore pressure and temperature using

$$\frac{\partial \rho_f}{\partial t} = \rho_f \beta_f \frac{\partial p}{\partial t} - \rho_f \lambda_f \frac{\partial T}{\partial t}, \tag{4.7}$$

$$\frac{\partial n^{el}}{\partial t} = n\beta_n \frac{\partial p}{\partial t} + n\lambda_n \frac{\partial T}{\partial t}, \tag{4.8}$$

where $T = T(y,t)$ is the temperature, β_n and β_f are the pore volume and pore fluid compressibility's, and λ_n and λ_f are the thermal expansion coefficients for pore volume and pore fluid

Platt et al. [2014][166] showed that dilatant effects that depend on strain rate alone are expected to have a minimal effect on strain localization at seismic depths, although they may play an important role at the lower effective stresses used in high-velocity friction experiments. Motivated by this we neglect dilatancy and assume that all inelastic porosity change is due to the thermal decomposition of the gouge material.

Denoting the mass of a chemical species x per unit reference volume of fluid saturated

gouge by m_x, and the density of that chemical species by ρ_x, we can express the rate of inelastic porosity change for the decarbonation reaction in equation (4.1) using the rate of volume change for each of the solid phases as

$$\frac{\partial n^{in}}{\partial t} = -\frac{1}{\rho_{CaCO_3}}\frac{\partial m_{CaCO_3}}{\partial t} - \frac{1}{\rho_{CaO}}\frac{\partial m_{CaO}}{\partial t}. \tag{4.9}$$

Next, using the molar masses M_x for a chemical species x and equation (4.1), we can tie the volume changes to the mass of pore fluid released

$$\frac{\partial m_{CaCO_3}}{\partial t} = -\frac{M_{CaCO_3}}{M_{CO_2}}\frac{\partial m_d}{\partial t}, \tag{4.10}$$

$$\frac{\partial m_{CaO}}{\partial t} = \frac{M_{CaO}}{M_{CO_2}}\frac{\partial m_d}{\partial t}. \tag{4.11}$$

Combining equations (4.9)-(4.11) we find

$$\frac{\partial n^{in}}{\partial t} = \left(\frac{M_{CaCO_3}}{\rho_{CaCO_3}M_{CO_2}} - \frac{M_{CaO}}{\rho_{CO_2}M_{CO_2}}\right)\frac{\partial m_d}{\partial t}. \tag{4.12}$$

The final term to be dealt with in equation (4.5) is the pore fluid flux q_f. To model this we use Darcy's law, which says that

$$q_f = -\frac{\rho_f k}{\eta_f}\frac{\partial p}{\partial y}, \tag{4.13}$$

where k is the intrinsic permeability and η_f is the pore fluid viscosity.

Combining equations (4.5)-(4.8), (4.12) and (4.13) and neglecting the dependence of the

hydraulic properties on pore pressure, temperature and porosity we arrive at

$$\frac{\partial p}{\partial t} = \Lambda \frac{\partial T}{\partial t} + \alpha_{hy} \frac{\partial^2 p}{\partial y^2} + \frac{1}{\rho_f \beta} \left(1 - \rho_f \phi\right) \frac{\partial m_d}{\partial t}, \tag{4.14}$$

where

$$\beta = n(\beta_f + \beta_n) \quad , \quad \Lambda = \frac{\lambda_f - \lambda_n}{\beta_f + \beta_n}. \tag{4.15}$$

Here β is the storage coefficient and Λ is the ratio of pore pressure change to temperature change for undrained, adiabatic deformation[127]. The hydraulic diffusivity is given as

$$\alpha_{hy} = \frac{k}{\eta_f \beta}. \tag{4.16}$$

The final parameter defined is the inelastic porosity created per unit mass of fluid released

$$\phi = \frac{1}{\rho_{CaCO_3}} \frac{M_{CaCO_3}}{M_{CO_2}} - \frac{1}{\rho_{CaO}} \frac{M_{CaO}}{M_{CO_2}}. \tag{4.17}$$

The three terms on the right hand side of equation (4.14) each have a physical interpretation. The first represents thermal pressurization of the pore fluid, the second term models hydraulic diffusion, and the final term models the pore pressures generated by thermal decomposition.

Reactant depletion may become important at large slips. To model this we must consider the total pore fluid mass than can be released per unit volume, m_d^{tot}. Using this we define the reaction progress ξ as the mass of pore fluid released divided by the total mass of

pore fluid that could be released in a fully completed reaction

$$\xi = \frac{m_d}{m_d^{tot}}. \tag{4.18}$$

For this definition $\xi = 0$ represents virgin material, while $\xi = 1$ indicates full reactant depletion. Using this definition we can write the final term in equation (4.14) as

$$\frac{1}{\rho_f \beta} \left(1 - \rho_f \phi\right) m_d^{tot} \frac{\partial \xi}{\partial t}. \tag{4.19}$$

The total pore fluid mass m_d^{tot} that can be released during decomposition will depend on the specific reactant as well as the mass fraction of this reactant within the gouge. To separate these two effects we write

$$\frac{1}{\rho_f \beta} \left(1 - \rho_f \phi\right) m_d^{tot} \frac{\partial \xi}{\partial t} = \bar{m} P_r \frac{\partial \xi}{\partial t}, \tag{4.20}$$

where we have defined

$$P_r = \frac{1}{\rho_f \beta} \left(1 - \rho_f \phi\right) m_d^{100\%} \quad , \quad \bar{m} = \frac{m_d^{tot}}{m_d^{100\%}}. \tag{4.21}$$

Here $m_d^{100\%}$ is the pore fluid mass per reference volume released by a completed reaction in a pure material, and thus P_r is the pore pressure generated by a completed reaction of a pure reactant under undrained and adiabatic conditions.

The final equation modeling the conservation of pore fluid mass is

$$\frac{\partial p}{\partial t} = \Lambda \frac{\partial T}{\partial t} + \alpha_{hy} \frac{\partial^2 p}{\partial y^2} + \bar{m} P_r \frac{\partial \xi}{\partial t}. \tag{4.22}$$

4.2.4 Conservation of energy

Assuming that energy is generated by frictional heating in the gouge layer, and absorbed by the endothermic reaction we can write the conservation of energy as

$$\frac{\partial T}{\partial t} + \frac{\partial q_h}{\partial y} = \frac{\tau \dot{\gamma}}{\rho c} - \frac{\Delta H}{\rho c}\frac{\partial m_d}{\partial t}, \tag{4.23}$$

where ρc is the effective heat capacity per unit reference volume, and ΔH is the enthalpy change associated with the generation of a unit mass of pore fluid through thermal decomposition. We will study endothermic reactions so $\Delta H > 0$. To model the heat flux we use Fourier's law,

$$q_h = -K\frac{\partial T}{\partial y}, \tag{4.24}$$

where K is the thermal conductivity, which is assumed to be constant. Equations (4.23) and (4.24) neglect small additional terms due to the work of the normal stress and pore pressure, and heat transfer due to flow of the fluid. This is a common assumption justified in *Mase and Smith* [1985,1987][144,145] for representative permeabilities of fault gouges. Combining equations (4.23) and (4.24) we find

$$\frac{\partial T}{\partial t} = \frac{\tau \dot{\gamma}}{\rho c} + \alpha_{th}\frac{\partial^2 T}{\partial y^2} - \frac{\Delta H}{\rho c}\frac{\partial m_d}{\partial t}, \tag{4.25}$$

where the thermal diffusivity is given as,

$$\alpha_{th} = \frac{K}{\rho c}. \tag{4.26}$$

As in the previous subsection we will recast the pore fluid mass released per unit reference volume m_d in terms of the reaction progress ξ by normalizing the total mass of pore fluid released by the total amount that would be released in a completed reaction. Equation (4.25) becomes

$$\frac{\partial T}{\partial t} = \frac{\tau\dot{\gamma}}{\rho c} + \alpha_{th}\frac{\partial^2 T}{\partial y^2} - \bar{m}E_r\frac{\partial \xi}{\partial t}, \tag{4.27}$$

where

$$E_r = \frac{\Delta H}{\rho c} m_d^{100\%}. \tag{4.28}$$

The parameter E_r is the total temperature rise buffered by a completed reaction in a pure material.

4.2.5 Reaction kinetics

Finally we model the reaction kinetics, which control how fast thermal decomposition progresses. We assume a first order reaction with an Arrhenius thermal dependence

$$\frac{\partial m_d}{\partial t} = \left(m_d^{tot} - m_d\right) A \exp\left(-\frac{Q}{RT}\right), \tag{4.29}$$

where A is the rate constant for the reaction, Q is the activation energy for the reaction, and R is the gas constant. To recast this in terms of the reaction progress ξ we divide through by m_d^{tot} to find,

$$\frac{\partial \xi}{\partial t} = (1-\xi) A \exp\left(-\frac{Q}{RT}\right). \tag{4.30}$$

The Arrhenius factor means that the reaction kinetic has a very sensitive dependence on temperature, with higher temperatures leading to a more vigorous reaction. For a fixed

temperature a lower value of ξ will lead to a faster reaction since there is a larger amount of material left to decompose, and when ξ reaches one the reaction will cease.

The strong temperature dependence of the reaction kinetic allows us to predict when each of the dynamic weakening mechanisms will dominate. At low temperatures the reaction rate for thermal decomposition will be slow and we expect thermal pressurization to dominate. As the temperature rises the reaction rate will increase and eventually we will reach a temperature where thermal decomposition dominates. We do not expect to exceed this temperature because any increase in temperature will be absorbed by the enthalpy change of the endothermic reaction. This can be seen clearly in the numerical simulations of *Sulem and Famin* [2009][217], *Sulem et al.* [2009][218], and *Brantut et al.* [2010][30].

4.3 Parameter values

The model presented above is rich in parameters. In this section we will choose typical values for these parameters and discuss how well constrained each parameter is. Not all parameters can be varied independently. In Appendix B.1 we nondimensionalize the model from the previous section, showing that there are eight dimensionless parameters, each with a clear physical meaning.

The hydraulic parameters are highly variable, and depend on pore pressure, temperature and the amount of damage the surrounding material has sustained. We will use the path-averaged parameters modeling a damaged material from *Rempel and Rice* [2006][180], which are based on Tables 1-3 in *Rice* [2006][186] and the procedures in *Rice* [2006][186]. This parameter set models a depth of 7 km, which is a typical centroidal depth for rupture zones of crustal earthquakes. The hydraulic diffusivity is chosen to be $6.71\ \mathrm{mm}^2/\mathrm{s}$, the storage

Parameter	Value
α_{th}, mm^2/s	0.54
ρc, MPa/K	2.7
Λ, MPa/K	0.3
α_{hy}, mm^2/s	6.71
β, $\times 10^{-10}$ Pa^{-1}	2.97
$\sigma_n - p_a$, MPa	126
f_0	0.6
$(a-b)$	0.025

Table 4.1: Representative parameters modeling a gouge material at a depth of 7 km, a typical centroidal depth for a crustal seismogenic zone. Thermal and hydraulic parameters are taken from [180] Table 1, and based on [186] Tables 1-3 and the procedures in *Rice* [2006] [186] to account for damage to the gouge material at the onset of shearing and parameter changes due to changes in pore pressure and temperature. Frictional parameters are based on *Blanpied et al.* [1998] [24]. A fuller discussion on the origin of the parameters can be found in *Rice et al.* [2014] [189].

capacity to be $\beta = 2.97 \times 10^{-10}$ /Pa, and $\Lambda = 0.3$ MPa/K. These parameters use the ideas from *Rice* [2006] [186] to account for variations in the hydraulic properties of the gouge due to damage as well as pore pressure and temperature changes. A detailed discussion of the assumptions and laboratory measurements used to develop these parameters can be found in *Rice* [2006] [186] and *Rempel and Rice* [2006] [180].

Compared to the hydraulic parameters, the thermal parameters α_{th} and ρc are relatively well constrained. Following our choice of the path-averaged parameter set modeling a damaged material taken from *Rempel and Rice* [2006] [180], we choose the effective heat capacity per unit reference volume to be $\rho c = 2.7$ MPa/K, and the thermal diffusivity to be $\alpha_{th} = 0.54$ mm^2/s. Both of these fall in the typical range of values quoted in *Rice* [2006] [186].

The frictional parameters are as variable as the hydraulic parameters. The friction law assumed here – given in equation (4.4) – is motivated by steady state friction values from low

strain rate experiments[57], and the applicability to the rapid shear considered here is unclear. However, the analysis provided below is qualitatively similar for any rate-strengthening friction law. *Rice et al.* [2014][189] shows how effective values of f_0 and $(a-b)$ could be inferred from a general friction law $f = f(\dot{\gamma})$, and the generality of our results allows them to be reinterpreted for other values of $(a-b)$ and f_0. Understanding these limitations we choose $f_0 = 0.6$ and $(a-b) = 0.025$, both in the observed range for low strain rate experiments on granite under hydrothermal conditions[24], though a wide range of other choices for f_0 and $(a-b)$ could be justified.

The numerical calculations in this paper are performed for calcite decarbonation and lizardite dehydration reactions, and will be discussed in the context of other possible reactants in section 4.6. We will first discuss the parameters associated with the decarbonation of calcite

$$\mathrm{CaCO_3} \rightarrow \mathrm{CaO} + \mathrm{CO_2}. \tag{4.31}$$

The parameter choices closely follow those in *Sulem and Famin* [2009][217]. For calcite mixed with silica *Dollimore et al.* [1996][63] report values of $Q = 319$ kJ/mol, and $A = 2.95 \times 10^{15}$ s^{-1}. These kinetic parameters neglect any dependence of reaction rate on the partial pressure of carbon dioxide, but more accurate models could be constructed to account for this. The sign of this effect can be understood using Le Chatelier's principle and, for a fixed temperature and reactant mass, as the partial pressure of carbon dioxide increases the reaction rate will decrease. For the isobaric mode the enthalpy change of the reaction is equal to the activation energy *L'vov* [2002][138]. Thus, using the molar mass of carbon dioxide, $M_{CO_2} = 44$ g/mol, we find $\Delta H = 7.25$ MJ/kg. The value of ϕ can be calculated using the parameter values from *Sulem et al.* [2009][218], leading to $\phi = 0.46 \times 10^{-3}$ m^3/kg. The

final reaction parameter is $m_{tot}^{100\%}$, which can be calculated via

$$m_{tot}^{100\%} = \rho_{CaCO_3}(1-n)\frac{M_{CO_2}}{M_{CaCO_3}}. \tag{4.32}$$

Using the molecular weights and density from *Sulem et al.* [2009][218] and the path-averaged porosity $n = 0.043$ from *Rempel and Rice* [2006][180] we find $m_{tot}^{100\%} = 1140\,\mathrm{kg/m^3}$.

Choosing the fluid density is hard for decarbonation reactions in a water-saturated gouge since the in-situ pore fluid is different from the fluid released by the decomposition reaction. We assume that the appropriate density is that of supercritical carbon dioxide and calculate this using the equation of state in *Saxena and Fei* [1987][194]. To determine the conditions at which to evaluate this equation of state at we need to estimate the conditions at which thermal decomposition operates. We assume that a typical pore pressure at which thermal decomposition becomes important is $p = p_a + 0.5(\sigma_n - p_a)$ where p_a is the ambient pore pressure. This is intended to model a gouge that has already experienced dynamic weakening due to thermal pressurization before the reaction becomes important. To estimate the temperature T_r at which thermal decomposition operates we assume that all of the frictional heating is absorbed by the reaction and that reactant depletion is negligible. These assumptions are consistent with the results in *Sulem and Famin* [2009][217]. This leads to

$$T_r = \frac{Q}{R\log(\bar{m}\rho c E_r A/\tau\dot{\gamma})}. \tag{4.33}$$

To evaluate this we use $\bar{m} = 0.5$, the shear stress consistent with our assumed pore pressure $\tau = f_0(\sigma_n - p_a)/2$, and the strain rate compatible with a slip rate of 1 m/s accommodated across a deforming zone 100 microns wide. These choices lead to $T_r = 960\,^\circ\mathrm{C}$, and a fluid

density of 418 kg/m^3. Combining all of the above we find $E_r = 3.06 \times 10^3$ °C and $P_r = 7.42$ GPa for calcite decarbonation.

Next we discuss the dehydration of lizardite into talc, olivine and water

$$5Mg_3Si_2O_5(OH)_4 \rightarrow Mg_3Si_4O_{10}(OH)_2 + 6Mg_2SiO_4 + 9H_2O. \tag{4.34}$$

Llana-Fúnez et al. [2007][135] provide a range of kinetic parameters associated with the dehydration of intact blocks or powders of lizardite. Here we use a rate constant $A = 6.40 \times 10^{17}$ s^{-1} and an activation energy $Q = 328$ kJ/mol, which correspond to the dehydration kinetics of a mixture of lizardite and brucite (originally reported in *Wegner and Ernst* [1983][240]). The reaction enthalpy is calculated using the thermodynamic software Geotab from *Berman* [1991][14], which yields $\Delta H = 2.56$ MJ/kg. From the stoichiometry of the reaction and the densities of the reactants and products, we calculate the solid volume change $\phi = 0.88 \times 10^{-3}$ m^3/kg and the total mass of water released by the reaction $m_{tot}^{100\%} = 240$ kg/m^3. Finally, we use a procedure similar to that outlined above in order to determine the density of water of 267 kg/m^3 at the reaction temperature. This set of parameters allows to determine $E_r = 275$ °C and $P_r = 2.80$ GPa for lizardite dehydration.

Aside from the decarbonation of calcite and the dehydration of lizardite, which we choose as the two main examples in our simulations, a wide variety of other devolatilisation reactions can be triggered during earthquake slip. Potential candidates for devolatilisation reactions include carbonates such as dolomite, magnesite and siderite, as well as hydrous minerals such as gypsum and phyllosilicates (e.g., clays, serpentines, talc). As described above, our model requires a number of reaction parameters that are rarely available in a consistent set in the published literature. The full set of reaction parameters could be obtained

	Decarbonation reaction	Dehydration reactions		
Parameter	Calcite[a]	Lizardite[b]	Illite/muscovite[c]	Talc[d]
$\log_{10}(A)$ (A in 1/s)	15.47	17.80	6.92	14.30
Q (kJ/mol)	319	328	152	372
$m_{tot}^{100\%}$ (kg/m^3)	1140	240	150	131
ΔH (MJ/kg)	7.25	2.56	5.49	5.17
ϕ ($\times 10^{-3}$ m^3/kg)	0.46	0.88	0.35	0.78
ρ_f (m^3/kg)	418	267	135	159
T_r	960 °C	885 °C	1733 °C	1454 °C
E_r (°C)	3.06×10^3	275	305	251
P_r (GPa)	7.42	2.80	3.56	2.43
W^{HT}	5.1 μm	1.2 μm	1.1 μm	1.3 μm
W	12.7 μm	6.8 μm	11.9 μm	8.6 μm

a From [63], as reported by [218]. *b* Kinetics from [135], reaction enthalpy from Geotab [14]. *c* From [105]. *d* Kinetics from [26], reaction enthalpy from Geotab [14].

Table 4.2: List of reaction parameters along with predictions for T_r, W^{HT} and W for four different thermal decomposition reactions.

for the dehydration reactions of illite–muscovite mixtures and talc. The dehydration of illite–muscovite was studied experimentally by *Hirose and Tanikawa* [2011] [105], who provide all the relevant parameters needed for our model. In the case of talc dehydration, we used the kinetics reported by *Bose and Ganguly* [1994] [26], and determined the enthalpy change using Geotab [14]. The list of parameter values for all four minerals are reported in Table 4.2.

4.4 Linear stability analysis

We now attempt to predict the localized zone width using a linear stability analysis. To make progress analytically we linearize the reaction kinetic about $\xi = 0$ and a current fault temperature $T = T_f$. This leads to the linearized reaction kinetic

$$\frac{\partial \xi}{\partial t} \approx \beta_1[1 + \beta_2(T - T_f)], \tag{4.35}$$

where

$$\beta_1 = A \exp\left(-\frac{Q}{RT_f}\right) \quad , \quad \beta_2 = \frac{Q}{RT_f^2}. \tag{4.36}$$

Given that the Arrhenius factor has a strong dependence on temperature, such a linearization will have a very limited range of validity. However, performing the linear stability analysis with the linearized reaction kinetic above is equivalent to performing the linear stability analysis with the Arrhenius reaction kinetic and then freezing the coefficients in the resulting time-dependent linear system. This means that the linearized reaction kinetic is valid provided that perturbations in temperature are small, which is expected to be true at the onset localization. Thus, despite the problems with linearizing a highly nonlinear function, we find that the linearized analysis does convey some key qualitative features of more precise nonlinear solutions presented later in this paper.

Inserting the linearized reaction kinetic into equations (4.22) and (4.27) we arrive at

$$\frac{\partial T}{\partial t} = \frac{\tau\dot{\gamma}}{\rho c} + \alpha_{th}\frac{\partial^2 T}{\partial y^2} - \bar{m}E_r\beta_1\left[1 + \beta_2(T - T_f)\right], \tag{4.37}$$

$$\frac{\partial p}{\partial t} = \Lambda\frac{\partial T}{\partial t} + \alpha_{hy}\frac{\partial^2 p}{\partial y^2} + \bar{m}P_r\beta_1\left[1 + \beta_2(T - T_f)\right]. \tag{4.38}$$

As in *Rice et al.* [2014][189] we now perturb about the solution for uniform shearing,

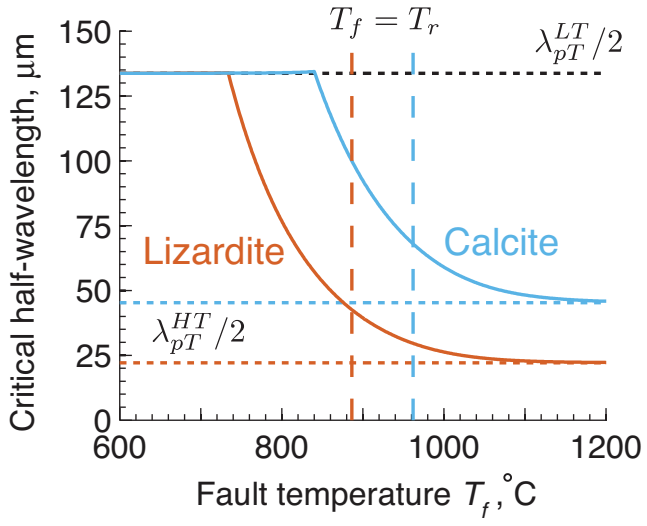

Figure 4.2: A plot showing how the critical half-wavelength $\lambda_{pT}/2$ from the linear stability analysis varies as a function of fault temperature T_f for calcite and lizardite. This plot was produced using the parameters in Tables 4.1 and 4.2, a mass fraction $\bar{m} = 0.5$, and the nominal strain rate $\dot{\gamma}_0 = 10,000\,\mathrm{s}^{-1}$. The horizontal dotted lines show λ_{pT}^{LT} and λ_{pT}^{HT} for both materials. The vertical lines show the location of the temperature T_r predicted by equation (4.33). As expected we see that at low temperatures the critical half-wavelength is equal to λ_{pT}^{LT} and for high temperatures the critical half-wavelength is equal to λ_{pT}^{HT}, with a smooth transition between the two regimes occurring for intermediate temperatures. Our prediction for the temperature at which thermal decomposition operates at lies in this intermediate temperature regime, so it is unlikely that the high temperature limit of the linear stability analysis will provide a good quantitative prediction for the localized zone thickness.

where the uniform shear solution is denoted by a subscript 0. This is done by setting

$$\tau(y,t) = f_0\bar{\sigma}_0(t) + \tau_1(y,t) \tag{4.39a}$$

$$\dot{\gamma}(y,t) = \dot{\gamma}_0 + \dot{\gamma}_1(y,t) \tag{4.39b}$$

$$p(y,t) = p_0(t) + p_1(y,t) \tag{4.39c}$$

$$T(y,t) = T_0(t) + T_1(y,t) \tag{4.39d}$$

where $\bar{\sigma}_0(t) = \sigma_n - p_0(t)$ is the effective stress for uniform shear. Somewhat surprisingly we do not actually have to solve for the uniform solution since it does not enter into the final form of the linearized system for perturbations in p and T.

Substituting (4.39) into the model and linearizing we find that

$$\frac{\partial \tau_1}{\partial y} = 0 \quad , \quad \tau_1 = (\sigma_n - p_0)\frac{(a-b)}{\dot{\gamma}_0}\dot{\gamma}_1 - f_0 p_1 \tag{4.40a}$$

$$\frac{\partial T_1}{\partial t} = \frac{f_0 \bar{\sigma}_0(t)\dot{\gamma}_1 + \dot{\gamma}_0 \tau_1}{\rho c} + \alpha_{th}\frac{\partial^2 T_1}{\partial y^2} - \bar{m} E_r \beta_1 \beta_2 T_1, \tag{4.40b}$$

$$\frac{\partial p_1}{\partial t} = \Lambda \frac{\partial T_1}{\partial t} + \alpha_{hy}\frac{\partial^2 p_1}{\partial y^2} + \bar{m} P_r \beta_1 \beta_2 T_1. \tag{4.40c}$$

Next we assume that the perturbation is proportional to a Fourier mode with a wavelength λ,

$$\{p_1, T_1, \dot{\gamma}_1\} = \Re\left[\{p_1, T_1, \dot{\gamma}_1\}(t) \exp\left(\frac{2\pi i y}{\lambda}\right)\right]. \tag{4.41}$$

This simplifies equations (4.40) to

$$\bar{\sigma}_0(t)\frac{(a-b)}{\dot{\gamma}_0}\dot{\gamma}_1 - f_0 p_1 = 0, \tag{4.42a}$$

$$\frac{\mathrm{d}T_1}{\mathrm{d}t} = \frac{f_0 \bar{\sigma}_0(t)}{\rho c}\dot{\gamma}_1 - \frac{4\pi^2 \alpha_{th}}{\lambda^2} T_1 - \bar{m} E_r \beta_1 \beta_2 T_1, \tag{4.42b}$$

$$\frac{\mathrm{d}p_1}{\mathrm{d}t} = \Lambda \frac{\mathrm{d}T_1}{\mathrm{d}t} - \frac{4\pi^2 \alpha_{hy}}{\lambda^2} p_1 + \bar{m} P_r \beta_1 \beta_2 T_1. \tag{4.42c}$$

We eliminate the only time dependent term in the system, $\bar{\sigma}_0(t)$, to arrive at a linear system

with constant coefficients,

$$\frac{\mathrm{d}T_1}{\mathrm{d}t} = \frac{f_0^2\dot{\gamma}_0}{(a-b)\rho c}p_1 - \frac{4\pi^2\alpha_{th}}{\lambda^2}T_1 - \bar{m}E_r\beta_1\beta_2T_1, \tag{4.43a}$$

$$\frac{\mathrm{d}p_1}{\mathrm{d}t} = \Lambda\frac{\mathrm{d}T_1}{\mathrm{d}t} - \frac{4\pi^2\alpha_{hy}}{\lambda^2}p_1 + \bar{m}P_r\beta_1\beta_2T_1. \tag{4.43b}$$

If we did not linearize the reaction kinetic, and instead tried to tackle the problem with the full Arrhenius reaction kinetic, then we would arrive at a linear system with time-dependent coefficients. This would make any further analytic progress almost impossible.

Equations (4.43) can be solved by assuming pore pressure and temperature perturbations of the form,

$$\begin{Bmatrix} T_1(t) \\ p_1(t) \end{Bmatrix} = \begin{Bmatrix} T_1(0) \\ p_1(0) \end{Bmatrix} \exp(st). \tag{4.44}$$

A non-trivial solution to the linear system exists only when

$$\left(s + \frac{4\pi^2\alpha_{th}}{\lambda^2} + \bar{m}E_r\beta_1\beta_2\right)\left(s + \frac{4\pi^2\alpha_{hy}}{\lambda^2}\right) = \frac{f_0^2\dot{\gamma}_0}{(a-b)\rho c}\left(\Lambda s + \bar{m}P_r\beta_1\beta_2\right). \tag{4.45}$$

Equation (4.45) allows us to solve for the growth rate s for a perturbation with a given wavelength λ, allowing us to determine the stability of the uniform shear. Whenever the real part of s is positive the perturbations will grow unstably, and whenever the real part of s is negative the perturbation will decay. The critical half-wavelength that separates growing and decaying perturbations in p and T, which we call λ_{pT} following the notation in *Rice et al.* [2014][189], occurs when the real part of s is zero. This critical wavelength will be used to predict a localized zone thickness.

We can identify two physically instructive limits from equation (4.45), one for low temperatures where thermal decomposition is negligible, and the other for high temperatures where the thermal decomposition dominates thermal pressurization.

To study the low temperature (LT) limit we set $\beta_1 = 0$, corresponding to a reaction rate so slow that thermal decomposition can be neglected. We recover the system of equations analyzed in *Rice et al.* [2014][189] and the critical wavelength for perturbations in p and T is given by

$$\lambda_{pT}^{LT} = 2\pi \sqrt{\frac{\alpha_{th} + \alpha_{hy}}{\Lambda} \frac{(a-b)\rho c}{f_0^2 \dot{\gamma}_0}}. \tag{4.46}$$

The critical wavelength is set by a balance between frictional rate-strengthening, thermal pressurization, and hydrothermal diffusion.

Next we study the high temperature (HT) limit where thermal decomposition dominates thermal pressurization. Numerical solutions of (4.45) show that when the real part of s is zero the imaginary component of s is also zero. This allows us to find a closed form solution for λ_{pT} by setting $s = 0$ and neglecting the thermal diffusion term, which is equivalent to assuming that at high temperatures the endothermic reaction eliminates temperature gradients much faster than thermal diffusion. Equation (4.45) then becomes

$$\bar{m} E_r \beta_1 \beta_2 \frac{4\pi^2 \alpha_{hy}}{\lambda^2} = \frac{f_0^2 \dot{\gamma}_0}{(a-b)\rho c} \bar{m} P_r \beta_1 \beta_2, \tag{4.47}$$

which can be solved to find

$$\lambda_{pT}^{HT} = 2\pi \sqrt{\frac{\alpha_{hy} E_r}{P_r} \frac{(a-b)\rho c}{f_0^2 \dot{\gamma}_0}}. \tag{4.48}$$

Interestingly the critical wavelength is independent of any reaction kinetic parameters (i.e. A and Q), and the reactant mass fraction. The reaction controls the localized zone width through the parameters E_r and P_r. We see that the endothermic absorption of heat acts to widen the localized zone, while the pore pressure generated by the reaction acts to thin the localized zone.

Next we test the above predictions by finding the critical wavelength λ_{pT} numerically for a wide range of values of T_a. Figure 4.2 shows how the critical wavelength varies for calcite and lizardite using the parameters in Tables 4.1 and 4.2, a mass fraction $\bar{m} = 0.5$, and a strain rate $\dot{\gamma}_0 = 10,000\ \text{s}^{-1}$, which is equivalent to a slip rate of 1 m/s accommodated across a zone 100 μm wide. For comparison we show the low and high temperature limits λ_{pT}^{LT} and λ_{pT}^{HT} for both materials using horizontal dotted lines. We see that the numerically calculated critical wavelength agrees with the appropriate limit for extreme values of T_f, and in the intermediate region we see a smooth transition between one critical wavelength and the other.

Finally, to determine where we expect typical temperatures during thermal decomposition to lie with respect to the high and low temperature limits we plot the reaction temperature T_r estimated in equation (4.33) for both materials using vertical dashed lines. We see that T_r lies in the intermediate temperature regime, and thus the simple formula in equation (4.48) may not give a good prediction for the localized zone thickness when thermal decomposition is active because the high temperature limit is never reached.

4.4.1 Predicting a localized zone thickness

It is important to note that the critical wavelengths λ_{pT}^{LT} and λ_{pT}^{HT} depend on the strain rate $\dot{\gamma}_0$. Following the procedure in *Rice et al.* [2014][189] we now eliminate $\dot{\gamma}_0$ from the two critical wavelengths to find a prediction of the localized zone thickness as a function of the gouge properties and the slip rate V by setting

$$W = \frac{\lambda_{pT}}{2} \quad , \quad \dot{\gamma}_0 = \frac{V}{W}. \tag{4.49}$$

For the high-temperature limit this leads to the formula

$$W^{HT} = \pi^2 \frac{\alpha_{hy} E_r}{P_r} \frac{(a-b)\rho c}{f_0^2 V}, \tag{4.50}$$

and in the low temperature limit we find

$$W^{LT} = \pi^2 \frac{\alpha_{th} + \alpha_{hy}}{\Lambda} \frac{(a-b)\rho c}{f_0^2 V}. \tag{4.51}$$

As shown in *Rice et al.* [2014][189], the linear stability analysis presented in this section can be specialized for a gouge layer of thickness h sheared between rigid, impermeable and thermally insulating blocks moving relative to each other with a slip rate V. In this case the width W is the widest possible gouge layer that can be sheared uniformly. These boundary conditions are different from the geometry used in the numerical simulations, but we will show that the linear stability analysis is still able to predict important features seen in the numerical simulations. It should also be noted that to predict the localized zone thickness we have used the critical half-wavelength separating growing and decaying perturbations

in pore pressure and temperature, not the critical half-wavelength that controls perturbations in strain rate. However, *Rice et al.* [2014][189] showed that for $(a-b) \ll f_0$ the two wavelengths are almost equivalent, so the use of λ_{pT} to predict the localized zone thickness is justified.

As shown in Figure 4.2, the reaction temperature T_r predicted in equation (4.33) does not fall in the high temperature regime. Motivated by this we now develop a more complicated prediction for the localized zone thickness W that is valid in the intermediate temperature range. The numerical solution of equation (4.45) that led to the results shown in Figure 4.2 show that throughout the intermediate regime the imaginary part of the growth rate s vanishes as the real part of s vanishes. This lets us find the critical wavelength by setting $s = 0$ in equation (4.45), leading to a quadratic equation for λ^2

$$\lambda^4 - \frac{4\pi^2 \alpha_{hy} E_r (a-b)\rho c}{P_r f_0^2 \dot{\gamma}_0}\lambda^2 - \frac{16\pi^4 \alpha_{th}\alpha_{hy}(a-b)\rho c}{f_0^2 \dot{\gamma}_0 \bar{m} P_r \beta_1 \beta_2} = 0. \tag{4.52}$$

As before we want to turn the critical half-wavelength into a prediction for the localized zone thickness W using the procedure outlined in *Rice et al.* [2014][189]. Inserting the definitions in equation (4.49) into equation (4.52) we arrive at

$$W^3 - \frac{\pi^2 \alpha_{hy} E_r (a-b)\rho c}{f_0^2 V P_r} W^2 - \frac{\pi^4 \alpha_{th}\alpha_{hy}(a-b)\rho c}{f_0^2 V \bar{m} P_r \beta_1 \beta_2} = 0. \tag{4.53}$$

As expected, in the high temperature limit (i.e. $\beta_1\beta_2 \to \infty$) the final term in equation (4.53) vanishes and we recover $W = W_{HT}$. In the intermediate temperature regime no such

neat solution exists, though the cubic can be solved using Cardano's formula. This leads to

$$W = p + \left[q + \left(q^2 - p^6\right)^{1/2}\right]^{1/3} + \left[q - \left(q^2 - p^6\right)^{1/2}\right]^{1/3}, \tag{4.54}$$

where

$$p = \frac{W_{HT}}{3} \quad , \quad q = \frac{{W_{HT}}^3}{27} + \frac{\pi^4 \alpha_{th} \alpha_{hy} (a-b) \rho c}{2 f_0^2 V \bar{m} P_r \beta_1 \beta_2}. \tag{4.55}$$

This formula is more cumbersome than that given in equation (4.50) but in the next section we will show that it provides predictions that agree more closely with the results of numerical simulations.

4.5 Shear of a finite width layer

In this section we solve numerically for a gouge layer with a finite width h sheared between two undeforming thermo-poroelastic half-spaces that conduct heat and pore fluid moving relative to each other with a slip rate V, the same geometry assumed in *Platt et al.* [2014][166]. A sketch of this geometry is shown in Figure 4.1. At each time step the pore pressure and temperature are updated using equations (4.22), (4.27) and (4.30). To update the shear stress we require one additional condition. As in *Platt et al.* [2014][166] we use

$$\int_{-h/2}^{h/2} \dot{\gamma}(y,t) \mathrm{d}y = V, \tag{4.56}$$

which ensures that the total straining within the gouge layer must equal the total slip rate V accommodated across the gouge layer.

The initial conditions are set to the ambient conditions $p = p_a$ and $T = T_a$, and a

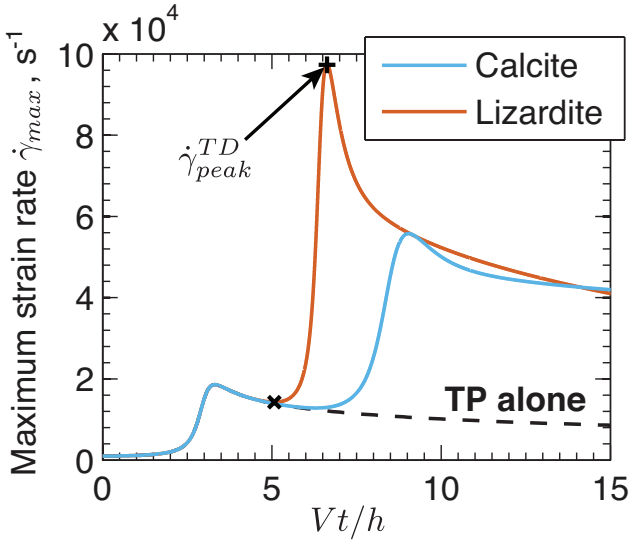

Figure 4.3: A plot showing the evolution of the maximum strain rate $\dot{\gamma}_{max}$ for calcite and lizardite. These simulations were performed using the parameters in Tables 4.1 and 4.2, a mass fraction $\bar{m} = 0.5$, a slip rate $V = 1$ m/s, and a gouge layer thickness $h = 1$ mm. For comparison the solution from *Platt et al.* [2014][166] that considers dynamic weakening from thermal pressurization alone (i.e. $E_r = P_r = 0$) is shown by the dashed black line. Initially our simulations agree with the simulations from *Platt et al.* [2014][166], indicating that thermal decomposition can be neglected during the initial stages of deformation. Eventually thermal decomposition becomes important and $\dot{\gamma}_{max}$ increases to a new peak value $\dot{\gamma}^{TD}_{peak}$. Following the peak $\dot{\gamma}_{max}$ decays, but the values are always above those for thermal pressurization alone. The minimum and maximum strain rates used to calculate $\Delta t_{\dot{\gamma}}$ are shown by the black plus and black cross.

uniform strain rate $\dot{\gamma} = \dot{\gamma}_0$ throughout the gouge layer. To be consistent with the parameters in *Rempel and Rice* [2006][180], which are intended to model a depth of 7 km, we choose $p_a = 70$ MPa and $T_a = 210\,^{\circ}$C. This is equivalent to an assumed geotherm of $30\,^{\circ}$C/km and an effective stress gradient of 18 MPa/km.

During the initial stages of deformation the reaction rate will be very slow, making thermal decomposition negligible. For certain gouge properties the maximum temperature within the gouge layer may eventually become large enough to trigger thermal decomposi-

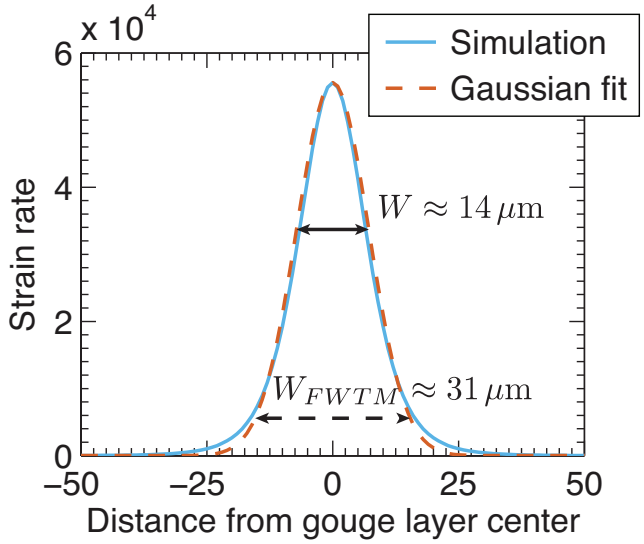

Figure 4.4: A plot showing the strain rate profile at peak localization alongside the Gaussian fit used to infer a localized zone thickness. This simulation was performed using the parameters in Table 4.1 and the calcite parameters in Table 4.2, a mass fraction $\bar{m} = 0.5$, a slip rate $V = 1$ m/s, and a gouge layer thickness $h = 1$ mm. Straining localizes to a zone a few tens of microns wide, and we see great agreement between the numerical simulation and the Gaussian fit. The horizontal lines show the two ways to infer a width from the Gaussian function. The solid black line shows where the width is calculated when we use the standard assumption that the width is equal to twice the residual means square of the Gaussian, and the dashed black line shows where the width is measured when we assume the localized zone thickness is equal to the full width at tenth maximum.

tion. Throughout this section we will focus on this transition from thermal pressurization to thermal decomposition, and the behavior of the system after thermal decomposition is triggered. The behavior before thermal decomposition is triggered, where dynamic weakening occurs due to thermal pressurization alone, is analyzed in *Platt et al.* [2014][166].

A simple test to determine if thermal decomposition will be triggered is to compare the

maximum temperature rise for a gouge layer undergoing thermal pressurization alone

$$T_{max}^{TP} = T_a + \frac{\sigma_n - p_a}{\Lambda}\left(1 + \sqrt{\frac{\alpha_{hy}}{\alpha_{th}}}\right) \tag{4.57}$$

with the temperature predicted by equation (4.33). If the two temperatures are comparable or the prediction from equation (4.57) is larger than the value from equation (4.33), then it is likely that thermal decomposition will be triggered. All simulations reported here were designed to trigger thermal decomposition.

We will begin by discussing how thermal decomposition controls the localized zone thickness during seismic shear, before moving on to investigate how thermal decomposition caps the peak temperature attained during seismic shear, and the stress drop that coincides with the onset of thermal decomposition.

4.5.1 Localized zone thickness

In this subsection we will study how the localized zone thickness evolves when thermal decomposition is triggered. Following *Platt et al.* [2014][166] we define the maximum strain rate within the gouge layer to be

$$\dot{\gamma}_{max}(t) = \max_y \left[\dot{\gamma}(y,t)\right]. \tag{4.58}$$

Because the total straining in the layer is fixed by the slip rate V, the maximum strain rate can be used as a proxy for the localized zone thickness, with a larger value of $\dot{\gamma}_{max}$ indicating a thinner localized zone.

Figure 4.3 shows $\dot{\gamma}_{max}$ as a function of time for calcite and lizardite. This plot was gen-

erated using the parameters in Tables 4.1 and 4.2, a gouge layer thickness $h = 1$ mm, a slip rate $V = 1$ m/s, and a reactant mass fraction $\bar{m} = 0.5$. For comparison the solution from *Platt et al.* [2014][166] that neglects thermal decomposition and models thermal pressurization alone (i.e. $E_r = P_r = 0$) is shown by the black dashed curve. As expected our results initially match the calculation that neglects thermal decomposition, corresponding to the initial stages of deformation when the reaction progresses so slowly it can be neglected. When thermal decomposition is triggered we see that $\dot{\gamma}_{max}$ rises to a new peak before decaying. We find that throughout the simulation $\dot{\gamma}$ the shape of the strain rate profile is well described by a Gaussian function, in agreement with the results of *Platt et al.* [2014][166] for thermal pressurization alone.

We use the Gaussian shape of $\dot{\gamma}$ and the peak strain rate after thermal decomposition is triggered $\dot{\gamma}^{TD}_{peak}$ to estimate the localized zone thickness W in the numerical simulations. Integrating condition (4.56) assuming the Gaussian shaped strain rate profile

$$\dot{\gamma}_{gau.} = \dot{\gamma}_{peak} \exp\left(-\frac{2y^2}{W^2}\right) \tag{4.59}$$

we find that the localized zone thickness is given by,

$$W = \sqrt{\frac{2}{\pi}} \frac{V}{\dot{\gamma}_{peak}}. \tag{4.60}$$

Following previous models for thermal pressurization (for example *Andrews* [2002][4], *Rice* [2006][186], and *Noda et al.* [2009][155]) we assume that the width of the deforming zone is equal to twice the root mean square width of the Gaussian. In addition we assume that the localized zone thickness is much less than the gouge layer width h. If the localized zone

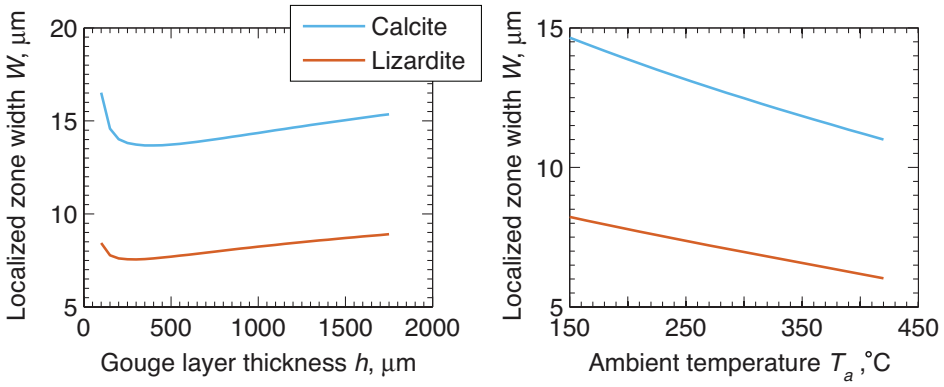

Figure 4.5: A plot showing how the localized zone thickness W depends on the gouge layer thickness h and ambient fault temperature T_a for calcite and lizardite. These simulations were performed using the parameters in Tables 4.1 and 4.2, a mass fraction $\bar{m} = 0.5$, a slip rate $V = 1$ m/s. In addition the simulations varying T_a use a gouge layer thickness $h = 0.5$ mm. We see that the localized zone thickness is almost independent of the gouge layer thickness. From this we can conclude that the localized zone thickness is controlled by the gouge properties and not the initial thickness of the deforming zone, in agreement with the conclusions from *Platt et al.* [2014][166] for strain localization driven by thermal pressurization alone. We also see that W is almost independent of T_a, which is to be expected since the temperature at which thermal decomposition is triggered does not depend on the ambient fault temperature.

thickness is comparable to the gouge layer thickness then equation (4.60) is not valid, though a more complicated formula can be found that depends on h, V and $\dot{\gamma}_{peak}$.

Figure 4.4 shows a plot of the strain rate profile at peak localization from the numerical simulations alongside the Gaussian function from equation (4.59). The solid black line indicates where the localized zone thickness is measured when we assume that W is equal to twice the root mean square width of the Gaussian. We see that the root mean square width may not be the best measure of the half-width, and a better option may be the full width at tenth of maximum, which is shown by the dashed black line. Following the usual convention the results in this paper are presented in terms of the root mean square

thickness, but it is easy to convert our results to the full width at tenth of maximum using $W_{FWTM} = \sqrt{2\log(10)}\, W$.

Next we investigate how the localized zone thickness depends on the gouge layer thickness and ambient fault temperature. Figure 4.5 shows W as a function of the gouge layer thickness h for the parameters in Tables 4.1 and 4.2, a mass fraction $\bar{m} = 0.5$, and a slip rate $V = 1$ m/s. We see that the localized zone thickness does not change much as h changes from 100 μm to 1750 μm. This replicates the behavior observed in *Platt et al.* [2014][166] for pressurization alone. The weak dependence of W on the gouge layer thickness suggests that the localized zone thickness is controlled by the gouge properties and not the initial width of the deforming zone. Figure 4.5 also shows W as a function of the ambient temperature T_a for the parameters in Tables 4.1 and 4.2, a mass fraction $\bar{m} = 0.5$, a slip rate $V = 1$ m/s, and a gouge layer thickness $h = 0.5$ mm. We see that the localized zone thickness does not vary dramatically as the ambient temperature varies from 150 °C to 420 °C, which makes sense since this range of ambient temperatures is much lower than the temperature at which thermal decomposition is triggered.

Having shown that the localized zone thickness depends weakly on the initial temperature and width of the deforming zone, we now study how W varies with the material properties of the gouge. This parameter sweep, shown by the solid curves in Figure 4.6, covers all the dimensionless parameters in the model except for T_I (see Appendix B.1). In each plot one parameter is varied while the remaining parameters are fixed to the values in Tables 4.1 and 4.2, a mass fraction $\bar{m} = 0.5$, a slip rate $V = 1$ m/s, and a gouge layer thickness $h = 0.5$ mm.

Figure 4.6: A plot showing a set of parameter sweeps tracking the localized zone thickness W as a function of eight parameters. For each sweep all other parameters are set to the values in Tables 4.1 and 4.2, a mass fraction $\bar{m} = 0.5$, a slip rate $V = 1$ m/s, and a gouge layer thickness $h = 0.5$ mm. For comparison we also show the linear stability prediction from equation (4.50) with the dotted curves, the prediction from equation (4.61) evaluated using the peak temperature from the numerical simulations with the dashed curves, and the prediction from equation (4.61) evaluated using the temperature from equation (4.33) assuming $\tau\dot{\gamma} = 252$ MPa/ms with the dash-dot curves. The predictions from equation (4.61) give the best agreement with the numerical simulations, especially when the peak temperature from the numerical simulations is used to evaluate (4.61).

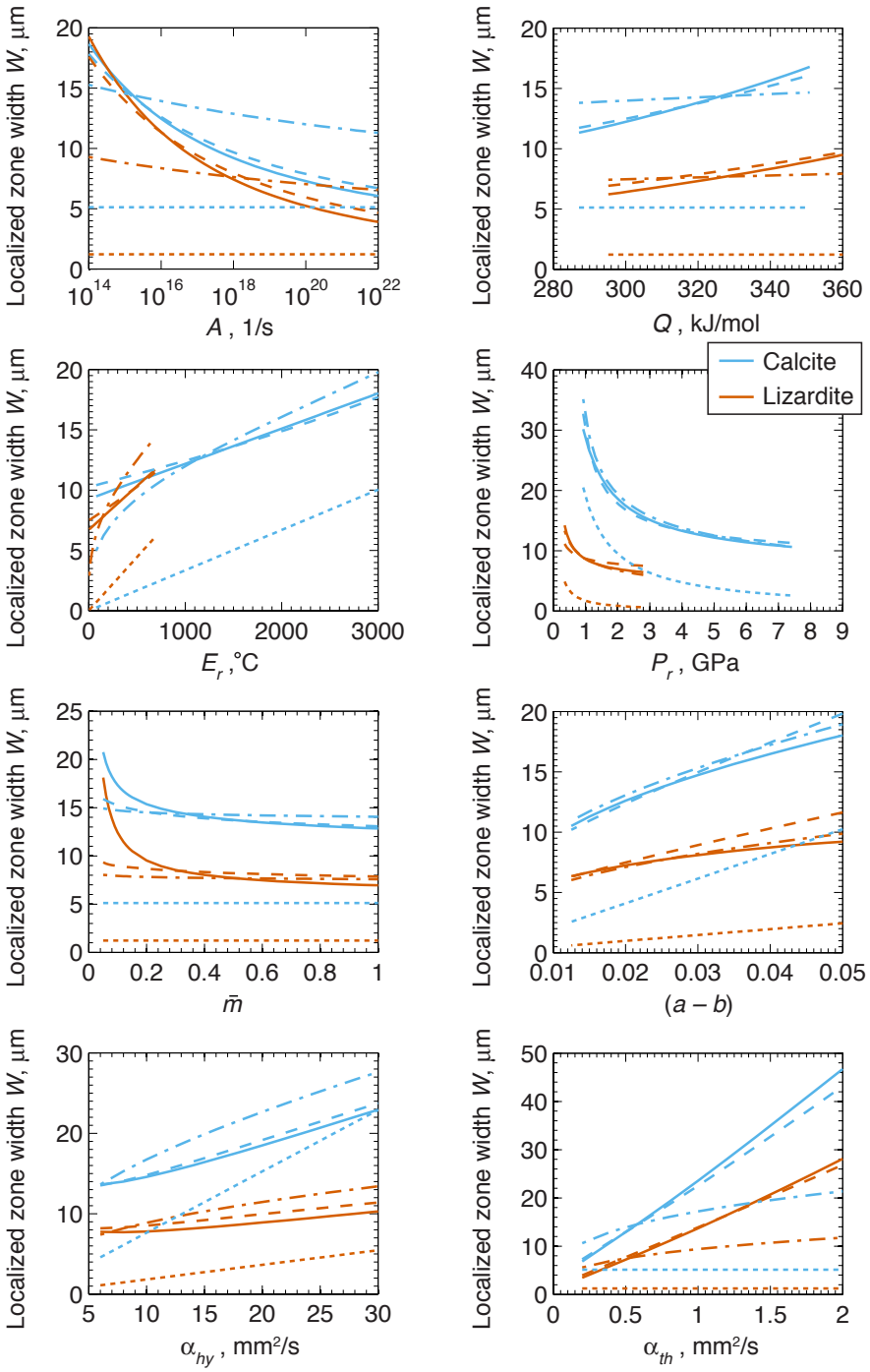

Figure 4.6: (continued)

We compare the localized zone thicknesses observed in numerical simulations with the linear stability predictions from Section 4.4. First we use the high temperature limit from the linear stability analysis, given in equation (4.50) and shown by the finely dashed curves in Figure 4.6. We see that the predictions from the high-temperature limit of the linear stability analysis are in qualitative agreement with the localized zone thickness predicted by the numerical simulations, with curves indicating the analytic prediction and numerical simulations have roughly similar shapes. However, the quantitative agreement between the two is often quite poor, with equation (4.50) consistently predicting localized zone thicknesses that are a factor of $\sim 2-3$ smaller than those observed in the numerical simulations. This can be understood by looking at Figure 4.2, which shows that the endothermic reaction caps the maximum temperature at a value that is less than the lower bound of the high-temperature regime.

Next we fit our simulations using the formula

$$W = \frac{C}{\pi^2}\left(p + \left[q + \left(q^2 - p^6\right)^{1/2}\right]^{1/3} + \left[q - \left(q^2 - p^6\right)^{1/2}\right]^{1/3}\right), \tag{4.61}$$

where

$$p = \frac{\pi^2 \alpha_{hy} E_r (a-b)\rho c}{3 f_0^2 V \left(P_r - \Lambda E_r\right)} \quad , \quad q = p^3 + \frac{\pi^4 \alpha_{th}\alpha_{hy}(a-b)\rho c}{2 f_0^2 V \bar{m}\left(P_r - \Lambda E_r\right)\beta_1\beta_2} \tag{4.62}$$

and

$$\beta_1 = A \exp\left(-\frac{Q}{RT_f}\right) \quad , \quad \beta_2 = \frac{Q}{RT_f^2}. \tag{4.63}$$

This is based on linear stability prediction valid for the intermediate temperature regime

given in equation (4.54), with the pore pressure generated $\bar{m}P_r$ replaced by $\bar{m}(P_r - \Lambda E_r)$. This change is needed because thermal pressurization is not accounted for when using the linear stability analysis to predict the localized zone thickness when thermal decomposition is active. Here we have assumed that thermal decomposition leads to pore pressure increases, and thus $P_r > \Lambda E_r$.

To evaluate the formula in equation (4.61) we must assume a current fault temperature T_f. In Figure 4.6 this is done in two ways. First we use the peak temperature from the numerical simulations, shown by the coarsely dashed curves. In addition we use the prediction T_r from equation (4.33), shown by the lines with alternating short and long dashes, assuming $\tau\dot{\gamma} = 252$ MPa/ms, which is equivalent to an effective stress equal to half of the ambient effective stress and a slip rate of 1 m/s accommodated across a deforming zone 150 μm wide

We see that the more general formula given in equation (4.61) gives a much better quantitative fit to the numerical simulations than the simpler high-temperature asymptote. Using a single fitting parameter $C = 5.5$ we get good agreement with a parameter sweep over seven dimensionless parameters for both calcite and lizardite. The best fit is obtained when we set T_f to be the peak temperature from the simulations, though using the temperature predicted by equation (4.33) still gives reasonable agreement.

As shown in Figure 4.3, $\dot{\gamma}_{peak}^{TD}$ is not achieved instantly when thermal decomposition is triggered. Instead $\dot{\gamma}_{max}$ increases smoothly from the value predicted by thermal pressurization alone at the moment the reaction becomes important to the new peak value over a finite time. To quantify the time taken for localization to occur after decomposition is triggered we define $\Delta t_{\dot{\gamma}}$ to be the time between the local minimum in $\dot{\gamma}_{max}$ and the second

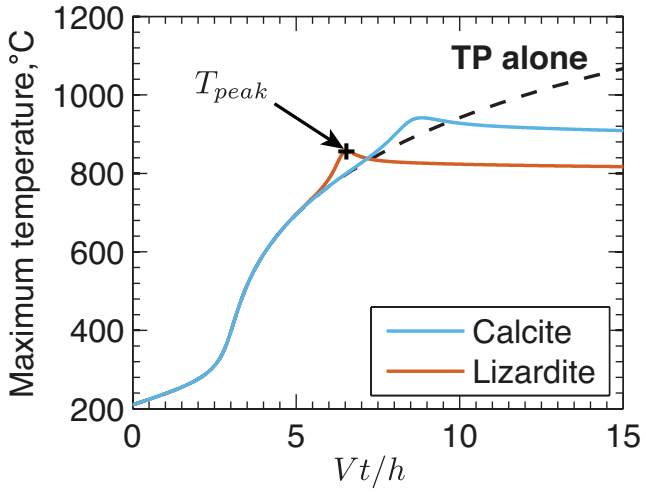

Figure 4.7: A plot showing the evolution of the maximum temperature T_{max} for calcite and lizardite. These simulations were performed using the parameters in Tables 4.1 and 4.2, a mass fraction $\bar{m} = 0.5$, a slip rate $V = 1$ m/s, and a gouge layer thickness $h = 1$ mm. For comparison the solution from *Platt et al.* [2014][166] that considers dynamic weakening from thermal pressurization alone (i.e. $E_r = P_r = 0$) is shown by the dashed black line. Initially our simulations agree with the simulations from *Platt et al.* [2014][166], indicating that thermal decomposition can be neglected during the initial stages of deformation. Eventually thermal decomposition becomes important and T_{max} rises to a new peak before settling onto a very slowly decaying plateau. As in *Sulem and Famin* [2009][217] and *Brantut et al.* [2010][30] thermal decomposition leads to a capping of the maximum temperature rise below a typical melting temperature.

maximum. Studying how $\Delta t_{\dot{\gamma}}$ varies in the parameter sweep that led to Figure 4.6 we find that for any given parameter sweep $\Delta t_{\dot{\gamma}}$ increases as the localized zone thickness decreases. This means that more intense localization develops faster than less intense localization.

Finally we study the decay from the peak strain rate shown in Figure 4.3. The simulations leading to Figure 4.6 show that larger values of $\dot{\gamma}_{peak}^{TD}$, and thus smaller values of W, correspond to more rapid decay after the peak strain rate, where we have used the peak value of $-\ddot{\gamma}$ to measure the speed of decay. This can be seen in Figure 4.3 by noting that $\dot{\gamma}_{max}$ decays more rapidly for lizardite than calcite. Decay from the peak strain rate indicates

that the localized zone thickens with increasing shear. Thickening of the localized zone makes it hard to describe the localized zone using a single width, and also means that materials that have very different localized zone thicknesses immediately after decomposition is triggered could have very similar thicknesses for the later stages of shear. This can be seen near the end of the simulations in Figure 4.3 where calcite and lizardite have similar values of $\dot{\gamma}_{max}$. We observe that the strain rate after decay is almost independent of some parameters, with this being particularly common for lizardite.

4.5.2 Limiting of peak temperature

Next we look at the temperature evolution in the gouge layer. To do this we define the maximum temperature to be

$$T_{max}(t) = \max_{y} \left[T(y,t) \right] . \tag{4.64}$$

Figure 4.7 shows the evolution of T_{max} for the same simulations shown in Figure 4.3. For comparison we also include the solution from *Platt et al.* [2014][166] that neglects thermal decomposition, shown by the dashed black line in Figure 4.7.

We see that the onset of thermal decomposition initially causes the maximum temperature rise to increase faster than for thermal pressurization alone, a surprising result for an endothermic reaction. This is due to the additional strain rate localization that accompanies the onset of decomposition. Frictional heating is being focused into a narrower zone and thermal diffusion and the endothermic reaction do not act fast enough to offset the additional frictional heating. However, the reaction kinetic and thermal diffusion quickly catch up, leading to a peak in T_{max} followed by a gradual decay. This limiting of the temperature

is qualitatively similar to the results from *Sulem and Famin* [2009][217] and *Brantut et al.* [2010][30] for a uniformly sheared layer with a thickness between 1 mm and 10 mm, though our peak temperature is higher because straining is more localized in our model.

To study the maximum temperature rise when thermal decomposition is triggered we define the peak temperature as

$$T_{peak} = \max_{t,y} \left[T(y,t) \right]. \tag{4.65}$$

Using the parameter sweeps that led to Figure 4.6 we now study how T_{peak} varies with the parameters in the model. Figure 4.8 shows how T_{peak} varies with eight parameters in the numerical simulations plotted alongside the predictions from equation (4.33) evaluated with $\tau\dot{\gamma} = 252$ MPa/ms. We see good agreement between the numerical simulations and equation (4.33). The maximum difference between the two temperatures is typically around $50\,^{\circ}$C, though larger discrepancies are seen for the smallest values of E_r and A.

To understand the differences between the numerical results and equation (4.33) we study the magnitude of the three terms on the right hand side of equation (4.27)

$$\frac{\tau\dot{\gamma}}{\rho c} \quad , \quad \alpha_{th}\frac{\partial^2 T}{\partial y^2} \quad , \quad -\bar{m}E_r\frac{\partial \xi}{\partial t}. \tag{4.66}$$

The first term models frictional heating, the second term models thermal diffusion, and the final term models the endothermic reaction. At the peak temperature the time derivative of T is zero so these three terms must sum to zero. Physically this means that at the peak temperature the frictional heating is exactly balanced by thermal diffusion and the endothermic reaction.

Figure 4.8: A plot showing a set of parameter sweeps tracking the peak temperature T_{peak} as a function of eight parameters. For each sweep all other parameters are set to the values in Tables 4.1 and 4.2, a mass fraction $\bar{m} = 0.5$, a slip rate $V = 1$ m/s, and a gouge layer thickness $h = 0.5$ mm. For comparison we include the temperature predictions from equation (4.33) assuming $\dot{\gamma} = 252$ MPa/ms. We see good agreement between our numerical simulations and the simple formula to estimate the temperature at which thermal decomposition operates, with typical discrepancies of $\sim 50\,^{\circ}$C.

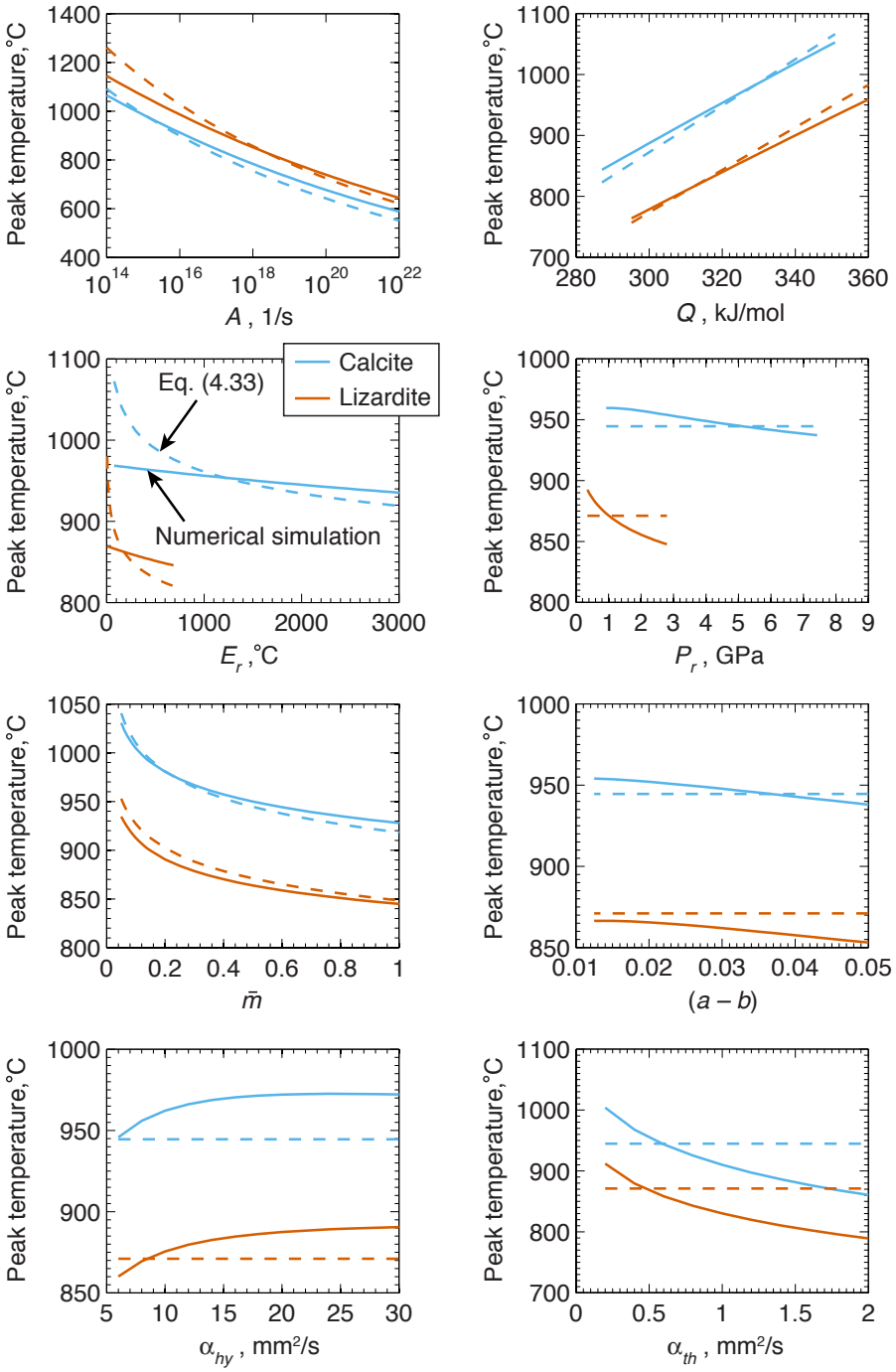

Figure 4.8: (continued)

Figure 4.9 shows how these three terms vary with E_r and α_{th} for the calcite simulations shown in Figure 4.8. We see that for all the simulations shown here thermal diffusion is more important than the endothermic reaction. As expected, for all parameters we see that the magnitude of the frictional heating and thermal diffusion terms increase as the localized zone thickness decreases. The dependence of the reaction term on W is not as clean, but in general a smaller value of W leads to a slightly larger magnitude for the reaction term. In almost all cases shown here thermal diffusion is a factor of $2 - 3$ larger than the reaction, and thus thermal diffusion is more important than thermal decomposition in limiting the maximum temperature.

Following the peak temperature we see a gradual decrease in the maximum temperature, coinciding with the thickening of the localized zone described in the previous subsection. During this gradual cooling the magnitude of all three terms in equation (4.27) fall. This is to be expected since frictional heating and thermal diffusion are largely controlled by the width of the deforming zone, and the reaction rate is controlled by the maximum temperature. The ratio of the reaction term to thermal diffusion and the ratio of the reaction term to frictional heating both decay along the plateau, so as expected thermal decomposition becomes less important as the maximum temperature decays. For some special cases we see an increasing temperature along the plateau, and this is particularly common for lizardite.

4.5.3 Strength drop due to thermal decomposition

In this subsection we study how the onset of thermal decomposition alters the shear strength evolution of the gouge layer. Figure 4.10 shows the shear strength evolution for calcite and lizardite for the same parameters as those used in Figures 4.3 and 4.7. We see that the onset

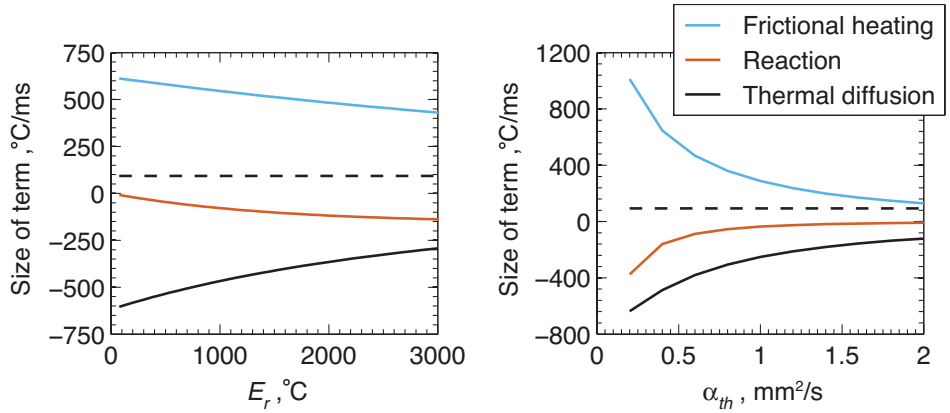

Figure 4.9: A plot showing how the magnitude of frictional heating, thermal diffusion and the endothermic reaction at peak temperature vary with E_r and α_{th} for calcite. These plots were generated using the parameters in Tables 4.1 and 4.2, a mass fraction $\bar{m} = 0.5$, a slip rate $V = 1$ m/s, and a gouge layer thickness $h = 0.5$ mm. In both parameter sweeps the magnitude of the frictional heating and thermal diffusion terms increases as the localized zone thins. For all simulations thermal diffusion plays a larger role than the reaction in limiting the maximum temperature. The units in this plot also reinforce the extreme heating rates associated with micron-scale strain rate localization.

of thermal decomposition leads to a rapid acceleration in dynamic weakening, followed by a return to more gradual weakening.

Platt et al. [2014][166] showed that for thermal pressurization alone the strength evolution after localization is in good agreement with the Mase-Smith-Rice slip on a plane solution[144,145,186]. The shear strength evolution after thermal decomposition is triggered obviously does not agree with the slip on a plane solution, but the rate of dynamic weakening is found to be in reasonable agreement with the slip on a plane solution. Figure 4.11 shows the weakening rate $-\mathrm{d}\tau/\mathrm{d}t$ for calcite and lizardite alongside the weakening rate for the slip on a plane solution. We clearly see a large increase in the weakening rate at the onset of thermal decomposition, but at later times the weakening rate is comparable to that predicted by the slip on a plane solution. This observation that the weakening rate returns to a value compa-

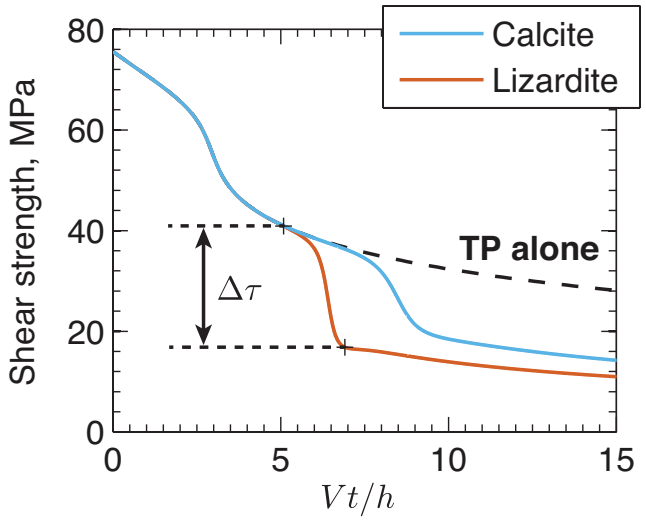

Figure 4.10: A plot showing the shear strength evolution for calcite and lizardite. These simulations were performed using the parameters in Tables 4.1 and 4.2, a mass fraction $\bar{m} = 0.5$, a slip rate $V = 1$ m/s, and a gouge layer thickness $h = 1$ mm. For comparison the solution from *Platt et al.* [2014][166] that considers dynamic weakening from thermal pressurization alone (i.e. $E_r = P_r = 0$) is shown by the dashed black line. Initially our simulations agree with the simulations from *Platt et al.* [2014][166], indicating that thermal decomposition can be neglected during the initial stages of deformation. Eventually thermal decomposition becomes important and the rate of dynamic weakening increases dramatically, before returning to a much slower weakening rate. This plot suggests that thermal decomposition can be roughly modeled as a discrete strength drop coinciding with the temperature reaching T_r. The location of the stresses used to calculate the strength drop associated with thermal decomposition are indicated by the black plus symbols.

rable to the value for the slip on a plane solution, which would be the long term weakening rate for a system that neglected thermal decomposition, means that the dynamic weakening due to thermal decomposition can be roughly described as a discrete strength drop coinciding with the onset of decomposition.

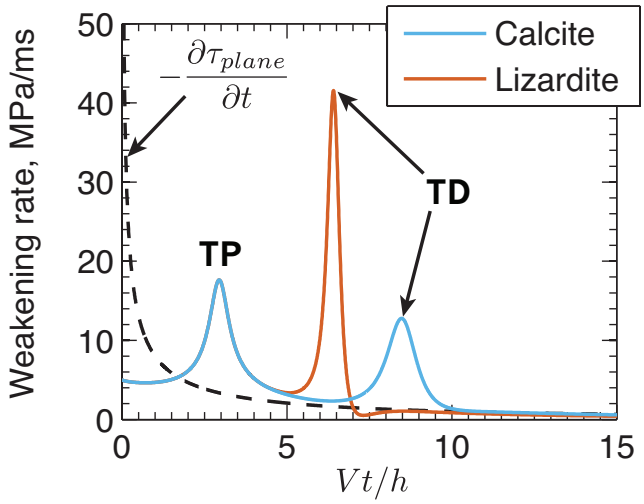

Figure 4.11: A plot showing the weakening rate $-\dot{\tau}$ for calcite and lizardite. These simulations were performed using the parameters in Tables 4.1 and 4.2, a mass fraction $\bar{m} = 0.5$, a slip rate $V = 1$ m/s, and a gouge layer thickness $h = 1$ mm. For comparison the weakening rate for the Mase-Smith-Rice slip on a solution is shown by the dashed black line. During the initial stages of deformation the two solutions agree, and we see a first spike in weakening rate associated with the onset of localization driven by thermal pressurization. Eventually thermal decomposition is triggered and we see a second spike in weakening rate, before the two numerical solutions return to a weakening rate comparable to the slip on a plane solution at large slips. The second spike is much larger for lizardite, corresponding to the larger strength drop. This plot shows how weakening due to thermal decomposition can be related to previous solutions for pore fluid weakening, and emphasizes the extreme weakening rates associated with the onset of thermal decomposition.

Figure 4.12: A plot showing a set of parameter sweeps tracking the strength drop associated with thermal decomposition $\Delta\tau$ as a function of eight parameters. All other parameters are set to the values in Tables 4.1 and 4.2, a mass fraction $\bar{m} = 0.5$, a slip rate $V = 1$ m/s, and a gouge layer thickness $h = 0.5$ mm. We see that a typical strength drop at the onset of thermal decomposition is $0.2 - 0.5\tau_0$. Comparing with Figure 4.6 we see that larger stress drops are associated with smaller values of W.

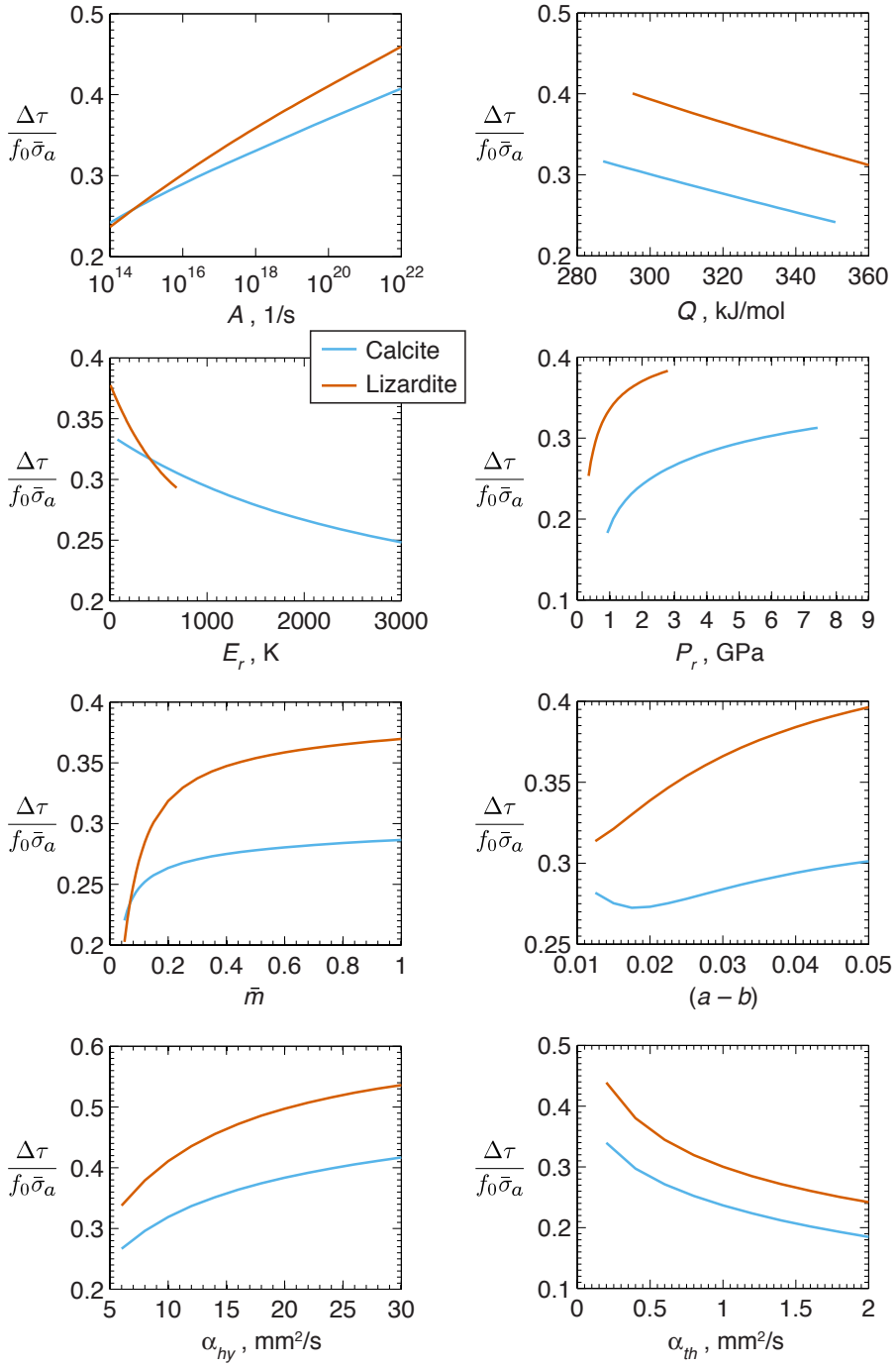

Figure 4.12: (continued)

Next we quantify how this strength drop depends on the gouge properties. To do this we define the strength before thermal decomposition to be the stress at the local minima in the weakening rate associated with the onset of decomposition, and the strength after decomposition to be that at which the weakening rate returns to the distance away from the slip on a plane solution it was before thermal decomposition was triggered. These two values are then used to define the strength drop coinciding with thermal decomposition. Figure 4.12 show how the stress drop varies with the parameters in the model. We see that typical strength drops are between 0.2 and 0.5 of the initial strength τ_0, meaning that in these simulations thermal decomposition is as important as thermal pressurization in controlling the total co-seismic strength drop of the gouge layer. We also see that in general a larger strength drop is associated with a smaller value of W, and that larger strength drops occur over a shorter time.

4.6 Predictions for other common fault materials

In this section we use the results from the previous section to make predictions for the peak temperature and localized zone thickness for the four materials listed in Table 4.2.

First we predict the maximum temperature during an earthquake, assuming that this temperature is controlled by the endothermic thermal decomposition reaction, using equation (4.33). We use the parameters from Tables 4.1 and 4.2, a reactant mass fraction $\bar{m} = 0.5$, an effective stress equal to half the ambient value, a slip rate $V = 1$ m/s, and a deforming zone thickness of 100 μm. This leads to the predictions

$$T_r^{calc.} = 960\,^{\circ}\mathrm{C} \quad , \quad T_r^{liz.} = 885\,^{\circ}\mathrm{C}, \tag{4.67}$$

$$T_r^{ill./musc.} = 1733\,^\circ\mathrm{C} \quad , \quad T_r^{talc} = 1454\,^\circ\mathrm{C}. \tag{4.68}$$

We see that the dehydration of talc and the illite/muscovite mixture limits the peak temperature at much higher values than those predicted for the decarbonation of calcite and the dehydration of lizardite.

Next we predict the localized zone thickness using the high-temperature limit given in equation (4.50). Using the parameters in Tables 4.1 and 4.2, and assuming an initial reactant mass fraction $\bar{m} = 0.5$ and a slip rate $V = 1$ m/s we predict

$$W_{calc.}^{HT} = 5.1\ \mu\mathrm{m} \quad , \quad W_{liz.}^{HT} = 1.2\ \mu\mathrm{m}, \tag{4.69}$$

$$W_{ill./musc.}^{HT} = 1.1\ \mu\mathrm{m} \quad , \quad W_{talc}^{HT} = 1.3\ \mu\mathrm{m}. \tag{4.70}$$

The localized zone thicknesses predicted for the other dehydration reactions are similar to the predictions for lizardite, with values of about a micron.

Finally we use the formula given in equation (4.61) that is motivated by the linear stability analysis in the intermediate regime and gives the best fit to the numerical simulations. To evaluate this formula we use the results in equations (4.69) and (4.70) to estimate the current temperature of the deforming gouge. Using the parameters in Tables 4.1 and 4.2, and assuming an initial reactant mass fraction $\bar{m} = 0.5$ and a slip rate $V = 1$ m/s we predict

$$W_{calc.} = 12.7\ \mu\mathrm{m} \quad , \quad W_{liz.} = 6.8\ \mu\mathrm{m}, \tag{4.71}$$

$$W_{ill./musc.} = 11.9\ \mu\text{m} \quad , \quad W_{talc} = 8.6\ \mu\text{m}. \tag{4.72}$$

These predictions are larger than the predictions from the high-temperature limit W^{HT}, as was observed in the numerical simulations shown in Section 4.5. For all four materials we predict that the localized zone thickness is approximately ten microns wide.

4.7 Discussion

4.7.1 Localized zone thickness during seismic shear

In this paper we showed how the localized zone thickness is expected to change during seismic shear. Thermal decomposition can be neglected during the initial stages of deformation and localization is driven by thermal pressurization. In this limit the localized zone thickness is set by a balance between thermal pressurization, hydrothermal diffusion and frictional rate-strengthening, and for a fixed slip rate the localized zone thickness can be predicted using the analysis in *Rice et al.* [2014][189] and *Platt et al.* [2014][166]. At high temperatures thermal decomposition dominates thermal pressurization. The maximum strain rate in the gouge layer increases to a new peak value before decaying, indicating that the onset of thermal decomposition drives additional strain rate localization.

We used a linear stability analysis to quantitatively predict the localized zone thickness as a function of the fault temperature. As expected, at low temperatures we recover the predictions from *Rice et al.* [2014][189], which studied strain localization driven by thermal pressurization alone. At high temperatures the localized zone thickness is independent of the fault temperature, and the formula for localized zone thickness has a simple form that is

independent of the reactant mass fraction and the reaction kinetics. The reaction controls the localized zone thickness only through the parameters E_r and P_r. For fault temperatures between the high and low temperature limits we solved for the localized zone thickness using Cardano's formula for roots of a cubic equation, leading to a more complicated formula than the simple solution in the high temperature limit. This formula shows a weak dependence on the reactant mass fraction and reaction kinetics, and requires a current fault temperature to be specified.

We tested our analytic predictions using numerical simulations. Performing a parameter sweep over all relevant dimensionless parameters we found that the more general cubic formula makes more accurate predictions than the simpler formula valid in the high temperature limit. This is because the endothermic nature of the reaction limits the peak fault temperature to a value below the region where the high temperature limit is valid. Based on this we conclude that the best predictions for localized zone thickness when thermal decomposition is active are given by equation (4.61). However, this means we must know the reaction kinetics and hope that the peak fault temperature is well approximated by equation (4.33). When the reaction kinetics are unknown a prediction for the localized zone thickness can still be made using the simpler formula in equation (4.50), and this is expected to be correct to within a factor of $\sim 2 - 3$.

The ubiquity of carbonates and hydrated clays in mature faults and the large temperature rises expected during an earthquake suggest that thermal decomposition is triggered during the majority of earthquakes. This suggests that it may be more appropriate to compare the predictions from equation (4.61) with field and laboratory observations of micron-scale strain localization than the low temperature limit studied in *Rice et al.* [2014][189] and

Platt et al. [2014][166]. The localized zone thicknesses predicted in this paper are in good agreement with the majority of observations of strain localization, and a detailed discussion of these observations can be found in the introduction of *Rice et al.* [2014][189]. When comparing with field and laboratory observations it may be more appropriate to use the full width at tenth maximum W_{FWTM}, which is equal to $\sqrt{2\log(10)}\,W$.

If we neglect grain size reduction or amorphization due to comminution and thermal decomposition, then the thinnest localized zone thicknesses predicted in this paper are comparable to a typical grain size in the gouge layer. This means that for the very thinnest localized shear zones the size of individual grains may be an important localization limiter. There are several ways to predict a localized zone thickness in this limit, as discussed in *Rice et al.* [2014][189] and *Platt et al.* [2014][166]. One option, which is based on a wide body of research on localization in granular systems, is to set the localized zone thickness equal to $\sim 10 - 20d_{50}$, where d_{50} is the grain size such that 50% by weight of the particles have larger size. Another option is to extend the model presented in this paper to account for the motion of individual grains. This might be done using a higher order continua or gradient theory that models the inertia of individual grains, and examples of how these models interact with thermal and pore fluid effects can be found in *Vardoulakis* [2002][230] and *Sulem et al.* [2011][219].

Our model makes many simplifications that may alter our quantitative predictions significantly, though we expect the results to be qualitatively unchanged with the localized zone thickness set by a balance between thermal decomposition, frictional rate-strengthening and diffusion. First we assume that the gouge properties are constant, and approximate the expected changes with pore pressure and temperature using the path-averaging approach

from *Rice* [2006][186]. *Rempel and Rice* [2006][180] suggested that this is a fair approximation for most parameters, but that the changes in hydraulic diffusivity accompanying pore pressure changes may be important. Since thermal decomposition leads to pore pressures much closer to the normal stress, it is possible that the hydraulic diffusivity at peak localization is much larger than the value we assumed, leading to a localized zone thickness that is much wider than our predictions. As noted in *Sulem et al.* [2009][218], the solid volume change accompanying thermal decomposition will also impact the hydraulic parameters, and we expect this porosity change to increase α_{hy} and lower P_r. Both of these changes will act to widen the localized zone. Since limited depletion has occurred at the moment when peak localization is achieved we do not expect this to alter the peak localized zone thickness, but it may lead to significant widening of the localized zone as the reactant is depleted.

Equation (4.61) shows that the localized zone thickness depends more sensitively on f_0 than any other parameter in the model. This means that other dynamic weakening mechanisms that alter the friction coefficient – such as flash heating and the low friction coefficients associated with nanoparticles – may lead to localized zones that are wider than our predictions. If we crudely approximate these dynamic weakening effects by assuming a lower friction value of $f_0 = 0.2$ then we predict that the localized zone thickness will increase by almost an order of magnitude.

Finally, all of the results presented in this paper assume a fixed kinematically applied slip rate. However, in a dynamically propagating rupture we expect the slip rate to vary by at least an order of magnitude along the fault, with the largest slip rates at the rupture tip. Our formulae for the localized zone thickness suggest that these variations in slip rate will lead to significant changes in the localized zone thickness during an earthquake. However,

Figure 4.3 shows that localization develops over a finite slip of a few millimeters, and thus it is not appropriate to just evaluate equation (4.61) as a function of V in a dynamic rupture simulation. Properly testing the effects of a variable slip rate requires a new study that imposes $V(t)$.

4.7.2 Limiting of peak temperature

In addition to studying how thermal decomposition drives strain localization, we also studied the evolution of the maximum temperature within the gouge layer. This builds on previous work by *Sulem et al.* [2009][218], *Brantut et al.* [2010][30] and *Brantut et al.* [2011][32] that showed how the endothermic decomposition reaction can limit the maximum temperature rise, possibly explaining the frequent lack of pseudotachylytes on mature faults.

Figure 4.7 shows that thermal decomposition is initially unimportant and the maximum temperature rise follows the solution for thermal pressurization alone from *Platt et al.* [2014][166]. When thermal decomposition becomes important the maximum temperature within the gouge layer begins to rise faster than for thermal pressurization alone. This is a surprising result for an endothermic reaction but can be understood by realizing that the pore pressure generated by the reaction is driving additional strain rate localization, focusing frictional heating into a narrower zone. Eventually the reaction kinetic becomes fast enough to offset the additional heating and we see a peak temperature followed by a gradual decay. We believe that this gradual decay is due to the strength drop that accompanies the onset of decomposition gradually lowering the amount of frictional heating that the reaction has to offset.

While *Sulem et al.* [2009][218] and *Brantut et al.* [2010][30] showed that the endothermic

reaction caps the maximum temperature rise, they did not provide a way to predict how this temperature will change with the gouge properties or reaction triggered. In this paper we estimated the peak temperature rise by assuming it occurs when the reaction progresses fast enough to offset all frictional heating. This highlights that the peak temperature is controlled by the kinetics, and is not well estimated by the temperatures from equilibrium phase diagrams. Our estimates for the peak temperature were tested using numerical simulations. Performing a parameter sweep over all relevant dimensionless parameters we showed that our estimate is generally accurate to within $\sim$ 50 °C when we assume a fixed frictional heating equal to a 50% strength drop and a localized zone that is 150 μm wide. From this we conclude that equation (4.33) can be used to estimate peak temperatures when thermal decomposition is active.

These simulations also allowed us to study the role of thermal diffusion in limiting the maximum temperature. We find that in general thermal diffusion is more important than thermal decomposition in limiting the maximum temperature. This is because diffusion occurs rapidly for micron-scale deforming zones, though it is possible that for much higher values for the hydraulic diffusivity, which leads to wider shear zones, thermal diffusion would be unimportant in limiting the peak temperature. This contradicts the assumptions that went into equation (4.33) but we still obtain a reasonable estimate for the peak temperature due to the weak dependence of the peak temperature on the assumed frictional heating.

It is important to note that our results are based on a large extrapolation in the reaction kinetics, and any change in A or Q will alter our results. One important physical process that is neglected here is the interaction between the pore fluid pressure and the reaction ki-

netics. We expect the reaction to proceed slower at higher pore pressures, which may replace the gradual decay after the peak temperature with a gradual increase.

Our predictions for talc and the illite/muscovite mixture show that thermal decomposition may not always preclude melting. However, it is likely that, on the timescales associated with seismic slip, melting is partially controlled by the kinetics, as was shown to be the case with thermal decomposition. This means that it may not be sufficient to just compare the predictions from equation (4.33) with a typical equilibrium melting temperature, and instead a melting temperature should be estimated by comparing the melting kinetics with a typical seismic slip duration. Quantitative predictions for a wider range of materials are made difficult due to the lack of data to constrain the reaction kinetics.

4.7.3 Impact on dynamic weakening

Previous work by *Sulem et al.* [2009][218] and *Brantut et al.* [2010][30] showed that the onset of thermal decomposition leads to a rapid pore pressure increase, and thus accelerated dynamic weakening. Our final focus in this paper was to study how the magnitude of this strength drop is controlled by the gouge properties.

As with the localized zone thickness and maximum temperature, the shear strength evolution initially follows the solution for thermal pressurization alone from *Platt et al.* [2014][166]. This means that the initial weakening follows the solution for uniform shear under undrained and adiabatic conditions from *Lachenbruch* [1980][127], and after the first strain rate localization driven by thermal pressurization the shear strength follows the Mase-Smith-Rice slip on a plane solution[144,145,186]. The onset of thermal decomposition is accompanied by an acceleration in dynamic weakening, leading to a lower shear strength than the

Mase-Smith-Rice slip on a plane solution. While the shear strength evolution no longer follows the slip on a plane solution, the weakening rate $-\dot{\tau}$ does approach that predicted by the slip on a plane solution at large slips.

Comparing the weakening rate from our numerical simulations and the slip on a plane solution we were able to quantify the strength drop associated with the onset of thermal decomposition. Typical strength drops are $\sim 20 - 40\%$ of the initial fault strength, though we see significant variations in the parameter sweep shown in Figure 4.12. In general larger strength drops are associated with more intense localization, and the larger stress drops also occur over shorter slips. From this we conclude that the strength drop due to thermal decomposition is comparable to the strength drop from thermal pressurization. Assuming that flash heating can be modeled by instantaneously reducing the friction coefficient from ~ 0.6 to ~ 0.2 at the rupture tip, we expect flash heating to account for $\sim 70\%$ of the co-seismic strength drop with thermal pressurization and decomposition each accounting for $\sim 15\%$ of the strength drop. However, this conclusion relies on a crude model for flash heating, and it is unclear how efficient flash heating is when deformation is distributed in a gouge material.

As discussed in section 4.7.1, it is important to remember that our model assumes a fixed kinematically applied slip rate. To truly determine how much of the co-seismic strength drop is due to thermal decomposition requires a dynamic rupture code that couples the strength evolution on the fault surface to an elastodynamic model for the material adjacent to the fault.

4.8 Conclusions

We used a model for deformation in a fluid-saturated gouge layer to study seismic strain localization driven by thermal decomposition. Combining a linear stability analysis with numerical simulations, we predicted the localized zone thicknesses as a function of the fault properties, showing that when thermal decomposition dominates thermal pressurization this thickness is set by a balance between thermal decomposition, hydraulic diffusion, and frictional rate-strengthening.

In addition we studied how the endothermic reaction combines with thermal diffusion to limit the temperature rise during an earthquake, producing the first estimate for how the peak temperature depends on reaction properties. For the materials studied here this peak temperature is controlled by the reaction kinetics, and is typically much larger than the equilibrium phase transition temperature.

Next we studied how the onset of thermal decomposition accelerates dynamic weakening, showing that the onset of decomposition leads to a rapid strength drop of $\sim$20-40% of the initial fault strength. The weakening rate after the onset of decomposition is shown to be roughly approximated by the slip on a plane solution for weakening driven by thermal pressurization, though thermal decomposition $-\dot{\tau}$ always leads to shear strengths that are lower than those predicted by thermal pressurization alone. A parameter sweep shows that larger strength drops at the onset of decomposition are associated with more intense strain localization.

Our results were used to predict the peak temperature and localized zone thickness for four different reactions. We predict localized zone thicknesses between 6 and 12 μm, and

peak temperatures between 885 and 1733 °C. Based on these predictions we conclude that thermal decomposition drives micron scale strain localization, but not all thermal decomposition reactions will limit the peak temperature below a typical melting temperature.

This project was a collaboration with Robert C. Viesca and Dmitry I. Garagash. I was the lead researcher on this project and primary author of the manuscript. The work in this chapter is in preparation for the Journal of Geophysical Research.

5

Steadily propagating slip pulses driven by thermal decomposition

5.0 Abstract

Geophysical observations suggest that mature faults weaken significantly at seismic slip rates. Thermal pressurization and thermal decomposition are two mechanisms commonly

used to explain this dynamic weakening. Both rely on pore fluid pressurization with thermal pressurization achieving this through thermal expansion of native solids and pore fluid and thermal decomposition by releasing additional pore fluid during a reaction. Several recent papers have looked at the role thermal pressurization plays during a dynamically propagating earthquake, but no current models have studied the role of thermal decomposition. In this paper we present the first solutions accounting for thermal decomposition during dynamic rupture, solving for self-healing slip pulses propagating at a constant rupture velocity. First, we show that thermal decomposition has a distinctive signature with longer slip durations, larger total slips, and peak slip rates near the trailing edge of the slip pulse. Next, we show that accounting for more than one weakening mechanisms allows for multiple steady slip pulses at a given background stress, with some slip solutions corresponding to different balances between thermal pressurization and thermal decomposition, and others corresponding to activating a single reaction multiple times. Finally, we study how the rupture properties – such as slip duration, rupture velocity and total slip – depend on the fault properties, and show that the impact of thermal decomposition is largely controlled by the ratio the hydraulic and thermal diffusivities $\chi = \alpha_{hy}/\alpha_{th}$ and the ratio of pore pressure generated to energy absorbed by the reaction P_r/E_r.

5.1 Introduction

Several lines of evidence suggest that mature faults weaken significantly at seismic slip rates. First, the driving stress resolved on mature faults is often low[222], suggesting that, to allow an earthquake to propagate, the fault must experience a significant co-seismic strength drop from a peak strength consistent with quasi-static measurements (e.g. *Byer-*

lee [1978][38]). Second, the lack of an observable heat anomaly on major faults[128,83] – and the scarcity of frictional melt products – suggests that the fault strength during seismic slip is much less than the strength predicted by Byerlee's law. Finally, high-velocity friction experiments performed on natural samples show a sharp drop in friction coefficient for slip rates above $\sim$ 0.1 m/s, which is an order of magnitude lower than a typical seismic slip rate of $\sim$ 1 m/s[61].

Several mechanisms have been proposed to explain this dynamic weakening. In this paper we will focus on just two of these mechanisms, thermal pressurization and thermal decomposition. Both mechanisms rely on elevated pore fluid pressures in a fluid-saturated gouge layer, with thermal pressurization achieving this through thermal expansion of native pore fluid and thermal decomposition by releasing additional pore fluid –for example H_2O or CO_2 – during a devolatilization reaction. These reactions are ubiquitous among common fault materials, with experimental evidence for the decarbonation of calcite[97,211], siderite[96] and dolomite[56] as well as dehydration of antigorite[106], kaolinite[29] and gypsum[32]. The activation of thermal decomposition has also been inferred in field observations of natural carbonate faults[49,37]. Other proposed weakening mechanisms such as flash heating[185,186,93] may also cause dynamic weakening by lowering the friction coefficient within the gouge, but these mechanisms are neglected in this paper.

Many theoretical studies have looked at the role of thermal pressurization during seismic slip. *Lachenbruch* [1980][127] solved for the slip weakening distance and maximum temperature rise for a finite thickness gouge layer deformed under undrained and adiabatic conditions, showing that thermal pressurization leads to total co-seismic weakening and a finite temperature rise. *Mase and Smith* [1985][144], *Mase and Smith* [1987][145], and *Rice* [2006][186]

extended the analysis in *Lachenbruch* [1980][127] to account for hydraulic and thermal diffusion into the adjacent material, solving for the shear strength and temperature evolution for slip on a mathematical plane. Finally, *Rempel and Rice* [2006][180] combined the two approaches, solving for a finite thickness shear zone during kinematically imposed slip while accounting for hydrothermal diffusion.

Recent work has also gone beyond the kinematically imposed slip rates used in the previous references and coupled thermal pressurization on a fault surface to an elastodynamic model for a propagating rupture. *Andrews* [2002][4] presented the first model to couple thermal pressurization with a dynamic rupture, showing that thermal pressurization may lead to an almost total co-seismic strength drop during large earthquakes. This was extended to account for additional frictional effects[20,155], and incorporated into earthquake cycle simulations in *Noda and Lapusta* [2010][156]. *Garagash* [2012][86] showed that thermal pressurization and the associated hydro-thermal diffusion in the gouge and surrounding rock supports self-healing pulse-like ruptures. Thermal pressurization is also important when determining how a rupture evolves in a heterogeneous fault system. *Urata et al.* [2012][228] showed that accounting for thermal pressurization allows a rupture to jump a wider stepover; *Noda and Lapusta* [2013][157] showed that thermal pressurization can weaken rate-strengthening sections of faults that would not normally slip seismically, leading to large earthquakes; *Urata et al.* [2014][229] showed that the ability of a fault to weaken through thermal pressurization is a first-order effect when determining if a rupture can branch.

Theoretical studies of thermal decomposition have been far fewer than theoretical studies of thermal pressurization. *Sulem and Famin* [2009][217] and *Sulem et al.* [2009][218] (here-

after cited together as *Sulem et al.* [2009][218]), and *Brantut et al.* [2010][30] studied thermal decomposition in a gouge layer deforming in response to a constant kinematically imposed slip rate. They showed that the endothermic nature of the reaction limits the maximum temperature rise below a typical melting temperature, and the onset of the reaction accelerates dynamic weakening. *Brantut and Sulem* [2012][33] relaxed the constant slip rate constraint by coupling the gouge layer to a spring-slider model. *Platt et al.* [*submitted*][167] studied how thermal decomposition could drive co-seismic strain localization. Finally, *Poulet et al.* [2014][170] studied how the thermal decomposition of serpentinite could lead to episodic tremor and slow slip. However, no previous studies have accounted for thermal decomposition in a dynamically propagating rupture.

In this paper we present the first dynamic rupture solutions to account for thermal decomposition. Building on the solutions for thermal pressurization alone from *Garagash* [2012][86], we solve for a self-healing slip pulse propagating at a constant rupture velocity. We aim to study the interplay between thermal pressurization and thermal decomposition, and look for a distinctive signature of thermal decomposition that might be looked for in seismic observations. In addition we want to determine what important fault properties control the amount of weakening driven by thermal decomposition.

Our decision to look for self-healing slip pulses is based on the seismological observations from *Heaton* [1990][100], which showed that in large earthquakes the slip duration at a point on a fault can be much shorter than the event duration. Theoretical work has also shown that slip pulse propagation is favored over expanding crack-like ruptures at the low driving stresses thought to be resolved on mature faults[24,5,155]. Many previous studies have solved for steady slip pulses using a range of models for fault strength evolution. These include

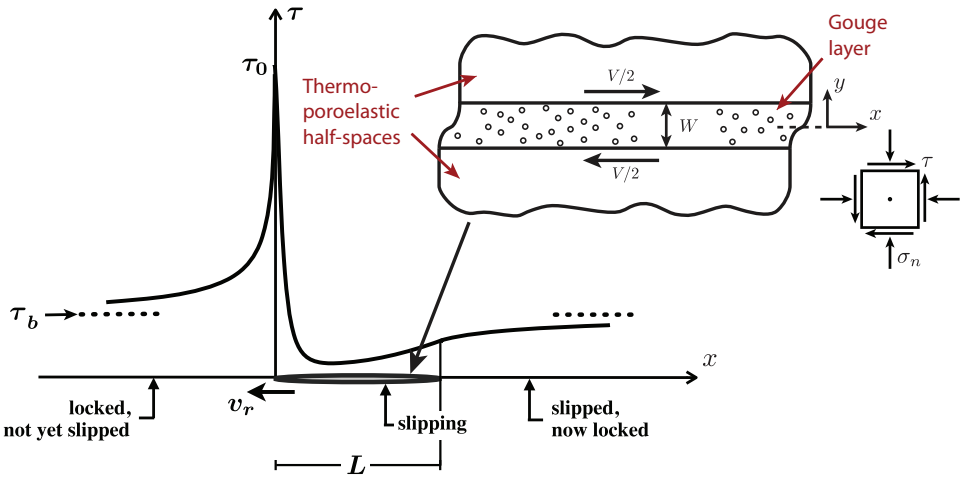

Figure 5.1: Plot showing the geometry used to solve for a slip pulse of length L propagating at a constant rupture velocity of v_r. The coordinate x is oriented parallel to the fault and is zero at the rupture tip; the coordinate y is oriented perpendicular to the fault and is zero at the centre of the gouge layer. The stress rises from the background driving stress τ_b far ahead of the pulse to the initial strength τ_0 at the rupture tip, is equal to the shear strength of the gouge layer within the slipping portion of the fault, and then rebounds back to the driving stress far behind the slip pulse. The shear strength at each point on the fault is calculated using a model for the deformation of a fluid-saturated gouge layer sheared between two undeforming thermo-poroelastic half-spaces accounting for thermal pressurization and thermal decomposition. This figure is based upon Figure 1 from *Garagash* [2012][86] and Figure 1 from *Platt et al.* [2014][166]

Broberg [1978][35], *Freund* [1979][79], *Perrin et al.* [1995][165], *Rice et al.* [2005][188], and *Garagash* [2012][86]. However, only a subset of these[165,86] address the self-healing nature of a slip pulse, where the stress on the fault is required to be below the strength whenever the fault is not slipping.

5.2 Model for steadily propagating slip pulses

In this section we develop our model for a self-healing slip pulse traveling from right to left at a constant rupture velocity v_r with dynamic weakening driven by a combination of ther-

mal pressurization and thermal decomposition. We consider a two-dimensional fault with the x-coordinate running parallel to the fault and the y-coordinate running perpendicular to the fault, as shown in Figure 5.1. The elastodynamic portion of our model is based on *Weertman* [1980][239] and *Garagash* [2012][86]. Our model for thermal decomposition is based heavily on the models derived in *Sulem et al.* [2009][218] and *Brantut et al.* [2010][30], but uses the notation from *Platt et al.* [*submitted*][167] to quantify the temperature rise buffered and pore pressure generated by thermal decomposition. We use the standard model for thermal pressurization.

5.2.1 Conservation of energy

Using the notation for thermal decomposition from *Platt et al.* [*submitted*][167] we write the conservation of energy at any point on the fault as

$$\frac{\partial T}{\partial t} = \frac{\tau_f \dot{\gamma}}{\rho c} + \alpha_{th} \frac{\partial^2 T}{\partial y^2} - \bar{m} E_r \frac{\partial \xi}{\partial t}, \tag{5.1}$$

where T is fault temperature, ρc is the effective heat capacity per unit reference volume, α_{th} is the thermal diffusivity, τ_f is the shear strength of the gouge layer, $\dot{\gamma}$ is the strain rate within the gouge layer, ξ is the reaction extent, $\bar{m}$ is the initial reactant mass fraction within the gouge layer, and E_r is the total temperature rise buffered by a completed reaction in a pure material. The definition of E_r can be found in *Platt et al.* [*submitted*][167].

Each term in equation 5.1 has a nice physical meaning. The first term on the right hand side models frictional heating in the gouge layer, the second term models thermal diffusion, and the final term models the latent heat associated with the endothermic reaction. Here we have neglected the work done by the normal stresses and the small heat flux associated

with pore fluid flow, a common assumption that is justified for typical fault gouge permeabilities[144,145]. We have also assumed that ρc, α_{th} and E_r do not change with temperature and pore pressure.

The importance of thermal decomposition at a given location within the slip pulse is determined by the reaction kinetic, which controls how fast the reaction progresses. We model the reaction rate using a first-order reaction kinetic with an Arrhenius temperature dependence

$$\frac{\partial \xi}{\partial t} = A(1-\xi)\exp\left(-\frac{Q}{RT}\right). \tag{5.2}$$

For simplicity we neglect reactant depletion – a good assumption for high initial reactant mass fractions or reactions with a large value of E_r – which is equivalent to setting $\xi \ll 1$ in equation (5.2). Next we assume that the reaction kinetic can be approximated as the product of the reaction rate in the middle of the gouge layer and a Gaussian function in y

$$\frac{\partial \xi}{\partial t} = A\exp\left(-\frac{Q}{RT_{mp}}\right)\exp\left(-\frac{\pi\beta^2 y^2}{W^2}\right), \tag{5.3}$$

where $T_{mp}(t) = T|_{y=0}$ is the temperature at the mid-plane of the deforming zone. This assumption about the shape of the reacting zone is motivated by the common approximation used to model frictional heating within the gouge layer, where the shear strength of the gouge layer is evaluated using the pore pressure at the center of the deforming zone and the strain rate is assumed to have a fixed shape. Without this assumption it would be impossible to leverage the Green's function approach used in *Garagash* [2012][86]. The additional factor β is included in equation (5.3) to allow the reacting zone to have a different thickness than the deforming zone, and β is equal to the ratio between the deforming zone thickness

W and the reacting zone thickness. We later validate our approximation of the reacting zone shape, and use these tests to select an optimal value of β.

Finally we convert equation (5.1) to a frame moving with the slip pulse – which propagates from right to left and has a rupture tip at $x = 0$ – using the transformation

$$\frac{\partial}{\partial t} \rightarrow v_r \frac{\partial}{\partial x}. \tag{5.4}$$

Combining this transformation with the simplified reaction kinetic from equation (5.3) we arrive at the final equation modeling the conservation of energy

$$v_r \frac{\partial T}{\partial x} = \frac{\tau_f \dot{\gamma}}{\rho c} + \alpha_{th} \frac{\partial^2 T}{\partial y^2} - \bar{m} E_r A \exp\left(-\frac{Q}{R T_{mp}}\right) \exp\left(-\frac{\pi \beta^2 y^2}{W^2}\right). \tag{5.5}$$

Different terms in this equation will be important at different portions of the rupture. During the initial stages of deformation the temperature will be low enough that thermal decomposition can be neglected. In this regime the temperature will rise as frictional heating occurs, with the most rapid rises happening at the beginning when the shear strength is high and thermal diffusion has limited time to act. If thermal decomposition is triggered then the endothermic reaction will offset some of the frictional heating and we expect the temperature to increase more slowly.

5.2.2 Conservation of pore fluid mass

Using the notation from *Platt et al.* [*submitted*][167] we write the conservation of pore fluid mass at any point on the fault as

$$\frac{\partial p}{\partial t} = \Lambda \frac{\partial T}{\partial t} + \alpha_{hy} \frac{\partial^2 p}{\partial y^2} + \bar{m} P_r \frac{\partial \xi}{\partial t}, \tag{5.6}$$

where p is the pore pressure, Λ is the thermal pressurization coefficient, α_{hy} is the hydraulic diffusivity, and P_r is the total pore pressure rise generated by a completed reaction in a pure material at constant temperature and undrained conditions. The first term on the right hand side models thermal pressurization, the second term models hydraulic diffusion, and the final term models the pore pressure generated by thermal decomposition. We have assumed that the hydraulic properties are constant, and thus do not change with temperature, pore pressure or reaction extent. As with the equation modeling the conservation of energy we transform equation (5.6) to a frame moving with the slip pulse and approximate the reaction kinetic as the product of the reaction kinetic evaluated using the temperature at the center of the deforming zone and a Gaussian function in y with a prescribed width. This leads to the final equation for the conservation of pore fluid mass

$$v_r \frac{\partial p}{\partial x} = v_r \Lambda \frac{\partial T}{\partial x} + \alpha_{hy} \frac{\partial^2 p}{\partial y^2} + \bar{m} P_r \exp\left(-\frac{Q}{R T_{mp}}\right) \exp\left(-\frac{\pi \beta^2 y^2}{W^2}\right). \tag{5.7}$$

As with the conservation of energy, different terms in equation (5.7) will be important at different locations within the slip pulse. Initially thermal decomposition can be neglected and all weakening will come from thermal pressurization. If the reaction is triggered the

results in *Sulem et al.* [2009][218] and *Brantut et al.* [2010][30] suggest that the onset of thermal decomposition will lead to an acceleration in dynamic weakening. Near the trailing edge of the slip pulse hydro-thermal diffusion will lower the pore pressure, providing the re-strengthening mechanism that allows self-healing slip pulses to occur.

5.2.3 Deformation within the gouge layer

Rice [2006][186] concluded that inertial effects within the gouge layer will be negligible during seismic shear due to the small distances over which hydraulic and thermal diffusion act. This conclusion was tested in *Platt et al.* [2014][166] and found to be true for typical seismogenic conditions, with the possible exception of the rupture tip where slip rates can become very large. Neglecting inertia within the gouge layer allows us to write the conservation of momentum using the conditions for mechanical equilibrium

$$\frac{\partial \tau}{\partial y} = 0 \quad , \quad \frac{\partial \sigma_n}{\partial y} = 0, \tag{5.8}$$

where τ is the shear stress on the fault and σ_n is the normal stress on the fault, which is assumed to be constant. This quasi-static approximation forces the shear stress within the gouge layer to be at most a function of x.

The shear strength within the gouge layer is controlled by a friction coefficient f and the Terzaghi effective stress,

$$\tau_f = f \times (\sigma_n - p). \tag{5.9}$$

It is important to note that when the gouge is deforming – and thus the stress on the fault is equal to the gouge layer strength – equation (5.9) is incompatible with equation (5.8)

if the friction coefficient is assumed to be constant. Only two forms of deformation are possible, uniform shear of the gouge under undrained and adiabatic conditions or slip on the plane of maximum pore pressure[186]. If the friction coefficient varies across the gouge layer then a localized zone with a finite thickness can develop, but this thickness may vary dramatically during seismic slip and should be solved for as part of the solution[189,166,167]. However, such a calculation is far beyond the scope of this paper, and we ignore the complications associated with strain rate localization by assuming that the deforming zone has a Gaussian shape with constant width W

$$\dot{\gamma} = \frac{V(x)}{W} \exp\left(-\frac{\pi y^2}{W^2}\right), \tag{5.10}$$

where V is the slip rate accommodated across the gouge layer. Fixing the deforming zone thickness – as opposed to solving for it as in *Platt et al.* [2014][166] – forces us to choose where in the deforming zone we want to evaluate the fault strength. We choose to use the pore pressure at the centre of the deforming zone, which is almost always equal to the peak pore pressure within the deforming zone, leading to

$$\tau_f = f\left(\sigma_n - p|_{y=0}\right). \tag{5.11}$$

Although the assumptions in this paragraph are severe, they are currently the only way to avoid the complicated process of modeling the evolution of strain rate localization within the gouge for every point on the fault during rupture propagation.

When thermal decomposition is accounted for it is possible that the pore pressure will become equal to – or even exceed – the normal stress. This is in contrast with thermal pres-

surization alone where the pore pressure is always less than the normal stress. Currently it is not clear what will happen when the pore pressure reaches the normal stress, though it may be possible for the fault to slide at zero shear strength for some period of time. Another possibility studied in *Brantut and Rice* [2011][31] is that the excess pore fluid pressure leads to fault opening, and this dilatancy returns the pore pressure to a value lower than the normal stress. Due to the uncertainty in mechanical response we will assume throughout this paper that any simulation that leads to $p \geq \sigma_n$ is unphysical. Any simulations with backslip (i.e. $V < 0$) are also unphysical, because frictional resistance must act in a direction opposite to the direction of the slip rate.

5.2.4 Elastodynamics for a steady slip pulse

In the previous subsections we developed a model for how the fault weakens in response to an imposed slip rate. In this subsection we show how the along-fault shear strength profile combines with the background stress driving the rupture to control the along-fault slip rate profile. We model a slip pulse with length L traveling at a constant rupture velocity v_r on a two-dimensional fault driven by a background stress τ_b. The half-spaces on either side of the fault have a shear modulus μ and shear wave speed c_s. For this geometry and a subsonic rupture velocity the stress on the fault is related to the slip rate profile through the integral equation[239]

$$\tau(x) = \tau_b - \frac{\bar{\mu}}{2\pi v_r} \int_0^L \frac{V(\xi)}{x-\xi} \mathrm{d}\xi \quad , \quad V(x) = v_r \frac{\partial \delta}{\partial x}. \tag{5.12}$$

Here $\bar{\mu} = \mu F(v_r/c_s)$ is the apparent shear modulus, and F decreases as the rupture velocity increases. We will model a mode-III rupture, for which $F = \sqrt{1-(v_r/c_s)^2}$, though

our work could be re-cast in the form of a mode-II rupture using the expression for F given in *Rice et al.* [2005][188].

To determine where on the fault slip occurs we compare the fault strength τ_f from equation (5.11) with the stress on the fault τ given by equation (5.12). Slip occurs when the stress is equal to the strength, and the fault locks when the stress is lower than the strength. For a slip pulse with length L and a rupture tip at $x = 0$ these conditions can be written in the slipping region as

$$\tau = \tau_f \quad , \quad V > 0 \quad , \quad x \in (0, L) \tag{5.13}$$

and in the locked region as

$$\tau < \tau_f \quad , \quad V = 0 \quad , \quad x \notin (0, L). \tag{5.14}$$

As shown by *Garagash* [2012][86] these conditions are met when the stress rate intensity factor at the trailing edge of the slip pulse

$$k_L = -\frac{4}{\pi\sqrt{L}} \int_0^L \sqrt{\frac{x}{L-x}} \frac{\mathrm{d}\tau}{\mathrm{d}x} \mathrm{d}x \tag{5.15}$$

is equal to zero. If $k_L > 0$ then the rate of stress rebound immediately behind the slip pulse is infinite, leading to a stress that exceeds the strength in the locked portion of the fault. This violates condition (5.14) and is obviously unphysical. We also consider $k_L < 0$ to be unphysical since this leads to backslip immediately ahead of the trailing edge of the pulse.

α_{th}, mm^2/s	0.54
ρc, MPa/K	2.7
Λ, MPa/K	0.3
α_{hy}, mm^2/s	6.71
E_r, °C	3060
P_r, GPa	7.42
$\bar{m}$	0.5
A, 1/s	2.95×10^{15}
Q, kJ/mol	319
R, J/(K mol)	8.31
W, μm	250
β	2
f	0.6
$\sigma_n - p_a$, MPa	180
T_a, °C	300
v^*, m/s	737

Table 5.1: Table outlining the base parameter choices used in our simulations. The thermal and hydraulic parameters are taken from *Rempel and Rice* [2006][180] and are based on the data in Tables 1-3 from *Rice* [2006][186] and the procedures in *Rice* [2006][186] used to account for variations damage, pore pressure, and temperature changes. The reaction parameters are taken from *Sulem et al.* [2009][218], but use the notation for E_r and P_r from *Platt et al.* [*submitted*][167]. The mechanical parameters follow the choices made in *Garagash* [2012][86]. Finally the ambient conditions model a depth of 10 km assuming a effectives stress gradient of 18 MPa/km and a goetherm of 30 °C/km.

5.3 Parameter values

In this section we discuss the parameter choices used for the majority of this paper. The model presented in the previous section has many parameters but the slip rate profile for a slip pulse is controlled by seven dimensionless parameters, as shown in Appendix C.1.

The most poorly constrained parameters in this problem are the hydraulic parameters α_{hy} and Λ, which will vary with pore pressure, temperature, and amount of damage to the gouge material. For the Green's function solution used in this paper we must assume

constant hydraulic properties, but we account for changes in the hydraulic properties with pressure and temperature using the path-averaged parameters modeling a damaged material from *Rempel and Rice* [2006][180]. This parameter set is based on the data in Tables 1-3 from *Rice* [2006][186] and uses the procedures in *Rice* [2006][186] to account for variations in the hydraulic properties due to damage as well as pore pressure and temperature changes. We choose $\alpha_{hy} = 6.71$ mm^2/s and $\Lambda = 0.3$ MPa/K.

The thermal parameters α_{th} and ρc are much more tightly constrained than the hydraulic parameters. Again we follow the path-averaged parameter set modeling a damaged material taken from *Rempel and Rice* [2006][180] and choose the specific heat capacity $\rho c = 2.7$ MPa/K and thermal diffusivity $\alpha_{th} = 0.54$ mm^2/s. Both of these fall in the typical range of values quoted in *Rice* [2006][186].

Next we discuss the reaction parameters, focusing on the decarbonation of calcite

$$\mathrm{CaCO_3} \rightarrow \mathrm{CaO} + \mathrm{CO_2}. \tag{5.16}$$

To model this reaction we use the kinetic parameters from *Dollimore et al.* [1996][63], and the values of E_r and P_r given in *Platt et al.* [*submitted*][167]. Our choices are $A = 2.95 \times 10^{15}$ 1/s, $Q = 319$ kJ/mol, $E_r = 3060$ °C and $P_r = 7.42$ GPa, and a more detailed discussion of these parameter choices can be found in *Sulem et al.* [2009][218] and *Platt et al.* [*submitted*][167]. All simulations in this paper are performed for an initial reactant mass fraction $\bar{m} = 0.5$, which is large enough to make reactant depletion negligible. For other reactions with lower values of E_r – such as the dehydration of lizardite – reactant depletion may become important even at such high reactant mass fraction.

Next we model the ambient state of the gouge before slip begins by assuming an effec-

tive stress gradient of 18 MPa/km, a hydrostatic pore pressure gradient of 10 MPa/km, and a geotherm of 30 °C/km. The majority of calculations are done for a depth of 10 km, which corresponds to an ambient effective stress $\bar{\sigma}_a = 180$ MPa, and an ambient temperature of 300 °C. This is slightly deeper than the depth of 7 km modeled by the parameter set from *Rempel and Rice* [2006][180] that we use for the hydraulic and thermal properties, but was chosen to ensure that thermal decomposition is triggered over a broad range of driving stresses.

All solutions in this paper are performed with a friction coefficient of $f = 0.6$, a value chosen to agree with low strain rate deformation governed by Byerlee's law. This means we implicitly ignore other dynamic weakening mechanisms such as flash heating that typically lower the friction coefficient to values close to $f = 0.1 - 0.2$. However, our results are presented with sufficient generality that they can be reinterpreted in terms of a lower friction coefficient that may be more appropriate for seismic slip. The other mechanical parameters that enter the model are the shear modulus μ and shear wave speed c_s. Following *Garagash* [2012][86] we choose $\mu = 30$ GPa and $c_s = 3$ km/s. Combining these with the parameter choices above we arrive at $v^* = 737$ m/s, which is used to solve for the rupture velocity and defined in equation (C.10).

Finally we choose the parameters describing the thickness of the deforming and reacting zones. We choose the deforming zone thickness $W = 250$ μm, which is in reasonable agreement with laboratory and field observations showing micron-scale localization as well as theoretical predictions for localized zone thicknesses for strain localization driven by thermal pressurization and thermal decomposition[189,166,167]. The localized zone thickness is chosen to be slightly larger than those predicted in *Rice et al.* [2014][189], *Platt et al.* [2014][166]

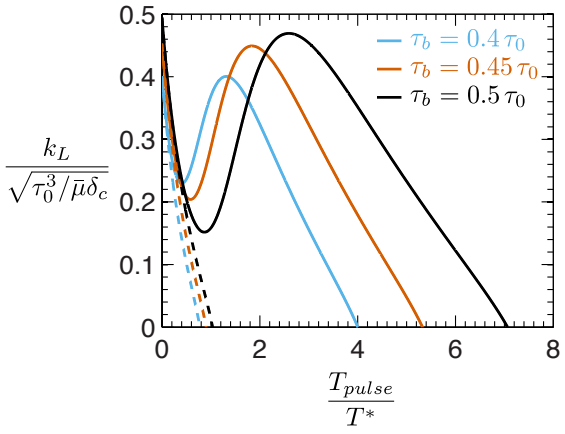

Figure 5.2: A plot showing how the stress rate intensity factor k_L at the trailing edge of the slip pulse varies with slip duration for three different driving stresses when thermal decomposition is accounted for (solid lines), alongside the corresponding solutions for thermal pressurization alone (dashed lines). For short slip durations the solutions with and without thermal decomposition agree closely, but as the slip duration increases thermal decomposition contributes more to the overall dynamic weakening and k_L rises above the values found for thermal pressurization alone. For the three driving stresses shown here we find self-healing slip pulses – where $k_L = 0$ – trigger thermal decomposition that have slip durations many times that expected for thermal pressurization alone. Qualitatively extrapolating to higher driving stresses we predict there will be a range of driving stress where multiple self-healing slip pulses exist, corresponding to multiple intercepts with the line $k_L = 0$.

and *Platt et al.* (submitted)[167] because our slip rates when thermal decomposition is active are often slightly smaller than the 1 m/s assumed in these studies, and the Gaussian shape used in our model has a slightly different parameterization than the one used in *Platt et al.* [2014][166] and *Platt et al.* [*submitted*][167]. Appendix C.3 uses finite difference simulations that make no assumptions about the reacting zone shape to validate our approximation of the reacting zone, and based on these results we choose $\beta = 2$. This means that the reacting zone is half the width of the deforming zone.

The parameters listed above are not definitive values, and strong arguments could be made for quite different values for some of the parameters. However, we will perform additional simulations that study the dependence on different key parameters, allowing our results to be reinterpreted for a much wider range of parameters choices than specified in this section.

5.4 The signature of thermal decomposition

In this section we solve for self-healing slip pulses using the parameters in Table 5.1. To find self-healing slip pulses we use the numerical methods outlined in Appendix C.2 to solve for a slip pulse with an imposed slip duration T_{pulse}, leading to curves for the stress rate intensity factor at the trailing edge of the pulse k_L as a function of the ratio of the slip duration and the timescale for hydrothermal diffusion to drain the gouge layer T_{pulse}/T^*. Figure 5.2 shows the results of these simulations, alongside the solutions for thermal pressurization alone from *Garagash* [2012][86], for three different ratios of the background stress τ_b and the initial shear strength of the gouge layer $\tau_0 = f(\sigma_n - p_a)$. Initially the curves with and without thermal decomposition agree, as the total slip accommodated across the slip pulses is not high enough to trigger thermal decomposition for the lowest values of T_{pulse}/T^*. However, thermal decomposition is eventually triggered as the total slip in the pulse rises with T_{pulse}/T^* and k_L rises above the values obtained for thermal pressurization alone. Eventually hydraulic diffusion causes k_L to decrease to zero and we find self-healing slip pulses driven by thermal decomposition at longer slip durations than for thermal pressurization alone. Figure 5.2 is the only plot in this paper that shows slip pulses that do not satisfy the self-healing condition $k_L = 0$. Henceforth all results contain only self-healing

slip pulses and the slip duration of a self-healing slip pulse is T_{sh}.

All three curves in Figure 5.2 have a triple-valued shape reminiscent of a cubic curve. Extrapolating the curves in Figure 5.2 to higher driving stress we expect three distinct self-healing slip pulses to exist for a finite range of τ_b. Numerical solutions that include the self-healing condition $k_L = 0$ in the Newton-Raphson iteration show that this expectation is met and the along-fault slip rate profiles for all three solutions are shown in Figure 5.3. All three solutions show peak slip rates on the order of a few m/s, and the peak slip rate increases as the slip duration of the solution decreases. The three solutions show quite different slip rate profiles. The short duration solution has peak slip rates near the tip followed by a gradual decay as the trailing edge of the rupture approaches. The intermediate duration solution has a similar shape to the short duration solution with an additional second peak near the trailing edge of the pulse corresponding to the onset of thermal decomposition. The long duration solution looks very different from the other two solutions with peak slip rates occurring near the trailing edge of the slip pulses at the onset of thermal decomposition. A rise in the slip rate above that expected for thermal pressurization alone corresponding to the onset of the reaction is observed for all solutions that trigger thermal decomposition.

Figure 5.3: A plot showing the slip rate, temperature, and shear stress and strength profiles for the three self-healing slip pulse solutions found using the parameters in Table 5.1 and a driving stress of $\tau_b = 0.68\tau_0$. In the temperature plot the dashed lines indicate the temperature evolution of the fault after slip ceases. In the shear stress plot the dashed lines show how the strength evolves after slip ceases. The blue curve shows the short duration slip pulse that does not trigger thermal decomposition where peak slip rates occur at the rupture tip and all weakening comes from thermal pressurization. The red curves show the long duration slip pulse with significant weakening from thermal decomposition, leading to peak slip rates at the onset of the reaction. The black curve shows the intermediate duration solution, which is a balance between the other two solutions. Thermal decomposition is triggered but peak slip rates still occur at the rupture tip, with a small increase in slip rate when the reaction is triggered. The temperature profile shows that peak temperatures are comparable to the reaction temperature estimated in *Platt et al.* [*submitted*][167].

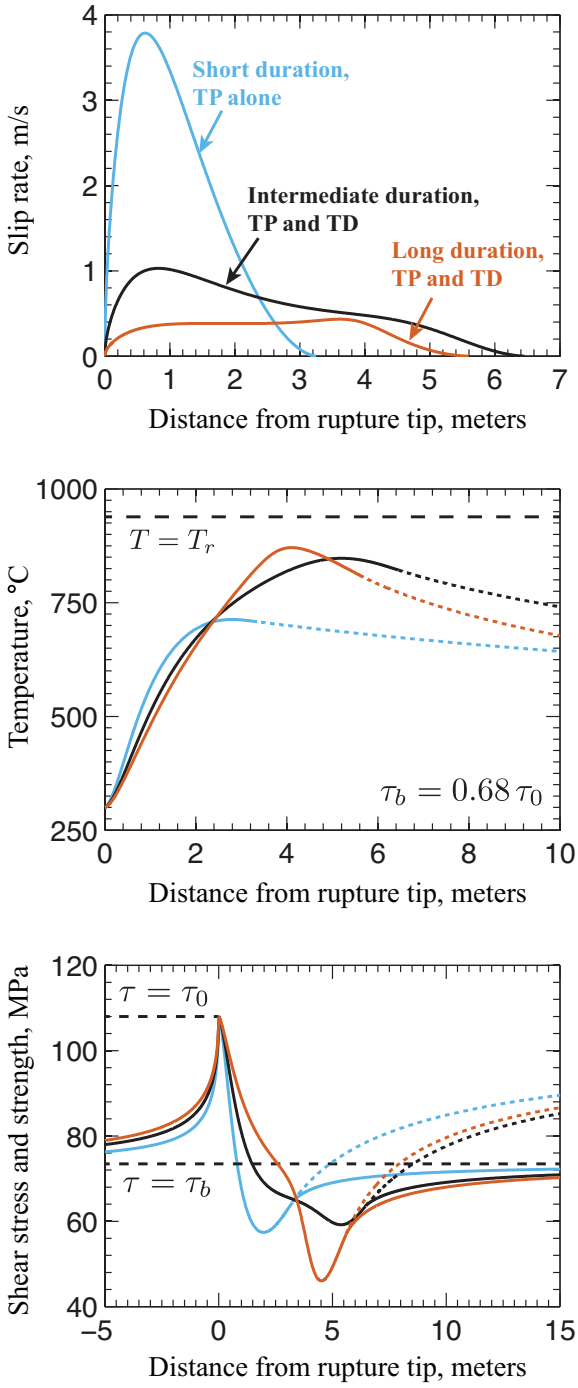

Figure 5.3: (continued)

Next we look at the temperature evolution for each slip pulse, shown in Figure 5.3. The short duration solution has a significantly lower maximum temperature than the other two solutions and does not trigger the reaction. This solution is exactly the same as the solutions from *Garagash* [2012][86] for thermal pressurization alone. Despite the different slip rate profiles – leading to distinctly different frictional heating – the intermediate and long duration solutions have comparable maximum temperatures of 847 °C and 871 °C.

We compare these values with the estimate for the peak reaction temperature from *Platt et al.* [*submitted*][167], which assumed that the peak temperature occurs when the endothermic reaction balances all of the frictional heating. This estimate is

$$T_r = \frac{Q}{R \log(\bar{m} \rho c E_r A / \tau \dot{\gamma})} \tag{5.17}$$

and is shown in Figure 5.3 for a heating rate of $\tau\dot{\gamma} = 216$ MPa/ms. This value of the heating rate was found by assuming that the pore pressure has risen halfway from the ambient value to the normal stress and a typical seismic slip rate of 1 m/s. T_r is larger than the peak temperature in our solutions – possibly indicating that for a deforming zone thickness of 250 μm thermal diffusion plays an important role in offsetting the frictional heating – but equation (5.17) still gives a rough estimate of the peak temperature. One interesting observation from Figure 5.3 is the short period of time spent at the peak temperature, a very different picture from that painted in *Sulem et al.* [2009][218], *Brantut et al.* [2010][30] and *Platt et al.* [*submitted*][167] where the constant slip rate led to a plateau at the peak temperature.

The smooth dependence of reaction rate on temperature implied by the reaction kinetic in equation (5.2) makes it difficult to define a single temperature that controls if thermal decomposition is activated or not. This is in contrast with the equilibrium approach to mod-

eling a reaction where the reaction is activated if and only if the peak temperature reaches the equilibrium reaction temperature. However, we can make a few comments about the temperature at which thermal decomposition operates. First, the sensitive dependence of the reaction rate on temperature – which increases by roughly an order of magnitude every 75 °C for temperatures between 700 °C and 1000 °C – allows thermal decomposition to be effectively turned on or off by small variations in temperature. Second, the simulations which activate thermal decomposition typically have peak temperatures within $\sim 100 - 150$ °C of the prediction given in (5.17), and thus we can use (5.17) to estimate if thermal decomposition is triggered or not. However, the peak temperature achieved during a slip pulse does not exceed the prediction from equation (5.17), and thus it may be more appropriate to think of (5.17) as an upper bound on the peak temperature. Finally, equation (5.17) allows us to see how the temperature at which thermal decomposition operates changes with the fault properties. For example increasing the reaction rate by increasing A or lowering Q allows thermal decomposition to be triggered at lower temperatures.

The temperature curves can be combined with equation (5.2) to test our assumption that reactant depletion is unimportant. We find that the final reaction extent $\Delta\xi$ at the cessation of slip is negligible ($< 0.01\%$) for the low duration solution, 1.2% for the intermediate duration solution and 4.5% for the longest slip duration solution, which confirms that reactant depletion is negligible for the decarbonation reaction studied here. Multiplying the final reaction extent by $\bar{m}E_r$ we can also find the total temperature rise offset by the reaction for each solution, finding 45 °C for the intermediate duration solution and 168 °C for the long duration solution. This suggests that reactant depletion may be important for the dehydration reactions from *Platt et al.* [*submitted*][167], which typically have lower values of

E_r comparable to the values for total temperature rise offset listed above.

We also solve for the along-fault stress and strength profiles, shown by the solid and dashed lines respectively in Figure 5.3. The behavior for both stress and strength can be easily understood in physical terms. Ahead of the slip pulse the strength is equal to the initial value $\tau_0 = f\bar{\sigma}_a$, during slip the strength is equal to the stress and we see dramatic weakening due to thermal pressurization and decomposition, and far behind the slip pulse the strength returns to the initial strength due to hydrothermal diffusion. Far ahead of the slip pulse the stress is equal to the background stress τ_b, but rises to the initial strength τ_0 as the stress concentration at the rupture tip approaches. During slip the stress is equal to the strength, and behind the slip pulse the stress rebounds to the background stress. We can see acceleration in the weakening rate corresponding to the onset of thermal decomposition in the intermediate and long duration solutions, with a much larger strength drop seen for the long slip duration solution.

To quantify the dynamic weakening due to thermal pressurization and thermal decomposition we integrate the first and third terms on the right hand side of equation (5.7) across the slip pulse, finding the total pore pressure rise due to thermal pressurization to be $\Lambda\Delta T$, where ΔT is the difference between the ambient and final temperature in the slip pulse, and the total pore pressure rise due to thermal decomposition to be $\bar{m}P_r\Delta\xi$. The total weakening due to thermal pressurization is 123 MPa, 156 MPa, 153 MPa for the short, intermediate and long slip duration solution respectively. The total weakening due to thermal decomposition is 45 MPa, 168 MPa for the intermediate and long slip duration solution respectively. From this we conclude that the three different solutions correspond to different balances between thermal pressurization, with the highest solution being most affected

by thermal decomposition and the lowest solution being unaffected by thermal decomposition. Note that thermal pressurization provides a significant amount of weakening in all three solutions. Finally we use the total strength drop in the pulse to calculate the total restrengthening due to hydrothermal diffusion, finding pore pressure rises of 50 MPa, 127 MPa, and 236 MPa for the low, intermediate and high slip duration solutions respectively. As expected hydrothermal diffusion becomes more effective as the slip duration increases.

Having shown that we can solve numerically for self-healing slip pulses, and the different balances between thermal pressurization and thermal decomposition in the different types of solutions, we next track these solution as a function of the background stress. Figure 5.4 shows how the slip duration, slip pulse length, total slip and rupture velocity vary as a function of τ_b/τ_0, which quantifies the proximity of the driving stress to the initial yield strength. For the highest values of τ_b we see that the solutions accounting for the reaction (solid lines) are the same as the solutions that consider thermal pressurization alone (dashed lines). This is because the total slip at these driving stresses is insufficient to raise the fault temperature to a point where the reaction is activated. As the driving stress decreases we eventually see thermal decomposition become important. For a finite range of τ_b three solutions exist – with the distinctive characteristics of each solution described in the previous paragraphs – and beneath a critical driving stress a unique solution exists that always triggers thermal decomposition. We see that thermal decomposition leads to longer slip durations – as was shown in Figure 5.2 – and a slip pulse length that is larger than the slip pulse length in solutions that consider thermal pressurization alone. The dependence of slip pulse length on driving stress when thermal decomposition first becomes impor-

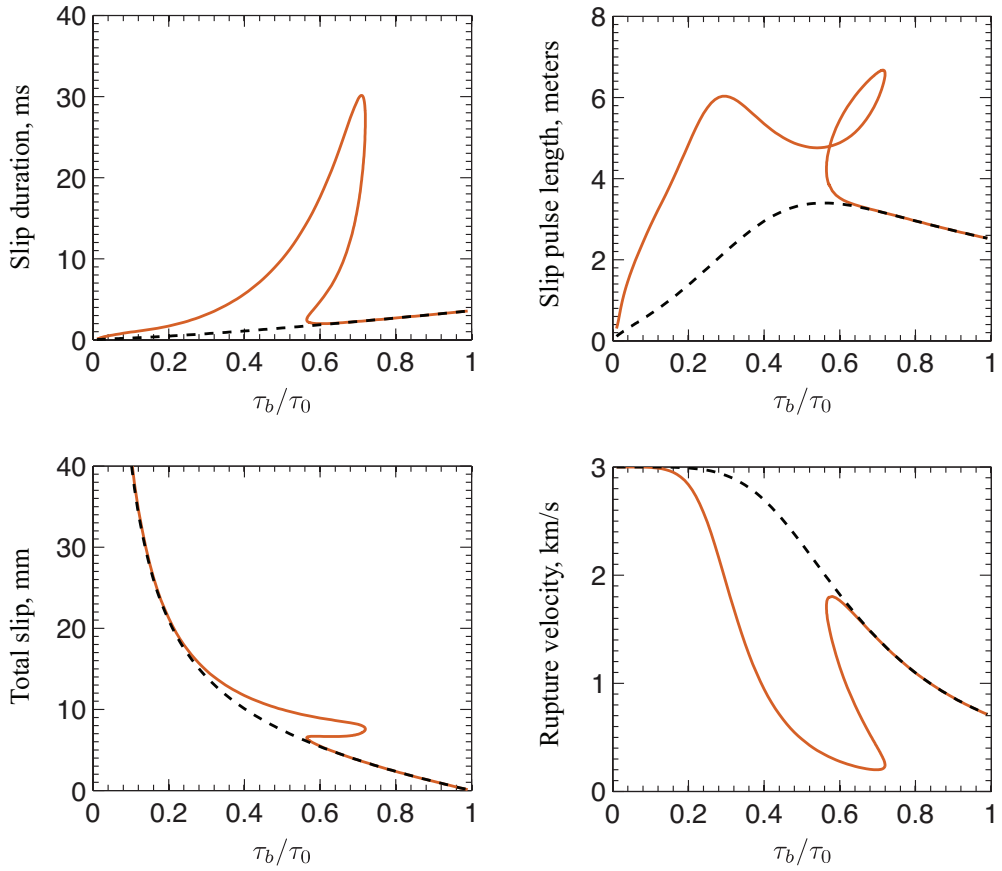

Figure 5.4: A plot showing how the slip duration, slip pulse length, total slip and rupture velocity vary with driving stress for the parameters in Table 5.1 (solid lines), alongside the corresponding curves for thermal pressurization alone (dashed lines). We see that at high driving stresses the temperature rise in a steadily propagating self-healing slip pulse is not large enough to trigger thermal decomposition. For intermediate driving stresses multiple solutions exist, corresponding to different balances between thermal pressurization and thermal decomposition. For all driving stresses the triggering of thermal decomposition is associated with larger values of slip duration, slip pulse length and total slip, and smaller rupture velocities when compared with slip pulses driven by thermal pressurization alone.

tant is complicated, with a loop formed in the region where multiple solutions exist. When multiple solutions exist we see that the longer slip duration solutions also accommodate a larger slip, though the difference in slips between the three solutions is at most a factor of two. Solving for the rupture velocity using the definition of v^* from *Garagash* [2012][86] we see that the rupture velocity decreases as the total contribution of thermal decomposition increases, and almost all rupture velocities are a significant fraction of the shear wave speed

One striking feature in Figure 5.4 is the close agreement of the solutions that account for thermal decomposition and the solutions for thermal pressurization alone as $\tau_b \to 0$, with this being especially notable for the plot showing total slip. Calculating the total pore pressure rise due to thermal pressurization and thermal decomposition as a function of driving stress shows that thermal pressurization dominates as the driving stress approaches zero, with thermal decomposition providing only a small amount of extra weakening far back from the rupture tip. This small additional slip leads to a slightly longer rupture duration and a larger slip pulse length due to the additional time taken for hydrothermal diffusion to overcome the additional weakening from thermal decomposition and heal the fault. Interestingly the maximum temperature achieved during a slip pulse is almost constant when thermal decomposition is active, varying by at most $15\ ^\circ\mathrm{C}$ as the driving stresses in the range $0.02 < \tau_b < 0.6$. This supports the idea that the endothermic nature of the reaction sets a cap on the maximum temperature rise on a fault regardless of the amount of slip experienced. We believe that the agreement between the two solutions is partly a coincidence due to our parameter choices, which led to a maximum temperature rise when thermal decomposition is active that is very similar to the maximum temperature rise for the thermal pressurization alone solutions as $\tau_b \to 0$. We tried to test the behavior as

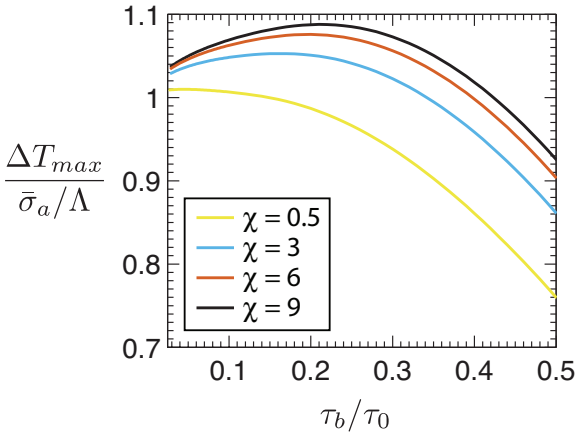

Figure 5.5: A plot showing how the maximum temperature rise during a slip pulse ΔT_{max} varies with background stress for slip pulses driven by thermal pressurization alone, shown for four values of χ. We see that as χ increases the peak value of ΔT_{max} increases and moves to higher background stresses. This behavior may explain why the effects of thermal decomposition are most pronounced for intermediate values of τ_b.

$\tau_b \rightarrow 0$ for different parameter sets that trigger thermal decomposition more vigorously – for example lowering the activation energy of the reaction Q – but found that this always led to pore pressures that exceed the normal stress, which is a situation we consider unphysical. We found that for $0 < \tau_b < 0.4$ the peak slip rate always occurs near the tip, and the slip rate profiles of all slip pulses look most like the black curve in Figure 5.3 with peak slip rates at the tip and a small secondary slip rate increase far back from the tip corresponding to thermal decomposition. This observation agrees well with our conclusion that thermal pressurization provides the majority of weakening at low values of τ_b.

One possible explanation for the lessening effects of thermal decomposition as $\tau_b \rightarrow 0$ can be found by studying the maximum temperature rise ΔT_{max} as a function of background stress for slip pulses driven by thermal pressurization alone, shown in Figure 5.5 for four values of χ. As expected we see that for all driving stresses the maximum temperature

rise increases with χ. We also see that increasing χ increases the peak value of ΔT_{max} and increases the background stress this peak value is attained at. For $\chi = 9$ the largest temperature rises are expected for $0.15 < \tau_b < 0.3$. Since the activation of thermal decomposition relies on reaching a typical reaction temperature, and the amount of weakening driven by thermal decomposition is controlled by the latent heat absorbed by the reaction, the movement of the peak value of ΔT_{max} may explain why thermal decomposition is most pronounced for intermediate values of τ_b.

5.5 Dependence on fault properties

In this section we study the dependence on different parameters in the problem, with the intention of allowing our results to be reinterpreted for different reactions or parameter choices other than those made in Section 5.4. To do this we vary different dimensional parameters in turn while all other parameters are fixed to the values given in Table 5.1. *Garagash* [2012][86] showed that self-healing slip pulses driven by thermal pressurization alone are controlled by just three dimensionless parameters. These are the ratio of the hydraulic and thermal diffusivities $\chi = \alpha_{hy}/\alpha_{th}$, the ratio of the background stress to the initial strength τ_b/τ_0, and ratio of a typical rupture velocity and the shear wave speed v^*/c_s. Accounting for thermal decomposition adds four additional dimensionless parameters. The first two new dimensionless parameters R_{th} and R_{hy} control how much heat is absorbed and pore pressure is generated by the reaction, and the other two new dimensionless parameters K and T_I quantify how much the reaction rate varies with temperature and where the ambient temperature lies on a dimensionless kinetic curve. All of the dimensionless parameters for the model can be found in Appendix C.1.

5.5.1 Influence of diffusion timescale

First we look at the dependence on the deforming zone thickness W, which alters the hydrothermal diffusion timescale $T^* = W^2/\alpha$ as well as the values of v^* and δ_c, which control the rupture velocity and total slip respectively. Figure 5.6 shows how the slip duration, slip pulse length, total slip and rupture velocity vary with the driving stress τ_b for four different deforming zone thicknesses varying by a factor of eight, alongside the corresponding solutions for thermal pressurization alone. As the deforming zone thickness is increased there is a tendency for the pore pressure to exceed the normal stress over a wide range of driving stresses. For all plots the curves are terminated when the pore pressure reaches the normal stress, and this termination is indicated by a circle. We see that the slip duration and slip pulse length increase with the deforming zone thickness but retain the same qualitative shape. The increase in slip duration is particularly large due to the quadratic dependence of T^* on W that accounts for the majority the change in slip duration between the different curves. Looking at the solutions in terms of the dimensionless variables we see that the ratio T_{sh}/T^* increases by less than a factor of two as W increases from 100 μm to 2 mm. A similar picture is seen for total slip, with wider deforming zones leading to a larger total slip. This variation is almost entirely due to the scaling of total slip with δ_c. Finally we see that the rupture velocity drops as the deforming zone thickness increases, and this is explained by noting that v^* decreases as W increases, forcing the rupture velocity away from the shear wave speed.

This behavior is qualitatively the same as the results for thermal pressurization alone from *Garagash* [2012][86], which showed that micron-scale shear zones are associated with rupture durations on the order of a milliseconds and seismic rupture velocities while millimeter-

scale shear zones are associated with rupture durations on the order of a second and rupture velocities that are far below the shear wave speed. This is to be expected because we use the same scalings in this paper as were used in *Garagash* [2012][86]. Appendix C.2 shows the dimensionless rupture properties for the parameters listed in Table 5.1, and the numbers in this figure do not changed dramatically as W changes from 100 μm to 2 mm.

The parameter sweep over W also allows us to see how the system will change with α and the kinetic parameter A. This is done by noting that the dimensionless parameters R_{th} and R_{hy} in Appendix C.1 depend only on the product T^*A. However, when A is changed the scalings δ_c and v^* will remain unchanged, and when α is changed the value of δ_c remains unchanged. The dependence on the product T^*A explains why the range of driving stresses with multiple solutions gradually moves to higher driving stresses as W increases. In the dimensionless variables increasing W is equivalent to having a higher reaction rate constant A, which allows the reaction to be triggered at smaller slips. This equivalence with a more vigorous reaction also explains why the range of driving stresses for which the pore pressure exceeds the normal stress expands as W increases.

For larger values of A the range of driving stress with multiple solutions moves to higher values of τ_b. Increasing A decreases the slip duration and total slip for a fixed driving stress – which can be understood by noting that a larger value of A allows the reaction to be triggered at a smaller slip – but leaves the rupture velocity almost unchanged. The dependence of slip pulse length on A is complicated by the presence of multiple solutions, but in general increasing A leads to a smaller value of L. However, the variations with A described above are much smaller than those seen in Figure 5.6 and for the parameters in Table 5.1 we still see slip durations of a few tens of milliseconds, slip pulse lengths of few meters, total

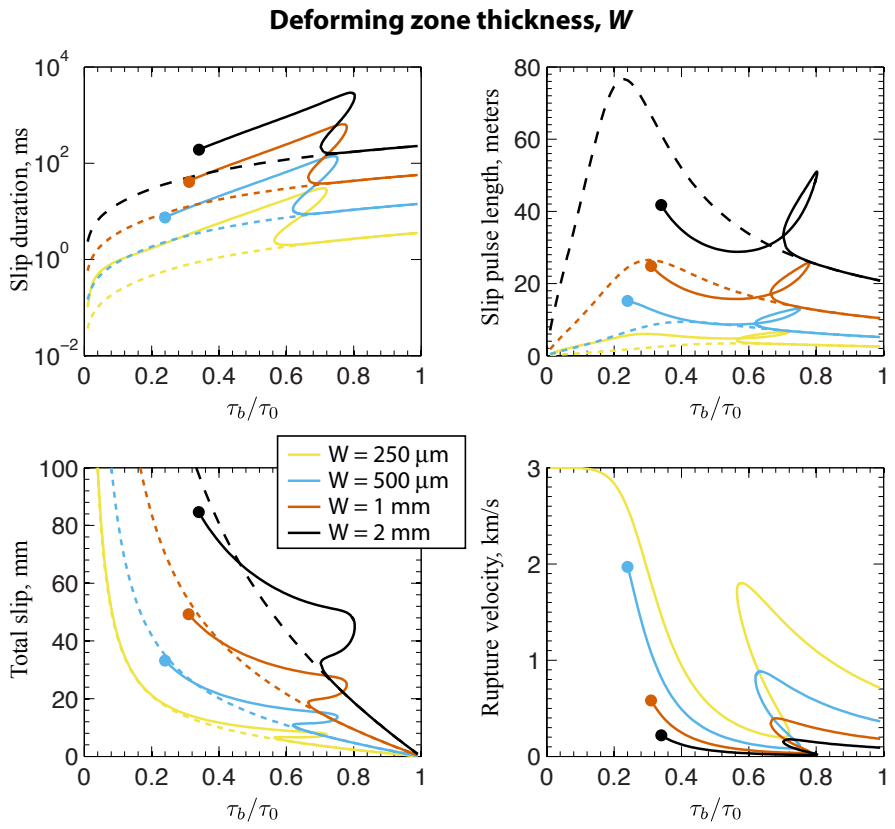

Figure 5.6: A plot showing how the slip duration, slip pulse length, total slip and rupture velocity vary with driving stress for four different values of the deforming zone thickness W and the parameters in Table 5.1, alongside the corresponding curves for thermal pressurization alone. The curves are terminated when the pore pressure exceeds the normal stress, and this point is noted by a circle. We see that increasing the localized zone thickness leads to larger values for slip duration, slip pulse length and total slip, and a lower rupture velocity. This is in good agreement with the results in *Garagash* [2012][86] that studied slip pulses driven by thermal pressurization alone.

slips of a few millimeters and rupture velocities that are a significant fraction of the shear wave speed. This is to be expected because changing A does not alter T^*, δ_c or v^*.

As α increases the slip duration and slip pulse length drops while the rupture velocity and total slip rise. The change in total slip is the smallest of these changes since the scaling for total slip is independent of α. The range of driving stresses over which thermal decomposition is triggered also shrinks as α increases. This is to be expected in our system since increasing α decreases T^*, and this is equivalent to lowering the rate constant of the reaction A.

5.5.2 Balance between hydraulic and thermal diffusion

One of the striking aspects of the slip pulses driven by thermal pressurization alone presented in *Garagash* [2012][86] is the insensitive dependence on the ratio of diffusivities $\chi = \alpha_{hy}/\alpha_{th}$, with the rupture properties varying by only a small amount as χ varies from 0 to ∞. However, the highly nonlinear coupling between temperature and reaction rate means that this conclusion does not transfer to our model. For a fixed value of α, the lower thermal diffusivity associated with large values of χ will lead to higher temperature rises, making thermal decomposition more likely to occur. Figure 5.7 shows how the rupture properties vary with driving stress for four different values of χ. As expected the signs of thermal decomposition – such as longer rupture duration – become more pronounced as χ increases. Interestingly, as χ decreases the range of driving stress over which multiple solutions exist shrinks, and for the lowest value of χ has no values of τ_b where multiple solutions exist, and the rupture properties look qualitatively similar to the solution for thermal pressurization alone. Initially we thought this could occur because lowering χ was lower-

ing the maximum temperature rise during thermal pressurization and shrinking the range of driving stresses over which thermal decomposition is triggered. However, other simulations not shown here using a rate constant A two orders of magnitude greater than the value given in Table 5.1 show that this appears to be a feature of all simulations with values of χ comparable to or less than one, even when thermal decomposition occurs and is important over a wide range of driving stresses. This means that for low values of χ thermal pressurization is the dominant dynamic weakening mechanism. We believe this occurs because the efficient thermal diffusion associated with low values of χ makes it hard to sustain peak temperatures long enough for thermal decomposition to be the dominant weakening mechanism.

5.5.3 Influence of reaction parameters

Next we look at the role played by the reaction parameters, beginning with the activation energy Q. Figure 5.8 shows how the rupture properties vary with driving stress for three different values of Q. We see that for a fixed driving stress lowering Q does not dramatically change the rupture properties – with only a small reduction in total slip and slip pulse length– but does control the range of τ_b over which thermal decomposition is triggered. This is consistent with a reaction that adjusts so that the energy absorbed by the reaction balances the frictional heating. Lowering Q allows this balance to occur at a lower temperature, effectively moving the ambient fault conditions closer to the reaction temperature and extending thermal decomposition to higher values of τ_b. We also find that lowering Q increases the range of driving stress for which the pore pressure exceeds the normal stress and increases the total pore pressure rise due to thermal decomposition during the slip pulse.

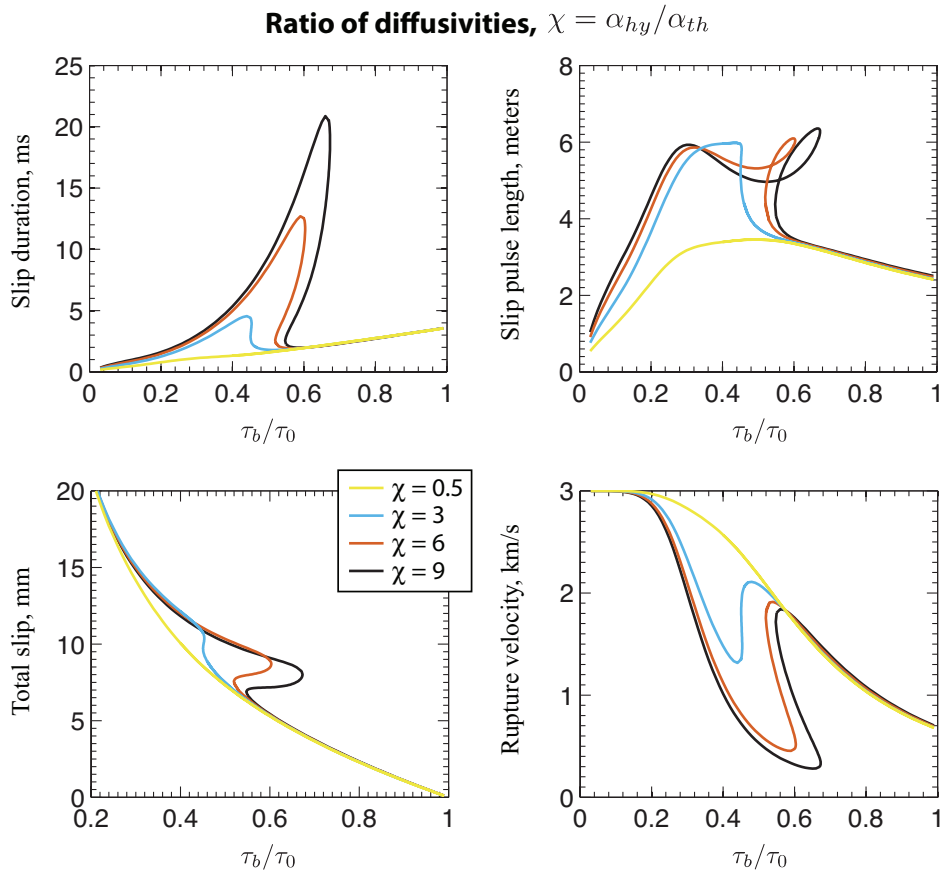

Figure 5.7: A plot showing how the slip duration, slip pulse length, total slip and rupture velocity vary with driving stress for four different values of the ratio between hydraulic and thermal diffusivities $\chi = \alpha_{hy}/\alpha_{th}$ and the parameters in Table 5.1, alongside the corresponding curves for thermal pressurization alone. We see that increasing χ leads to a more pronounced signature of thermal decomposition, with longer slip durations, larger slip pulse lengths, and lower rupture velocities. In addition we see that for the lowest values of χ the range of τ_b for which multiple solutions exist vanishes, and the results look qualitatively similar to those for thermal pressurization alone.

These observations are both consistent with the reaction becoming more vigorous as Q decreases.

Next we look at the dependence on the temperature rise buffered by the reaction E_r and pore pressure generated by the reaction P_r, shown in Figures 5.9 and 5.10. Our results show that lowering E_r is qualitatively similar to raising P_r, and that higher values of P_r lead to more distinctive features of thermal decomposition with longer slip durations, lower rupture velocities. Interestingly the regions where the pore pressure exceeds the normal stress occur at intermediate values of τ_b for these parameter sweeps. We find that the total pore pressure generated by thermal decomposition increases as P_r increases, and drops as E_r increases.

The link between E_r and P_r can be motivated by looking at the high-temperature limit examined in *Platt et al.* [*submitted*][167] where the temperature is constant, thermal diffusion is neglected and the reaction exactly balances the frictional heating,

$$\frac{\tau\dot{\gamma}}{\rho c} = \bar{m} E_r \frac{\partial \xi}{\partial t}. \tag{5.18}$$

This allows us to rewrite the pore pressure equation as

$$\frac{\partial p}{\partial t} = \alpha_{hy} \frac{\partial^2 p}{\partial y^2} + \frac{P_r}{E_r} \frac{\tau\dot{\gamma}}{\rho c}. \tag{5.19}$$

Note that this is similar to the equation for pore pressure evolution during thermal pressurization and the ratio P_r/E_r acts as an effective value of Λ. For the parameters modeling the decarbonation of calcite in Table 5.1 $P_r/E_r = 2.43$ MPa/K. This value is much larger than the value of Λ given in Table 5.1, possibly explaining why the onset of thermal decomposi-

tion accelerates dynamic weakening. As shown in *Platt et al.* [*submitted*][167], the limit described in equation (5.18) is likely never reached but we still advocate using the ratio P_r/E_r – which is equal to the pore pressure generated per degree of temperature rise buffered – to estimate if one thermal decomposition reaction will drive more or less weakening than another reaction. A similar substitution of P_r/E_r for Λ is found in *Platt et al.* [*submitted*][167] where the role P_r/E_r plays in controlling the localized zone thickness when thermal decomposition is active is the same as the role Λ plays in setting the localized zone thickness when thermal pressurization dominates.

Equation (5.18) also shows us how E_r acts independently of P_r to control the reaction depletion, with a larger value of E_r requiring a larger amount of frictional heating to make reactant depletion important. In the simulations shown in Figure 5.9 we observe that as E_r drops the total reactant depletion during the slip pulses rises. These conclusions will be very important when extrapolating the results presented here to the dehydration reactions considered in *Platt et al.* [*submitted*][167], which typically have a much lower value of E_r and a higher value of P_r/E_r.

5.5.4 Influence of depth

Finally we look at how the slip pulses driven by thermal decomposition depend on depth. To do this we follow the choices made in Section 5.4 and assume a geotherm of 30 °C/km and an effective stress gradient of 18 MPa/km. Figure 5.11 shows how the rupture properties depend on driving stress for 10 km, 12 km, and 14 km. These three depths were selected for two reasons. First, we need to be deep enough that thermal decomposition is triggered over a wide range of driving stresses, which does not occur for the decarbonation reaction

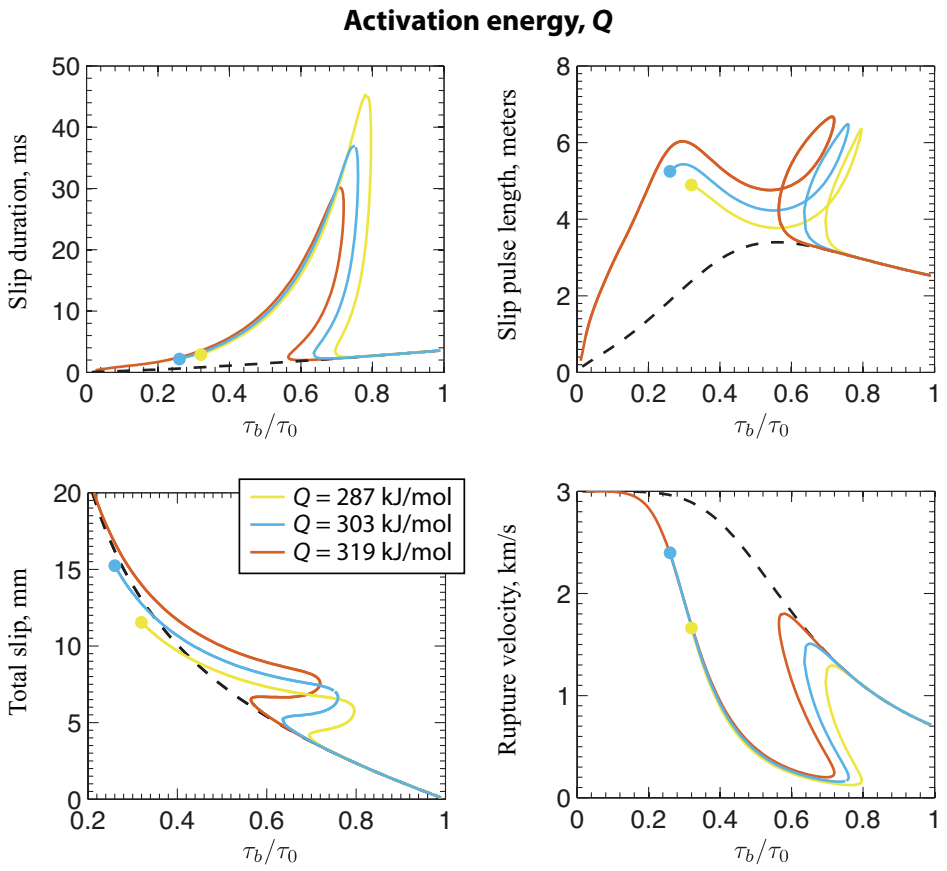

Figure 5.8: A plot showing how the slip duration, slip pulse length, total slip and rupture velocity vary with driving stress for three different values of the activation energy for the reaction Q and the parameters in Table 5.1, alongside the corresponding curves for thermal pressurization alone. The curves are terminated when the pore pressure exceeds the normal stress, and this point is noted by a circle. Lowering the activation energy makes it easier to activate thermal decomposition, leading to lower total slips and longer slip durations at high values of τ_b. A lower value of Q also leads to pore pressures that exceed the normal stress over a wide range of τ_b.

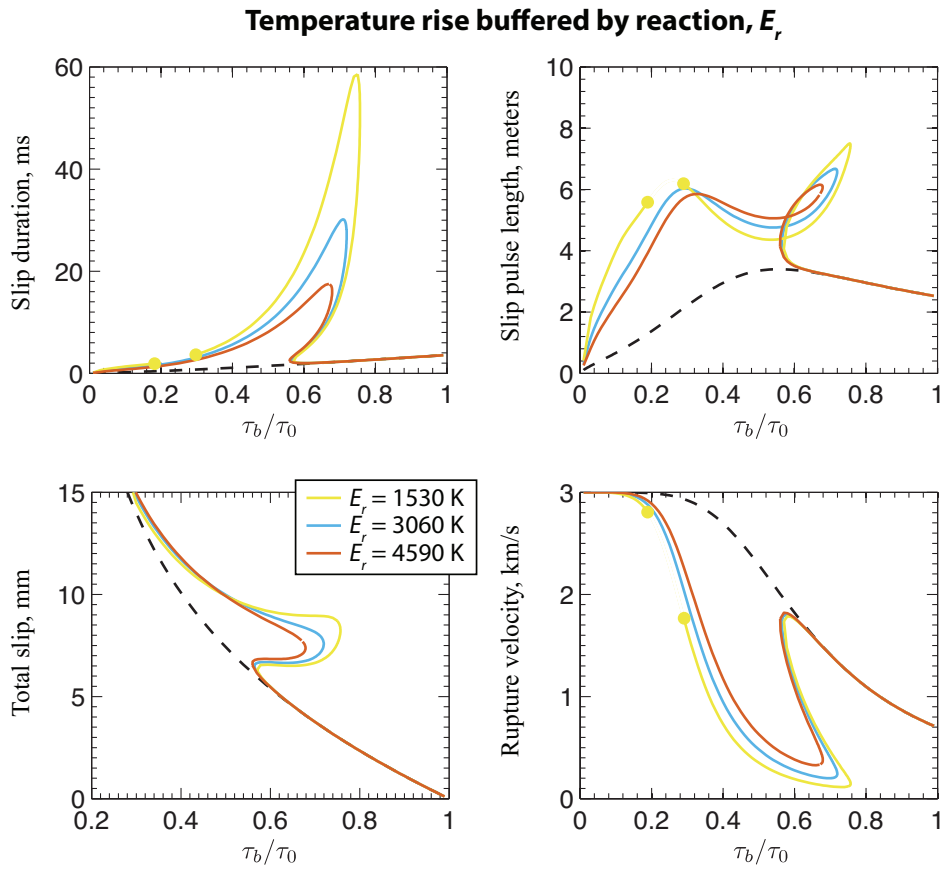

Figure 5.9: A plot showing how the slip duration, slip pulse length, total slip and rupture velocity vary with driving stress for three different values of E_r and the parameters in Table 5.1, alongside the corresponding curves for thermal pressurization alone. The curves are terminated when the pore pressure exceeds the normal stress, and this point is noted by a circle. We see that increasing E_r makes the effects of thermal decomposition less pronounced. Interestingly the range of τ_b for which the pore pressure exceeds the normal stress occurs at intermediate values of τ_b.

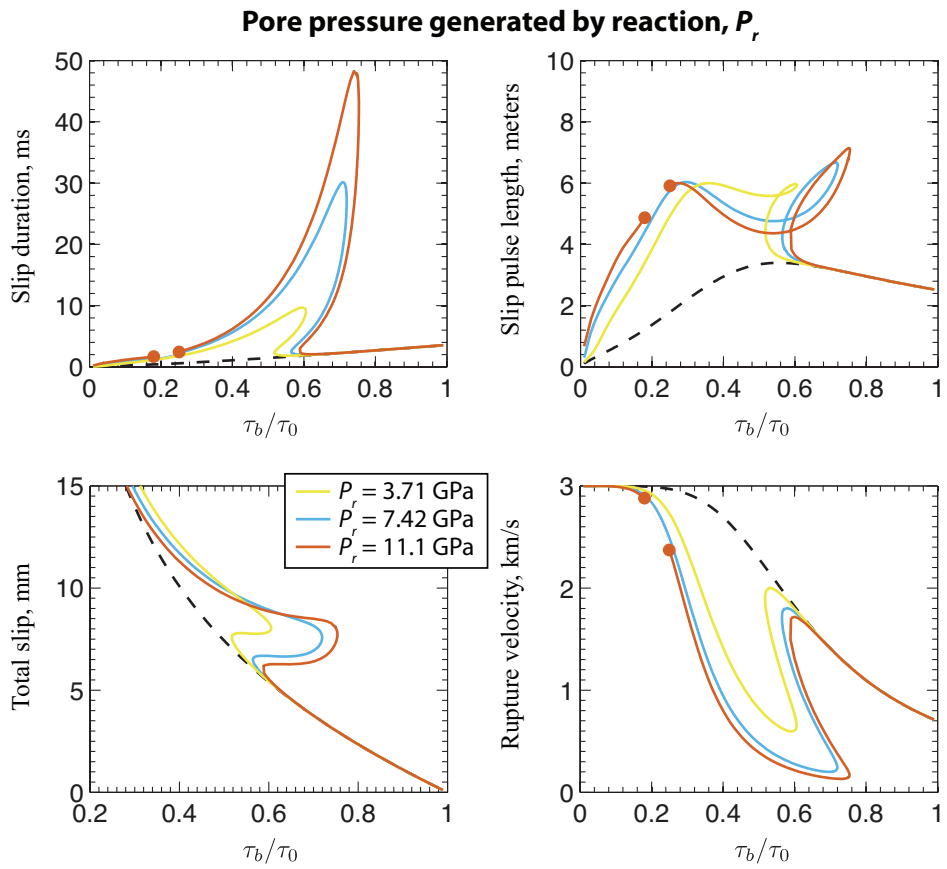

Figure 5.10: A plot showing how the slip duration, slip pulse length, total slip and rupture velocity vary with driving stress for three different values of P_r and the parameters in Table 5.1, alongside the corresponding curves for thermal pressurization alone. The curves are terminated when the pore pressure exceeds the normal stress, and this point is noted by a circle. We see that increasing P_r makes the effects of thermal decomposition more pronounced. As in Figure 5.9 the range of τ_b for which the pore pressure exceeds the normal stress occurs at intermediate values of τ_b.

considered for depths shallower than ∼8 km if we assume the path-averaged parameters modeling a damaged material from *Rempel and Rice* [2006][180]. Second, we want to limit the range of driving stresses for which the pore pressure exceeds the normal stress, and we found that as the depth increases the pore pressure exceeds the normal stress for a wider range of driving stresses. Figure 5.11 shows that increasing the depth extends the range of driving stress for which thermal decomposition is triggered, which is expected since the ambient temperature moves closer to the reaction temperature as the depth increases and the temperature rise increases as the ambient effective stress increases. The maximum temperature achieved during the simulations shown in Figure 5.11 shows only a modest increase with depth – varying from $\sim$ 900 °C at 10 km to $\sim$ 975 °C at 14 km – that can be explained by the increase in the heating rate $\tau\dot{\gamma}$ with ambient effective stress. The increase in heating rate also makes reactant depletion more important as the depth increases, though not enough to be important for the decarbonation reaction considered here.

Next we look at the balance between thermal pressurization and thermal decomposition, and find that the total pore pressure rise generated by thermal decomposition normalized by the ambient effective stress increases with depth, while the pore pressure rise generated by thermal pressurization normalized by the ambient effective stress decreases with depth. From this we conclude that the importance of thermal decomposition as a dynamic weakening mechanism increases with depth. This may seem surprising since the dimensionless parameters R_{th} and R_{hy} decrease as $\bar{\sigma}_a$ increases. However, this can be understood by noticing that as the depth increases the reaction is triggered after a smaller slip, forcing the amount of weakening due to thermal pressurization to decrease. We believe that the increase in the contribution to total weakening from thermal decomposition is the

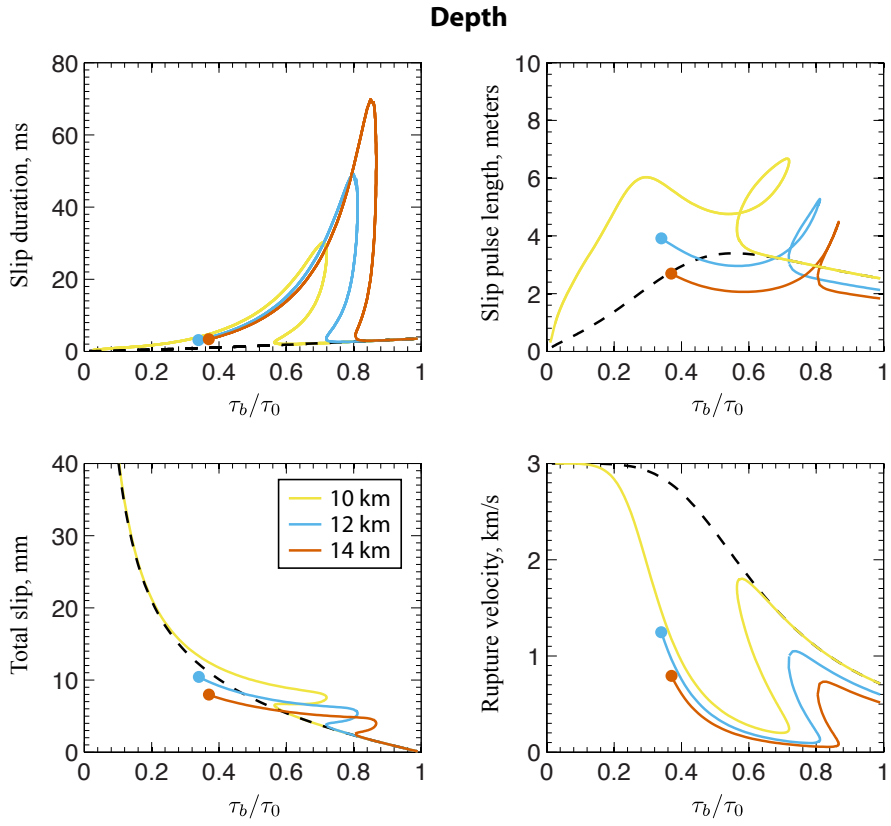

Figure 5.11: A plot showing how the slip duration, slip pulse length, total slip and rupture velocity vary with driving stress for three different depths and the parameters in Table 5.1, alongside the corresponding curve for thermal pressurization alone. Here we assume the ambient fault conditions follow an effective stress gradient of 18 MPa/km and a geotherm of 30 °C/km. The curves are terminated when the pore pressure exceeds the normal stress, and this point is noted by a circle. We see that the range of τ_b over which thermal decomposition is triggered expands with depth, as does the range of τ_b for which the pore pressure exceeds the normal stress. This indicates that thermal decomposition is more vigorous deeper in the seismogenic zone.

reason that Figure 5.11 shows more distinctive signs of thermal decomposition as the depth increases.

5.6 Train-like solutions

When the self-healing condition $k_L = 0$ is included in the Newton-Raphson iteration we found that some initial guesses converge to solutions with greater complexity than those shown above that have a single local maximum in the slip rate profile. Figure 5.12 shows four such solutions with between one and four local maxima in the slip rate profile found using the parameters in Table 5.1 with the deforming zone thickness set to $W = 3$ mm and a driving stress $\tau_b = 0.4$. When plotted against distance from the rupture tip the four solutions show strong overlap, suggesting that the two-peak solution is nearly equivalent to the one-peak solution with additional structure added at the trailing edge of the pulse. The length of each peak in the x direction is approximately constant, meaning that the slip pulse length in the four-peak solution is about four times greater than the slip pulse length in the one-peak solution. The solutions with two and four peaks naturally emerged from initial guesses designed to find solutions with one peak, while the three-peak solution was deliberately searched for using an initial guess consisting of the first three peaks of the four-peak solution. The solutions with multiple peaks arise due to the reaction effectively being triggered multiple times in the same slip pulse as the temperature rises and falls. The endothermic nature of the reaction and thermal diffusion combine to lower the temperature from the peak values, and frictional heating raises the temperature to the new peak. The frictional heating is aided by hydraulic diffusion raising the shear strength while the temperature falls.

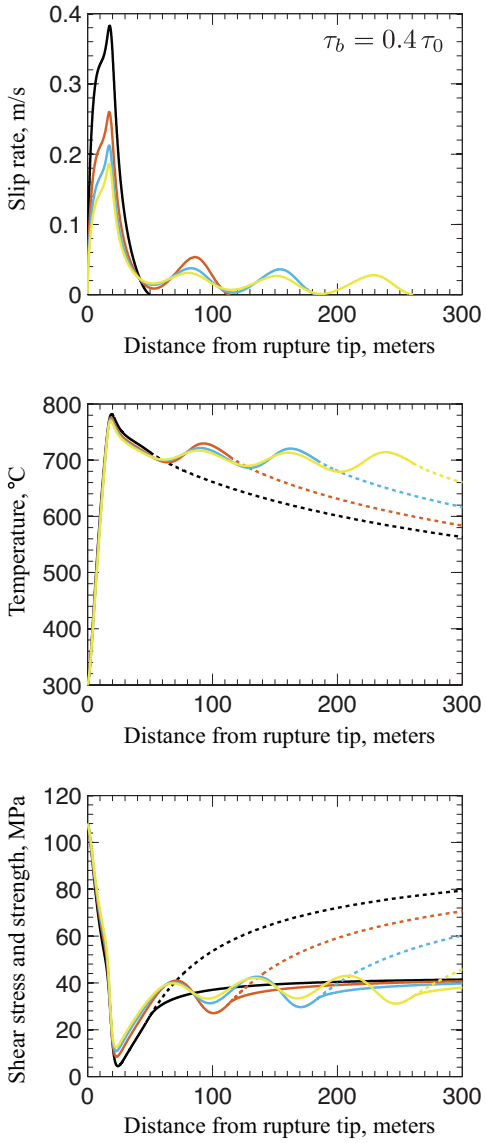

Figure 5.12: A plot showing the along-fault slip rate, temperature, and shear stress and strength for the train-like slip pulses with one, two, three and four peaks. These results we produced using the parameters in Table 5.1, a deforming zone thickness $W = 3$ mm, and a driving stress of $\tau_b = 0.4\tau_0$. In the temperature plot the dashed lines indicate the temperature evolution of the fault after slip ceases. In the shear stress plot the dashed lines show how the strength evolves after slip ceases. These solutions correspond to a single reaction being triggered multiple times within a single slip pulse. Note the similarity between the solutions, for example the two-peak solution looks similar to the first two peaks in the three-peak solution.

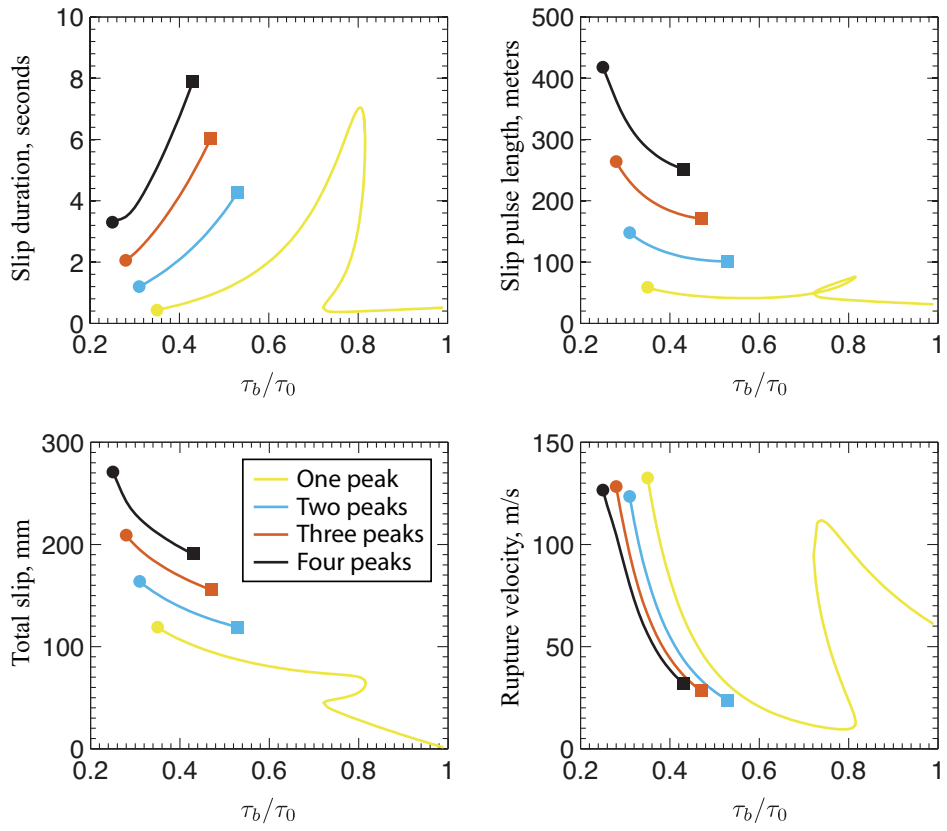

Figure 5.13: A plot showing how the slip duration, slip pulse length, total slip and rupture velocity vary with driving stress for the train-like slip pulses with one, two, three and four peaks. These results we produced using the parameters in Table 5.1 and a deforming zone thickness $W = 3$ mm. The curves are terminated when the pore pressure exceeds the normal stress, which is denoted by a circle, and where the slip rate becomes negative, which is denoted by a square. We see that the slip pulses with more peaks have larger slip durations, slip pulse lengths and total slips, but the rupture velocity is relatively consistent between all four solutions.

Next we see how the rupture properties vary with driving stress for the four solutions, shown in Figure 5.13. We see that adding more peaks to the solution increases the slip duration, slip pulse length, and total slip, and slightly reduces the rupture velocity. The more complex solutions appear to exist only for a narrow range of driving stresses, with the maximum pore pressure exceeding the normal stress for lower driving stresses and the slip rate becoming negative for higher driving stresses. We found that the range of driving stresses for which the solutions with multiple slip rate peaks exist increases as the deforming zone thickness W increases, leading to the choice of $W = 3$ mm used to find the solutions shown in Figure 5.12. As before we have discounted solutions with $V < 0$ – suggesting that a portion of the fault is slipping in the opposite direction to the applied shear stress – as they are unphysical. The physical significance of these solutions is still unclear, and we do not know if it would be possible to arrive at a propagating rupture that triggers the reaction multiple times in a time-dependent dynamic rupture model that allows for solutions that are not steady slip pulses.

5.7 Discussion

5.7.1 Thermal decomposition during dynamic rupture

In this paper we presented the first dynamic rupture models to account for thermal decomposition. We found that the activation of thermal decomposition leads to distinctive features in the rupture properties, with longer rupture durations and larger total slips. In addition, our calculations showed that thermal decomposition should lead to lower rupture velocities and larger slip pulse lengths, though we think this may be an artifact of our decision to solve for steadily propagating self-healing slip pulses. Along with studying the

rupture properties, we also showed that thermal decomposition can lead to a distinctive along-fault slip rate profile. For intermediate values of τ_b – where the influence of thermal decomposition is most pronounced for steady slip pulses – the peak slip rate occurs towards the trailing edge of the pulse, coinciding with the onset of the reaction. Since all other dynamic weakening mechanisms lead to peak slip rates at the rupture tip, this along-fault slip rate profile makes thermal decomposition unique.

The distinctive nature of thermal decomposition may allow it to be identified in seismic observations. While it may never be possible to image details such as along-fault slip rate profile, it may be possible to see variations in slip duration, which our results suggest will change dramatically if thermal decomposition is triggered. It may also be possible to observe a seismic signature for thermal decomposition by studying the propagation of an earthquake across the equilibrium phase boundary for a reaction. For depths above the equilibrium phase boundary thermal decomposition may be an important dynamic weakening mechanism, while below the phase boundary it will produce no weakening.

Our results show that the balance between thermal pressurization and thermal decomposition can change significantly with the background stress on the fault. We found that thermal decomposition is most active at intermediate background stress, though this may be an artifact of the decision to look only for self-healing steady slip pulses. Regardless of this, our results definitively demonstrate that thermal decomposition can be an important dynamic weakening mechanism in a dynamically propagating rupture.

One problem we encountered frequently was the tendency for thermal decomposition to drive the pore pressure above the normal stress. Due to the uncertainty over what the mechanical response of the fault will be when the pore pressure exceeds the normal stress

we decided to consider all slip pulses with $p > \sigma_n$ unphysical. We expect this problem to occur frequently when thermal decomposition is accounted for in other more complex dynamic rupture models, and not just in our model for steady slip pulses. While preparing this paper we produced some additional solutions that accounted for the dependence of permeability on effective stress. Assuming a semi-log dependence of permeability on effective stress commonly seen in laboratory measurements – for example *Wibberley and Shimamoto* [2003][243] – we found this feedback was almost always able to limit the pore pressure to values lower than the normal stress. Since the Green's function approach used to produce the majority of the results in this paper is not valid when the hydraulic diffusivity depends on pore pressure, these simulations were performed using the finite difference procedure outlined in Appendix C.3. We advocate including this dependence of permeability on effective stress in future rupture models accounting for thermal decomposition.

The coupling between pore pressure and permeability also produced interesting results for thermal pressurization alone, and appeared to show that the initial weakening that begins at the ambient pore pressure and the re-strengthening due to hydraulic diffusion that happens at higher pore pressures are governed by different values of the hydraulic diffusivity. This effect is particularly pronounced for slip pulses at low driving stresses, since these slip pulses experience the largest pore pressure changes.

All of the parameters choices in this paper were designed to trigger thermal decomposition over some range of τ_b. However, many simulations failed to activate thermal decomposition, allowing us to determine when and where thermal decomposition is likely to be activated. We found that the activation of thermal decomposition is controlled by the ambient temperature T_a, the temperature rise during thermal pressurization alone which is

approximately $\bar{\sigma}_a/\Lambda$, and the kinetic parameters A and Q. The kinetic parameters determine at what temperature the reaction is activated, the ambient temperature controls how far the initial state is from this reaction temperature, and the temperature rise $\bar{\sigma}_a/\Lambda$ determines if the slip pulse can bridge this temperature gap and trigger the reaction. Our simulations showed that if we assume the parameters in Table 5.1 then decarbonation of calcite is common when the depth is 10 km or greater. However, if we choose $\Lambda = 0.9$ MPa/K – a value *Rice* [2006][186] showed is in good agreement with lab measurements – then our slip pulse solutions will not trigger thermal decomposition at any points in the seismogenic zone. Similarly we found that if $\bar{\sigma}_a = 126$ MPa – corresponding to a pore fluid pressure that tracks the lithostatic gradient below a depth of 7 km – then decarbonation is not activated for any background stresses at a depth of 10 km. It is important to note that these conclusions about the depth at which thermal decomposition is triggered may change dramatically in a more realistic time-dependent rupture that may have a larger total slip, and thus a higher temperature rise.

5.7.2 The possibility of multiple rupture modes

Our results show that when thermal decomposition is accounted for there can be several different ways to propagate a steady slip pulse. To begin we showed that often for intermediate values of τ_b there are three ways to balance thermal pressurization and thermal decomposition when propagating a steady slip pulse. Following this we showed that it is possible for a single reaction to be activated multiple times, leading to a rupture mode that looks like a train of slip pulses. We note that train-like rupture modes have been observed before[48,131,209], though all of these solutions assumed a rate-and-state friction law at the slid-

ing surface, and our train-like solutions are the first to be driven by dynamic weakening mechanisms thought to be active during seismic slip.

Given this complexity, it is not clear how a fault would select from this range of possible rupture modes. There is also the possibility that a rupture switches between different modes, possibly by only activating thermal decomposition on discrete parts of a fault. Another possibility is that a fault selects different rupture modes in different events, explaining how a single fault could host large and small earthquakes. If the rupture mode is selected by the manner of nucleation then it is important to properly couple models for dynamic weakening to realistic models for nucleation. Such complexity may exist when other dynamic weakening mechanisms are coupled, and our results highlights the need for thorough parameter sweeps when modeling earthquake ruptures.

5.7.3 Dependence on important parameters

In this subsection we highlight the four parameters that exert the greatest control over our system, beginning with the deforming zone thickness W. By studying self-healing slip pulses driven by thermal pressurization alone *Garagash* [2012][86] was able to define a parameter h_{dyna} and show that when the deforming zone thickness is less than or comparable to h_{dyna} the slip pulse propagates seismically, and when the deforming zone thickness is much greater than h_{dyna} the slip pulse propagates aseismically. *Garagash* [2012][86] also showed that the slip duration and total slip increase with the deforming zone thickness. Our simulations show that the conclusions in *Garagash* [2012][86] are still valid when thermal decomposition is accounted for. The majority of the change in rupture properties with W is the result of how W changes T^* and δ_c, which scale the slip duration and total slip respectively,

allowing our results to be extrapolated to deforming zone thickness not shown here. These dimensionless plots shows that increasing W makes the reaction slightly more vigorous, in agreement with our observation that as the deforming zone thickness increases the range of background stress for which the maximum pore pressure exceeds the normal stress grow. We believe this increased tendency for pore pressures to exceed the normal stress occurs because it is harder for hydraulic and thermal diffusion to relieve elevated pore pressures and temperatures in a wider deforming zone.

The sensitive dependence of the rupture properties on W highlights the importance of modeling strain localization during an earthquake. *Rice et al.* [2014][189] and *Platt et al.* [2014][166] showed that thermal pressurization leads to significant strain localization at the onset of deformation, and *Platt et al.* [*submitted*][167] showed that the onset of thermal decomposition drives additional localization. Physical intuition suggests that if the deforming zone thins at the onset of thermal decomposition then hydro-thermal diffusion will become more efficient when the reaction is triggered, possibly offsetting a large amount of the increase in slip duration predicted by this paper.

Rice et al. [2014][189], *Platt et al.* [2014][166], *Platt et al.* [*submitted*][167] also showed that the localized zone thickness should evolve as the slip rate changes during a rupture. This could have interesting feedbacks with the large variations in slip rate in our slip pulse solutions, possibly slowing re-strengthening due to hydraulic diffusion as the slip rate approaches zero near the trailing edge of a slip pulse. These hypotheses could be tested by coupling the model for a self-healing slip pulse presented in this paper with the type of calculations used to model strain localization in *Rice et al.* [2014][189], *Platt et al.* [2014][166], *Platt et al.* [*submitted*][167], but this is complicated by the specific rate-strengthening friction law assumed

by these localization models. Equation (3) from *Platt et al.* [2014][166] shows that the friction coefficient vanishes ahead of the slip pulse and thus the fault has zero strength. It may be possible to get around this by accounting for state evolution in the localization calculations. Another option may be to alter the slip pulse model to allow a small but finite slip rate to occur everywhere on the fault, instead of setting $V = 0$ for $x \notin [0, L]$.

Our simulations show that the amount of weakening generated by a specific reaction is controlled by the ratio P_r/E_r. We found that increasing P_r by a factor of two produces results that are similar to the results found when E_r is decreased by a factor of two. Furthermore we presented a physical motivation for the importance of this ratio based upon the assumption that the temperature changes slowly when thermal decomposition is active. We showed that P_r/E_r plays a role similar to that played by Λ in classic models of thermal pressurization. It is no coincidence that the units of the ratio P_r/E_r – MPa/K – are the same as the units of Λ. Also note that the same ratio appears in *Platt et al.* [*submitted*][167] in the formula for the localized zone thickness when thermal decomposition is active, and plays the same role that Λ does in the low-temperature limit dominated by thermal pressurization.

Having demonstrated the importance of the ratio P_r/E_r we can now predict which decomposition reactions will drive the most weakening. We find that all of the dehydration reactions listed in *Platt et al.* [*submitted*][167] lead to values of P_r/E_r of approximately ten. This agrees with preliminary self-healing slip pulse solutions found using the parameters from *Platt et al.* [*submitted*][167] modeling the dehydration of lizardite that showed a pronounced signature of thermal decomposition, pore pressures exceeding the normal stress over a wide range of background stresses, and slip durations longer than those found using

the parameters modeling the decarbonation of calcite.

It is important to note that the use of P_r/E_r to estimate the potency of a thermal decomposition is only valid when reactant depletion is negligible, and that reactant depletion is controlled by the total temperature that can be buffered by the reaction $\bar{m}E_r$. We showed that the large value of E_r makes reactant depletion negligible for the decarbonation of calcite, but depletion is expected to be important for the dehydration reactions listed in *Platt et al.* [*submitted*][167]. Our model could easily be extended to account for reactant depletion, and this may provide another mechanism to limit the pore pressure to values lower than the normal stress. The sudden loss of weakening associated with reactant depletion may also provide another way to get rapid re-strengthening at the trailing edge of a slip pulse. The solid volume change associated with reactant depletion may also lead to additional strengthening by increasing the hydraulic diffusivity.

Another important parameter that dictates the impact of thermal decomposition is the ratio of the hydraulic and thermal diffusivities, $\chi = \alpha_{hy}/\alpha_{th}$. Figure 5.7 shows that the signature of thermal decomposition becomes much more pronounced as χ increases. We see that for $\chi = 0.5, 3$ the range of background stresses with multiple solutions vanishes, and for $\chi = 0.5$ the results look qualitatively the same as for thermal pressurization alone. This is in stark contrast with the results for thermal pressurization alone, which showed a very modest dependence on χ. We believe χ plays such an important role by controlling the amount of time spent at the peak temperature. The efficient thermal diffusion associated with low values of χ will shorten the amount of time spent at the peak temperature, and decrease the total weakening thermal decomposition can deliver.

This dependence on χ will be important when trying to predict how thermal decom-

position will operate at different depths in the seismogenic zone. We expect α_{hy} to fall significantly as the depth increases while α_{th} remains roughly constant. This means χ will decrease with depth and for a given reaction the signature of thermal decomposition would be most distinctive in shallow ruptures.

The final parameter that plays the largest role in controlling the balance between thermal pressurization and thermal decomposition is the background stress on the fault τ_b. Our results show that the balance between thermal pressurization and thermal decomposition can change dramatically as τ_b changes. However, this observation may not be physically realistic, and may be an artifact of our decision to only search for self-healing steady slip pulses. Thermal decomposition cannot be triggered in the slip pulses found at the highest values of τ_b because the weakening provided by the reaction would be so large that healing would be impossible. In contrast, the non-steady rupture simulations in *Noda et al.* [2009][155] showed that the peak temperature rise increases with driving stress, suggesting that we should expect thermal decomposition to be most prevalent at the highest background stresses. Even if the steady self-healing pulse constraint is not realistic, we still believe that the balance between thermal pressurization and thermal decomposition will change with background stress in more realistic rupture models.

5.7.4 Relationship between steady slip pulses and time-dependent ruptures

One of the major limitations of our model is that we only solve for steadily propagating slip pulses, and it is not clear how these steady solutions relate to a time-dependent rupture that nucleates at a point on the fault and then propagates along the fault. The dynamic rupture simulations presented in *Noda et al.* [2009][155] did not produce steadily propagat-

ing slip pulses, instead finding only growing slip pulses, decaying slip pulses and crack-like ruptures. *Noda et al.* [2009][155] also found that the transition from decaying pulse to growing pulse occurred over a very narrow range of background stress (see Figure 4 in *Noda et al.* [2009][155]), possibly indicating that steadily propagating slip pulses could only exist for a very narrow range of background stress. *Gabriel et al.* [2012][84] studied the boundary between growing and decaying pulses in more detail, and managed to find pulses that propagated steadily for the entire length of the rupture simulation. *Gabriel et al.* [2012][84] also showed that the steady pulses form the boundary between growing and decaying slip pulses in parameter space. Both *Noda et al.* [2009][155] and *Gabriel et al.* [2012][84] suggest that the steady pulses are not stable, and thus a time-dependent rupture model will not select one of the steady pulse solutions presented here. However, it is important to note that neither *Noda et al.* [2009][155] nor *Gabriel et al.* [2012][84] accounted for thermal decomposition. It is possible that the complicated phase diagram shown in Figure 5.4 may lead to steady pulses that are stable, though this can only be tested using a non-steady rupture accounting for thermal decomposition.

Even if the steady slip pulse solutions never occur in more realistic rupture models we expect many of our conclusions to hold. We still expect the activation of thermal decomposition to lead to a longer slip duration and a larger total slip. Furthermore we expect P_r/E_r to control the additional weakening triggered by the onset of thermal decomposition, and χ to control the amount of time spent at the peak temperature.

5.8 Conclusions

In this paper we produced the first dynamic rupture simulations to account for thermal decomposition. We studied the balance between thermal pressurization and thermal decomposition, showing that this balance can change significantly with driving stress. In addition, we demonstrated that thermal decomposition can provide as much total weakening as thermal pressurization during a dynamic rupture.

Our results show that the activation of thermal decomposition significantly alters the rupture properties, and leads to longer slip durations and larger total slips. Furthermore we showed that for some background stress thermal decomposition leads to distinctive along-fault slip rate profiles with peak slip rates near the trailing edge of the slip pulse, coinciding with the onset of the reaction.

We showed that accounting for thermal decomposition allows multiple self-healing slip pulses. Some of these solutions correspond to different balances between thermal pressurization and thermal decomposition, while other solutions correspond to triggering a single reaction multiple times. The wide range of possible rupture modes highlights the importance of coupling models for dynamic rupture with realistic models for nucleation, which may allow us to determine which of the many rupture modes is selected by a fault.

Based on our results we highlighted two key parameters that are expected to control the impact of thermal decomposition. First, we showed that the additional weakening associated with thermal decomposition is largely controlled by the ratio P_r/E_r, which balances the amount of pore pressure generated with the amount of energy absorbed by the reaction. We presented a physical motivation for this ratio and used this ratio to evaluate the

potency of different decomposition reactions. Second, we showed that the ratio of hydraulic and thermal diffusivities χ plays an important role in controlling the amount of weakening produced by thermal decomposition. This is in stark contrast with the results for thermal pressurization alone, which are insensitive to changes in χ.

This project was a collaboration with Jenny Suckale, Thibaut Perol, and James R. Rice. The numerical simulations presented in this paper were performed by Jenny Suckale, who was also the primary author of the resulting manuscript. My role involved developing the model, helping to use the analytic solution to benchmark the numerical simulations, and analyzing the results of the numerical simulations, all of which were done in collaboration with Jenny, Thibaut and Jim. The work in this chapter has already been published and the relevant citation is: Suckale, J., J. D. Platt, T. Perol, and J. R. Rice (2014), Deformation-induced melting in the margins of the West Antarctic ice streams, Journal of Geophysical Research, 119, 1004-1025.

6

Deformation-induced melting in the margins of the West-Antarctic ice streams

6.0 Abstract

Flow of glacial ice in the West Antarctic Sheet localizes in narrow bands of fast flowing ice streams bordered by ridges of nearly stagnant ice, but our understanding of the physical

processes that generate this morphology is incomplete. Here, we study the thermal and mechanical properties of ice-stream margins, where flow transitions from rapid to stagnant over a few kilometers. Our goal is to explore under which conditions the intense shear deformation in the margin may lead to deformation-induced melting. We propose a 2D model that represents a cross-section through the ice-stream margin perpendicular to the downstream flow direction. We limit temperature to the melting point to estimate melt rates based on latent heat. Using rheology parameters as constrained by laboratory data and observations, we conclude that a zone of temperate ice is likely to form in active shear margins.

6.1 Introduction

The West-Antarctic Ice Sheet is thought to lose over 80% of its mass[5] through outlet glaciers and arterial drainage routes called ice streams, which are typically about a kilometer thick, tens of kilometers wide and hundreds of kilometers long. Contrary to outlet glaciers, topography cannot fully explain the location of the fast-flowing ice streams in the Ross Ice Shelf, Antarctica[202,203]. Further evidence that ice-stream width is not controlled by topography alone comes from evidence that some margins have shifted in the past[114,47,73,115] or are migrating currently[19,99,69]. These observations suggest that a physical mechanism must exist that selects the location of the margin and the flow speed of the stream self-consistently.

The Ross Ice Streams rest on weak and unconsolidated sediment, commonly referred to as till, which overlays former seafloor[64,224]. Drilling into several active ice streams has confirmed near-lithostatic fluid pressure in the till below the ice streams[120,121], and inverse methods have shown that the till layer is nearly everywhere weak[119]. These findings imply that

only a very modest shear stress can be supported by the bed and highlight that till deformation is probably the primary mechanism that allows ice streams to move rapidly despite relatively small gravitational stresses[3]. Measurements of shear stresses in the margins of the Ross Ice Streams[118] and a laboratory study of ice cores retrieved from depth[113] confirmed that a significant portion of the driving stress is balanced by stresses on an approximately vertical interface parallel to the edge of the ice stream. We refer to these lateral boundaries of ice streams, where the surface velocity drops by two to three orders of magnitude over as little as a few kilometers, as the shear margins.

While force-balance considerations clarify that shear margins play an important role in ice-stream dynamics[241,113,99,242,119], if probably to a different degree for different streams[174], they do not offer any direct insights into the mechanism through which the margin affects the ice-stream flow. One possibility is that shear margins represent not only the transition from fast to slow flow, but may also coincide with the boundary between temperate and frozen conditions at the bed[116,199]. One problem with this idea is that even a small perturbation in ice-stream width would lead to either run-away growth or to stoppage of an ice stream[116]. *Schoof* [2004][198] questioned the assumption that the transition between a temperate and a frozen bed determines, or even coincides with, the position of the shear margin. As previously suggested by *Raymond* [1996][173], *Schoof* [2004][198] invokes a spatially variable yield stress in the till layer, analogous to Barenblatt-Dugdale concepts in fracture mechanics[183,184], but does not offer an explanation for the assumed functional forms of the yield stress along the glacial bed.

The goal of this study is to investigate the possibility of deformation-induced melting in active shear margins. There are two reasons why melting and the associated presence

of meltwater in ice-stream margins might have important consequences for the dynamics of ice streams. First, glacial till can be approximated as a Coulomb plastic material with a yield strength that is strongly dependent on porosity, which is controlled by the water content for full saturation[112,225,172] and diminishes with effective pressure[120,112,226] in agreement with critical-state soil mechanics[196]. The sensitive dependence of shear strength on water content suggests that the spatial variability of basal stress and the positions of the shear margins could be intricately linked to meltwater generation. Second, if significant quantities of meltwater are produced in the margin, the water may accumulate in a channelized drainage system as pointed out by *Perol and Rice* [2011][161]. The presence of a channel alters both the basal stresses outside of it and the pore-pressure distribution in its vicinity, which could contribute to locking of the bed of a widening stream.

The possibility that the shear margins of active ice streams may be temperate has been pointed out before[116,9], but it remains unclear how pervasive melting is. *Perol and Rice* [2011][161] suggested that the shear-strain rates measured by *Joughin et al.* [2002][118] for the five Ross Ice Streams are consistent with internal melting for all stream margins except the currently inactive Kamb Ice Stream. However, their model based on a 1D heat-transfer model was not versatile enough to include ice advection perpendicular to the margin. While observational evidence constraining the thermal properties of shear margins at depth is scarce, *Clarke et al.* [2000][47] identified a prominent bottom diffractor extending to about 230 m above the bed in the ice sheet close to Unicorn ridge (Figure 6.1), which they interpreted as a delineation of a zone of wet and reflective ice. Further, drilling into the currently inactive Kamb Ice Stream margin revealed flowing water in a 1.6 m cavity between the bottom of the ice sheet and its bed[236].

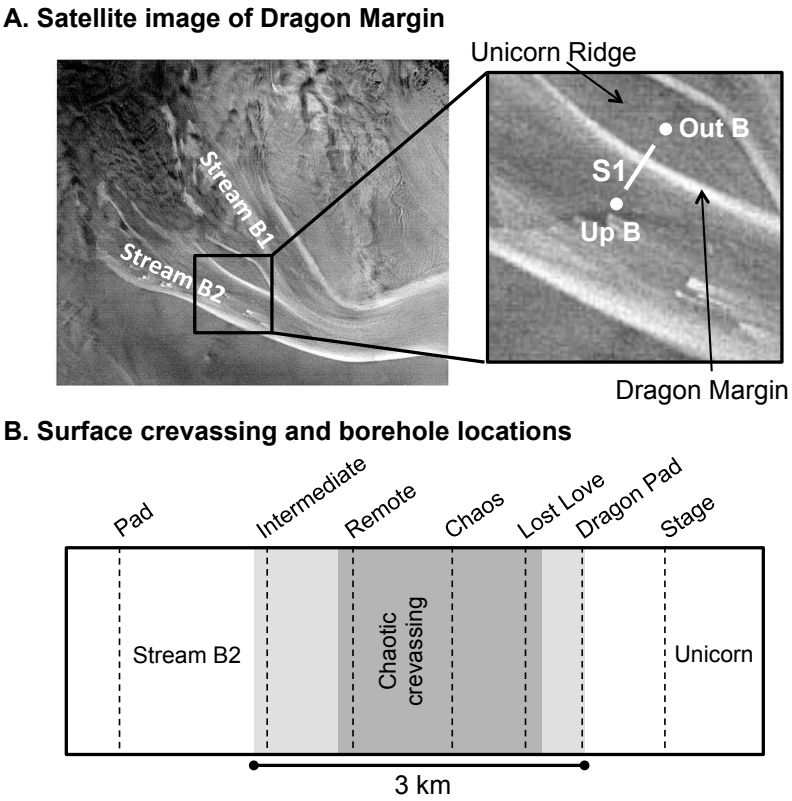

Figure 6.1: A: The left panel shows a satellite image of the confluence between ice streams B1 and B2 in the upstream portion of Whillans Ice Stream, taken by the Radarsat Antarctic Mapping Project. The right panel is a detailed view of Dragon margin, Unicorn ridge and the profile S1 along which *Echelmeyer and Harrison* [1999][69] measured surface velocities and *Harrison et al.* [1998][99] reported temperature for the upper few hundred meters. We have highlighted the positions of the two outermost boreholes, "Out B" and "Up B", used in *Harrison et al.* [1998][99]. B: Approximate locations of the seven boreholes in the vicinity of the shear margin with respect to surface crevassing (after *Harrison et al.* [1998][99]). The dark grey area represents the roughly 2 km-wide zone of chaotic crevassing. The light grey zones exhibit less intense crevassing.

Here, we devise a 2D thermomechanical model of an ice stream moving over a plastic bed in steady state. We consider a cross-section through the ice-stream margin perpendicular to the downstream flow direction and analyze the effect of the anti-plane shear stress components on the mechanical equilibrium and energy dissipation. Our ice rheology takes

multiple creep mechanisms into account, which dominate at different stress levels. In addition to diffusion and advection of heat, we include the temperature dependence of material properties and a simplified representation of surface crevassing assuming a temporally steady state of stress and flow velocity. To estimate melt rates based on latent heat, we limit temperature to the melting point and estimate melt rates based on latent heat. As detailed in Appendix D.1, we solve the governing equations numerically using finite differences for a Cartesian grid with three refinement levels after carefully benchmarking our computational technique against approximate analytical results.

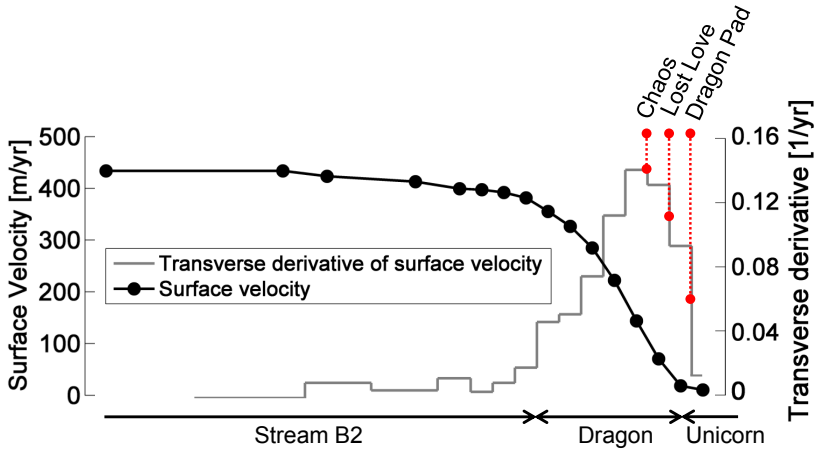

Figure 6.2: Surface velocities across Dragon margin as measured by *Echelmeyer and Harrison* [1999][69] and the transverse derivative of surface velocities, $\mathrm{d}u/\mathrm{d}y$, computed from the measured surface velocities. Highlighted in red are the approximate transverse velocity derivatives for boreholes "Dragon Pad", "Lost Love", and "Chaos" quoted from *Harrison et al.* [1998][99].

Our model is intended as a representation of the Ross Ice Streams. Despite the general scope of the model, we chose the southern margin of Whillans Ice Stream B2, commonly referred to as Dragon margin (Figure 6.1), as a specific test case for our study. Dragon margin is located near research camps and skiways and has been studied extensively. The two

most important data sets for our purposes are detailed observations of surface velocities[68,69] and temperature measurements from nine boreholes distributed across Dragon margin[99] (Figure. 6.2). In addition, *Jackson and Kamb* [1997][113] measured the enhancement factor at Dragon margin to fit the observed rheology with the standard parameterization of Glen's Law, and *Clarke et al.* [2000][47] provided valuable insights into the complex deformational history of the area over the last few hundred years.

6.2 Model setup

We consider a slab of ice flowing in the downstream direction x (Figure 6.3). The height coordinate, z, is taken positive upward from the base of the ice. In the transverse direction, the ice stream extends from the left boundary of the domain to its center ($-W/2 \leq y \leq 0$) and the ridge from the center to the right boundary of the domain ($0 \leq y \leq W/2$). The left boundary of our modeling domain thus coincides with the middle of the stream, and the origin of our coordinate system ($y = 0, z = 0$) represents the transition point from slipping to locking at the bed, indicated as a black dot in Figure 6.3. We do not explicitly model the process that would lead to such a transition. We distinguish the locked-to-sliding transition point from the shear margin itself, which constitutes the ice column at the lateral boundary of the stream where the surface velocity of ice increases rapidly over a few kilometers. We assume negligible variation of ice-sheet thickness in the transverse direction (along the y axis) and neglect topography at the bed such that the ice surface is parallel to the bed. We also neglect downstream variation of ice properties and flow speed u, which reduces our model to two dimensions, and assume a lithostatic pressure field.

6.2.1 Mechanical model

The only free variable of our mechanical model is the downstream velocity $u(y, z)$, which reduces the conservation of momentum (or static equilibrium in this case) to

$$\frac{\partial}{\partial y}\left(\mu\frac{\partial u}{\partial y}\right) + \frac{\partial}{\partial z}\left(\mu\frac{\partial u}{\partial z}\right) + \rho g \sin\alpha = 0, \tag{6.1}$$

where ρ is the ice density, g is the acceleration due to gravity, α is the inclination angle of the ice, and μ is the temperature- and strain rate-dependent effective dynamic viscosity. Accordingly, we assume that the strain rate tensor $\dot{\boldsymbol{\epsilon}}$ and the deviatoric stress tensor $\boldsymbol{\tau}$ have only two non-negligible components, the shear strain rates and shear stresses in horizontal ($\dot{\epsilon}_{xy}$ and τ_{xy}) and vertical ($\dot{\epsilon}_{xz}$ and τ_{xz}) directions on a face where x is constant. Note that by reducing our analysis to anti-plane deformation as in equation (6.1), we inevitably neglect small components of in-plane deformation that must accompany the marginal melting and drainage that we later infer.

The stream-ridge system in Figure 6.3 is underlain everywhere by a thick layer of glacial till. Underneath the ice stream, the till is failing in shear, which justifies equating the basal shear stress, τ_{base}, underneath the ice stream with the yield stress. In the interest of simplicity, we assume that the basal stress is constant. Underneath the ridge, we assume that the shear stress at the ice-till interface does not exceed the yield stress, implying that failure and sliding do not occur. The full details that explain locking are yet to be fully understood.

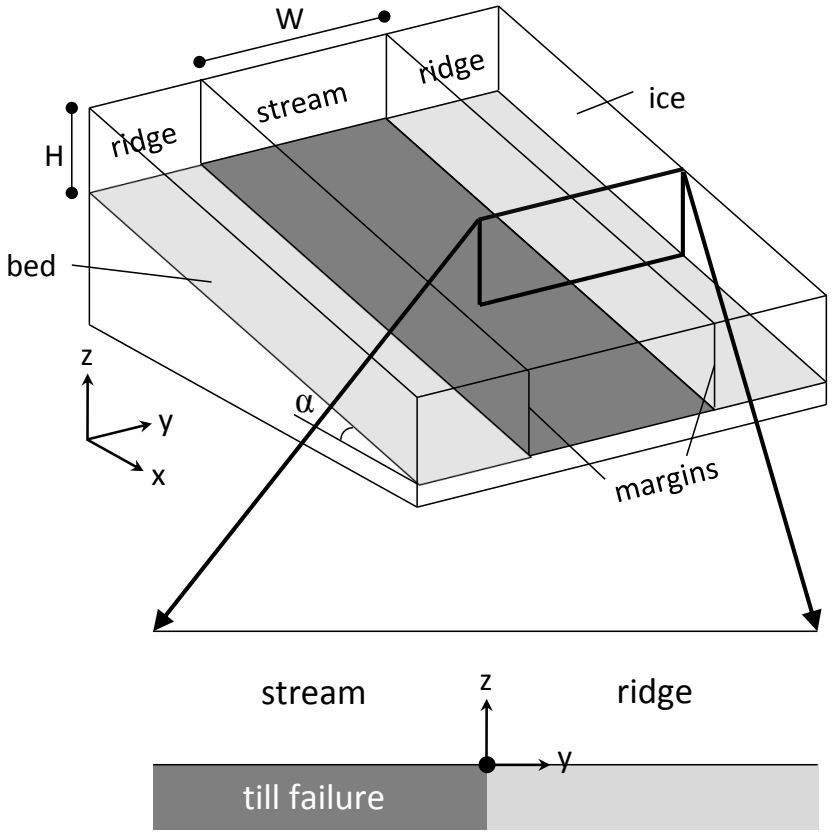

Figure 6.3: Simplified geometry of our model setup. The ice thickness is H and the total width of the stream is W. The 2D setup (bottom) is equivalent to assuming a 3D stream-ridge geometry with no downstream variation (top).

The appropriate boundary conditions at the bed are then

$$\tau_{xz} = \tau_{base} \quad \text{at} \quad z = 0,\, y \leq 0 \tag{6.2}$$

$$u = 0 \quad \text{at} \quad z = 0,\, y > 0\,. \tag{6.3}$$

The ice surface is assumed to be stress free. On the sides of the modeling domain, we use symmetric boundary conditions, implying an infinite juxtaposition of ice streams and

ridges. Later, we estimate τ_{base} to best match measured surface flow rates and borehole temperature profiles.

The boundary conditions defined in equations (6.2) and (6.3) imply a stress singularity at the bed ($z = 0,\ y = 0$). This singularity is caused by the assumed till rheology, which posits that till transitions from locking to yielding almost discontinuously. The extreme stress concentration at the locked-to-sliding transition in the shear margin has important ramifications for understanding ice-stream dynamics because it implies an inherent instability in which ice streams that experience slight perturbations might be prone to instability[116]. That being said, it is possible that the singularity would be smoothed out by melting, as discussed later in detail, or a Dugdale-Barenblatt cohesive zone.

6.2.2 Ice rheology

There is no single mechanism that captures how ice deforms over a wide range of stresses[53]. For our modeling domain, which encompasses both high and low stress conditions, we approximate the rheology of ice as a combination of diffusional creep $\dot{\boldsymbol{\epsilon}}_{\boldsymbol{D}}$ and Glen's Law $\dot{\boldsymbol{\epsilon}}_{\boldsymbol{G}}$

$$\dot{\boldsymbol{\epsilon}} = \dot{\boldsymbol{\epsilon}}_{\boldsymbol{D}} + \dot{\boldsymbol{\epsilon}}_{\boldsymbol{G}}\,. \tag{6.4}$$

Diffusional creep

$$(\dot{\epsilon}_D)_{ij} = \frac{42\Omega}{k_B T d^2} B \exp\left(-\frac{Q}{RT}\right) \tau_{ij} \tag{6.5}$$

dominates the deformational behavior of ice at low stresses, and Glen's Law

$$(\dot{\epsilon}_G)_{ij} = AE \exp\left[-\frac{Q}{R}\left(\frac{1}{T_h} - \frac{1}{T^*}\right)\right] \tau_E^2 \tau_{ij} \tag{6.6}$$

dominates at intermediate to high stresses, where τ_E is the effective shear stress defined by the second invariant of the deviatoric stress tensor, in our case $\tau_E^2 = \tau_{xy}^2 + \tau_{xz}^2$, and $\dot{\epsilon}_E$ is the effective tensorial deviatoric strain rate, in our case $\dot{\epsilon}_E^2 = \dot{\epsilon}_{xy}^2 + \dot{\epsilon}_{xz}^2$.

The parameters specifying diffusional creep in equation (6.5) are the molecular volume $\Omega = 3.27\,10^{-29}\,\mathrm{m}^3$, the Boltzmann constant $k_B = 1.38\,10^{-23}\,\mathrm{m}^2\,\mathrm{kg}\,\mathrm{s}^{-2}\,\mathrm{K}^{-1}$, the grain size d =1-10 mm, the exponential prefactor $B = 9.1\,10^{-4}\,\mathrm{m}^2\,\mathrm{s}^{-1}$, the activation energy $Q = 59.4\,\mathrm{kJ\,mol}^{-1}$ and the gas constant $R = 8.314\,\mathrm{J\,K}^{-1}\mathrm{mol}^{-1}$ [81]. For Glen's Law, we follow *Cuffey and Paterson* [2010] [53] in using the pre-exponential constant $A = 3.5\,10^{-25}\,\mathrm{s}^{-1}\mathrm{Pa}^{-3}$, the temperature adjusted for the pressure effect on the melting point depression $T_h = T + p_0 P$ with $p_0 = 7 \times 10^{-8}\,\mathrm{K\,Pa}^{-1}$ and T in K and the activation energy $Q = 60\,\mathrm{kJ\,mol}^{-1}$ for $T_h < T^*$ and $Q = 115\,\mathrm{kJ\,mol}^{-1}$ for $T_h > T^*$ where $T^* = 263.15\,\mathrm{K} = -10\,^\circ\mathrm{C}$. The sum of the coefficients of τ_{ij} in equations (6.5) and (6.6) defines $1/(2\mu)$.

The rheological parameter that is most difficult to constrain is the enhancement factor. Enhancement is not a physical variable by itself but rather represents effects of grain size, impurities, fabrics and possibly other variables [53]. As a consequence, estimates for enhancement vary widely. For the specific case of Dragon margin, *Jackson and Kamb* [1997] [113] determined enhancement factors between $E \approx 1.12$ and $E \approx 2.55$ for different ice specimens retrieved from Dragon margin. Because of the significant ambiguity introduced into our model results even by this moderate variation, we set $E = 1$ for most of our computations to allow for easier comparisons. We discuss the ramifications of varying enhancement in Section 6.4.

6.2.3 Thermal model

Our thermal model captures the effect of both diffusion and advection of heat. In addition, we cap temperature at the melting point to estimate melt production based on latent heat and include the effect of cold surface air pooling in crevasses[99]. For a spatially-variable thermal conductivity k, the steady-state temperature field is thus given by

$$\frac{\partial}{\partial y}\left(k\frac{\partial T}{\partial y}\right)+\frac{\partial}{\partial z}\left(k\frac{\partial T}{\partial z}\right)-\rho c\left(v\frac{\partial T}{\partial y}+w\frac{\partial T}{\partial z}\right)+2\tau_E\dot{\epsilon}_E-L\dot{m}=0\,, \tag{6.7}$$

where v and w are the lateral and vertical advection speeds, respectively, c is the specific heat of ice, τ_E is the effective shear stress, $\dot{\epsilon}_E$ is the effective tensorial shear strain rate, L is the latent heat of ice per unit mass and $\dot{m}$ is the mass melting per unit time and unit volume. The thermal conductivity k and specific heat c vary with temperature as summarized in *Cuffey and Paterson* [2010][53]:

$$k(T)=k_1\,\exp(-k_2\times 10^{-3}\,T) \tag{6.8}$$

$$c(T)=c_1+c_2\,T\,, \tag{6.9}$$

where T is in Kelvin and the forefactors are $k_1 = 9.828\,\mathrm{W\,m^{-1}\,K^{-1}}$, $k_2 = 5.7\,\mathrm{K^{-1}}$, $c_1 = 152.5\,\mathrm{J\,kg^{-1}\,K^{-1}}$ and $c_2 = 7.122\,\mathrm{J\,kg^{-1}\,K^{-2}}$, respectively.

To compute the melt rate per unit volume $\dot{m}$ in equation (6.7), we assume that shear heating in the temperate zone is absorbed as latent heat. This assumption implies that the temperature in the temperate zone is capped at the melting point, which allows us to re-

duce equation (6.7) to the following non-linear Poisson problem:

$$\frac{\partial}{\partial y}\left(k\frac{\partial T}{\partial y}\right)+\frac{\partial}{\partial z}\left(k\frac{\partial T}{\partial z}\right)-\rho c\left(v\frac{\partial T}{\partial y}+w\frac{\partial T}{\partial z}\right)+[1-H(T-T_m)]\,2\tau_E\dot{\epsilon}_E=0\,, \quad (6.10)$$

where $H(T-T_m)$ denotes the Heaviside function. $H(T-T_m)$ is one in the temperate zone and zero outside such that $L\dot{m}$ is non-zero only in the temperate zone where it equals the shear heating $2\tau_E\dot{\epsilon}_E$.

The mechanical model set up in Section 6.2.1 solves only for the downstream velocity u. To include the horizontal and vertical velocities into our thermal model, we constrain the functional forms for both v and w a priori, assuming that the associated strain rates, stresses and work rates are negligible. Considering horizontal and vertical velocities in the thermal but not the mechanical model is, of course, strictly inconsistent. This inaccuracy is warranted by the potentially important effect that the advection of cold ice into the shear margin is likely to have on deformation-induced melting[116]. In the mechanical model, however, the strain rates associated with the horizontal and vertical velocities are two orders of magnitude smaller than the anti-plane rates, implying that the strain rate components in these directions can be neglected in $\dot{\epsilon}_E$ of the creep law and the equilibrium equation.

For the vertical advection component we assume that w varies linearly with depth[246]

$$w(y,z)=-a\frac{z}{H}\,, \quad (6.11)$$

where a is the surface accumulation rate of ice in m/yr, and a uniform contribution to w equal to the melt rate at the bed of the ice sheet is neglected. Equation (6.11) implies that accumulation of ice at the surface is compensated by downslope stretching of ice and that

basal melting or freeze-on are negligible[246], which is probably not strictly true in the shear margin.

Several studies have suggested that the position of Dragon margin has shifted in the past and may even be shifting currently with speeds on the order of $1 - 10\,\mathrm{m/yr}$[99,69] to potentially $\approx 100\,\mathrm{m/yr}$[19,47]. The simplest way to include ongoing margin migration at a constant rate into our ice-stream model is through the influx of cold ice from the ridge based on the rationale that in a coordinate system moving with the margin, outward expansion of the stream is equivalent to influx of cold ice from the ridge (as also argued in *Schoof* [2012][199]). To be consistent with the zero-slip boundary condition at the bed underneath the ridge, we impose

$$v(y,z) = v_0 \left[1 - \left(\frac{H-z}{H}\right)^4\right] \tag{6.12}$$

instead of a depth-independent horizontal velocity as suggested by *MacAyeal* [1989][139]. We performed computations with both expressions for the horizontal velocity component and found only slight differences.

Similar to the mechanical model, we use a symmetric boundary condition on the sides of the domain. On the top, we specify the surface temperature of ice (see Section 6.2.5). Underneath the stream, we assume that the bed is at the melting point as supported by observations[70]. Underneath the ridge, we do not specify a priori whether the bed is temperate or not. Instead, we adjust the geothermal heat flux G directly beneath the ice sheet such that the bed reaches a temperature of $-5\,^\circ\mathrm{C}$ at large distances from the margin in agreement with observations[190]. Depending on the computation, this condition typically requires geothermal heat fluxes on the order of $G = 48 - 85\,\mathrm{mW/m^2}$. We assume the same geothermal heat flux underneath the stream. The assumption of a finite geothermal heat

flux underneath the ice stream has no effect on the solution for the downstream velocity and temperature because the additional heating does not raise the base temperature above the melting point. It does, however, affect the total meltwater generation associated with both the geothermal heat flux and the frictional heating at the base of the ice stream (see Section 6.2.4).

6.2.4 Meltwater production

Despite the fact that our mechanical model (Section 6.2.1) entails a stress singularity, it is an integrable singularity from the standpoint of both force equilibrium and heat balance, which allows us to use the dissipation in the temperate zone to obtain an estimate for the melt rate per unit volume (see Section 6.2.3). In 2D, the mass balance for the meltwater produced in the temperate zone is

$$\frac{\partial q_y}{\partial y} + \frac{\partial q_z}{\partial z} = -\frac{2\tau_E \dot{\epsilon}_E}{L\rho_w}\,, \tag{6.13}$$

where q_y and q_z represent the meltwater flux in horizontal and vertical directions, respectively, and ρ_w is the density of water.

For simplicity, we neglect meltwater flux in the horizontal direction, $q_y = 0$, noting that we have previously assumed a hydrostatic pressure in our mechanical model (Section 6.2.1). We then integrate equation (6.13) numerically to obtain the basal meltwater flux due to shear heating in the temperate zone very simply as

$$q_{temp} = -\int_0^{H_m} \frac{\dot{m}}{\rho_w}\mathrm{dz} = -\int_0^{H_m} \frac{2\tau_E \dot{\epsilon}_E}{L\rho_w}\mathrm{dz}\,, \tag{6.14}$$

where H_m indicates the height of the temperate zone measured from the bed upwards. The possibility of a finite meltwater flux in vertical direction raises the question whether the permeability entailed by the flux we compute is consistent with measurements. Assuming that meltwater percolation occurs through Darcy's law[137] and that the water pressure in veins equals the ice overburden pressure, $\mathrm{d}p/\mathrm{dz} = -\rho g$, we estimate the permeability of the temperate ice as[161]

$$\kappa = \frac{q_{temp}\,\mu_w}{(\rho - \rho_w)g}\,. \tag{6.15}$$

The meltwater fluxes we later infer imply temperate-ice permeabilities on the order of 10^{-16} m^2, which agrees with experimental results[117].

Permeabilities in the estimated range are sufficiently high to allow for meltwater percolation to the base over the time scales considered here, and we will thus assume for the remainder of the paper that all of the water created in the temperate zone rains down to the bed. In addition to melt production from shear heating, frictional heat dissipation at the bed and the difference between heat in- and out-flux may contribute to the meltwater flux, yielding

$$q_{base} = q_{temp} + \frac{1}{L\rho_w}\left[u(y,0)\tau_{base} + G - k\frac{\partial T}{\partial z}\right]\,. \tag{6.16}$$

6.2.5 Surface crevassing

The crevassed zone at Dragon margin consists of an approximately 2 km-wide zone of intense, chaotic crevassing[237,99,69]. On the ridge side of the margin, the chaotic crevasses transition to large arcuate crevasses and on the stream-side to somewhat organized and widely spaced crevasses that tend upstream[99,69]. The crevasses are thought to extend about 30 m into the ice[99]. The location of the crevassed zone and the positions of the nine boreholes

for which *Harrison et al.* [1998][99] reported temperature measurements are reproduced in Figures 6.1A and B. *Harrison et al.* [1998][99] also indicate the transverse derivatives of the surface velocities at the three boreholes, "Dragon Pad", "Lost Love" and "Chaos" (Figure 6.2), which indicates that borehole "Dragon Pad" is located closest to the locked-to-sliding transition but on the ridge side at approximately $y = 200$ m in our modeling domain (Figure 6.3).

We represent the zone of chaotic crevassing as a 2 km-wide rectangular area in our y, z-plane that extends from the surface 30 m into the ice. We assume that the dense spacing of open crevasses lowers the effective viscosity in this area by an order of magnitude as compared to uncrevassed ice (i.e., from μ to $\mu/10$). We refer to the drop in effective viscosity as the mechanical-weakening factor. While this choice is somewhat arbitrary, we verified that the results are not sensitive to the assumed value, mostly because the crevassed zone is relatively shallow. To capture the zones of arcuate and upstream crevassing on the ridge and stream sides of the chaotic zone, we gradually lower the effective viscosity unaffected by crevassing to the mechanically weakened effective viscosity representative of chaotic crevassing over 400 m on both the stream and the ridge sides. We include the effect of cool winter air pooling in the crevasses by enforcing a surface temperature of $-34\,^{\circ}$C in the crevassed zone, which gradually increases to $-26\,^{\circ}$C in the uncrevassed ice.

There is no doubt that the representation of surface crevassing considered here is extremely simplified. A more complete model would allow the crevassed zone to evolve self-consistently instead of specifying its extent a priori. Nonetheless, we argue that the approach we have chosen here provides a reasonable first step for considering crevassing in the context of a steady-state model and is preferable to not including crevassing at all be-

cause it allows us to compare computed temperature fields to the borehole measurements from *Harrison et al.* [1998][99].

6.3 Results

To gain a better understanding of the different effects that contribute to the thermomechanics of ice streams, we start by reducing our model to its bare minimum. In its most simplistic form, the model is reminiscent of models that are amenable to analytical solution like *Schoof* [2004][198]. Then, we add in one term after another, gradually obtaining a more realistic representation of the behavior of a stream-ridge system. The sequence of effects that we consider is as follows: First, we investigate the ramifications of a temperature-dependent creep rheology. Second, we consider the ramifications of vertical and horizontal advection of cold ice into the margin. Third, we take into account crevasses along the surface expression of the margin. To quantify the explanatory potential of this sequence of approximations, we attempt to reproduce the surface velocities measured for Dragon margin[69] at each step and compare the respective fits. We limit the ambiguity introduced into our model by a large number of parameters by varying only the basal stress to fit observed surface velocities in Sections 6.3.1 and 6.3.2 while all other model parameters are fixed. We find that the best-fitting basal stresses depend sensitively on the model assumptions, which highlights the strongly nonlinear nature of the thermomechanical behavior of ice streams. When comparing our computations to the temperature data by *Harrison et al.* [1998][99] in Section 6.3.3, we additionally adjust the accumulation rate and the speed of margin migration because we are unable to obtain a satisfactory fit by focusing exclusively on basal stress.

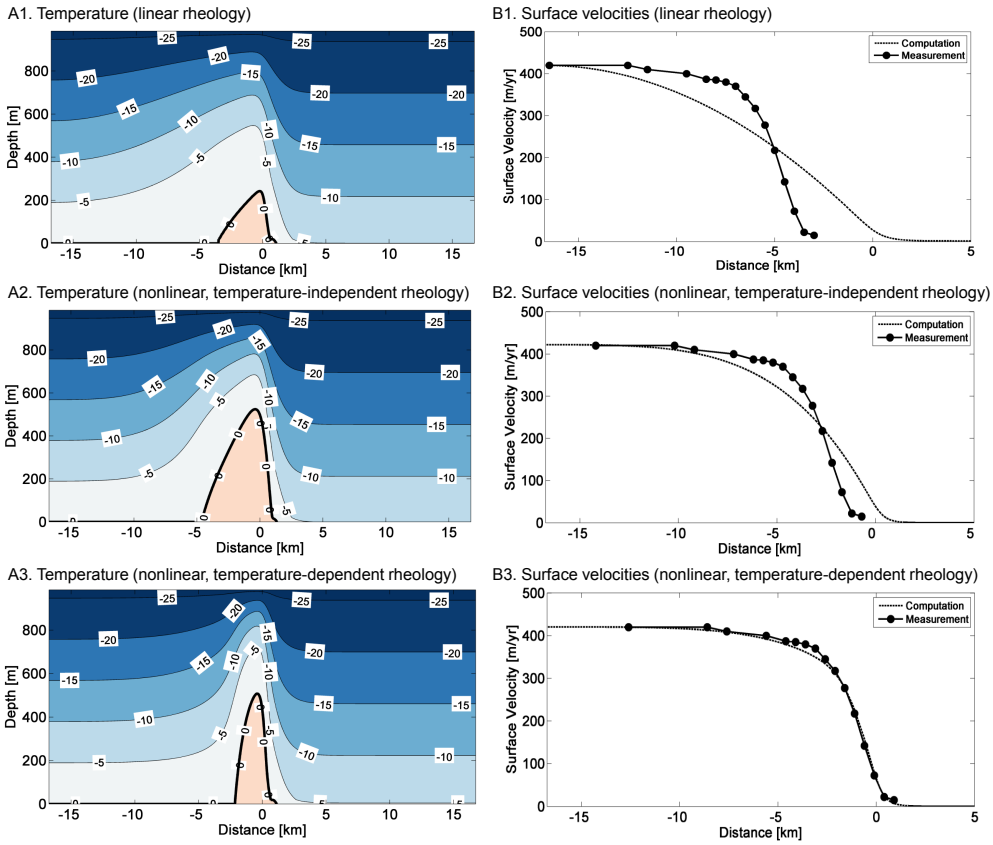

Figure 6.4: Top: Temperature field (A1) and surface velocities (B1) assuming a Newtonian rheology of $\mu = 10^{14}$ Pa s. Middle: Temperature field (A2) and surface velocities (B2) for a power-law rheology that accounts for the strain rate dependence of the effective viscosity, but neglects the temperature dependence. Bottom: Temperature field (A2) and surface velocities (B2) for a realistic rheology that captures both strain rate and temperature dependence. The best fitting basal stresses are $\tau_{base} = 2.56$ kPa (A1, B1), $\tau_{base} = 1.12$ kPa (A2, B2) and $\tau_{base} = 4.07$ kPa (A3, B3), respectively. All computations neglect advection and surface crevassing. Measured surface velocities are from *Echelmeyer and Harrison* [1999][69].

6.3.1 The importance of a temperature-dependent rheology

The most significant assumption in analytical models of ice-stream dynamics is probably the usage of a simplified rheology, such as a constant Newtonian viscosity[198,199] or a

temperature-independent power-law rheology. In this section, we quantify the ramifications of using a simplified rheology by comparing our model predictions to the surface velocities at Dragon margin observed by *Echelmeyer and Harrison* [1999][69]. All computations in this section are based on the reduced thermal model

$$\frac{\partial}{\partial y}\left(k\frac{\partial T}{\partial y}\right)+\frac{\partial}{\partial z}\left(k\frac{\partial T}{\partial z}\right)+\left[1-H(T-T_m)\right]2\tau_E\dot{\epsilon}_E=0\,, \tag{6.17}$$

which neglects the advective terms and the effect of surface crevassing as compared to the full thermal model defined in Section 6.2.3. The latter two effects are discussed in detail in the subsequent sections.

In Figure 6.4, we compare the temperate zones and predicted surface velocities for three different rheologies. We adjust the basal stress to reproduce the surface velocity in the center of the stream exactly, and then we align the computed velocity profile to minimize the mean square error in the shear margin. The computation on top (Figures 6.4A1 and B1) is based on a constant Newtonian rheology of $\mu = 10^{14}$ Pa s, which clearly gives the worst fit to observational data. The computation in the middle (Figures 6.4A2 and B2) takes the strain rate dependence of the rheology into account but neglects the temperature dependence. While this scenario is clearly more realistic than the Newtonian case, the width of the shear margin is overestimated by approximately a factor of two. Considering a realistic rheology that takes both the strain rate and the temperature dependence into account improves the fit to observations dramatically (Figures 6.4A3 and B3). The extent of the temperate zone in the last computation (Figures 6.4A3 and B3) is roughly comparable to the observations by *Clarke et al.* [2000][47].

Figure 6.5 demonstrates why the temperature dependence of the ice rheology is such an

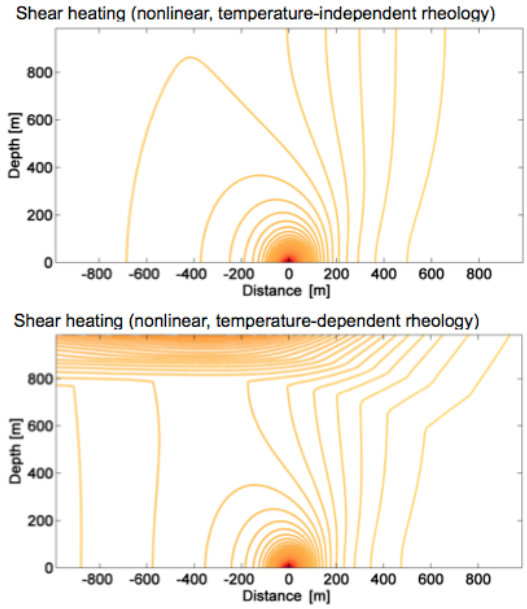

Figure 6.5: Eighty contours of constant shear heating in units of [Pa/yr] in the vicinity of the singularity when neglecting (top) and including (bottom) the temperature-dependence of the rheology.

important effect. It shows the spatial variation in shear heating in the vicinity of the singularity for the strain rate dependent rheologies (Figures 6.4A2, B2 and A3, B3). Both cases show a pronounced peak in shear heating at the slip singularity. When taking temperature into account, we find a second local maximum in shear heating at the ice surface above the singularity. The reason is that the ice is coldest on the surface, which translates into higher effective viscosity and higher shear heating than in the ice below. We conclude that the width of the high-strain region at the margin is controlled primarily by differences in the temperature of ice and thereby in its effective viscosity. To reproduce the rapid increase in surface speeds observed at Dragon margin[69], the ice in the margin has to be significantly warmer and thus weaker than the ice outside.

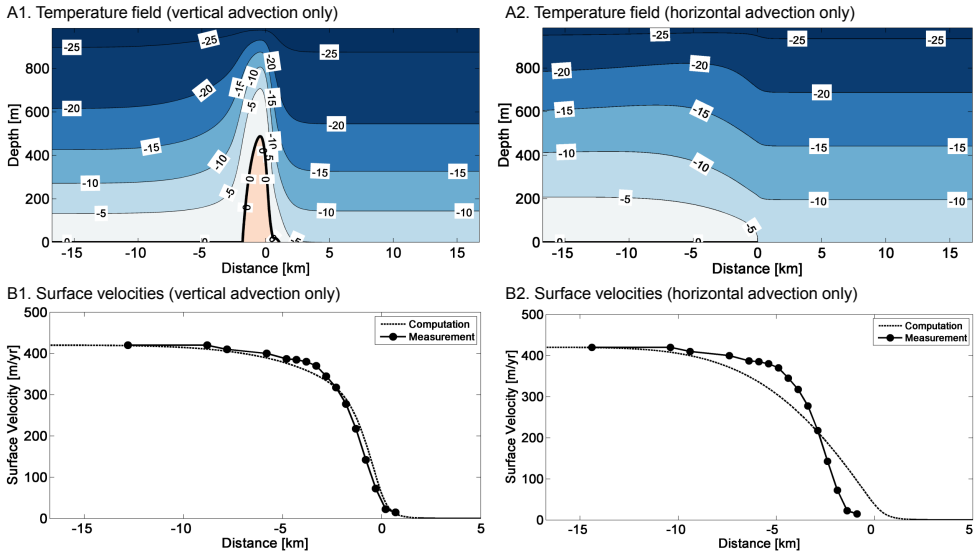

Figure 6.6: Temperature fields and surface velocities for Dragon margin when including only vertical advection (A1 and B1) with $a = 0.1$ m/yr and only horizontal advection (A2 and B2) with $v = -7.3$ km/yr, respectively. The best fitting basal stresses are $\tau_{base} = 5.31$ kPa (A1 and B1) and $\tau_{base} = 0.94$ kPa (A2 and B2), respectively. Both computations neglect surface crevassing.

6.3.2 The effect of advection

The computations in Figure 6.4 indicate that a significant portion of the ice in Dragon margin is temperate. However, both models may overestimate the volume of temperate ice because they do not consider the effect of cold ice being advected into the margin both from the surface and from the ridge. To better isolate the effect of horizontal as opposed to vertical advection, we study them through separate simulations. The thermal model we consider is thus equation (6.10) with $v = 0$ and $w = 0$, respectively.

To test the effect of vertical advection only, we first assume the same basal stress ($\tau_{base} = 4.07$ kPa) as in Figures 6.4A3 and B3. We add vertical advection assuming an accumulation of $a = 0.1$ m/yr, which is on the low end of the estimated accumulation of $0.1 - 0.2$ m/yr

for Antarctica[87,118,213]. We find that the temperate zone vanishes almost entirely. The associated surface velocities in the ice stream, however, are now much lower than observations suggest[69]. The reason is that by cooling the margin, vertical advection makes the margin stronger, and a strong margin provides more resistance against gravity than a weak one. To reproduce the observed surface velocities, we have to lower the assumed basal stress underneath the ice stream to $\tau_{base} \approx 3.17\,\text{kPa}$. Figures 6.6A1 and B1 show the resulting temperature field and surface velocities. Interestingly, the extent of the temperate zone is now comparable to that in Figure 6.4A3. We thus conclude that the main effect of vertical advection, if we insist that the surface deformation data be matched, is to slightly shift the force balance between the resistance to flow provided by the shear margin as compared to basal friction. The extent of the temperate zone in the margin changes only slightly after accounting for the different basal stress required to balance gravity. We have verified that this conclusion remains valid for accumulation rates of $a = 0.2\,\text{m/yr}$.

Observations suggest that Dragon margin is currently moving outwards at a constant speed of $7.3\,\text{m/yr}$[99], which is equivalent to including horizontal advection at $-7.3\,\text{m/yr}$, and possibly more rapidly[69]. The effect of including horizontal advection at $-7.3\,\text{m/yr}$ is shown in Figures 6.6A2 and B2. As a consequence of the lateral influx of cold ice from the ridge, the temperate zone vanishes entirely, and it becomes impossible to reproduce the rapid increase in the observed surface speed of ice in our computations. The finding that horizontal advection on the order of m/yr precludes the formation of a temperate zone is consistent with the previous study by *Jacobson and Raymond* [1998][116]. Our simulations indicate that horizontal advection with speeds on the order of $0.1\,\text{m/yr}$ are associated with finite temperate zones, albeit smaller ones than in the absence of a horizontal influx of cold

ice.

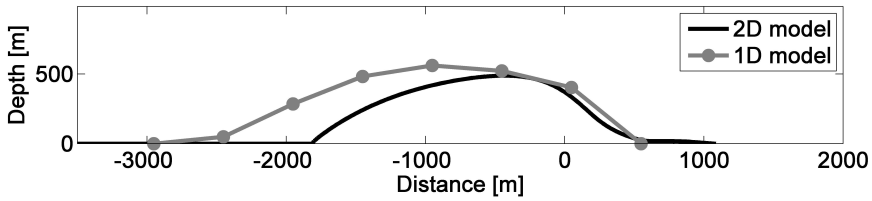

Figure 6.7: Comparison of the temperate zone from Figures 6.6A1 and B1, replotted on a 1:1 scale, with the simplified 1D model by *Perol and Rice* [2011][161] using measured surface velocities *Echelmeyer and Harrison* [1999][69] with a surface accumulation of $a = 0.1$ m/yr in both cases.

Our inability to reproduce observed surface velocities for the estimated migration speeds is clearly an important caveat. We argue that the main problem is that our simplified representation of horizontal advection does not adequately represent the physics of margin migration. The two most important concerns are: First, it is highly questionable that margin migration as rapid as several m/yr can be treated through a steady-state model. Indeed, the evidence in favor of migration of Dragon margin comes primarily from surface lineations and subsurface diffractors that indicate a complex deformational history[99,69,47] and both inward and outward migration of the margin[47]. The observational evidence thus suggest that the system has not reached a steady state. Second, Dragon margin is located close to the confluence between Ice Streams B1 and B2. The interaction between the two streams and the interjacent Unicorn ridge may be an important factor to consider in modeling the evolution of the system. An example of observational evidence that supports a non-trivial geometric connection between the two branches of Whillans Ice Stream is a hook-shaped surface lineation called "Fishhook", which connects the two streams and correlates with several near-surface strain features[47].

Nonetheless, the simulations including horizontal advection lend additional support

to our previous conclusion that Dragon margin is at least partially temperate. Our computations show that only temperate ice is weak enough to concentrate strain to the degree necessary for the surface speed to increase from approximately zero to its maximum value over as little as 8 km. Cold ice as predicted in Figures 6.6A2 and B2 is more rigid than temperate ice and is consequently associated with a much wider margin than observed. The finding that Dragon margin is likely temperate over a significant portion of its thickness is consistent with *Perol and Rice* [2011][161]. Albeit not including horizontal advection, they predicted temperate zones in the shear margins of the active Siple-Coast Ice Streams using a 1D heat-transfer model in conjunction with the shear-strain rates measured by *Joughin et al.* [2002][118] to constrain shear heating. In fact, the size of the temperate zone estimate here for Dragon margin and the results by Perol and Rice match moderately well (Figure 6.7).

6.3.3 The ramifications of surface crevassing

The ice streams of West Antarctica were first identified by radar detection of their crevassed margins[190], which highlights that intense surface crevassing is a characteristic feature of the Ross Ice Streams. This observation raises the question of how surface crevasses affect the thermomechanics of ice-stream margins. Within the framework of our model, surface crevassing has two competing effects: On the one hand, crevasses lower the creep resistance of the ice because of the void space they introduce into the ice. We refer to this effect as mechanical weakening. On the other hand, crevasses lower the temperature in the ice through cool winter air pooling in the crevasses[99] thus increasing the creep resistance. We call this effect thermal strengthening.

While we are able to reproduce the velocity data for Dragon margin[69] with a wide range

of modeling parameters, compatibility with temperature measurements[99] poses more constraints. Figures 6.8 and 6.9 illustrate a computation that attempts to match both data sets simultaneously. To facilitate the comparison with our simulations, we briefly summarize four key observations by *Harrison et al.* [1998][99]. In the interest of consistency with the rest of this manuscript, we continue to use "depth" to describe distance from the bed despite the fact that "depth" in boreholes is typically measured from the surface. First, the temperature for the two boreholes in the ridge, named "OutB" and "Stage" (see Figure 6.1 for approximate borehole locations), is approximately constant at $-26\,^{\circ}\mathrm{C}$ over the depth range measured (Figure 6.8). Second, out of the nine boreholes, the boreholes "Remote", "Intermediate" and "Pad" exhibit the warmest temperature at depth ($-22\,^{\circ}\mathrm{C}$ at a depth of approximately 700 m) with "Intermediate" being slightly cooler than the other two. Third, borehole "UpB," located well into the stream, is slightly cooler yet ($-25\,^{\circ}\mathrm{C}$ at a depth of approximately 700 m, see Figure 6.8). Fourth, the $-26\,^{\circ}\mathrm{C}$ contour extends from borehole "Dragon Pad" to borehole "Intermediate" and attains the largest depths (≈ 830 m) at boreholes "Lost Love" and "Chaos" (Figure 6.9).

Supposing that the temperatures measured by *Harrison et al.* [1998][99] resemble a steady state, these four observations translate into the following constraints for our modeling. First, the finding that the boreholes in the ridge maintain a typical surface temperature of $-26\,^{\circ}\mathrm{C}$ over a 300 m depth interval suggests high rates of vertical advection. High vertical advection in turn implies high accumulations on the order of $a = 0.20 - 0.24\,\mathrm{m/yr}$, which is reasonable for Antarctica[87,213]. Second, the relatively warm temperatures measured for "Remote", "Intermediate" and "Pad" points to internal heating at these locations. The offset between the locations of highest strain rate and highest internal heating may indicate

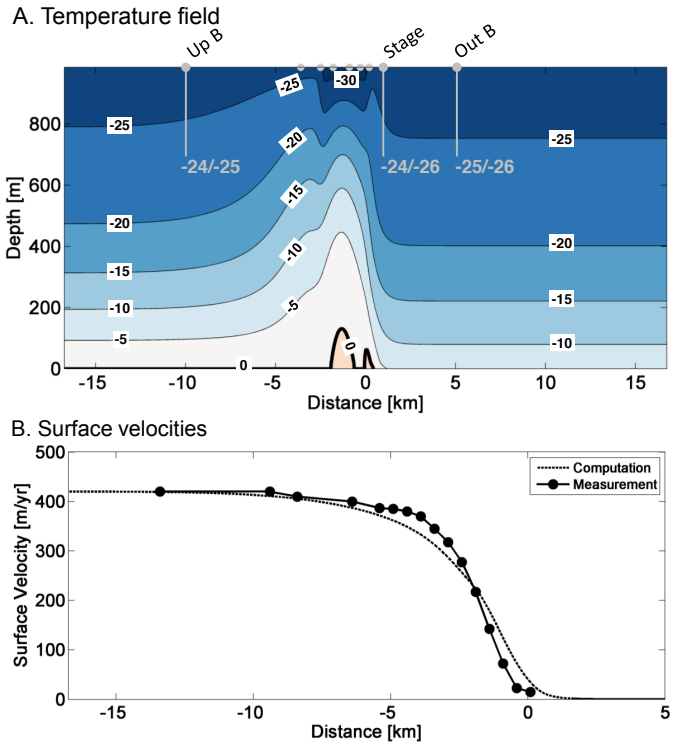

Figure 6.8: Temperature field (A) and surface velocities (B) for Dragon margin when attempting to match the observed borehole temperatures[99], see Figures 6.1 and 6.2 for borehole locations, and surface velocities[69] simultaneously. The computation is based on the model parameters $\tau_{base} = 1.22$ kPa, accumulation $a = 0.23$ m/yr, geothermal heat flux $G = 85$ mW/m^2 and horizontal advection at $v = -0.35$ m/yr. The approximate locations of the nine boreholes considered in *Harrison et al.* [1998][99] are indicated as grey dots. We highlight the boreholes located far from margin as grey lines in accordance with their depth. The left numbers represent the computed value and the right number the measured value at maximum depth. The corresponding temperature estimates for the boreholes in the vicinity of the margin are shown in the next figure.

horizontal advection probably relating to margin migration[99,69]. Third, the comparatively cooler temperatures at "UpB" are consistent with a localized heat source close to "Remote", "Intermediate" and "Pad" that does not extend far into the stream. Fourth, we take the -26 °C contour as a proxy for the extent and location of the crevassed zone at Dragon margin, which stretches from "Dragon Pad" to "Intermediate".

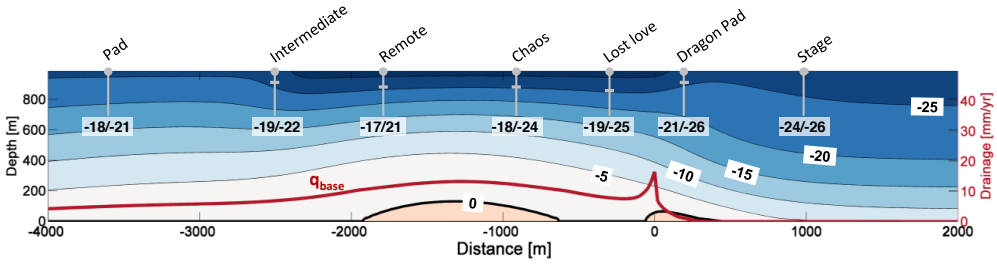

Figure 6.9: Extent of a potential temperate zone at Dragon margin plotted on a 1:1 scale and meltwater flux at the base of the ice, q_{base}, in mm/yr (grey line) for the computation also shown in Figure 6.8. The total meltwater produced in the temperate zone is 25 m^2/yr. The approximate locations of the boreholes from *Harrison et al.* [1998][99] are highlighted in grey with the left number representing the computed temperature and the right value the measured temperature at a depth of approximately 700 m. Small horizontal dashes along the boreholes in the vicinity of the shear margin indicate the approximate position of the $-26\,^{\circ}$C contour.

Figure 6.8A shows the computed temperature in our modeling domain. The cooling effect of crevassing depresses the temperature notably in the vicinity of the shear margin. We also compare computed and measured temperatures at a depth of 700 m for the three boreholes that are located far from the margin. The temperatures we estimate are $1-2\,^{\circ}$C higher than the measured values. The agreement with surface velocities (Figure 6.8B) is slightly less satisfactory than in previous simulations (e.g., Figures 6.4B3 and 6.6B1). While it is certainly possible to improve the agreement with surface velocities, doing so comes at the cost of deteriorating the consistency with available temperature data. Figure 6.9 compares the computed and measured temperatures for the boreholes in the vicinity of the shear margin at a depth of 700 m for the computation shown in Figure 6.8. We successfully reproduce the extent and approximate depths of the $-26\,^{\circ}$C contour from *Harrison et al.* [1998][99], highlighted on the boreholes "Dragon Pad" to "Intermediate" as short horizontal dashes. Our computations are also consistent with the observation that the three leftmost boreholes are warmest and that the borehole "Intermediate" is colder than its two

neighboring boreholes. We suggest that the relatively warmer temperatures at these three boreholes could result from their proximity to a temperate zone instead of non-steady state effects as argued in *Harrison et al.* [1998][99]. Despite being able to reproduce these key features, the temperatures we compute are systematically too high by $1-6\,^{\circ}\mathrm{C}$ with the highest errors occurring at the boreholes closest to the margin (i.e., "Dragon Pad", "Lost Love" and "Chaos").

Figure 6.10 summarizes the relationship between the average absolute errors in reproducing the observational data and the properties of the temperate zones for various speeds of horizontal advection v_0. The speed of horizontal advection is the most consequential parameter when reproducing both data sets simultaneously because it has a strong effect on the position and extent of the temperate zone and thereby on the surface velocities. The speed of vertical advection, in comparison, is reasonably well constrained by fitting the temperature measurements in boreholes "OutB" and "Stage" (Figure 6.8A) and does not affect the shear margin as sensitively (see also the discussion in Section 6.3.2). Figure 6.10 highlights that the maximum height and the shape of the temperate zones are highly dependent on the assumed speed of horizontal advection. It is also evident from Figure 6.10 that large temperate zones entail more realistic surface velocities, while small temperate zones produce more realistic temperatures. We argue that horizontal advection on the order of $v_0 = -0.3$ to $-0.35\,\mathrm{m/yr}$ probably provide a reasonable compromise (Figures 6.8 and 6.9 show the case where $v_0 = -0.35\,\mathrm{m/yr}$). Increasing the speed of horizontal advection beyond $v_0 \approx -0.35\,\mathrm{m/yr}$ deteriorates the fit to observed surface velocities notably (similar to Figure 6.6B2) while improving the match to measured temperatures only minimally.

The temperate zones for horizontal-advection speeds between $v_0 = -0.3$ and $-0.35\,\mathrm{m/yr}$

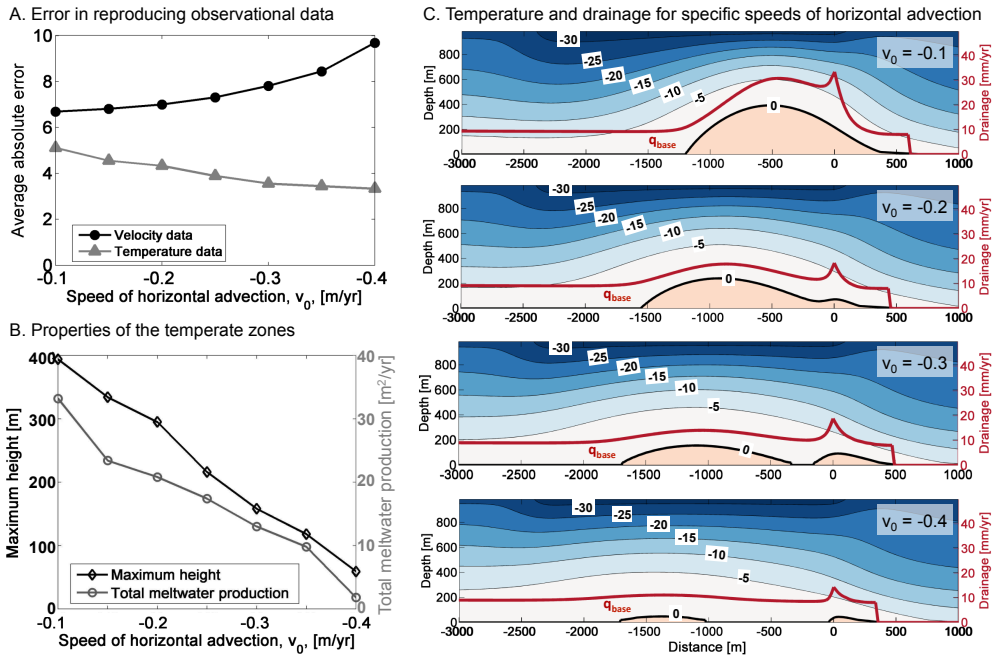

Figure 6.10: A. Average absolute error in reproducing observed temperatures and velocities for horizontal advection speeds between $v_0 = -0.1$ and -0.4 m/yr. B. Maximum height of the temperate zones and total meltwater production for horizontal advection speeds between -0.1 and -0.4 m/yr. The total meltwater production is computed by integrating the basal meltwater flux, q_{base}, over the width of the zone where ice is temperate not only at the bed but at finite depth. C. Temperature fields and drainage curves for the four horizontal advection speeds $v_0 = -0.1, -0.2, -0.3$ and -0.4 m/yr, respectively. The best-fitting basal stresses for the four computations are $\tau_{base} = 1.57, 1.44, 1.31$ and 1.13 kPa from the top to the bottom. Apart from the horizontal-advection speed and basal stress, all computations are based on the same model parameters, most importantly $a = 0.23$ m/yr and $G = 85$ mW/m^2.

reach a maximum height of $120 - 160$ m. In the vicinity of the locked-to-sliding transition point, the height of the temperate zone has a second maximum of approximately 80 m. The widths of the temperate zones, which we define as the maximum width range over which ice is temperate not only at the bed but at a finite depth, are approximately 2.2 and 2.3 km. We obtain the total meltwater production by integrating the basal meltwater flux over the temperate zone, which extends from about $y = -16.94$ km to $y = 512$ m for

$v_0 = -0.30$ m/yr and from $y = -19.30$ km to $y = 413$ m for $v_0 = -0.35$ m/yr, is 26.5 and 25 m^3 per year and per meter in downstream direction, respectively. Increasing the rate of outward margin migration shifts the temperate zone further into the stream, depresses the maximum depth to which temperate ice extends and decreases the total meltwater production (Figure 6.10).

When weighing how to prioritize the two data sets, it is important to keep in mind that a steady-state approach to modeling the temperatures throughout Dragon margin is in itself highly questionable (see also Section 6.3.2). A simple scaling analysis shows that the time it takes for the full ice thickness to reach steady state, $t = H^2/\alpha_{th}$, is approximately 10^4 years. In contrast, *Harrison et al.* [1998][99] estimated that the residence time of ice in Dragon margin is approximately a half century. It is thus clear that the stream-ridge system can not possibly be in steady state. This insight is supported by field observations that indicate a complex deformational history dating back over the last few hundred years[99,69,47]. Non-steady state effects should be most significant for the boreholes closest to the margin because of the rapid margin migration in recent years[99,69]. The observation that the deviations between computed and observed temperatures are indeed highest in the shear margin lends support to the interpretation that non-steady effects are probably the main reason for the temperature mismatch between model and data.

6.4 Discussion

While several previous models of ice streams[116,198,9,161] have raised the possibility of melting in active ice-stream margins, only *Perol and Rice* [2011][161] discuss the extent of a potential temperate zone in detail (see Figure 6.7 for a comparison with their results). In this study,

we provide additional constraints on how different factors such as the assumed ice rheology (Section 6.3.1), horizontal and vertical advection (Section 6.3.2) and surface crevassing (Section 6.3.3) affect deformation-induced melting and the size of a potential temperate zone.

While the simulations presented in Sections 6.3.1 and 6.3.2 raise the possibility that a temperate zone may extend several hundred meters above the bed at Dragon margin, the borehole measurements by *Harrison et al.* [1998][99] indicate variable but cold temperatures in the upper $300 - 400$ m of the ice. In Section 6.3.3 we thus attempt to fit velocity[69] and temperature data[99] simultaneously. We find that the two data sets provide somewhat conflicting constraints on the size of a potential temperate zone: While the agreement with surface velocities improves for a large temperate zone, the agreement with temperature measurements improves for a small temperate zone. We suggest that the computation shown in Figures 6.8 and 6.9 represents a reasonable compromise between the two constraints. This particular computation entails a temperate zone with a maximum height of ≈ 120 m and entails a meltwater production of 25 m^3/yr per meter in the downstream direction (Figure 6.9).

As discussed in more detail in Section 6.3.3, it is unreasonable to expect that temperature data can be reproduced exactly within the confines of a steady-state model (see Section 6.3.3), particularly for a location with a complex deformational history like Dragon margin[47]. To remedy the difficulties associated with replicating measured surface velocities without allowing for melting, *Echelmeyer et al.* [1994][68] and *Scambos et al.* [1994][195] have chosen to adjust the enhancement factor and its spatial variability in the model. It is certainly possible to match the surface velocity *Echelmeyer and Harrison* [1999][69] and temperature[99] data for Dragon margin only by varying enhancement in different parts of the

stream-ridge system. However, we require very high enhancement values on the order of $15 - 20$ in the shear margin to obtain a satisfactory fit to observational data, which conflicts with the results of *Jackson and Kamb* [1997][113], who determined enhancement factors between $E \approx 1.12$ and $E \approx 2.55$ for different ice specimens retrieved from Dragon margin.

Our simulations show that it is not necessary to resort to very high enhancement factors to reproduce rapid velocity increases in shear margins. We obtain excellent agreement with surface velocities even when neglecting enhancement entirely. This insight is not meant to imply that varied effects such as fabric, impurities or grain-size variations, which are usually integrated into a single enhancement factor, are not important. Instead, we argue that the relatively small enhancement factors measured at Dragon margin[113], in combination with our simulations, suggest that enhancement effects are probably not the whole story and that deformation-induced melting may play an important role in the thermomechanics of ice-stream margins, as is also supported by some observations[47,236].

6.5 Conclusion

In this study, we investigate the possibility of deformation-induced melting in active shear margins. Melting and the associated presence of meltwater in ice-stream margins might have important consequences for the dynamics of ice streams, primarily because the yield strength of glacial till depends sensitively on porosity, which is controlled by the water content if saturated. The position of the shear margins could thus be intricately linked to meltwater production[173,174], which remains poorly constrained. We devise a 2D thermomechanical model of an ice stream moving over a plastic bed in steady state. We solve our model numerically after carefully benchmarking our computational approach against an

asymptotic analytic solution. In combination with previous studies[116,198,161], our simulations lend theoretical support to the hypothesis that active shear margins are partially temperate. For Dragon margin, we estimate a temperate zone with a maximum height of $\sim$ 120 to 150 m that produces approximately 25 to 26.5 m^3 meltwater per year and per meter in the downstream direction. This estimate for the extent of a temperate zone is roughly comparable to the height of the bottom diffractor identified by *Clarke et al.* [2000][47] under Unicorn ridge. Despite focusing primarily on Dragon margin, we argue that our insights may generalize to the other active Ross Ice Streams.

This project was a collaboration with Thibaut Perol, Jenny Suckale, and James R. Rice, and the crack blunting mechanism was initially suggested by James Rice. My role was to compare the maximum stress on the bed with the till strength to determine when locking occurs, and I was the primary author of the manuscript. The work in this chapter is in preparation for the Journal of Geophysical Research.

7

Basal stress and strength immediately adjacent to a channel in an ice stream shear margin

7.0 Abstract

The mass loss from the West Antarctic ice sheet is dominated by numerous rapidly flowing ice streams, which are separated from the stagnant ice in the adjacent ridge by a zone of concentrated deformation known as a shear margin. Since the discharge from a single ice stream is thought to depend sensitively on the ice stream width, determining the physical processes that control the shear margin location is crucial to understanding how ice streams may respond to a changing climate. The transition from a deforming to an undeforming bed at a shear margin concentrates large stresses on the undeforming bed beneath the ridge, and thus for a stable margin configuration to exist there must also be a mechanism that raises the till strength in the shear margin. Two main mechanisms have been hypothesized. *Jacobson and Raymond* [1998][116] and *Schoof* [2012][199] investigated how the strengthening associated with the transition from a temperate to a frozen bed could control the shear margin location; *Perol and Rice* [2011][161] and *Perol et al.* [*in preparation*][163] showed that the presence of a drainage channel raises the basal strength in a several kilome-

ter wide zone in the shear margin and may allow a stable margin configuration to occur. In this paper we determine what conditions must be met for the transition from a deforming to an undeforming bed to be collocated with a drainage channel. We show that the channel limits the maximum shear stress resolved on the undeforming bed, building on *Perol et al.* [2012][162], and alters the yield strength of the till by changing the normal stress applied to the ice-till interface. We also compare the maximum stress on the bed with the till strength at the channel wall and show that a transition from a deforming to an undeforming bed at a channel is a stable margin configuration if the water flux in the channel exceeds a critical value.

7.1 Introduction

Surface velocity observations of the West Antarctic Ice Sheet show that ice flow is highly non-uniform, with narrow regions known as ice streams flowing much faster than the surrounding ice sheet[118]. Although ice streams account for a small fraction of the surface area of the ice sheet, the large velocities present in ice streams allow them to dominate the discharge of ice from the continent, with *Bamber et al.* [2000][5] estimating that ice streams provide 80% of the total discharge. Thus, determining the physical processes that govern ice stream dynamics is of the utmost importance if we want to understand how Antarctica will respond to a changing climate.

A typical ice stream has an ice thickness of one kilometer, a width of a few tens of kilometers, and a length of a few hundred kilometers. The surface velocity in the centre of an ice stream is typically a few hundreds of meters per year, significantly larger than a typical surface velocity of a few meters per year in the surrounding ice sheet. These large veloci-

ties are made possible despite the low gravitational stress driving deformation – typically $\sim$ 10 kPa – due to the presence of a subglacial till layer beneath the ice stream[21,22]. This saturated till layer has a pore pressure that is close to the ice overburden, leading to a low failure strength for the Coulomb plastic rheology typically observed in laboratory experiments on subglacial till[120,112,226]. Thus, the ice stream bed fails even at low driving stresses and a significant fraction of the ice stream surface velocity is due to till deformation[3].

The boundary between the rapidly flowing ice stream and the stagnant ice in the adjacent ridge forms a zone of concentrated deformation known as the shear margin. These shear margins are typically a few kilometers wide and marked be extensive surface crevassing[18,68,195]. Since the weak subglacial till provides limited resistance to motion, the margins are expected to balance a significant fraction of the gravitational driving stress[68,113,99,118]. The location of the shear margins also sets the width of the ice stream, and thus plays an important role in determining the ice stream discharge if we assume that a wider ice stream leads to a higher discharge as suggested in *van der Veen and Whillans* [1996][231]. Furthermore, observations have shown that ice stream margins migrate[19,69,47], with observations of migration both towards and away from the adjacent ridge. Despite the obvious importance of the shear margins, there is still some question about what physical processes select their location. In contrast with mountain glaciers, topography alone does not appear to explain current shear margin locations[202,203]. We hope that understanding the different physical mechanisms that control shear margin migration may lead to further insight into the physical processes governing the margin.

The transition from a deforming bed beneath the ice stream to an undeforming bed beneath the ridge concentrates stress on the undeforming bed. This means that for a stable

margin configuration to exist there must also be a mechanism that raises the yield strength of the undeforming bed. One mechanism that is commonly appealed to is freezing of the subglacial till, and *Jacobson and Raymond* [1998][116] and *Schoof* [2012][199] studied how the strengthening associated with the transition from a temperate to a frozen bed could select the shear margin location and allow margin migration to occur. Another mechanism suggested in *Perol and Rice* [2011][161] is that melt generated in the shear margins drives the formation of a subglacial drainage channel at the base of the shear margin. *Perol et al.* [in preparation][163] then showed that the presence of a subglacial drainage channel will allow much more efficient drainage than the distributed hydrologic system that operates under the remainder of the ice stream, and thus decreases the pore pressure in the immediate vicinity of the channel. Since subglacial till has a Coulomb plastic rheology this will raise the yield strength of the till, possibly allowing a stable margin configuration to form.

Previous work has examined how a stable margin configuration can be created by increasing the basal strength in the shear margin through the two proposed strengthening mechanisms, one thermal and one hydrologic. In this paper we will take a different approach and look at how the presence of a drainage channel alters the stress field around a transition from a deforming to an undeforming bed. To begin we study a sharp transition, showing that this transition concentrates large stresses on the undeforming bed and that all of the information about the far field loading is transmitted to the transition point through a single parameter. Next we investigate how the presence of a channel limits the maximum shear stress on the undeforming bed – extending the analysis of *Perol et al* [2012][162] – and alters the yield strength of the till by changing the normal stress on the ice-till interface. Finally, we compare the maximum stress on the bed with the till strength to determine when

the transition from a deforming to an undeforming bed at a channel leads to a stable margin configuration, showing that a stable margin configuration can occur when the water flux in the channel exceeds a critical value.

7.2 Model derivation

In this section we develop a model for ice deformation near the transition from a deforming to an undeforming bed. We define the coordinate vector $\mathbf{x} = (x, y, z)$ so that x is parallel to the direction of ice stream flow, y is parallel to the bed and perpendicular to the ice stream margin, and z is the vertical height above the bed. The transition from a deforming to an undeforming bed occurs at $y = 0$ with the ice stream located in $y < 0$, and the ridge located in $y > 0$. This coordinate vector is used to define the velocity vector $\mathbf{u} = (u, v, w)$ with u the velocity in the x-direction, v the velocity in the y-direction, and w the velocity in the z-direction.

In this model we will assume that all flow is in the downstream direction, making u the only non-zero component in the velocity vector. We also assume that the ice flow field varies slowly in the downstream direction, and thus u is independent of x. These assumptions are commonly made when modeling flow in ice stream margins[116,198,216], and are justified when the anti-plane strain rates are much larger than the in-plane strain rates. The single velocity $u(y, z)$ leads to two non-zero shear strain rates

$$\dot{\varepsilon}_{xy} = \frac{1}{2}\frac{\partial u}{\partial y} \quad , \quad \dot{\varepsilon}_{xz} = \frac{1}{2}\frac{\partial u}{\partial z}. \tag{7.1}$$

The two non-zero strain rates lead to two non-zero shear stresses τ_{xy} and τ_{xz}, and the equa-

tions for mechanical equilibrium simplify to

$$\frac{\partial \tau_{xy}}{\partial y} + \frac{\partial \tau_{xz}}{\partial z} = 0. \tag{7.2}$$

Here we have assumed that the gravitational driving stress can be neglected when compared with the stress concentration near the transition from a deforming to an undeforming bed, though the gravitational driving stress still enters into our model by providing the far field loading on the transition point. It should be noted that later in the paper we will model the creep closure of a drainage channel and for this case the in-plane strain rates may become important as first noted in *Röthlisberger* [1972][191] and *Weertman* [1972][238].

To close the model we need a rheological law linking strain rate and shear stress. Though ice can deform through a variety of mechanisms linked to physical phenomena such as dislocation motion and diffusion, we will assume a single deformation mechanism with a power law dependence. This leads to

$$\epsilon_{ij} = A \tau_E^{n-1} \tau_{ij}, \tag{7.3}$$

where $\tau_E = [\tau_{xy}^2 + \tau_{xz}^2]^{1/2}$ is the effective shear stress and $\epsilon_E = [\epsilon_{xy}^2 + \epsilon_{xz}^2]^{1/2}$ is the effective strain rate. Equation (7.3) can be used to model different deformation mechanisms by assuming different values of A and n.

The concentrated deformation present in ice stream shear margins is thought to lead to the formation of temperate ice[116,198,161,216], which suggests that the transition from a deforming to an undeforming bed may occur within temperate ice. Motivated by this insight we have neglected any dependence of the rheology on temperature and used values of A

W, km	34
H, km	1
S	0.0012
τ_b, kPa	3.5
g, m s^{-2}	9.81
ρ_i, kg m^{-3}	917
ρ_w, kg m^{-3}	1000
L, kJ/kg	335
f	0.6
n_m	0.01

Table 7.1: A table showing the parameters used in this paper. The values of slope, ice thickness, ice stream width, and slope are not intended to model a specific ice stream but are in general agreement with typical values for major West Antarctic ice streams [118]. As shown in the text, when we study the transition from a deforming to an undeforming bed these parameters cannot be varied independently, and variations in these parameters only alter the stress around the transition point through J_{tip}.

inferred from experiments performed at 0 °C. This assumption is justified as long as the size of the zone of concentrated stress is smaller than the smallest dimension of the zone of temperate ice. Using the models of *Jacobson and Raymond* [1998] [116], *Schoof* [2004] [198], and *Suckale et al.* [2014] [216] we can crudely estimate the size of this smallest dimension to be $\sim$ 100 m, though this value could be much smaller if there is significant horizontal advection of cold ice into the shear margin. We have also neglected any dependence of A and n on the melt fraction in the temperate ice, which may be important if the melt fraction of the ice immediately adjacent to the channel is $\geq 1\%$.

The majority of calculations in this paper assume a Glen's law rheology, which is modeled using $n = 3$ and $A = 2.4 \times 10^{-24}$ Pa^{-3} s^{-1}. This value of A is the value recommended in *Cuffey and Paterson* [2010] [53] for $T = 0$ °C. We will also produce some analytic results using a Newtonian rheology with $n = 1$ and $A = 5 \times 10^{-14}$ Pa^{-1} s^{-1}, where this

Pre-factor, A	Stress exponent, n
5×10^{-14}, $\text{Pa}^{-1}\,\text{s}^{-1}$	1
2.4×10^{-24}, $\text{Pa}^{-3}\,\text{s}^{-1}$	3
2.2×10^{-30}, $\text{Pa}^{-4}\,\text{s}^{-1}$	4

Table 7.2: A table showing the parameters for the three different rheological models used in this paper. The value of A used for $n = 1$ is based upon the ice viscosity assumed in *Hewitt* [2011][102]. The rheology with $n = 3$ is Glen's law and we use the recommended value of A at $0\,^{\circ}\text{C}$ from *Cuffey and Paterson* [2010][53]. The $n = 4$ rheology is based upon the dislocation creep experiments rheology proposed in *Durham et al.* [1997][66] and is expected to dominate at the highest stresses.

value of A assumes the ice viscosity of 10^{13} Pa s used in *Hewitt* [2011][102]. Finally, we reinterpret our results for the dislocation creep rheology of *Durham et al.* [1997][66], which is modeled using $n = 4$ and $A = 2.2 \times 10^{-30}$ $\text{Pa}^{-4}\,\text{s}^{-1}$, and is thought to dominate at the largest shear stresses. However, we present our results in a general fashion that allows other values of A and n to be inserted.

7.3 Deformation around a sharp transition

As noted in *Suckale et al.* [2014][216], an analogy can be drawn between the transition from a deforming to an undeforming bed and a mode-III fracture. Downstream velocity is analogous to the anti-plane displacement, the transition point to the crack tip, the deforming till beneath the ice stream to the crack face, and the undeforming bed beneath the ridge to the unfractured material ahead of the crack.

Recognizing this, we use classic methods from fracture mechanics to solve for the stress field around the transition from a deforming to an undeforming bed. Following *Rice* [1967][182], *Rice* [1968][183] and *Suckale et al.* [2014][216], Appendix E.1 develops a solution for the stress field and velocity field around a sharp transition from a deforming to an undeforming bed.

The stress on the undeforming bed is given by

$$\tau_{sharp} = \left(\frac{n J_{tip}}{(n+1) A \pi y} \right)^{1/(n+1)}, \tag{7.4}$$

where the far-field loading is linked to the stress at the transition point using the path-independent J-integral[184], generalized from the nonlinear elastic case to the nonlinear creep rheology given in equation (7.3), to find

$$J_{tip} = \frac{4 H A \tau_{lat}^{n+1}}{n+1} \quad , \quad \tau_{lat} = \left(\rho g S - \frac{\tau_{base}}{H} \right) \frac{W}{2}. \tag{7.5}$$

Here H is the ice thickness, W is the width of the ice stream, ρ is the ice density, g is gravity, S is the slope of the bed in the downstream direction, and τ_{base} is the basal resistance provided by the deforming bed, which is assumed to be constant. Using a simple force balance for the ice stream it can be shown that τ_{lat} is equal to the average lateral drag supported by the shear margin. Equation (7.4) has three distinctive features. First, the shear stress on the locked portion of the bed is singular. Second, the power of the singularity depends on the stress exponent n, with larger values of n leading to less severe singularities. Finally, larger values of J_{tip} concentrate larger stresses on the undeforming bed. Inserting equation (7.5) into equation (7.4) we find that

$$\tau_{sharp} = \tau_{lat} \left(\frac{4 H n}{(n+1)^2 \pi y} \right)^{1/(n+1)}. \tag{7.6}$$

Thus, the lateral stress supported by the shear margin is transmitted to the undeforming bed beneath the ridge, and the stress on the bed is directly proportional to the lateral drag

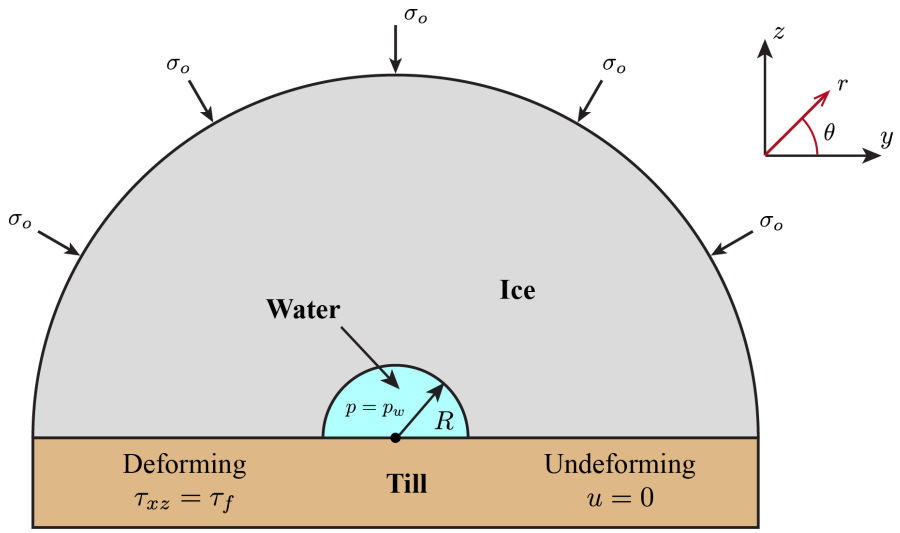

Figure 7.1: A sketch of the geometry used in our calculations for the deformation around the channel. We assume a semi-circular channel with a radius R incised into the ice, which rests upon a subglacial till layer. The anti-plane strain rates are calculated assuming that the bed is deforming to the left of the channel, and undeforming to the right of the channel. We model the creep closure of the channel using the pressure difference between the channel operating at a pressure p and the ice overburden σ_o.

supported by the shear margin. It is important to note that equations (7.5) and (7.6) are only valid when the J-integral is evaluated using the constant basal resistance beneath the ice stream assumed in *Suckale et al.* [2014][216], though a more complete analysis that allows for large variations in basal resistance can be found in *Perol et al.* [in preparation][163]. Note that the solution for the stress around a sharp transition was developed in *Suckale et al.* [2014][216], but the physical significance of the singular stress field and the implications for the mechanical structure of the shear margins was not explicitly emphasized.

A singular stress field on the bed cannot exist in reality due to the finite yield strength of the bed. *Schoof* [2004][198] avoided this problem by assuming a spatially variable shear strength profile at the bed and finding solutions where the stress concentration vanished,

which is equivalent to solving for the transition point from a deforming to an undeforming bed that satisfies $J_{tip} = 0$. This leads to a non-singular stress profile that is continuous at the transition from a deforming to an undeforming bed, and corresponds to the cohesive zone models commonly used in fracture mechanics to eliminate crack tip singularities[6,65]. In this paper we take a different approach in which a finite value of J_{tip} is allowed but the maximum stress on the bed is limited by the presence of a channel, allowing a configuration where the stress on the bed is always less than some finite yield strength. The limiting of the maximum stress by a channel is analogous to the dependence of maximum stress concentration on radius of curvature of the crack tip commonly seen in fracture mechanics, with a large radius of curvature leading to a lower stress concentration. Note that our mechanism for a finite value of J_{tip} only works if the transition from a deforming to an undeforming bed occurs at a channel, while the cohesive zone models of *Schoof* [2004][198] and *Perol et al.* [in preparation][163] would work even when the channel is not located at the transition point.

Before studying the stress on the undeforming bed immediately adjacent to the channel, we first show that for typical channel sizes all the information about the far-field loading is transmitted to the transition point through J_{tip}. To do this we compare the analytic prediction for the velocity field near the transition point given in equation (E.28) with the results from a numerical simulation for the whole ice stream. Figure 7.2 shows this comparison for a numerical simulation for a whole ice stream performed using the methods from *Suckale et al.* [2014][216] as a function of θ at four different values of r. We find a single value of J_{tip} by fitting the analytic result to the numerical simulation for $r = 10$ m, and this value of J_{tip} is then used to compare with the numerical simulation for $r = 25$ m, $r = 50$ m, and

$r = 75$ m. We see that the agreement is very good for $r = 10$ m, and reasonable for $r = 25$ m, $r = 50$ m, and $r = 75$ m. From this we estimate that the asymptotic solution presented in Appendix E.1 provides a good approximation to the full numerical solution that assumes a realistic ice stream geometry for at least a few tens of meters around the transition point. Note that the lengthscale over which the two solutions agree well is over an order of magnitude greater than a typical channel radius estimated by *Perol and Rice* [2011][161] and *Perol et al.* [in preparation][163], allowing us to make the small scale yielding approximation commonly used in fracture mechanics when the process zone is much smaller than the region of validity of the asymptotic solution near the crack tip. This small scale yielding approximation allows us to draw two important conclusions. First it tells us that all information about the far field loading is carried to the transition point through the single parameter J_{tip} corresponding to evaluating the J-integral along paths through temperate ice where the ice viscosity depends on strain rate alone. This greatly reduces the number of parameters we must consider and says that ice stream scale parameters such as W and τ_{base} influence the stress at the transition point only in so much as they influence J_{tip}. Second, it allows us to study deformation around a channel at the transition point by imposing the asymptotic solution from Appendix E.1 as a boundary condition far from the channel.

7.4 Stress field around a channel

In this section we investigate how the presence of a semi-circular channel with a radius R at the transition from a deforming to an undeforming bed alters the stress resolved on the undeforming bed. To begin we use a complex variable method to solve analytically for a Newtonian rheology. This analysis is then extended to a power law rheology using numerical

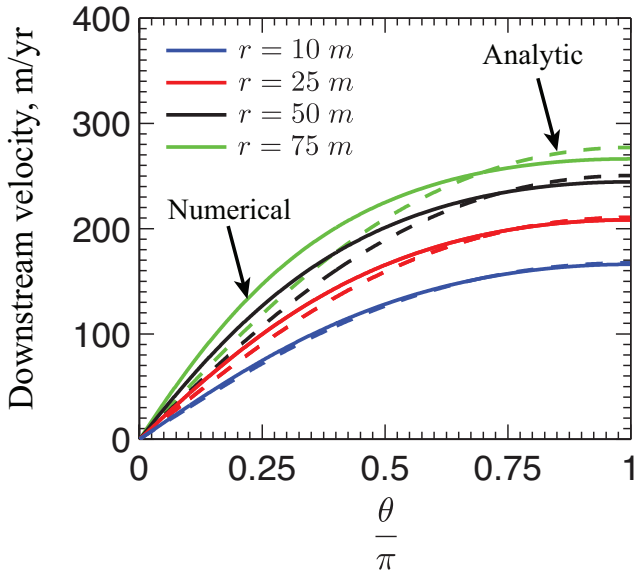

Figure 7.2: A plot showing the comparison between the analytic solution given in equation (E.28) valid right at the locking point and numerical simulations for a whole ice stream. Both solutions for the downstream velocity are shown as a function of θ for $r = 10$ m, $r = 25$ m, $r = 50$ m, and $r = 75$ m. The curve at $r = 10$ m is used to infer a best-fitting value of J_{tip} that is then used to fit all remaining curves. We see good agreement between the analytic and numerical solutions for several tens of meters, allowing us to make a small scale yielding approximation.

simulations. A sketch of the geometry assumed in our calculation can be found in Figure 7.1.

The small scale yielding approximation justified in the previous section allows us to use dimensional analysis to simplify the functional form of the stress on the undeforming bed. We find that the stress on the bed is a function of J_{tip}/A, R, n, and y alone. There is a single way to combine these parameters to find a stress, and thus we can write the stress on the undeforming bed as

$$\tau = \tau_{sharp}(R) f\left(\frac{y}{R}, n\right), \tag{7.7}$$

where τ_{sharp} is the singular solution for a sharp transition given in equation (7.4) and f is the function we must solve for. The maximum stress on the bed occurs at the channel wall and is equal to

$$\tau_{max} = \chi \tau_{sharp}(R), \tag{7.8}$$

where $\chi = f(1, n)$ is a function of the stress exponent n alone.

7.4.1 Newtonian rheology

For a Newtonian rheology we can make significant progress analytically. When $n = 1$ we must solve Laplace's equation,

$$\frac{\partial^2 u}{\partial r^2} + \frac{1}{r}\frac{\partial u}{\partial r} + \frac{1}{r^2}\frac{\partial^2 u}{\partial \theta^2} = 0, \tag{7.9}$$

in the domain $R < r < \infty$. The no slip boundary condition on the undeforming bed is

$$u = 0 \quad \text{on} \quad \theta = 0,\ R < r < \infty \tag{7.10}$$

and the traction free boundary condition on the deforming bed is

$$\frac{\partial u}{\partial \theta} = 0 \quad \text{on} \quad \theta = \pi,\ R < r < \infty. \tag{7.11}$$

There is an additional traction free boundary condition on the channel wall

$$\frac{\partial u}{\partial r} = 0 \quad \text{on} \quad r = R,\ 0 < \theta < \pi, \tag{7.12}$$

which is justified if the shear stress exerted on the channel wall by the turbulent flow in the channel is much smaller than the large stresses associated with the transition from a deforming to an undeforming bed. Finally we assume that as $r \to \infty$ the solution approaches the solution for a sharp transition, in agreement with the small scale yielding approximation made in the previous section.

Equations (7.9)-(7.12) can be solved using complex variables, and the details of the solution are outlined in Appendix E.2. We find that the shear stress on the undeforming bed is given by

$$\tau_{xz} = \left(\frac{J_{tip}}{2A\pi y}\right)^{1/2}\left(1+\frac{R}{y}\right). \tag{7.13}$$

We notice two distinctive features about this solutions. First, the solution for a sharp transition is the asymptotic limit of equation (7.4) when $y \gg R$, which is to be expected after making a small scale yielding approximation. Thus, the presence of a channel only alters the stress field on the bed in the immediate vicinity of the channel, and far from the channel the stress field is the same as that predicted for a sharp transition. Second, the presence of the channel caps the maximum shear stress on the bed at a finite value. This maximum value occurs at the edge of the channel and is equal to

$$\tau_{max} = \left(\frac{2J_{tip}}{A\pi R}\right)^{1/2}. \tag{7.14}$$

Note that a larger channel radius R leads to a lower maximum shear stress on the bed. As in equation (7.8) we can relate equation (7.14) to the solution for a sharp transition by noting that

$$\tau_{max} = 2\tau_{sharp}(R), \tag{7.15}$$

and thus $\chi = 2$ for $n = 1$. The maximum stress applied to the bed is equal to twice the stress predicted by evaluating the singular solution for a sharp transition at the channel radius R. As highlighted before, the finite size of the maximum stress allows for the possibility of a stable margin configuration where the stress on the undeforming bed is always less than the yield strength of the bed even when $J_{tip} \neq 0$.

7.4.2 Nonlinear rheology

The complex variable solution presented in the previous subsection cannot be generalized to a non-linear rheology so we study other values of the stress exponent n through numerical solutions using a finite difference method. We cannot work with an infinite domain in our numerical simulations so we enforce the far-field velocity field given by equation (E.28) on a semi-circular boundary with radius D and study the behavior when $D \gg R$. The traction free boundary condition on the channel wall remains the same as in the previous subsection and the boundary conditions on the bed are now applied for $R < r < D$. The finite size of the domain introduces an additional dimensionless parameter R/D into equation (7.7), and we expect that as $R/D \to 0$ we will recover the solution where the boundary conditions are applied at infinity.

The homogeneous boundary conditions at the bed and channel wall allow us to calculate the dependence of χ on R/D analytically for $n = 1$. We find

$$\chi = 2\left(1 + \frac{R}{D}\right)^{-1}. \tag{7.16}$$

As expected, $\chi = 2$ as $R/D \to 0$, which is the value found when the boundary conditions are applied at infinity. Next we use a parameter sweep to determine how χ depends

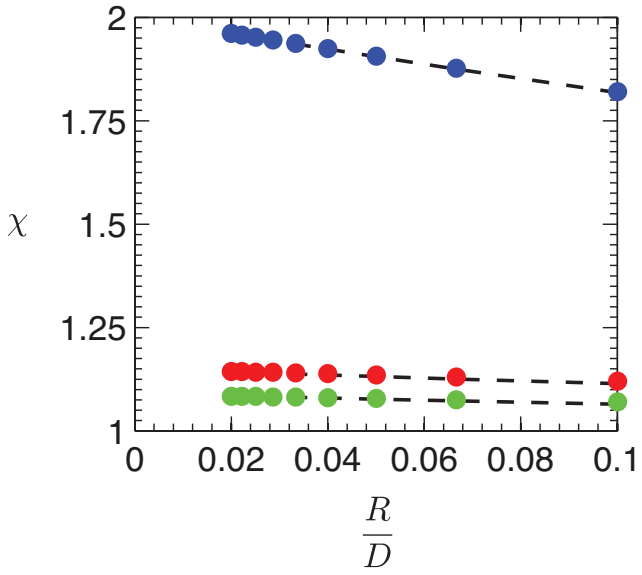

Figure 7.3: A plot showing how χ depends on R/D for $n = 1, n = 3$, and $n = 4$, alongside the fitting function $\chi = \chi_{inf}(1 + R/D)^{-1/n}$. This plot allows us to infer values of χ_{inf} that are then used to determine the maximum stress resolved on the undeforming bed. We find best fitting values of χ_{inf} to be 2 for $n = 1, 1.15$ for $n = 3$, and 1.09 for $n = 4$.

on R/D for several values of n. Figure 7.3 shows how χ varies with R/D for $n = 1$, $n = 3$, and $n = 4$ when the channel radius is fixed at $R = 1$ m and the outer radius D is varied. To perform these simulations we calculated J_{tip} using equation (7.5) assuming an ice thickness of 1 km, an ice stream width of 34 km, a slope $S = 0.0012$, and a basal stress of $\tau_b ase = 3.5$ kPa. These parameters are equivalent to an average lateral stress at the margins of 124 kPa. Figure 7.3 shows us that for all values of n there is a weak dependence of χ on R/D, with larger values of R/D leading to smaller values of χ. This is identical to the behavior found analytically for $n = 1$. Our analytic solution for $n = 1$ allows us to guess a

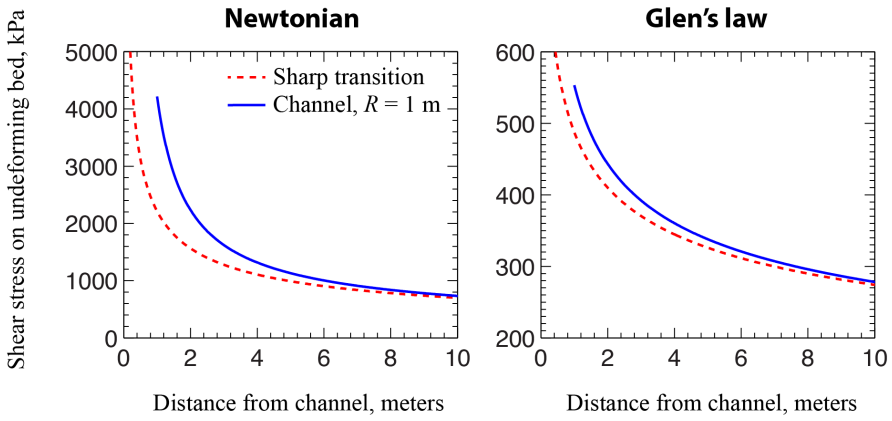

Figure 7.4: A plot showing the maximum stress on the bed accounting for the channel in blue alongside the prediction using the solution for a sharp margin given in equation (7.4) for $n = 1$ and $n = 3$. We see that the Newtonian rheology leads to significantly higher shear stresses on the bed than the Glen's law rheology, and that the solution for a sharp margin provides a reasonable approximation to the stress field accounting for the channel for all y.

functional form for this dependence,

$$\chi = \chi_{inf}(n)\left(1 + \frac{R}{D}\right)^{-1/n}. \tag{7.17}$$

The dashed curves in Figure 7.3 shows this fit and allows us to determine best fitting values of χ_{inf} of 1.15 for $n = 3$ and 1.09 for $n = 4$. This leads to our final form for the maximum stress on the bed

$$\tau_{max} = \chi(n)\left(\frac{nJ_{tip}}{(n+1)A\pi R}\right)^{1/(n+1)}, \tag{7.18}$$

where the value of χ for each value of n is equal to the best fitting value of χ_{inf} inferred from the results shown in Figure 7.3.

The simulations performed to produce Figure 7.3 also allow us to study the shape of the

stress on the bed away from the channel wall. The stress on the undeforming bed is shown in Figure 7.4 for $n = 1$ and $n = 3$. We see that as the stress exponent increases the maximum stress on the undeforming bed drops significantly, in excellent agreement with the behavior predicted for a sharp transition in equation (7.4) that showed a strong dependence of the singularity on the stress exponent. We also see that for $n = 3$ the solution for a sharp transition gives a good approximation to the stress field near a channel for several tens of meters adjacent to the channel. This observation is in good agreement with the results in Figure 7.3 that show $\chi = 1.15$ for $n = 3$. Other simulations for $n = 4$ not shown also show that the stresses calculated numerically accounting for the channel are comparable to the predictions for a sharp transition given in equation (7.4) for several tens of meters adjacent to the channel.

7.4.3 The importance of the basal stress

Up until now we have neglected the basal resistance beneath the ice stream, arguing that it will be much smaller than the concentrated stress near the transition from a deforming to and undeforming bed. While this may be true for values of the basal resistance inferred beneath the majority of an ice stream – typically $\sim 1-5$ kPa – it may not be true when we account for the large effective stresses thought to occur near a channel. It is difficult to extend our analysis of the maximum stress on the undeforming bed to account for basal resistance but we can make some progress analytically if we assume that $n = 1$ and the basal resistance immediately adjacent to the channel takes a constant value τ_f. Appendix E.2 shows how the complex variable method can be extended to account for a uniform basal strength allowing

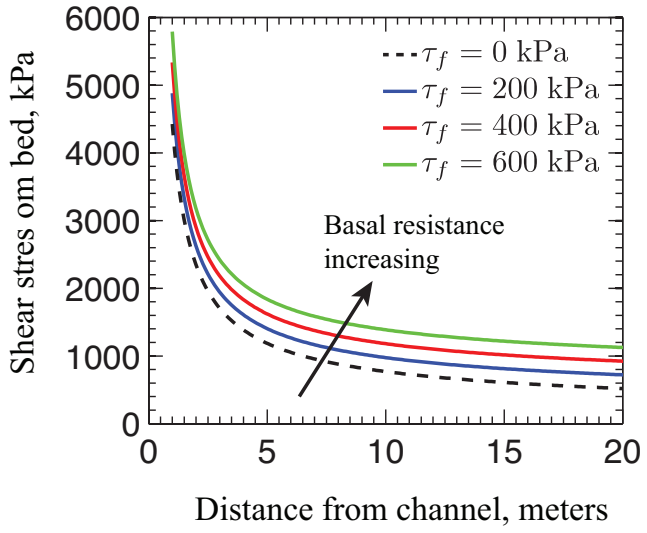

Figure 7.5: A plot showing how the stress on the undeforming bed varies with the basal resistance of the deforming bed τ_f if we assume $n = 1$. We see that as τ_f increases the maximum stress on the bed increases. However, reasonable values of τ_f are much smaller than the maximum stresses on the bed when $n = 1$ so the dependence of maximum stress on τ_f is not significant. This conclusion may not be true for higher values of n where the maximum stress on the bed is much lower.

us to solve for the stress on the undeforming bed

$$\tau_{xz} = \tau_f + \sqrt{\frac{J_{tip}}{2\pi A y}} \left(1 + \sum_{n=1}^{\infty} C_n \left(\frac{R}{y} \right)^n \right), \tag{7.19}$$

where the values of C_n are given in equations (E.48) and (E.49). As expected when τ_f is much smaller than the stresses adjacent to the channel we recover equation (7.13). Assuming different values of τ_f we can plot the basal stress for the parameters in Tables 7.1 and 7.2, as shown in Figure 7.5. We see that increasing τ_f leads to larger shear stresses on the undeforming bed at all locations along the bed, though for reasonable values of τ_f these changes are smaller than the large stresses concentrated at the transition from a deforming to an un-

deforming bed. Equation (7.19) also allows to calculate the maximum stress on the bed

$$\tau_{max} = \left(1 + \frac{4}{\pi}\right) \tau_f + \sqrt{\frac{2J_{tip}}{\pi AR}}. \tag{7.20}$$

Note that for a fixed value of J_{tip} increasing the basal resistance τ_f increases the maximum stress resolved on the bed, and this increase can be significant if τ_f is comparable to $\tau_{sharp}(R)$. It is important to note that J_{tip} also depends on the basal resistance beneath the entire ice stream τ_{base} – which presumably increases with τ_f – and a more detailed discussion of how J_{tip} depends on a spatially variable basal resistance can be found in *Perol et al.* [in preparation][163].

7.5 Basal yield strength adjacent to channel

In this section we determine the yield strength of the undeforming bed adjacent to the channel, which for a temperate bed is governed by a Coulomb plastic rheology controlled by the effective stress in the till and a friction coefficient,

$$\tau_{yield} = f(\sigma_n - p). \tag{7.21}$$

Here σ_n is the normal stress acting on the bed, p is the pore pressure, and f is the friction coefficient of the till.

To determine the normal stress acting on the bed and the pore pressure in the channel we must model the physical processes that allow a channel to form. This is done by following the approach from *Röthlisberger* [1972][191] using the notation in *Perol et al.* [in preparation][163]. First we use the Gauckler-Manning law for turbulent flow in a conduit to relate

the channel geometry and water flux through

$$\frac{Q_w}{A_{ch}} = \frac{R_h^{2/3} S^{1/2}}{n_m}, \tag{7.22}$$

where Q_w is the flux through the channel, A_{ch} is the area of the channel, R_h is the hydraulic radius of the channel, and n_m is the Gauckler-Manning coefficient. For the semi-circular channel shown in Figure 7.1 we find

$$A_{ch} = \frac{\pi R^2}{2} \quad , \quad R_h = \frac{R}{2(1+2/\pi)}. \tag{7.23}$$

Combining equations (7.22) and (7.23) we can solve for the channel radius

$$R = 2^{5/8} \left(\frac{n_m Q_w}{\pi S^{1/2}} \right)^{3/8} \left(1 + \frac{2}{\pi} \right)^{1/4}. \tag{7.24}$$

Note that for fixed values of n_m and S the channel radius is a function of the water flux alone. We see that a large water flux or a larger value of n_m – corresponding to a rougher channel wall that provides more resistance to flow – leads to a larger channel radius.

The heat generated by turbulent flow in the channel leads to melting at the channel wall[191,204]. By calculating the rate at which the flowing water converts gravitational potential energy into heat we can calculate the rate at which melting expands the channel radius to be

$$\dot{R}_{melt} = \frac{\rho_w g S Q_w}{\pi L \rho_i R}, \tag{7.25}$$

where ρ_w and ρ_i are the densities of water and ice respectively, and L is the latent heat of fusion for ice. Melting at the channel interface is balanced by creep closure of the channel due

to the ice overburden. For the power law rheology given in equation (7.3) we can estimate the closure rate using the solution from *Nye* [1953][158] for the channel to be

$$\dot{R}_{creep} = \frac{AR\left(\sigma_o - p\right)^n}{n^n}, \tag{7.26}$$

where σ_o is the pressure due to the ice overburden. The steady state channel size occurs when melting at the channel wall exactly balances creep closure. Setting (7.25) equal to (7.26) we find that the pore pressure in the channel is equal to

$$p = \sigma_o - n\left(\frac{\rho g S Q_w}{\pi A L \rho_i R^2}\right)^{1/n}. \tag{7.27}$$

Note that the pore pressure decreases as the flux within the channel increases.

When calculating the strength of the undeforming bed we assume that the pore pressure in the till is the same as the pore pressure in the channel for the few tens of meters immediately adjacent to the channel. This is a good approximation for our steady state model with a constant water flux since the hydraulic gradients predicted in *Perol et al.* [in preparation][163] show that pore pressure changes over this lengthscale are negligible. However, this assumption may not be a good approximation if the water flux in the channel varies faster than hydraulic diffusion can equilibrate the pore pressures in the channel and the adjacent till.

In the previous section we showed how the presence of a channel alters the shear stress resolved on the bed. Using the creep closure solution from *Nye* [1953][158] we can show that the channel alters the normal stress on the ice-till interface in a similar fashion and calculate

the effective stress profile on the undeforming bed

$$\sigma_n - p = (\sigma_o - p)\left(1 + \frac{2-n}{n}\left(\frac{R}{y}\right)^{2/n}\right), \tag{7.28}$$

where $\sigma_o - p$ is given by equation (7.27). Combining this with the Coulomb plastic rheology from equation (7.21) we predict that the strength of undeforming bed is

$$\tau_y = f\left(\frac{\rho g S Q_w}{\pi A L \rho_i R^2}\right)^{1/n}\left(n + (2-n)\left(\frac{R}{y}\right)^{2/n}\right). \tag{7.29}$$

Note that equation (7.29) indicates that there may be large changes in the yield strength of the undeforming bed in the immediate vicinity of the channel due to changes in the normal stress resolved on the till. One surprising conclusion that follows from equation (7.29) is that the strength will increase near the channel if $n < 2$, and will decrease near the channel if $n > 2$. This dependence on n highlights the importance of accurately determining the dominant deformation mechanisms at the high shear stresses associated with the transition from a deforming to an undeforming bed.

Equation (7.29) can be used to calculate the yield strength at the channel wall, which is where the highest shear stress is resolved on the bed, leading to

$$\tau_y = 2f\left(\frac{\rho_w g S Q_w}{\pi A L \rho_i R^2}\right)^{1/n}. \tag{7.30}$$

We see that the difference between the effective stress at the channel wall and the far field effective stress calculated using the ice overburden can be large. For $n = 1$ the effective stress at the channel wall will be twice the far field value, while for $n = 4$ the strength of the

till adjacent to the channel will be half the far field value.

The changes in normal stress associated with the channel suggest that the assumption of a constant bed strength used to estimate the effects of a finite basal resistance on the maximum stress resolved on the undeforming bed is a poor one. Our solution could be extended to account for the additional strengthening that equation (7.29) predicts near the channel using an eigenfunction expansion, though this fine detail may not be worth calculating given the large approximations already present due to the assumption of a Newtonian rheology. It should be noted that while equation (7.29) predicts an increase in the basal resistance for $n = 1$, it also predicts a decrease in basal resistance for $n > 2$.

There is one major caveat that must be applied to equation (7.29) first highlighted in *Röthlisberger* [1972][191] regarding the boundary conditions at the bed. We have used the Nye solution to calculate the closure rate for the semi-circular channel at the bed even though this solution is developed for the closure of a circular channel enclosed entirely in ice. The only non-zero velocity in the Nye solution is the radial velocity, and this is found to be axisymmetric around the channel. This symmetry implies that the Nye solution can only be used to calculate the closure of a subglacial channel if we assume free slip boundary conditions at the bed, while our geometry shown in Figure 7.1 assumes no slip on one side of the channel and a deforming bed providing a significant shear resistance on the other. Physical intuition suggests that the switch from the free slip used in the Nye solution to the boundary conditions appropriate for the geometry shown in Figure 7.1 will lower the closure rate from that predicted in equation (7.26). This implies a lower pore pressure in the channel than that predicted by equation (7.27), and thus larger basal strengthening in the immediate vicinity of the channel. As well as altering the pore pressure in the channel, changing

the boundary conditions will alter the normal stress acting on the bed, and thus the yield strength of the undeforming till. *Weertman* [1972][238] argued that far from a channel in a Newtonian material –which was justified by noting that far from the channel any out of plane strain rate is likely much larger than the in-plane strain rate – the change from free to no slip boundary conditions at the bed leads to the effective stress profile

$$\sigma_n - p \approx (\sigma_o - p)\left(1 + \frac{1}{2}\left(\frac{R}{y}\right)^2\right). \tag{7.31}$$

Thus, *Weertman* [1972][238] concluded that far from the channel the no slip boundary conditions lowers the additional hoop stress resolved on the bed, leading to a weaker undeforming bed. However, *Weertman* [1972][238] was unable to produce a formula for the hoop stress immediately adjacent to the channel or for a nonlinear rheology, though he did note the curious switch behavior seen in equation (7.28) where the normal stress at the channel wall is greater than the ice overburden when $n < 2$ and less than the ice overburden when $n > 2$. The asymmetry in boundary conditions across the channel may also lead to asymmetry in the channel shape – possibly invalidating our assumption of a semi-circular channel – and if melting is equally distributed around the channel wall then the asymmetric closure rate may force the channel to migrate towards the undeforming bed. Finally, if the asymmetry in boundary conditions leads to changes in hoop stress across the channel then the strength of the deforming and undeforming bed may be very different even though they have the same pore pressure. Dealing with these many issues is beyond the scope of this paper but we hope to address them in future work.

7.6 Stable margin configurations

In this section we determine when the transition from a deforming to an undeforming bed at a channel leads to a stable margin configuration. To do this we compare the maximum stress on the undeforming bed with the yield strength of the bed at the channel wall. We focus on a Glen's law rheology but generalize our approach to other stress exponents in Appendix E.3. A stable margin configuration exists when the stress on the bed is less than the yield strength of the till across all of the undeforming bed. If we assume that the most likely location for the bed to yield is right at the channel wall where the maximum shear stress on the bed is greatest then we can use equations (7.18) and (7.30) to write the condition for a stable margin configuration as

$$\chi \left(\frac{3J_{tip}}{4\pi AR} \right)^{1/4} < 2f \left(\frac{\rho_w g S Q_w}{\pi A L \rho_i R^2} \right)^{1/3}. \tag{7.32}$$

Note that both the stress on and strength of the bed depend on the channel radius R. This allows us to rearrange the inequality to find

$$R < R_{lock}. \tag{7.33}$$

A stable margin configuration only occurs when the channel radius is less than the critical locking radius R_{lock}, which is defined as

$$R_{lock} = (2f)^{12/5} \left(\frac{\rho_w g S Q_w}{\pi A L \rho_i} \right)^{4/5} \left(\frac{4\pi A}{3J_{tip}} \right)^{3/5}. \tag{7.34}$$

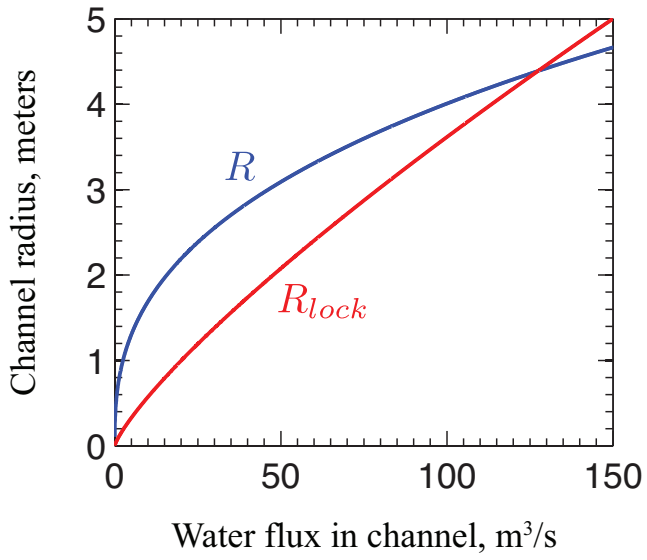

Figure 7.6: A plot showing how the channel radius R and locking radius R_{lock} vary for the parameters in Tables 1 and 2 assuming a Glen's law rheology. We see that $R < R_{lock}$ – and thus a stable margin configuration exists – whenever the water flux exceeds a critical value of ~ 127 m^3/s. This water flux corresponds to a channel with a radius of 4 m.

The form of this result – with a stable margin configuration only occurring below a critical channel radius – surprised us because we expected larger channel sizes to lead to lower maximum stresses on the bed, and thus a higher chance of a stable configuration occurring. However, we had not considered the dependence of till strength on channel size, which turns out to be more sensitive than the dependence of the maximum stress on channel size given in equation (7.18). This conclusion may not be true in a non-steady state model for a channel.

Equations (7.24) and (7.34) show that for fixed material properties and far field loading (parameterized through J_{tip}) the channel radius R and the locking radius R_{lock} are a function of the water flux in the channel Q_w alone. Motivated by this we plot R and R_{lock} as a

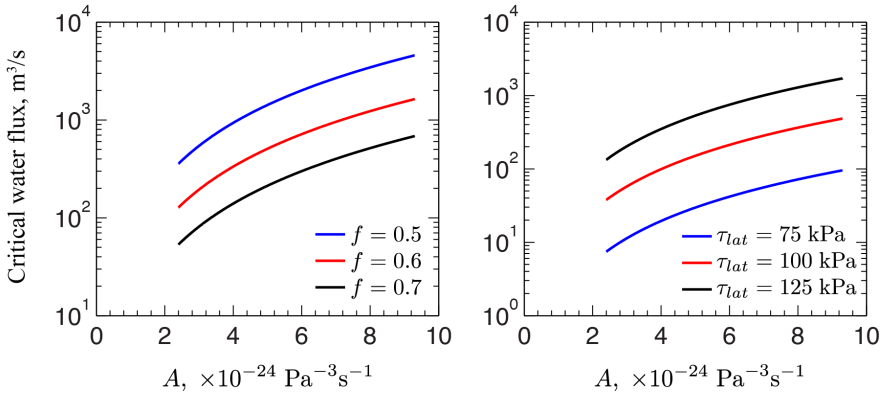

Figure 7.7: A plot showing how the critical water flux Q_{lock} varies for a Glen's law rheology across the range of values for A at $0\,^{\circ}$C outlined in *Cuffey and Paterson* [2010][53] for different values of f and τ_{lat}. These plots were produced using the parameters in Tables 1 and 2. We see significant variability with A with higher values of A leading to larger critical fluxes. This sensitive dependence on the poorly constrained A makes it hard to predict values of Q_{lock}.

function of Q_w, as shown in Figure 7.6. We see that at low water fluxes the channel radius is larger than the locking radius R_{lock}, and thus the margin configuration is not stable. However, R_{lock} increases faster with Q_w than R, leading to a stable margin configuration above a critical flux water flux of $\sim$ 127 m^3/s. This critical flux is much larger than the fluxes typically thought to exist under ice streams in West Antarctica, and thus we conclude that for this far field loading the transition from a deforming to an undeforming bed across a channel will never lead to a stable margin configuration.

Using this dependence of R and R_{lock} on Q_w we can solve for the critical water flux that must be exceeded for a stable margin to occur, leading to

$$Q_{lock} = 2^{25/17} \left(\frac{n_m}{\pi S^{1/2}}\right)^{15/17} \left(1 + \frac{2}{\pi}\right)^{10/17} \left(\frac{\chi}{2f}\right)^{96/17} \left(\frac{\pi A L \rho_i}{\rho_w g S Q_w}\right)^{32/17} \left(\frac{3 J_{tip}}{4\pi A}\right)^{24/17}. \tag{7.35}$$

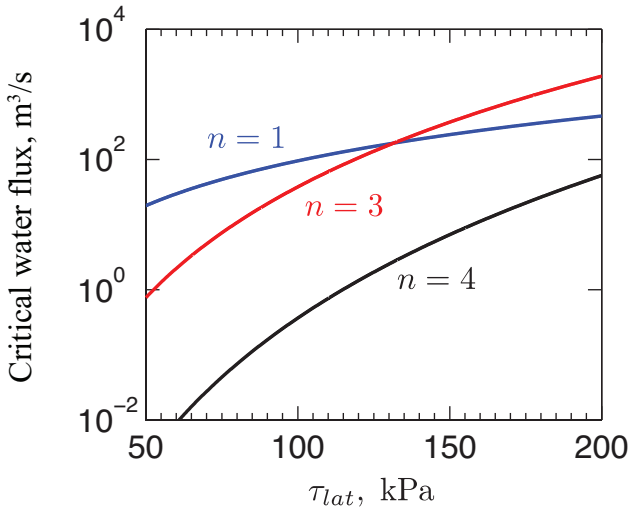

Figure 7.8: A plot showing how the critical water flux Q_{lock} varies with the average stress at the shear margin τ_{lat} for $n = 1, n = 3$, and $n = 4$. This plot was produced using the parameters in Tables 1 and 2. We see that Q_{lock} increases rapidly with τ_{lat}. Note that the $n = 4$ curve predicts much lower critical water fluxes that $n = 1$ and $n = 3$.

This is plotted in Figure 7.7 as a function of the most poorly constrained parameter A for different values of f and τ_{lat}. We chose this range of A based on the scatter in the experimentally measured values of A at 0 °C reported in *Cuffey and Paterson* [2010][53]. We plot the variation with f and τ_{lat} because the critical water flux defined in equation (7.35) depends most sensitively on these parameters. Figure 7.7 shows a strong dependence of the critical water flux on A, with the smallest values of A leading to the smallest values of Q_{lock}. If we assume that a typical water flux in a channel is approximately 1 m^3/s then Figure 7.7 suggests that the transition from a deforming to an undeforming bed across a channel will not be stable if the ice deforms with a Glen's law rheology. To further investigate the dependence on τ_{lat} we plot Q_{lock} as a function of τ_{lat} for all three stress exponents, as shown in Figure 7.8. As in Figure 7.7 we see a strong dependence on τ_{lat}. We see that a stable mar-

gin configuration may occur for values of τ_{lat} less than $\sim$ 50 kPa if $n = 3$, and for values of τ_{lat} less than $\sim$ 125 kPa if $n = 4$. As before this result highlights the importance of determining the appropriate value of n for the shear margin.

7.7 Discussion

7.7.1 Uncertainties in model

A major limitation of our model is the creep closure solution from *Nye* [1953][158] used to predict the effective stress in the channel, which assumes free slip boundary conditions at the bed. This assumption does not agree with the boundary conditions shown in Figure 7.1 with no slip on one side of the channel and a deforming bed with a finite resistance on the other. *Weertman* [1972][238] suggests that the change to more realistic boundary conditions will alter our model for the strength of the undeforming bed in two ways. First, it will lower the creep closure rate, leading to a larger pore pressure decrease in the channel for a given flux, and thus a stronger bed. This behavior is particularly pronounced for larger values of n, and if the realistic boundary conditions lead to a creep closure rate that is half the value predicted by equation (7.26) then the effective stress in the channel increases by a factor of 2^n. Second, *Weertman* [1972][238] showed that the no slip boundary condition may reduce the normal stress applied to the bed, though this conclusion needs to be further tested. If the normal stress is reduced then the yield strength of the till will fall. Our creep closure model also neglects to couple the in-plane strain rates from channel closure with the large anti-plane strain rates expected at the transition from a deforming to an undeforming bed. This important coupling was first noted in *Röthlisberger* [1972][191] and *Weertman* [1972][238], and is expected to lead to easier channel closure. Easier channel closure will lead

to a lower effective stress in the channel, and thus a lower yield strength of the till adjacent to the channel. It is unclear how the three uncertainties associated with the closure model – one of which leads to a stronger bed and two of which lead to a weaker bed – balance each other, though we hope to determine this in future work.

One final comment must be made about the channel geometry assumed in our model. The asymmetry of the boundary conditions across the channel will likely lead to asymmetric closure of the channel, suggesting that our assumption of a semi-circular may not be valid. If melting remains evenly distributed around the channel wall the asymmetry in closure rate also implies that the channel should migrate towards the undeforming bed. If migration occurs – and closure is less rapid near the undeforming bed – then the radius of curvature of the channel wall at the undeforming bed may be larger than the channel radius. This will make the stress limiting effects of the channel more effective, leading to a lower maximum stress on the bed for a given value of J_{tip}. Furthermore, the asymmetry of the boundary conditions will likely lead to different normal stresses on the bed in the deforming and undeforming bed, leading to a discontinuous change in the yield strength of the bed across the channel.

Another limitation of the model regards the structure of the subglacial till. We have assumed a deforming bed on one side of the channel and an undeforming bed on other, but have not explicitly modeled how this transition occurs in the till. We have also assumed that the entirety of the channel is incised in the ice, ignoring the possibility that a channel may develop in the till. More work is needed to determine how the presence of a channel in the till will alter our predictions, though the results in *Perol and Rice* [2011][161] and *Perol et al.* [in preparation][163] indicate that any channelized drainage system that operates at a high

effective stress could select the shear margin location regardless of whether the channel is incised into the ice or into the till. Other possible extensions to the model could look at the effects of a non-steady water flux, the time-dependent transport of water to the channel, and other physical effects that be important at high effective stresses such as the penetration of ice into the till studied in *Rempel* [2009][181].

7.7.2 Relation between three critical points on bed

As highlighted in this paper – and noted in *Schoof* [2004][198] and *Suckale et al.* [2014][216] – the transition from a deforming bed to an undeforming bed concentrates large stresses on the undeforming portion of the bed. Thus, for a stable margin configuration to occur where the stress on the undeforming bed is always lower than the yield strength of the bed there must be a mechanism to greatly increase the basal strength within a shear margin. Two main possibilities have been proposed. First, the required increase in basal strength has been linked to freezing of the till. Second, *Perol and Rice* [2011][161] and *Perol et al.* [in preparation][163] argued that a subglacial drainage channel within a shear margin could raise the yield strength. We advocate thinking of the structure of an ice stream shear margin in terms of three critical points. The first of these is the locking point where the transition from a deforming to an undeforming bed occurs. The second critical point is the freezing point where the bed transitions from temperate to frozen. The final critical point is the channel location.

Having defined these three critical points we can describe three possible shear margins configurations. In the first configuration the locking point and the freezing point are collocated, and the channel location – or even the presence of a channel within the shear mar-

gin – is unimportant. For this configuration, which was studied in *Jacobson and Raymond* [1998][116] and *Schoof* [2012][199], the increased basal resistance required for a stable margin configuration comes from the presumably large yield strength of the frozen till.

The second possible margin configuration is the one studied in this paper where the locking point is collocated with the channel location. As discussed in Section 7.6, our analysis indicates that this configuration will only be stable if the flux in the channel exceeds a critical value. As shown in this paper, when the channel is collocated with the locking point it is important to properly understanding how a channel alters the basal stress and strength at the locking point.

The third possible margin configuration none of the three critical points are collocated, and the freezing point is closer to the ridge than the other two critical points. In this case the presence of a channel increases the basal strength in a broad zone within the shear margin, allowing a non-singular stress profile at the transition point through the kind of cohesive zone model proposed by *Barenblatt* [1959][6] and *Dugdale* [1960][65]. This is analogous to the solutions in *Schoof* [2004][198] but with a physical model for spatial (and potentially temporal if the margin migrates) variations in the basal strength. Note that for the third type of configuration the locking point occurs on a temperate bed, and thus parts of the locked bed are temperate. For a temperate yet locked bed to occur the basal strength of the till between the locking point and the freezing point must be greater than the gravitational stress driving the ice stream. For this to be consistent with the experiments of *Kamb* [1991][120], *Iverson et al.* [1998][112] and *Tulaczyk et al.* [2000][226] the pore pressure in the subglacial till must be lower than the pore pressures inferred beneath major ice streams or the bed will fail. These lower pore pressures may be possible due to the lack of melt generated

by basal deformation in the undeforming bed – and the proximity of the undeforming bed to the channel – and we highlight the importance of modeling the pore pressure evolution in the entire temperate bed, and not just in the deforming portion of the bed as was done in *Perol et al.* [in preparation][163].

There is no reason that the type of margin configuration must be the same throughout an ice stream, and we will briefly hypothesize how the type of margin configuration could vary with distance from the grounding line. The calculations in *Perol and Rice* [2011][161] and *Perol et al.* [in preparation][163] predict the total melt generated per unit downstream length and then calculate a total water flux in the channel by assuming a upstream length that the channel drains, suggesting that the flux in the channel will be larger near the grounding line than near to where the ice stream initiates. It can be shown that both of the hydrologic mechanisms for a stable margin configuration outlined above – one with the locking point collocated with the channel and the other with the locking point occurring on the temperate bed – become more effective as the flux in the channel increases. From this we conclude that the ability of a channel to select the location of a shear margin may be greater in the downstream end of an ice stream rather than in the upstream region, suggesting that if there is limited subglacial water near where an ice stream initiates the locking point is likely collocated with the freezing point of the subglacial till.

The three margin configurations outlined above are not the only possibilities. For example there may be some locations where topography does select the shear margin location, either alone or in combination with one of the mechanisms described above. In addition the three possible configurations outlined above assumed a single locking point, freezing point and channel location. This is a strict assumption that possibly should be relaxed.

7.7.3 Links with margin migration

The analysis presented in this paper focuses on the stress on and strength of the subglacial till in the few tens of meters immediately adjacent to a channel. However, using the different types of margin configurations defined in subsection 7.7.2 we can discuss the role a channel may play in shear margin migration. Previous work by *Jacobson and Raymond* [1998][116] and *Schoof* [2012][199] studied how margin migration could occur when the locking point is collocated with the freezing point, and thus the strengthening required for a stable margin configuration to occur comes from freezing of the subglacial till. In this description the frictional heating associated with the stress concentration at the locking point raises the bed underneath the ridge to the melting point allowing migration to occur.

Observations show that ice stream shear margins can migrate at a range of speeds. Using repeated measurements of the surface velocity *Echelmeyer and Harrison* [1999][69] estimated that Dragon margin of Ice Stream B was migrating towards the ridge at a velocity of 9.7 ± 1.1 m a^{-1}; *Bindschadler and Vornberger* [1998][19] used satellite images taken several decades apart to show that further downstream the margin of Ice Stream B had migrated 3973 ± 986 m towards the ridge in 29 years, corresponding to an average migration rate of 137 ± 34 m a^{-1}. The two different migration velocities over an order of magnitude apart may indicate that multiple mechanisms can lead to margin migration, with one mechanism leading to slow migration on the order of 10 m a^{-1} and another allowing faster migration. As noted in *Perol et al.* [in preparation][163], if the locking point is not collocated with the channel location then the channel selects the margin location by raising the basal strength in a zone several kilometers wide within the shear margin, which acts like a cohesive zone commonly used in fracture mechanics[6,65]. However, sustained basal sliding within the

strengthened region will generate melt, which will weaken the bed if this melt generation occurs faster than hydraulic diffusion. The analogy with the cohesive zone models and the form of the J-integral given in *Suckale et al.* [2014][216] and *Perol et al.* [in preparation][163] suggest that this weakening of the bed in the shear margin will allowing the locking point to migrate towards the ridge, and thus we expect gradual margin migration to occur as the subglacial pore pressure profile changes.

The observations of *Bindschadler and Vornberger* [1998][19] are only able to measure the total distance that the shear margin migrated during the 29 year period that elapsed between the satellite images. This means that a discrete event where the margin migrated several kilometers in a short period of time is as consistent with the observations as the uniform migration at a rate of 137 ± 34 m a^{-1} calculated in *Bindschadler and Vornberger* [1998][19]. The second and third stable margin configurations described in subsection naturally allow for such a rapid migration event. When the locking point is collocated with the channel location then the limiting of the maximum stress by the channel allows a stable margin configuration to exist for a finite value of J_{tip} provided that the water flux in the channel exceeds a critical value. However, if the water flux falls beneath this critical value then the locking point will migrate away from the channel location to the point where the additional basal resistance leads to a situation with $J_{tip} = 0$. The channel may thus pin and then release the locking point as the flux in the channel varies.

The discussion in this subsection neglected transient effects such as the time taken for hydraulic diffusion to occur or the rate at which advection of cold ice from the adjacent ridge cools the ice within the shear margin. We hope to extend the models used in *Perol and Rice* [2011][161], *Suckale et al.* [2014][216], and *Perol et al.* [in preparation][163] to account

for non-steady state effects, and see how these could control margin migration. We also neglected to discuss how changes in ice stream geometry with distance from the grounding line could alter shear margin migration. It is possible that the large differences between the observations of *Bindschadler and Vornberger* [1998][19] and *Echelmeyer and Harrison* [1999][69] could be explained by a single mechanism controlling margin migration operating differently in the upstream and downstream portions of the ice stream.

7.7.4 Importance of ice rheology

While a simple Glen's law rheology may be a good approximation for ice stream scale simulations, the work presented in this paper shows the importance of properly determining the dominant physical processes that allow ice to deform over a range of stresses. Figures 7.7 and 7.8 show that the critical water flux that controls if the transition from a deforming to an undeforming bed across a channel is stable depends sensitively on the assumed values of n and A. The closure rate of and pore pressure in a channel – an important consideration in all models of subglacial drainage channels – also depend strongly on A and n.

The high shear stresses associated with the transition from a deforming to an undeforming bed mean that the ice may deform solely through dislocation creep, which is the dominant deformation mechanism at the highest stress possible in ice streams[89]. Thus, the proper rheology in the immediate vicinity of the channel is likely to be the $n = 4$ rheology from *Durham et al.* [1997][66]. One potential caveat to this conclusion relates to the grain size. If we assume a grain size of 4 mm – a typical grain size observed in the shear margin cores from *Jackson and Kamb* [1997][113] – we can use Figure 60.3 from *Goldsby* [2006][90] to predict that $n = 4$ is the appropriate stress exponent for stresses exceeding $\sim$ 200 kPa.

Figure 7.4 tells us that this critical value is lower than the shear stress expected on the undeforming bed for a channel with radius 1 m. However, the stress concentration at the transition point could drive significant grain size reduction. Again using *Goldsby* [2006][90] we see that if the grain size is reduced to 1 mm then we must exceed a stress of $\sim$ 1 MPa before dislocation creep dominates, and if the grain size reaches 100 μm then we must exceed a stress of $\sim$ 2 MPa. These stresses may be higher than the concentrated stresses at the locking point. If $n = 4$ is not the dominant deformation mechanism then we expect to fall into the grain-boundary sliding regime described in *Goldsby and Kohlstedt* [2001][89], which is governed by $n = 1.8$. The concentrated stresses present at the locking point may also allow a fabric to develop in the ice, and if this occurs then the value of A governing the creep closure of the channel will not be the same as the value of A governing the shear stress resolved on the bed.

Finally, in Section 7.2 we assumed that the melt content of the ice immediately adjacent to the channel could be neglected when determining values of A and n. However, this assumption may not be valid for all shear margins, especially if a large amount of temperate ice is present. Accurately determining the effect of melt fraction on rheology is beyond the capability of current experiments, though the experiments in *Duval* [1977][67] and *Lliboutry and Duval* [1985][136] showed that a melt fraction of just 1.1% increases A by about a factor of three. Other experiments performed on partially molten olivine – which deforms through the same physical mechanisms as ice – showed increasing the melt fraction promotes grain boundary diffusion creep, which is governed by a stress exponent of one[50]. Thus, it may not be sufficient to just make A a function of the melt fraction, and there may also be a change in n at a given shear stress.

When predicting the melt content in the ice adjacent it may be helpful to think of two end-member behaviors. First, for the case where the subglacial transport of melt – either through the till or the ice-till interface – is more efficient than englacial transport then we expect melt to first be routed to the bed and then flow along the bed to the channel. This may imply a low water content in the ice immediately adjacent to the channel. Second, if the subglacial hydrology is inefficient then melt may be routed to the channel through the ice, implying a large water content in the ice next to the channel. A significant melt content will lead to large increases in A, and possible cause the dominant deformation mechanism to switch to diffusion creep. The implications of these changes for the locking mechanism analyzed in this paper are evident in Figure 7.7, which shows that as A increases the critical water flux required for the locking point to occur at a channel increases dramatically and that unrealistically large fluxes are required to cause locking if $n = 1$.

7.8 Conclusions

Building on *Rice* [1967][182] we began by analyzing a sharp transition from a deforming to an undeforming bed at a shear margin, showing that this leads to a singular stress on the undeforming bed. The power of the singularity depends on the stress exponent n, with larger values of n leading to a less severe singularity. If we assume a uniform basal resistance beneath the ice stream then the stress on the bed is directly proportional to the average lateral stress supported by the margins.

Next we showed how the presence of a channel limits the maximum stress on the undeforming bed, extending the analysis in *Perol et al.* [2012][162]. Using a combination of analytic and numerical methods we solved for this maximum stress as a function of all of the

parameters in the problem. We found that the maximum stress is sensitive to the choice of stress exponent, with a Newtonian rheology leading to unrealistically large stress on the undeforming bed.

In addition we looked at how a subglacial drainage channel alters the strength of the bed and possibly selects the margin location, as suggested in *Perol and Rice* [2011][161] and *Perol et al.* [in preparation][163]. As shown in *Röthlisberger* [1972][191] and *Shreve* [1972][204], the presence of a channel decreases the pore pressure of the subglacial till and thus leads to strengthening. We also discussed how the presence of a channel alters the normal stress applied to the ice-till interface, though this behavior is still poorly understood due to the issues with boundary conditions and the coupling of in-plane and anti-plane strain rates highlighted in *Weertman* [1972][238].

Finally we compared the maximum stress on the undeforming bed with the yield strength of the till to determine when the transition from a deforming to an undeforming bed at a channel is a stable margin configuration. We found that a stable configuration occurs when the water flux in the channel exceeds a critical value. Determining this value is hard due to uncertainties in our model and the appropriate ice rheology, but it seems likely that a stable configuration never occurs for $n = 3$, but can exist for $n = 4$ and typical values of the lateral drag at the margin.

8

Conclusion

The aim of this thesis has been to study the rapid weakening accompanying seismic slip and the thermal and mechanical structure of ice stream shear margins. Both of these problems were tackled using a combination of analytic and numerical methods, and highlighted how the different feedbacks between temperature, stress, and chemistry can dominate complicated geophysical systems. Detailed conclusions can be found at the end of each chapter but

we will highlight a few key results and possible extensions below.

Chapters 2-5 studied the role thermal pressurization and thermal decomposition play during an earthquake. We showed how the positive feedback between heating and weakening drives micron-scale strain localization, and that the onset of localization concentrates frictional heating into a narrow zone and accelerates co-seismic weakening. Following this we showed how thermal pressurization and thermal decomposition can combine to propagate a slip pulse, showing that different balance between the two weakening mechanisms exist and correspond to different rupture modes, and determining the key physical balances that control the severity of weakening that accompanies the onset of the reaction. There are several extensions to these projects of which we will discuss one. All of the work in this thesis used parameters determined for a single depth – either 1 km or 7 km – and did not account for the depth dependence of the different co-seismic weakening mechanisms. As our understanding of the physics underlying dynamic weakening increases it will become important to determine how dynamic weakening deteriorates with depth, possibly due to the closure of pores or the crossing of an equilibrium phase boundary. The current paradigm for the base of the seismogenic zone relies on failure conditions derived from experiments performed at low slip rates, which appears to contradict geophysical observations showing that mature faults operate at driving stresses far below those predicted by Byerlee's law. Based on these observations we suggest that it could be possible that the base of the seismogenic zone is set by the inability to propagate a rupture – rather than the inability to nucleate a rupture – and thus seismicity should rarely occur at depths where dynamic weakening is inefficient.

Chapter 6 looked at how the concentrated deformation present at ice stream shear mar-

gins could lead to the formation of temperate ice. We showed that properly accounting for the temperature dependence of the rheology is crucial, and that surface velocity observations of an ice stream shear margin can only be explained by the presence of a large body of temperate ice within the shear margin. In addition we highlighted the importance of properly constraining the advection of cold ice from the adjacent ridge into the shear margin. Finally we showed that the shear margin can be a significant source of melt, as previously shown in *Schoof* [2004][198] and *Perol and Rice* [2011][161]. Chapter 7 presented one mechanism for how the presence of a drainage channel could select the location of an ice stream shear margin. By studying how the drainage channel alters the stress field, we showed that the transition from a deforming to an undeforming bed could be collocated with the channel if the water flux in the channel exceeds a critical value. However, determining the value of this critical water flux is complicated by current uncertainties in the appropriate rheology for the ice near a channel, and we briefly discussed how different balances between englacial and subglacial hydrology could control the melt content of the ice immediately adjacent to the channel. Future work in this area should determine how this mechanism balances the cohesive zone mechanism proposed in *Perol and Rice* [2011][161] that could also allow a channel to select the shear margin location. For fixed material properties, both hydrologic mechanisms are determined by a critical water flux in the channel, highlighting the importance of developing physically realistic models for melt generation and transport within an ice stream.

A

Additional Materials for Chapter Two

A.1 Possible responses for frictional rate-strengthening only

Here we present a more detailed discussion of the possible responses for the frictional strengthening only system. Equation (2.38) relates the growth exponent s for the perturbations to the wavelength λ of the perturbations. This equation can be solved using standard

techniques for quadratic equations to find

$$s = \frac{1}{2}\left(zH\dot{\gamma}_o - \frac{4\pi^2}{\lambda^2}(\alpha_{th} + \alpha_{hy})\right) \pm \frac{\sqrt{D}}{2}, \tag{A.1}$$

where D is the discriminant of the equation,

$$D = \frac{16\pi^4}{\lambda^4}(\alpha_{th} - \alpha_{hy})^2 - \frac{8\pi^2}{\lambda^2}(\alpha_{th} + \alpha_{hy})zH\dot{\gamma}_o + z^2H^2\dot{\gamma}_o^2. \tag{A.2}$$

For simplicity we have used the definitions

$$H = \frac{f_o\Lambda}{\rho c} \quad , \quad z = \frac{f_o}{a-b}. \tag{A.3}$$

Noting that D itself is a quadratic in λ^{-2}, we can solve to find the range for which $D < 0$. When $D < 0$ the exponential coefficient s will have a non-zero imaginary component, signaling an oscillatory response to perturbation with exponentially growing or decaying amplitude. We find that $D < 0$ for the finite range of wavelengths $\lambda_1 < \lambda < \lambda_2$, where

$$\lambda_1 = 2\pi\frac{\left|\sqrt{\alpha_{hy}} - \sqrt{\alpha_{th}}\right|}{\sqrt{zH\dot{\gamma}_o}} \quad , \quad \lambda_2 = 2\pi\frac{\sqrt{\alpha_{hy}} + \sqrt{\alpha_{th}}}{\sqrt{zH\dot{\gamma}_o}}. \tag{A.4}$$

Assuming that $D < 0$ when $Re(s) = 0$ we can find the critical wavelength separating growing and decaying perturbations in p and T to be

$$\lambda_{pT} = 2\pi\sqrt{\frac{\alpha_{th} + \alpha_{hy}}{zH\dot{\gamma}_0}}. \tag{A.5}$$

For $\lambda > \lambda_{pT}$ perturbations in p and T will grow. Recalling equation (2.37), which shows that the time dependence for the strain perturbation $\dot{\gamma}_1$ is $s + H\dot{\gamma}_o$, we can determine a similar critical wavelength for the strain rate perturbation $\dot{\gamma}_1$,

$$\lambda_{shr} = 2\pi\sqrt{\frac{\alpha_{th} + \alpha_{hy}}{(z+2)H\dot{\gamma}_0}}. \tag{A.6}$$

For $\lambda > \lambda_{shr}$ the perturbation $\dot{\gamma}_1$ will grow and homogeneous shear is unstable. For all physical parameter choices

$$\lambda_{shr} < \lambda_{pT} < \lambda_2. \tag{A.7}$$

A final ordering $\lambda_1 < \lambda_{shr}$ can also be proven provided that $z > z_c$ where the critical value of z is

$$z_c = \frac{(\sqrt{\alpha_{hy}} - \sqrt{\alpha_{th}})^2}{\sqrt{\alpha_{th}\alpha_{hy}}}. \tag{A.8}$$

If $z > z_c$ then the assumption $D < 0$ used to calculate the formulas for λ_{pT} and λ_{shr} is true, and the formulae in equations (A.5) and (A.6) are exactly the critical wavelengths separating growing and decaying perturbations in $\{p, T\}$ and $\dot{\gamma}$ respectively. The four parameters sets considered in this paper lead to the range $z_c = 0.01 - 1.81$, meaning that $z > z_c$ for any realistic values of f_o and $(a - b)$, which have $f_o \gg (a - b)$. When $z < z_c$ the formulae for λ_{pT} and λ_{shr} are no longer valid. Noting that the value of α_{th} is relatively well constrained[186], a parameter set with $z < z_c$ would require a value of α_{hy} at least an order of magnitude greater than the largest values assumed here.

Having solved for the critical wavelengths controlling the system we next discuss how perturbations of different wavelengths will evolve. As mentioned before, for $\lambda > \lambda_{pT}$ perturbations in p and T will grow exponentially; similarly for $\lambda > \lambda_{shr}$ perturbations

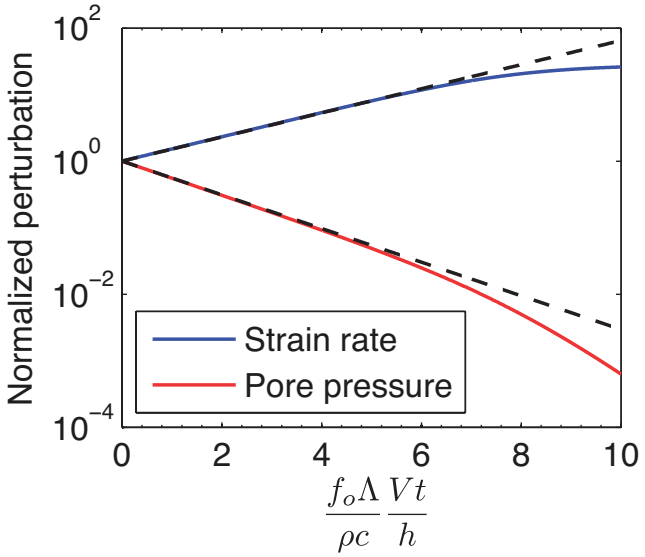

Figure A.1: Rate-strengthening friction: A plot showing the normalized perturbations $\dot{\gamma}_1(t)/\dot{\gamma}_1(0)$ and $p_1(t)/p_1(0)$for the nominal parameters for a damaged material, a uniform strain rate $\dot{\gamma}_o = 1000\,\mathrm{s}^{-1}$, and a perturbation wavelength $\lambda = 310\,\mu$m. The linear stability predicts an exponential form for the two perturbations, as shown by the dashed black lines. For the chosen parameters we see that the linear stability analysis predicts that the strain rate perturbation will grow while the pore pressure and temperature perturbations decay. This is supported by the numerical simulations (solid lines) which use the logarithmic friction law as in equation (2.6), rather than its linearization in equation (2.4). After the strain rate perturbation has grown sufficiently nonlinear effects become important. We see that the exponential growth predicted by the linear stability analysis does not continue indefinitely and nonlinear effects limit the strain rate perturbation to a finite value.

in $\dot{\gamma}$ will grow, making uniform shear of the gouge material unstable. The small difference between λ_{pT} and λ_{shr} means that for a narrow range of wavelengths $\dot{\gamma}_1$ will grow while p_1 and T_1 decay. Figure A.1 shows $\dot{\gamma}_1$ and p_1, normalized by the initial perturbation size, for a system with periodic boundary conditions. This calculation uses the nominal parameters for a damaged material, a uniform strain rate $\dot{\gamma}_o = 1000\ \text{s}^{-1}$, a perturbation wavelength $\lambda = 310\ \mu\text{m}$, and the logarithmic friction law in equation (2.6).

For $\lambda_1 < \lambda < \lambda_2$ there will be an imaginary component to s. This is associated with propagation of the perturbations, with the two complex conjugate roots corresponding to propagation in the positive and negative y-direction. This propagation is compatible with a formulation that uses periodic boundary conditions to model an infinite domain, but not with zero flux boundary conditions at the edge of a finite thickness gouge layer. Any propagation of the Fourier mode in the y-direction will lead to a perturbation that no longer satisfies the zero flux boundary conditions at the edge of the gouge layer. In the system with zero flux boundary conditions at the boundary of the gouge layer a complex value of s leads to oscillatory growth or decay, provided that the initial conditions are symmetric about the center of the layer this can be thought of as a standing wave. Figure A.2 shows $\dot{\gamma}(y,t)$ for a system with periodic boundary conditions using the nominal parameters for a damaged material, a uniform strain rate $\dot{\gamma}_o = 1000\ \text{s}^{-1}$, and a perturbation wavelength $\lambda = 360\ \mu\text{m}$. This is based on numerical simulations, again like in Figure A.1, but using the logarithmic friction law from equation (2.6) rather than the linearization given in equation (2.4). As predicted by the linear stability analysis, we see growth and propagation of the perturbation. The perturbation does not grow indefinitely but is instead capped by nonlinear effects at a finite value. The black line indicates the phase velocity predicted by the linear

stability analysis, and we see excellent agreement between the predicted propagation speed and that initially observed in the numerical simulations. Once nonlinear effects become important the perturbations continue to propagate, but now do so with a velocity faster than the phase velocity predicted by the linearized analysis.

A.2 Numerical methods

In this section we briefly describe the numerical methods used to solve for the strain rate evolution in chapters 2,3, and 4. For simplicity this method is outlined using the dimensionless equations for strain localization driven by thermal pressurization alone and stabilized by rate-strengthening friction alone, but can be easily extended to account for dilatancy or thermal decomposition. In what follows we drop the primes on dimensionless variables to reduce notation.

To begin we use the assumed friction law to write $\dot{\gamma}$ as a function of τ and p,

$$\dot{\gamma} = 2\sinh\left(\frac{z\tau}{1-p}\right)\exp(-z). \tag{A.9}$$

This leads to three equations

$$\frac{\partial T}{\partial t} = 2\tau\sinh\left(\frac{z\tau}{1-p}\right)\exp(-z) + D_{th}\frac{\partial^2 T}{\partial y^2}, \tag{A.10}$$

$$\frac{\partial p}{\partial t} = \frac{\partial T}{\partial t} + D_{hy}\frac{\partial^2 p}{\partial y^2}, \tag{A.11}$$

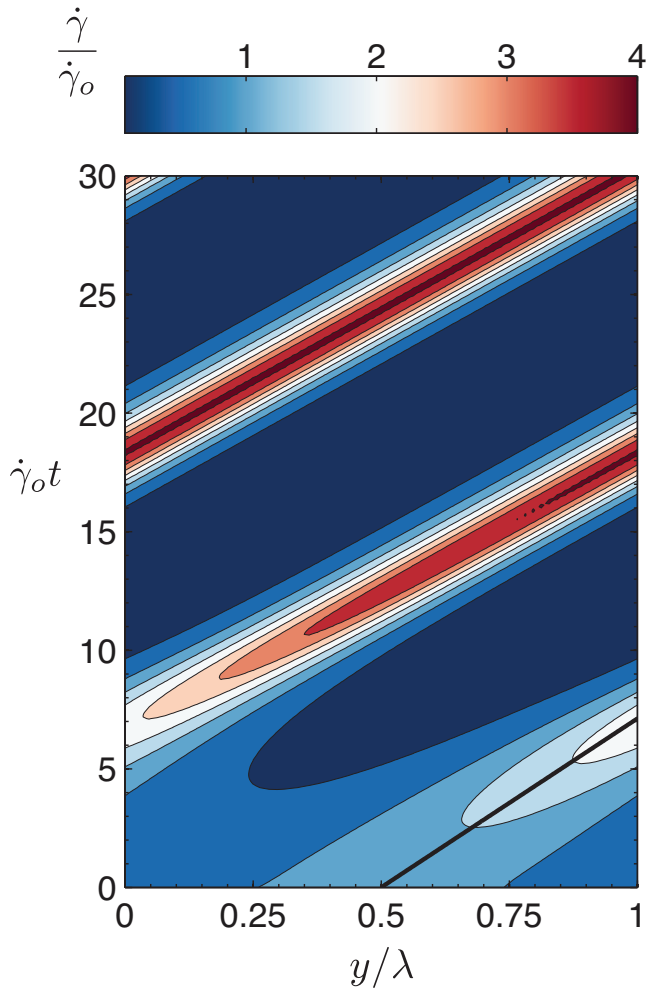

Figure A.2: Rate-strengthening friction: A plot showing $\dot{\gamma}(y,t)$ for a system with periodic boundary conditions using the nominal parameters for a damaged material, a uniform strain rate $\dot{\gamma}_o = 1000$ s^{-1}, a perturbation wavelength $\lambda = 360\,\mu$m and an initial pore pressure perturbation that is 1% of the ambient effective stress $\bar{\sigma}_a$. The parameters and uniform strain rate determine the critical wavelength λ_{shr}, and this determines if the perturbation grows or decays. For this case, as predicted by the linear stability analysis, the initial strain rate perturbation propagates as it grows. The black line in the bottom-right corner indicates the predicted propagation speed, which is in excellent agreement with initial speed observed in the numerical simulations. Once nonlinear effects become important the strain rate perturbation ceases growing but continues to propagate at a speed slightly faster than the predicted phase velocity.

$$\int_{-1/2}^{+1/2} 2\sinh\left(\frac{z\tau}{1-p}\right)\exp(-z)\mathrm{d}y = 1, \tag{A.12}$$

where the final equation ensures that the total straining accommodated across the gouge layer equals the slip rate applied across the gouge layer. These three equations are used to solve numerically for T, p, and τ on a uniform grid defined by

$$y_i = i\Delta y \quad , \quad i = -N_{tot}/2, \ldots, N_{tot}/2, \tag{A.13}$$

where N is the number of nodes within the gouge layer, Ω is the ratio of the width of the domain adjacent to the gouge layer and the gouge layer thickness (making $N_{tot} = 2\Omega N$), and the grid size is

$$\Delta y = \frac{1}{N}. \tag{A.14}$$

For the simulations with periodic boundary conditions shown in this Appendix we set $\Omega = 0$ and set $T_{-N/2} = T_{+N/2}$ and $p_{-N/2} = p_{+N/2}$. For the simulations with a gouge layer confined between two hydraulically and thermally conducting half spaces presented in chapters 3 and 4, Ω is chosen to be sufficiently large that the gouge layer does not feel the boundaries during the simulation. This makes the solution independent of Ω and we use the Dirichlet boundary conditions $T(y_{-N_{tot}/2}) = T(y_{+N_{tot}/2}) = p(y_{-N_{tot}/2}) = p(y_{+N_{tot}/2}) = 0$.

We define the values of T and p on the uniform grid by $T_i(t) = T(y_i, t)$ and $p_i(t) = p(y_i, t)$. Next we approximate the second derivatives in T and p on all internal grid-points using centered finite differences, which turns the partial differential equations for tempera-

ture and pore pressure into a system of ordinary differential equations

$$\frac{\mathrm{d}T_i}{\mathrm{d}t} = 2\tau \sinh\left(\frac{z\tau}{1-p_i}\right)\exp(-z)I(y_i) + D_{th}\frac{T_{i+1}-2T_i+T_{i-1}}{\Delta y^2}, \tag{A.15}$$

$$\frac{\mathrm{d}p_i}{\mathrm{d}t} = \frac{\partial T_i}{\partial t} + D_{hy}\frac{p_{i+1}-2p_i+p_{i-1}}{\Delta y^2}, \tag{A.16}$$

where $I(y_i) = H(y_i + 1/2) - H(y_i - 1/2)$ and $H(x)$ is the Heaviside function. The final variable τ is updated by discretizing equation (A.12) using a standard quadrature such as the trapezoidal rule or Simpson's rule. This leads to the algebraic equation

$$\sum_{i=-N/2}^{+N/2} w_i 2\sinh\left(\frac{z\tau}{1-p_i}\right)\exp(-z) = 1, \tag{A.17}$$

where w_i are the weights for the chosen quadrature. In this numerical solution we solve for p and T using standard techniques for ordinary differential equations and find τ at each time-step by applying standard root-finding techniques to equation (A.17).

An alternative method involves differentiating equation (A.17) to find

$$\sum_{i=-N/2}^{+N/2} w_i \cosh\left(\frac{z\tau}{1-p_i}\right)\left(\frac{\mathrm{d}\tau}{\mathrm{d}t}\frac{1}{1-p_i} + \frac{\tau}{(1-p_i)^2}\frac{\mathrm{d}p_i}{\mathrm{d}t}\right) = 0. \tag{A.18}$$

Rearranging equation (A.18) and noticing that τ is the same at all points within the gouge layer we find an ordinary differential equation for τ

$$\frac{\mathrm{d}\tau}{\mathrm{d}t} = -\frac{\sum_{i=-N/2}^{+N/2}\frac{w_i\tau}{(1-p_i)^2}\frac{\mathrm{d}p_i}{\mathrm{d}t}\cosh\left(\frac{z\tau}{1-p_i}\right)}{\sum_{i=-N/2}^{+N/2}\frac{w_i}{(1-p_i)}\cosh\left(\frac{z\tau}{1-p_i}\right)} \tag{A.19}$$

In the alternative method we can use standard solvers for ordinary differential equation to update p, T and τ simultaneously, and thus no longer need to solve the root-finding problem.

The majority of the simulations presented in this thesis were performed using the root-finding method, though both methods were tested and found to be consistent with each other. The simulations in which localization is stabilized by dilatancy alone were performed using a similar root-finding method to update the pore pressure, which is spatially uniform across the gouge layer. Finally, when inertial effects within the gouge layer are accounted for we are not required to solve an algebraic equation and can update the strain rate directly using the dimensionless partial differential equation,

$$I^2 \frac{\partial \dot{\gamma}}{\partial t} = \frac{\partial^2 \tau}{\partial y^2} \quad , \quad I = \sqrt{\frac{\rho V^2}{(\sigma_n - p_a)}}. \tag{A.20}$$

B

Additional Materials for Chapter Four

B.1 Dimensionless parameters

The model presented in Section 4.2 is rich in parameters. In this appendix we nondimensionalize the model to determine the number of parameters that can be varied independently, and discuss the physical significance of each dimensionless parameter.

First we scale the spatial coordinate y using the gouge layer thickness h. Combining

this thickness with the slip rate we get the nominal strain rate $\dot{\gamma}_0 = V/h$, which is used to nondimensionalize the strain rate. Combining the nominal strain rate with the critical weakening strain for thermal pressurization leads to the weakening timescale $t_w = \rho ch/f_0 \Lambda V$ for thermal pressurization, which is used to scale t. Finally, we use the ambient effective stress to scale the pore pressure rise, and the total temperature rise from the uniform solution $\bar{\sigma}_a/\Lambda$ for thermal pressurization alone to scale the temperature. To summarize, the scalings used are

$$y = hy' \quad , \quad t = \frac{\rho ch}{f_o \Lambda V} t' \quad , \quad \dot{\gamma} = \dot{\gamma}_o \dot{\gamma}' \tag{B.1}$$
$$p = p_a + (\sigma_n - p_a) p' \quad , \quad T = \frac{\sigma_n - p_a}{\Lambda} T',$$

where primes indicate dimensionless variables. The only difference between these scalings and those used in *Platt et al.* [2014][166] is that here we scale the temperature T and not the temperature rise above an ambient temperature $T - T_a$. We do not need to scale ξ because it is already dimensionless.

Using these scalings we find the dimensionless set of equations,

$$\frac{\partial T'}{\partial t'} = \tau' \dot{\gamma}' + D_{th} \frac{\partial^2 T'}{\partial y'^2} - R_{th} \frac{\partial \xi}{\partial t'}, \tag{B.2}$$

$$\frac{\partial p'}{\partial t'} = \frac{\partial T'}{\partial t'} + D_{hy} \frac{\partial^2 p'}{\partial y'^2} + R_{hy} \frac{\partial \xi}{\partial t'}, \tag{B.3}$$

$$\frac{\partial \tau'}{\partial y'} = 0 \quad , \quad \tau = f(\dot{\gamma}')(1 - p'), \tag{B.4}$$

$$f(\dot{\gamma}') = 1 + z^{-1} \log \dot{\gamma}', \tag{B.5}$$

$$\frac{\partial \xi}{\partial t'} = F(1 - \xi) \exp\left(-\frac{G}{T'}\right). \tag{B.6}$$

The initial conditions for pore pressure and temperature are

$$p' = 0 \quad , \quad T' = T_I, \tag{B.7}$$

and the initial uniform strain rate profile within the gouge layer is $\dot{\gamma}' = 1$.

The system is controlled by eight dimensionless parameters,

$$D_{th} = \frac{\alpha_{th}\rho c}{f_0 \Lambda V h} \quad , \quad D_{hy} = \frac{\alpha_{hy}\rho c}{f_0 \Lambda V h} \quad , \quad z = \frac{f_0}{a-b} \quad , \quad T_I = \frac{T_a \Lambda}{\sigma_n - p_a},$$

$$R_{th} = \frac{\bar{m} E_r \Lambda}{\sigma_n - p_a} \quad , \quad R_{hy} = \frac{\bar{m} P_r}{\sigma_n - p_a} \quad , \quad F = \frac{A\rho c}{\dot{\gamma}_0 f_0 \Lambda} \quad , \quad G = \frac{Q\Lambda}{R(\sigma_n - p_a)}.$$

Each of these dimensionless parameters has a clear physical meaning. First, D_{th}, D_{hy} and z are identical to the dimensionless parameters found in *Platt et al.* [2014][166], and control the behavior of the system before thermal decomposition is triggered. D_{th} and D_{hy} measure the efficiency of thermal and hydraulic diffusion respectively, and z measures the rate-strengthening component of the friction law. As shown in *Platt et al.* [2014][166], D_{th} and D_{hy} can be linked to the ratio of the gouge layer thickness and the diffusion distances for thermal and hydraulic diffusion on timescales comparable to the weakening timescale

for thermal pressurization. Next, the parameters R_{th} and R_{hy} quantify the magnitude of the temperature rise buffered and pore pressure generated by the thermal decomposition reaction. R_{th} is the temperature rise buffered by a completed reaction normalized by the temperature rise for a gouge layer sheared uniformly under undrained and adiabatic conditions, and R_{hy} is the total pore pressure rise generated by a completed reaction normalized by the ambient effective stress. Finally, the parameters F, Q and T_I control the kinetics of the reaction. If A is thought of as a reaction attempt frequency then F is the attempts that occur during the weakening timescale for thermal pressurization, G is a dimensionless activation energy for the reaction, and T_I determines where the initial conditions lie on the dimensionless reaction kinetic.

C

Additional Materials for Chapter Five

C.1 Nondimensionalization

To nondimensionalize our model we use the scalings from *Garagash* [2012][86]. First we normalize the along-fault distance x using the slip pulse length L, and normalize the across fault coordinated y using the deforming zone thickness W. Next we normalize the slip δ using the characteristic slip weakening distance for thermal pressurization under undrained

and adiabatic conditions $\delta_c = \rho c W/f\Lambda$. Finally we use the ambient effective stress to normalize the pore pressure rise, and the maximum temperature rise $(\sigma_n - p_a)/\Lambda$ for a uniformly sheared gouge undergoing thermal pressurization under undrained and adiabatic conditions to normalize the temperature. This leads to

$$x = \frac{L}{2}(\tilde{x}+1) \quad , \quad y = h\tilde{y} \quad , \quad \delta = \frac{\rho c h}{f\Lambda}\tilde{\delta}, \tag{C.1}$$

$$p = p_a + (\sigma_n - p_a)\tilde{p} \quad , \quad T = \frac{\sigma_n - p_a}{\Lambda}\tilde{T}, \tag{C.2}$$

where we have used tildes to indicate dimensionless variables. Inserting the scalings for δ and x into the formula for the slip rate

$$V(x) = v_r \frac{\partial \delta}{\partial x} \tag{C.3}$$

we can find the scaling for the slip rate

$$V(x) = 2\frac{v_r \delta_c}{L}\tilde{V}(\tilde{x}) \quad , \quad \tilde{V}(\tilde{x}) = \frac{\partial \tilde{\delta}}{\partial \tilde{x}}. \tag{C.4}$$

Inserting this scaling into the integral equation linking the stress on the fault to the slip rate – equation (5.12) – we find a dimensionless integral equation for the stress along the fault as well as a scaling for the slip pulse length L,

$$\tilde{\tau}(\tilde{x}) = \tau_d - \frac{1}{\pi \tilde{L}} \int_{-1}^{1} \frac{V'}{x' - \xi'} \mathrm{d}\xi', \tag{C.5}$$

$$\tilde{L} = \frac{L}{\bar{\mu}\delta_c / f(\sigma_n - p_a)} \quad , \quad \tau_d = \frac{\tau_b}{f(\sigma_n - p_a)}. \tag{C.6}$$

The first dimensionless parameter in the model is τ_d, which measures the proximity of the background driving stress τ_b to the initial strength of the gouge layer τ_0. Using the slip rate scaling in the equations for conservation of energy and pore fluid mass we find the two dimensionless equations,

$$\begin{aligned} \frac{\partial \tilde{T}}{\partial \tilde{x}} = \tilde{\tau}_f \tilde{V} \exp\left(-\pi \tilde{y}^2\right) + \frac{T_{pulse}}{8T^*} \frac{1}{(1+\sqrt{\chi})^2} \frac{\partial^2 \tilde{T}}{\partial \tilde{y}^2} \\ - R_{th} \frac{T_{pulse}}{T^*} \exp\left(-\frac{K}{\tilde{T}_{mp}}\right) \exp\left(-\pi \beta^2 \tilde{y}^2\right), \end{aligned} \tag{C.7}$$

$$\frac{\partial \tilde{p}}{\partial \tilde{x}} = \frac{\partial \tilde{T}}{\partial \tilde{x}} + \frac{T_{pulse}}{8T^*} \frac{\chi}{(1+\sqrt{\chi})^2} \frac{\partial^2 \tilde{p}}{\partial \tilde{y}^2} + R_{hy} \frac{T_{pulse}}{T^*} \exp\left(-\frac{K}{\tilde{T}_{mp}}\right) \exp\left(-\pi \beta^2 \tilde{y}^2\right), \tag{C.8}$$

and four more dimensionless parameters

$$\chi = \frac{\alpha_{hy}}{\alpha_{th}} \ , \ K = \frac{Q\Lambda}{R(\sigma_n - p_a)} \ , \ R_{th} = \frac{\bar{m} E_r \Lambda T^* A}{2(\sigma_n - p_a)} \ , \ R_{hy} = \frac{\bar{m} P_r T^* A}{2(\sigma_n - p_a)}. \tag{C.9}$$

Another dimensionless parameter is needed to extract the rupture velocity – and thus the slip pulse length – from the dimensionless solutions. As shown in *Garagash* [2012][86] this parameter is v^*/c_s where c_s is the shear wave speed and v^* is a characteristic rupture velocity defined by

$$v^* = \frac{\mu}{\tau_0} \frac{\delta_c}{T^*} = \frac{\mu}{\tau_0} \frac{\rho c}{f\Lambda} \frac{4\alpha}{W}. \tag{C.10}$$

As will be shown in the next section, the slip duration of a self-healing slip pulse T_{sh} is solved for using the self-healing condition $k_L = 0$, so our dimensionless problem is controlled by seven dimensionless parameters. These are τ_d, χ, K, R_{th}, R_{hy}, v^*/c_s, and the scaled initial temperature,

$$T_I = \frac{T_a}{(\sigma_n - p_a)/\Lambda}. \tag{C.11}$$

Motivated by the definitions of α and χ, which measure the total impact of hydrothermal diffusion and the balance between hydraulic and thermal diffusion respectively rather than quantifying the impact of hydraulic and thermal diffusion separately, we can recast the two dimensionless parameters R_{th} and R_{hy} in the following form,

$$R_{react} = \left(\sqrt{R_{th}} + \sqrt{R_{hy}}\right)^2 = \frac{\bar{m}T^*A}{2(\sigma_n - p_a)}\left(\sqrt{\Lambda E_r} + \sqrt{P_r}\right)^2, \tag{C.12}$$

$$X = \frac{P_r}{\Lambda E_r}. \tag{C.13}$$

Here R_{react} measures the total impact of the decomposition reaction and X measures the balance between the energy absorbed and the pore pressure generated by the reaction. Using these new definitions we find,

$$R_{th} = \frac{1}{(1+\sqrt{X})^2}R_{react} \quad , \quad R_{hy} = \frac{X}{(1+\sqrt{X})^2}R_{react}. \tag{C.14}$$

Note that when $X = 1$ the shear strength evolution for uniform shear under undrained and adiabatic conditions is identical to the solution for thermal pressurization alone from *Lachenbruch* [1980][127]. The natural appearance of the parameter X further justifies our

interpretation of P_r/E_r as an effective value of Λ that can used to crudely estimate how much dynamic weakening a specific reaction will provide. The two parameter sweeps over E_r and P_r shown in Figures 5.9 and 5.10 vary one of R_{th} and R_{hy} while keeping the other one constant. We also performed parameter sweeps that fix R_{react} and vary X finding very similar results to those shown in Figures 5.9 and 5.10. As X increases – corresponding to a larger value of P_r/E_r – the effects of thermal decomposition become more pronounced.

C.2 Numerical methods

Here we outline the numerical method used to solve for steady slip pulses propagating at a constant rupture velocity, closely following the numerical method used in *Viesca and Garagash* [2012] [233,234]. For simplicity this is done for the dimensionless model from Appendix C.1, and to reduce notation we drop the tildes used to denote dimensionless variables.

C.2.1 Green's function formulation for integral equations

To begin we define the dimensionless diffusivities in equations (C.7) and (C.8),

$$D_{th} = \frac{T_{pulse}}{8T^*}\frac{1}{(1+\sqrt{\chi})^2} \quad , \quad D_{hy} = \frac{T_{pulse}}{8T^*}\frac{\chi}{(1+\sqrt{\chi})^2}, \tag{C.15}$$

allowing us to write the equations for temperature and pore pressure in matrix form as,

$$\begin{pmatrix} T \\ p \end{pmatrix}_x = \begin{pmatrix} \omega_T \\ \omega_T + \omega_p \end{pmatrix} + \begin{pmatrix} D_{th} & 0 \\ D_{th} & D_{hy} \end{pmatrix} \begin{pmatrix} T \\ p \end{pmatrix}_{yy}, \tag{C.16}$$

where ω_T are the source terms from frictional heating and thermal decomposition in the energy equation and ω_p is the source term from thermal decomposition in the pore pressure equation. Next we use a matrix diagonalization valid when $D_{th} \neq D_{hy}$ to decouple our pair of diffusion equations, leading to

$$\begin{pmatrix} T \\ \Pi \end{pmatrix}_x = \begin{pmatrix} \omega_T \\ \frac{D_{hy}}{D_{hy}-D_{th}}\omega_T + \omega_p \end{pmatrix} + \begin{pmatrix} D_{th} & 0 \\ 0 & D_{hy} \end{pmatrix} \begin{pmatrix} T \\ \Pi \end{pmatrix}_{yy}, \tag{C.17}$$

where we have defined,

$$\Pi = p + \frac{D_{th}}{D_{hy} - D_{th}} T. \tag{C.18}$$

The decoupled diffusion equations can now be solved independently using the Green's function,

$$G(x - x', y - y'; \alpha) = \frac{1}{\sqrt{4\pi\alpha(x - x')}} \exp\left(-\frac{(y - y')^2}{4\alpha(x - x')}\right). \tag{C.19}$$

This leads to the solutions for T and Π on the fault plane $y = 0$,

$$T_{mp}(x) = T_I + \int_{-1}^{x}\int_{-\infty}^{\infty} G(x - x', y'; D_{th})\omega_T(x', y')\mathrm{d}y'\mathrm{d}x', \tag{C.20}$$

$$\Pi_{mp}(x) = \int_{-1}^{x}\int_{-\infty}^{\infty} G(x - x', y'; D_{hy}) \left(\omega_p(x', y') + \frac{D_{hy}}{D_{hy} - D_{th}}\omega_T(x', y')\right)\mathrm{d}y'\mathrm{d}x'. \tag{C.21}$$

Following *Viesca and Garagash* [2012][233], we now take advantage of the fact that the integrals over y' can be done exactly. For example we will show how this works for the integral representing the frictional heating term in the heat equation

$$\int_{-1}^{x}\int_{-\infty}^{\infty}\frac{\tau(x')V(x')}{\sqrt{4\pi D_{th}(x-x')}}\exp\left(-\pi y'^2\right)\exp\left(-\frac{y'^2}{4D_{th}(x-x')}\right)\mathrm{d}y'\mathrm{d}x'. \tag{C.22}$$

Combining the exponentials and separating the integrals over y' and x' we find

$$\int_{-1}^{x}\frac{\tau(x')V(x')}{\sqrt{4\pi D_{th}(x-x')}}\int_{-\infty}^{\infty}\exp\left(-\frac{1+4\pi D_{th}(x-x')}{4D_{th}(x-x')}y'^2\right)\mathrm{d}y'\mathrm{d}x'. \tag{C.23}$$

The integral over y' can be done exactly, leading to

$$\int_{-1}^{x}\frac{\tau(x')V(x')}{\sqrt{1+4\pi D_{th}(x-x')}}\mathrm{d}x'. \tag{C.24}$$

The other integrals in equations (C.20) and (C.21) can be done in a similar fashion, leading to the equations for the pore pressure and temperature on $y=0$

$$T_{mp}(x)=T_I+\int_{-1}^{1}\widehat{A}(x-x')\tau(x')V(x')+\widehat{B}(x-x')\exp\left(-\frac{K}{T_{mp}(x')}\right)\mathrm{d}x', \tag{C.25}$$

$$p_{mp}(x)=\int_{-1}^{1}\widehat{C}(x-x')\tau(x')V(x')+\widehat{D}(x-x')\exp\left(-\frac{K}{T_{mp}(x')}\right)\mathrm{d}x', \tag{C.26}$$

where the functions A, B, C and D are defined as,

$$\widehat{A} = \frac{H(x-x')}{\sqrt{1+4\pi D_{th}(x-x')}} \quad , \quad \widehat{B} = -R_{th}\frac{H(x-x')}{\sqrt{1+4\pi\beta^2 D_{th}(x-x')}}, \tag{C.27}$$

$$\widehat{C} = \frac{H(x-x')}{D_{hy}-D_{th}}\left(\frac{D_{hy}}{\sqrt{1+4\pi D_{hy}(x-x')}} - \frac{D_{th}}{\sqrt{1+4\pi D_{th}(x-x')}}\right), \tag{C.28}$$

$$\begin{aligned}\widehat{D} = &\left(R_{hy} - \frac{D_{hy}R_{th}}{D_{hy}-D_{th}}\right)\frac{H(x-x')}{\sqrt{1+4\pi\beta^2 D_{hy}(x-x')}} \\ &+\frac{D_{th}R_{th}}{D_{hy}-D_{th}}\frac{H(x-x')}{\sqrt{1+4\pi\beta^2 D_{th}(x-x')}}\end{aligned} \tag{C.29}$$

and H is the Heaviside function. Functions similar to $\widehat{A}$ and $\widehat{C}$ where previously used by *Andrews* [2002][4] to model thermal pressurization alone.

Next, we use the pore pressure on the mid-plane predicted by equation (C.26) to find the fault strength

$$\tau_f(x) = 1 - \int_{-1}^{1} \widehat{C}(x-x')\tau(x')V(x') + \widehat{D}(x-x')\exp\left(-\frac{K}{T_{mp}(x')}\right)\mathrm{d}x'. \tag{C.30}$$

We know that within the slipping region $x \in [0, L]$ this strength must be equal to the shear stress predicted by equation (C.5) leading to the integral equation

$$\begin{aligned}1 - \int_{-1}^{1} \widehat{C}(x-x')\tau(x')V(x') + \widehat{D}(x-x')\exp\left(-\frac{K}{T_{mp}(x')}\right)\mathrm{d}x' \\ = \tau_d - \frac{1}{\pi L}\int_{-1}^{1}\frac{V(\xi)}{x-\xi}\mathrm{d}\xi.\end{aligned} \tag{C.31}$$

A second integral equation can be found using the conservation of energy accounting for thermal decomposition,

$$T_{mp}(x) = T_I + \int_{-1}^{1} \widehat{A}(x-x')\tau(x')V(x') + \widehat{B}(x-x') \exp\left(-\frac{K}{T_{mp}(x')}\right) \mathrm{d}x'. \quad \text{(C.32)}$$

In the next subsection we solve this pair of integral equations for the slip rate and temperature profiles within the slip pulse as well as the slip pulse length and slip duration.

C.2.2 Solution using Gauss-Chebyshev quadrature

To solve this pair of integral equations we use the numerical methods outlined in *Viesca and Garagash* [2012][233,234], which combine the Green's function approach from *Garagash* [2012][86] with the Gauss-Chebyshev quadrature methods for singular integral equations from *Erdogan and Gupta* [1972][71] and *Erdogan et al.* [1973][72]. To begin we define the two sets of Chebyshev nodes

$$x_i = \cos\left(\frac{2i-1}{n+1}\frac{\pi}{2}\right) \quad , \quad i = 1, \ldots, n+1, \quad \text{(C.33)}$$

$$x_j = \cos\left(\frac{j}{n+1}\pi\right) \quad , \quad j = 1, \ldots, n. \quad \text{(C.34)}$$

The set of points x_j are the base for the Gauss-Chebyshev quadrature rule,

$$\int_{-1}^{+1} \sqrt{1-x^2} f(x) \mathrm{d}x = \sum_{j=1}^{n} w_j f(x_j), \quad \text{(C.35)}$$

with the weights,

$$w_j = \frac{\pi}{n+1} \sin^2\left(\frac{j}{n+1}\pi\right). \tag{C.36}$$

Defining the function $v(x)$ through $V(x) = \sqrt{1-x^2}\, v(x)$ we can write the stress at the points x_i as

$$\tau_i = \tau_d - \frac{1}{L} K_{ij} v_j \quad , \quad K_{ij} = \frac{w_j}{\pi(x_i - x_j)}. \tag{C.37}$$

The Gauss-Chebyshev quadrature is next used to evaluate the fault strength, leading to

$$\tau_i = 1 - C_{ij}(\tau v)_j - D_{ij} \exp\left(-\frac{K}{T_j}\right), \tag{C.38}$$

where

$$C_{ij} = w_j C(x_i - x_j) \quad , \quad D_{ij} = \frac{w_j D(x_i - x_j)}{\sqrt{1-x_j^2}}. \tag{C.39}$$

Setting the fault stress from equation (C.37) equal to the fault strength from equation (C.38) at every point of the x_i grid we obtain $n+1$ equations. More equations can be obtained by applying the quadrature to the integral equation modeling the conservation of energy. This leads to

$$T_i = T_I + A_{ij}(\tau v)_j + B_{ij} \exp\left(-\frac{K}{T_j}\right), \tag{C.40}$$

$$A_{ij} = w_j A(x_i - x_j) \quad , \quad B_{ij} = \frac{w_j B(x_i - x_j)}{\sqrt{1-x_j^2}}. \tag{C.41}$$

Note that to evaluate equations (C.38) and (C.40) we must know τ on the x_j grid, but equation (C.38) gives us the shear stress on the x_i grid. Similarly, in equation (C.40) we

require the temperature profile on the x_j grid, yet equation (C.40) gives us the temperature profile on the x_i grid. To move between the two grids we use the barycentric Lagrange interpolation matrix

$$I_{ji} = \prod_{m=1, m\neq j}^{n+1} \frac{x_j - x_{i=m}}{x_i - x_{i=m}} \quad , \quad \tau(x_j) = I_{ji}\tau(x_i), \tag{C.42}$$

which is accurate and efficient for functions approximated on Chebyshev nodes[15]. Equations (C.38) and (C.40) lead to a nonlinear system of $2n+1$ equations, where $n+1$ come from setting the stress equal to the strength on the x_i grid and the other n coming from multiplying equation (C.40) through by I_{ji} to find a consistent temperature profile on the x_j grid. This nonlinear system can be solved for v on the x_j grid, T on the x_j grid, and L using Newton-Raphson iteration. Once a solution is found we calculate k_L using

$$k_L = -\frac{4}{\pi\sqrt{L}} \int_{-1}^{1} \sqrt{\frac{x}{1-x}} \frac{\mathrm{d}\tau}{\mathrm{d}x} \mathrm{d}x = 0. \tag{C.43}$$

Repeating this for many imposed slip durations leads to k_L as a function of T_{pulse}/T^*. This curve is then tracked until k_L vanishes and a self-healing solution is found.

We perform a convergence test on the system above for several values of the driving stress τ_b and the parameters from Table 5.1. The results from this convergence test are shown in Figure C.1. We see that the method is second order – as found in *Erdogan and Gupta* [1972][71] – and that the percentage error in the values of T_{sh} and L at which self-healing occurs is acceptable when $n > 400$. The majority of calculations in this paper are performed with $n = 1000$, though sometimes we use a higher value of n at the lowest values of τ_b where the slip is confined to a narrow zone very close to the rupture tip.

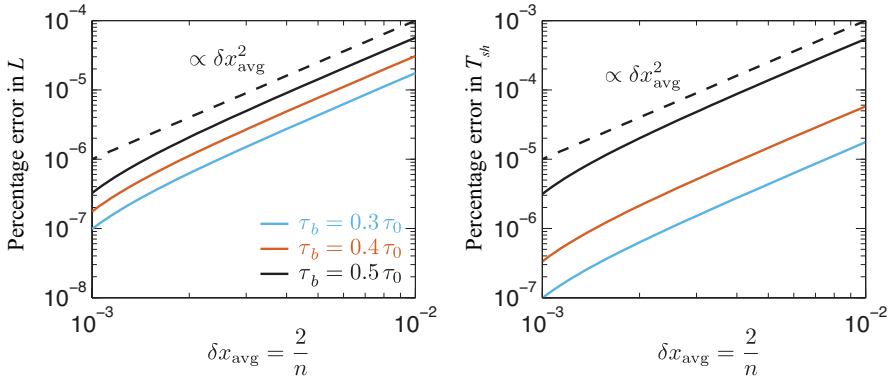

Figure C.1: A plot showing a convergence test for the numerical scheme outlined in Appendix C.2. This test was done using the parameters in Table 5.1 and three different values of the driving stress τ_b. We see that the method is second order – as found in *Erdogan and Gupta* [1972][71] – and the percentage error in T_{sh} and L is small once $n > 1000$. The majority of the simulations in this paper are done using $n = 1000$, with a few higher resolutions for the smallest values of τ_b where slip is confined to a small zone immediately adjacent to the rupture tip.

C.3 Validation of reaction kinetics approximation

The Green's function solution outlined above relies on approximating the reaction kinetics in the deforming zone as the product of the reaction kinetic on $y = 0$ and an assumed Gaussian shape in the across fault direction. Here we test this approximation by replacing equations (5.5) and (5.7) with

$$v_r \frac{\partial T}{\partial x} = \frac{\tau_f \dot{\gamma}}{\rho c} + \alpha_{th} \frac{\partial^2 T}{\partial y^2} - \bar{m} E_r \exp\left(-\frac{Q}{RT}\right), \tag{C.44}$$

$$v_r \frac{\partial p}{\partial x} = v_r \Lambda \frac{\partial T}{\partial x} + \alpha_{hy} \frac{\partial^2 p}{\partial y^2} + \bar{m} P_r \exp\left(-\frac{Q}{RT}\right). \tag{C.45}$$

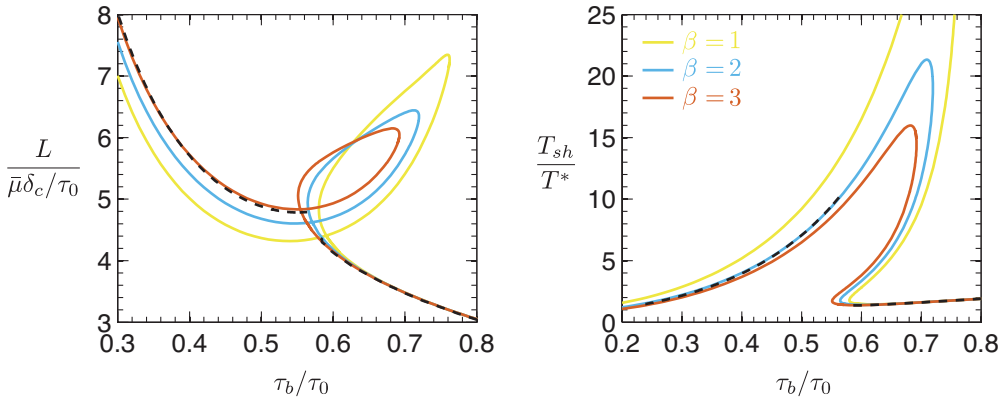

Figure C.2: A plot showing how the results from the Newton-Raphson method outlined in appendix C.2 compare with the finite difference simulations outlined in Appendix C.3. These results were produced using the parameters in Table 5.1. The good agreement between the two methods validates the assumptions we made about the reacting zone shape. We see that for the dimensionless slip pulse length the best agreement occurs for $\beta = 3$, and for the slip duration the best agreement occurs for $\beta = 2$. Based on these plots we choose an optimal value of $\beta = 2$ that is used in all other simulations in this paper.

Note that these equations make no assumptions about the shape of the reacting zone, and the reaction rate is calculated for all y using the temperature at that location.

These equations are solved numerically via an iterative procedure that starts with a velocity profile $V(x)$ and solves for the shear strength and temperature evolution within the pulse using finite differences. Assuming that the shear strength and shear stress are equal within the slip pulse this new shear strength profile can be used to predict a new slip rate profile using *Rice* [1968][183] and *Garagash* [2012][86],

$$V(x) = \frac{2}{\pi}\frac{v_r}{\bar{\mu}}\int_0^L \sqrt{\frac{x(L-x)}{\xi(L-\xi)}}\tau(\xi)\frac{\mathrm{d}\xi}{x-\xi}. \tag{C.46}$$

This new slip rate profile is then used as the input for the next finite difference calculation

and we continue to iterate until the difference between the slip rate profile used to drive the finite difference calculation and the new slip rate profile predicted by equation (C.46) agree to within a small tolerance, which is typically assumed to be $\sim 10^{-4} - 10^{-3}$ in dimensionless units.

Figure C.2 shows how the method that makes no assumption about the reacting zone shape compares with the method that assumes a reacting zone with a Gaussian shape and fixed thickness for different values of β. We see good agreement between the two methods with the best agreement in the value of T_{sh} occurring for $\beta = 2$ and the best agreement in L occurring for $\beta = 3$. These observations validate the assumptions made about the shape of the reacting zone and suggest an optimal value of $\beta = 2$. This value of β is used for the rest of the calculations presented in this paper. Another slightly more complicated method that we use extensively in this paper includes the dimensionless self-healing condition $k_L = 0$ in the Newton-Raphson iteration. This leads to one additional equation that is used to solved for the slip duration T_{sh} at which self-healing occurs. This second method is found to be much more computationally efficient and is used to generate the majority of the results in this paper.

D

Additional Materials for Chapter Six

D.1 Numerical methodology

Our numerical implementation uses centered finite-differences on a Cartesian grid, yielding a second-order accurate approximation to the governing equations. Our grid setup allows for three refinement levels in the vicinity of the singularity at the transition point between stream and ridge in the mechanical model (see Section 6.2.1). We do not use grid refinement

in our solution to the thermal model (see Section 6.2.3) because our temperature field is capped at the melting point, which implies constant temperature in the vicinity of the stress singularity.

We solve the mechanical and thermal models iteratively by repeating the following computational steps: First, we seek an approximate solution to our mechanical model (equation (6.1)). Second, we compute the dissipative heating associated with the estimated velocity field and interpolate it to coincide with the temperature grid. Third, we compute the temperature field resulting from this dissipative heating term by solving equation (6.10). Fourth, we update our estimates for the effective viscosity, thermal conductivity and specific heat based on the new temperature field. Once the coupled mechanical and thermal models have converged to a stable solution for the temperature and velocity fields of the stream-ridge system, we estimate melt production (equation (6.16)).

Solving our thermal model (equation (6.10)) requires an iterative procedure in itself because the extent of the temperate zone depends on temperature. At each iteration, we update the source term based on the revised estimate for the extent of the temperate zone. We also shift the transition between the boundary condition at the base of the domain such that geothermal heat flux is imposed only underneath the portion of the ridge that is frozen (although we continue to maintain a no-slip condition underneath the entire ridge). We construct two Heaviside distributions, the first representative of the temperate zone and the second representative of the crevassed zone as described in Section 6.2.5. In both cases, we use a standard trigonometric taper to regularize the Heaviside distribution. We solve equation (6.10) through a multigrid solver[34] in which we cycle through a hierarchy of four grids. We have also found satisfactory results with classical iterative techniques such as suc-

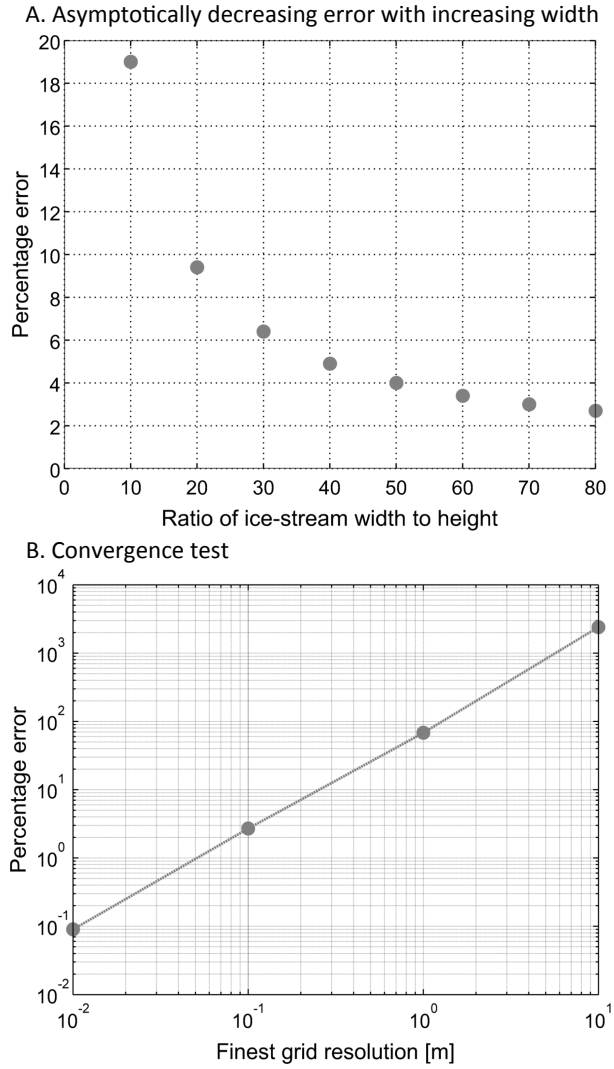

Figure D.1: Validation of our computational approach. Panel A shows that the percentage error between the numerical and analytical estimates for the nonsingular shear heating, $2\tau_E\dot{\epsilon}_E \times r$, at $\theta = 0°$, decreases as the ice-stream width increases. The grid resolution in the vicinity of the singularity is 0.1 m for all computations. Panel B summarizes the results of a convergence test performed for a wide ice stream with $W/H \approx 80$ at $\theta = 0°$.

cessive overrelaxation, but the multigrid is computationally more efficient and less prone to error oscillations, particularly along the bed.

An important concern when solving our mechanical model numerically for a creep-type rheology is to sufficiently resolve the singularity at the base between stream and ridge. To validate our computational approach, we benchmark it against an approximate analytic result valid for very wide ice streams with a temperature-independent viscosity sliding over a stress-free bed. Our analytic derivation is based on the insight that the transition from a slipping ice stream to a locked ridge is analogous to a crack problem. In this analogy, the singularity at the bed between stream and ridge represents the crack tip and the base of the ice stream can be thought of as a shear crack. Using this parallel, we can study the dissipation in the near-tip field with the analytical techniques developed for crack mechanics.

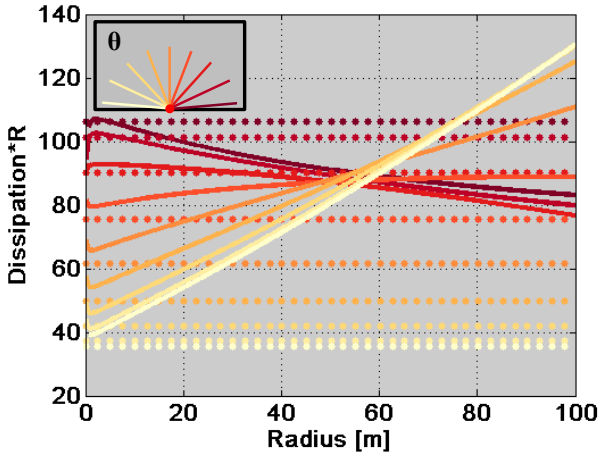

Figure D.2: Plot of the angular dependence of dissipation for nine different angles from $5^\circ - 175^\circ$ represented by a specific color as detailed in the inlet on the upper left. For each angle, the dotted lines represent the analytic and the full lines the numeric result. Evidently, the importance of the far-field contribution to shear heating depends primarily on the distance from the singularity, but also on the angle.

Our strategy for solving for the stress, strain rate and dissipation in the near-tip field consists of two steps: First, we can deduce from *Rice* [1967][182], reinterpreted for nonlinear vis-

cous flow, and *Rice* [1968][183] that the shear heating in the near-tip region is given by

$$2\tau_E\dot{\epsilon}_E = \frac{3J_{tip}}{2\pi r}\left(\sqrt{4-\sin^2\theta}+\cos\theta\right)^{-1}, \tag{D.1}$$

where r and θ are the polar coordinates centered on the slip singularity such that r is the radial distance from the slip singularity and θ the angle taken to be zero at the bed underneath the ridge (see Appendix D.2 for details). Second, we derive an approximate estimate of the unspecified constant, J_{tip} in equation (D.1), which captures the intensity of straining at the crack tip due to far-field loading, using the path-independence of J-type integrals as detailed in Appendix D.3. We estimate J_{tip} as

$$J_{tip} = H\tau_{lat}\dot{\epsilon}_{lat}\,, \tag{D.2}$$

where τ_{lat} is the average shear stress, τ_{xy}, at the margin that would balance the gravitational load of the ice stream and $\dot{\epsilon}_{lat}$ is the strain rate associated with that average lateral shear stress. Note that contrary to the exact result for the near-tip field (see equation (D.1)), the evaluation of the J-integral in equation (D.2) is approximate and based on the simplifying assumptions that (1) the rheological behavior of ice is independent of position, hence neglecting the effect of temperature variations and (2) ice streams are much wider than thick ($H \ll W$).

It is unreasonable to expect the numerical and analytical solutions to match exactly for two reasons: First, the analytical solution is an approximate result that applies strictly only to very wide ice streams. We can still use it to benchmark our computational technique, however, by verifying that the error between analytical and numerical results decreases with

increasing ice-stream width. Second, the analytical treatment only captures the contribution to shear heating that results from the stress singularity at the bed. The effect of the nonsingular, but still intense, shear heating throughout the entire depth extent of the ice is not accounted for by the singular term only. The numerically estimated shear heating will thus never agree exactly with the analytical estimate, but the error should be smallest in the immediate vicinity of the singularity ($r \rightarrow 0$) and increase with increasing distance. To ensure comparability between our numerical model and the analytical benchmark results, we neglect crevassing, the temperature-dependence of the ice rheology and thermal conductivity and the advection terms for all computations in this section. We also assume zero basal stress underneath the ice stream.

Figure D.1A confirms that the percentage error between the numerical and the analytical estimates for the non-singular dissipation, $2\tau_E\dot{\epsilon}_E \times r$ at $\theta = 0°$, decreases with increasing ice-stream width. To isolate the asymptotic effect of ice-stream width, all computations were performed at the same grid resolution of 0.1 m in the vicinity of the singularity. The flattening of the error curve in Figure D.1A indicates that ice-streams with widths of about $100\,H$ are well approximated by the assumption of a very wide stream and suggests that the remaining error is dominated by the finite resolution of our computations. In Figure D.1B, we demonstrate that the percentage error between numerical and analytical results for an ice stream of $W = 80\,H$ at $\theta = 0°$ drops well below 1% for grid resolutions of < 0.1 m, highlighting that we can accurately reproduce the analytical behavior with a sufficiently refined grid.

Beyond serving as a benchmark, the comparison between analytical and numerical results also allows us to verify if and when the far-field contribution to shear heating starts

dominating the total dissipation in the shear margin. Figure D.2 shows that for a wide ice stream with $W = 80\,H$ and a fine-grid resolution of 0.1 m, the far-field contribution to shear heating already becomes important at radial distances of just a few meters, rendering the analytical solution that only captures heating in the near-field of the singularity less adequate. As the radius approaches zero, however, the numerical solutions become increasingly dominated by numerical errors associated with the quickly diverging stresses and are less reliable. As demonstrated in Figure D.1B, the singularity can be captured more accurately with sufficient computational expense, but ultimately there will always be a finite, if vanishingly small, radius below which the analytical result is more accurate.

D.2 The near-tip field parameterized by J_{tip}

By reinterpreting the material rheology, a parallel can be drawn between the downstream velocity profile in a two-dimensional margin and an anti-plane crack problem. In an elastic (or "deformation theory" elastic-plastic) body, the stress depends on the strain, while in the viscous material considered here the stress depends on the strain rate. The stress fields in the elastic and viscous problems are identical. Strain rate in the viscous problem is analogous to strain in the elastic problem and downstream velocity is analogous to displacement.

In this section, we will solve analytically for the shear heating profile near the point where the bed transitions from slipping to locking. To develop the analytic solution, we must neglect the temperature dependence of the rheology and assume a relationship of the form

$$\dot{\epsilon}_E = A\tau_E^n, \tag{D.3}$$

where A and n are constant. Our problem is now mathematically equivalent to the anti-

plane crack problem solved in *Rice* [1967,1968][182,183], which solved for the stress field in a material with a linear stress-strain relationship up to a given yield stress and an arbitrary nonlinear stress-strain relationship (including a power-law relationship as a special case) above the yield stress. The solution in[182] relies on a transformation to the hodograph plane. This transformation interchanges the dependent and independent variables, allowing us to solve for y and z as a function of the strain rate components $\dot{\epsilon}_{xz}$ and $\dot{\epsilon}_{yz}$. As shown in[182], the solution for the field near the crack tip takes the form

$$y = X(\dot{\epsilon}_E) + F(\dot{\epsilon}_E)\cos 2\phi \quad \text{and} \quad z = F(\dot{\epsilon}_E)\sin 2\phi\,, \tag{D.4}$$

where we have used the polar coordinates

$$\dot{\epsilon}_{xy} = -\dot{\epsilon}_E \sin\phi \quad \text{and} \quad \dot{\epsilon}_{xz} = \dot{\epsilon}_E \cos\phi. \tag{D.5}$$

For the power-law rheology given in equation (D.3) the functions $X(\dot{\epsilon}_E)$ and $F(\dot{\epsilon}_E)$ are

$$F(\dot{\epsilon}_E) = \frac{J_{tip}}{2\pi\dot{\epsilon}_E\tau_E(\dot{\epsilon}_E)} \quad \text{and} \quad X(\dot{\epsilon}_E) = \frac{n-1}{n+1}F(\dot{\epsilon}_E), \tag{D.6}$$

where the constant J_{tip} is determined by the far-field loading on the margin, and the evaluation of J_{tip} will be discussed in detail in Appendix D.3. The function $F(\dot{\epsilon}_E)$ can then be related to the shear-heating rate through

$$2\tau_E\dot{\epsilon}_E = \frac{J_{tip}}{\pi F(\dot{\epsilon}_E)}. \tag{D.7}$$

To solve for $F(\dot{\epsilon}_E)$, we first eliminate ϕ from equation (D.4), which uncovers the equa-

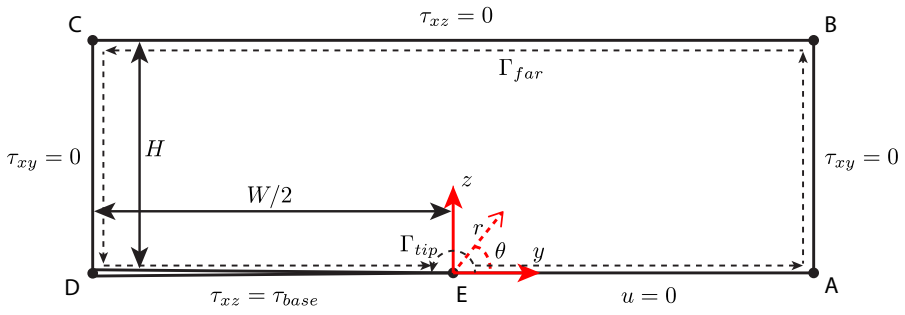

Figure D.3: Sketch showing the two paths Γ_{tip} and Γ_{far} used to evaluate the path independent integral defined in equation (D.13). Γ_{tip} is taken sufficiently close to the transition point so that the stress field is described by the solution in Appendix D.2, and Γ_{far} is evaluated along the border of the domain.

tion for a circle

$$(y - X(\dot{\epsilon}_E))^2 + z^2 = F(\dot{\epsilon}_E)^2. \tag{D.8}$$

Thus, lines of constant shear heating form circles in the (y, z)-plane with a radius of $F(\dot{\epsilon}_E)$ and a center at $y = X(\dot{\epsilon}_E)$, $z = 0$.

For a Newtonian rheology ($n = 1$), $X(\dot{\epsilon}_E) = 0$ and thus equation (D.8) simplifies to

$$2\tau_E \dot{\epsilon}_E = \frac{J_{tip}}{\pi r}, \tag{D.9}$$

where $r = \sqrt{y^2 + z^2}$. This means that lines of constant frictional heating form circles about the point where the bed transitions from slipping to locking. Consequently, the shear heating within the ridge and the ice stream is the same. For the more realistic Glen's Law ($n = 3$), the solution is more complicated. In this case, $X(\dot{\epsilon}_E) = F(\dot{\epsilon}_E)/2$ and therefore equation (D.8) is a quadratic equation in $F(\dot{\epsilon}_E)$. Noting that $F > 0$ is required for a

physically relevant frictional heating profile, the only solution is

$$F(\dot{\epsilon}_E) = \frac{2}{3}\left(\sqrt{4y^2 + 3z^2} - y\right). \tag{D.10}$$

This can be simplified by using polar coordinates centered on the transition point,

$$y = r\cos\theta \quad \text{and} \quad z = r\sin\theta \tag{D.11}$$

leading to the final from of the frictional heating profile

$$2\tau_E\dot{\epsilon}_E = \frac{3J_{tip}}{2\pi r}\left(\sqrt{4 - \sin^2\theta} - \cos\theta\right)^{-1}. \tag{D.12}$$

For Glen's law, the circles that show the lines of constant shear heating are no longer centered on the transition point, but are shifted towards the ridge by an amount $X(\dot{\epsilon}_E) = J_{tip}/(4\pi\tau_E\dot{\epsilon}_E)$ that varies with the magnitude of shear heating. This means that the shear heating is skewed, with more intense heating in the ridge than in the ice stream.

D.3 J-integral evaluation for an anti-plane flow

In this section, we use a path independent integral to evaluate the constant J_{tip} from Appendix D.2, linking the far-field loading on the ice stream to the shear heating singularity near the transition from a slipping to a locking bed. This is an extension to J-type integrals, which were pioneered by *Rice* [1968][184], *Cherepanov* [1968][40] and *Bilby and Eshelby* [1968][17] in the context of cracks in elastic solids, but have been generalized to more complex, nonlinear creep rheologies[88,130,126,10] relevant for our case and applied to glaciers by

McMeeking and Johnson [1986][146].

Our domain of ice is made to coincide with that of a classical anti-plane crack problem, for an ice slab of thickness $2H$, when we add to our domain its mirror image about the base. We thus have a classical crack problem, with $u = 0$ along the prolongation of the slipping zone into the locked zone $z = 0$ and $y > 0$, gravity loadings in the respective domains $z > 0$ and $z < 0$, traction-free surfaces, $\tau_{zx} = 0$, at $z = \pm H$ and with $\tau_{zx} = \tau_{base}$ on both sides of $z = 0$ where $y < 0$.

Assuming that the properties of ice do not change with temperature (or that temperature varies only with z), the appropriate path-independent integral for our problem is

$$J = \int_\Gamma \left(\Phi(\dot{\epsilon_E}, z) - \rho g \sin\alpha\, u\right) \mathrm{d}z - \boldsymbol{\tau} \cdot \mathbf{n} \frac{\partial u}{\partial y} \mathrm{d}s, \tag{D.13}$$

where $\boldsymbol{\tau} = (\tau_{xy}, \tau_{xz})$, Φ is analogous to the strain energy density function from elasticity and is defined for a creeping solid as

$$\Phi(\dot{\epsilon}_E) = \int_0^{\dot{\epsilon}_E} \tau_E\left(\xi\right) \mathrm{d}\xi \tag{D.14}$$

$\mathbf{n}$ is the outward unit normal to the curve Γ, and $\mathrm{d}s$ is evaluated in a counter-clockwise fashion. For any closed curve Γ that does not enclose the transition point (i.e., the crack tip), $J = 0$ so that the integral is path-independent.

For classical crack problems, Γ is taken to start on the lower crack surface $z = 0^-$, $y < 0$, encircle the crack tip and end on the upper crack surface $z = 0^+$, $y < 0$. J is independent of path Γ for all paths with the same starting and ending points. If there is no traction on the crack faces ($\tau_{base} = 0$), J is independent of where we start and end along the

faces. When $\tau_{base} \neq 0$, we start and end at a point close to the tip on the crack face where $y < 0$. Then we take the limit $y \to 0$ on both faces and define J_{tip} as the value of J. Subsequently, we focus on the part of any path Γ in the domain $z \geq 0$ so that the result of equation (D.13), taken along that part of the path, is $J_{tip}/2$.

We now evaluate J_{tip} along the two curves Γ_{tip} and Γ_{far} shown in Figure D.3, which meet these specifications, with Γ_{tip} sufficiently close to the transition point that the deformation can be described by the solution in Appendix D.2. Evaluation along Γ_{tip} just confirms the relations involving J_{tip} in that appendix. For a typical ice-stream geometry, the contribution to J from the portion of Γ_{far} in the center of the ridge is negligible, so for the boundary conditions highlighted in Figure D.3

$$\frac{J_{tip}}{2} = \int_H^0 \left[\Phi\left(\dot{\epsilon}_{xz}\right) - \rho g \sin\alpha u\right]_{y=-W/2} \mathrm{d}z + \int_{-W/2}^0 \tau_{base} \, \frac{\partial u(y,0)}{\partial y} \mathrm{d}y. \tag{D.15}$$

To calculate the two integrals in equation (D.15), we need to know u within the ice stream. An approximate evaluation can be produced using a simple one-dimensional model with a constant basal stress τ_{base} beneath the ice stream. Assuming that τ_{xy} and u are functions of y alone, we integrate the equation for mechanical equilibrium from $z = 0$ to $z = H$, arriving at

$$\frac{\mathrm{d}\tau_{xy}}{\mathrm{d}y} = -\left(\rho g \sin\alpha - \frac{\tau_{base}}{H}\right) \quad \text{and} \quad \dot{\epsilon}_{xy} = A\tau_{xy}^n \,, \tag{D.16}$$

where it may be noted that the first of these is exact if we reinterpret τ_{xy} as its average over the thickness H in the z direction. This average becomes arbitrarily larger than the average of τ_{xz} as W/H becomes increasingly large. In that same limit, $\dot{\epsilon}_{xy}$ becomes much larger than $\dot{\epsilon}_{xz}$, and the flow law reduces to the second equation. Treating the problem in that

large W/H limit, we integrate outwards from the stress free boundary at $y = -W/2$ to calculate $\tau_{xy}(y)$ and hence the strain rate profile

$$\frac{\mathrm{d}u}{\mathrm{d}y} = -2A\left(\rho g \sin\alpha - \frac{\tau_{base}}{H}\right)^n \left(y + \frac{W}{2}\right)^n . \tag{D.17}$$

To create the single boundary condition needed to integrate this equation, we assume that the downstream velocity vanishes at the margin, as is appropriate to the large W/H limit, and find

$$u = \frac{2A}{n+1}\left(\rho g \sin\alpha - \frac{\tau_{base}}{H}\right)^n \left[\left(\frac{W}{2}\right)^{n+1} - \left(y + \frac{W}{2}\right)^{n+1}\right]. \tag{D.18}$$

The boundary condition used here is an approximation since the velocity field in the vicinity of the margin will be a function of both y and z and will not completely vanish. However, comparing the predictions for velocity in the center of the ice stream from equation (D.18) and two-dimensional computational models, we find that in the limit $H \ll W/2$, equation (D.18) is the asymptotic limit of such models.

Using the one-dimensional model to evaluate J_{tip}, which relies only on the value of u at the center of the ice stream, equation (D.15) gives

$$\frac{J_{tip}}{2} = \frac{2AH}{n+1}\left(\rho g \sin\alpha - \frac{\tau_{base}}{H}\right)^{n+1} \left(\frac{W}{2}\right)^{n+1} . \tag{D.19}$$

Defining the average lateral shear stress at the margins and the corresponding equivalent strain rate

$$\tau_{lat} = \left(\rho g \sin\alpha - \frac{\tau_{base}}{H}\right)\frac{W}{2} \quad \text{and} \quad \dot{\epsilon}_{lat} = A\tau_{lat}^n , \tag{D.20}$$

we can simplify the equation for J_{tip} to

$$J_{tip} = \frac{4H}{n+1}\tau_{lat}\dot{\epsilon}_{lat} \tag{D.21}$$

when $W \gg H$.

E

Additional Materials for Chapter Seven

E.1 Derivation of near-tip solution

In this appendix we solve for the stress field and velocity near the transition from a deforming to an undeforming bed, assuming a sharp transition that occurs at $y = z = 0$. To do this we use the hodograph plane methods from *Rice* [1967][182], *Rice* [1968][183] and *Suckale et al.* [2014][216], though we use a slightly different approach than *Suckale et al.* [2014][216]

because we want to solve for the downstream velocity profile as well as the stress field.

To begin we define the Legendre transform of the downstream velocity u as

$$\psi = y\dot{\gamma}_y + z\dot{\gamma}_z - u, \tag{E.1}$$

where $\dot{\gamma}_y$ and $\dot{\gamma}_z$ are the engineering strain rates defined by

$$\dot{\gamma}_y = \frac{\partial u}{\partial y} \quad , \quad \dot{\gamma}_z = \frac{\partial u}{\partial z}. \tag{E.2}$$

These engineering strain rates are equal to twice the tensor strain rates defined in equation (7.1), the effective engineering strain rate is equal to $[\dot{\gamma}_y^2 + \dot{\gamma}_z^2]^{1/2}$, and the power law rheology given in equation (7.3) can be written as $\dot{\gamma} = 2A\tau^n$. Differentiating equation (E.1) with respect to $\dot{\gamma}_y$ and $\dot{\gamma}_z$ and noting that

$$\frac{\partial u}{\partial \dot{\gamma}_y} = \dot{\gamma}_y \frac{\partial y}{\partial \dot{\gamma}_y} + \dot{\gamma}_z \frac{\partial z}{\partial \dot{\gamma}_y} \quad , \quad \frac{\partial u}{\partial \dot{\gamma}_z} = \dot{\gamma}_y \frac{\partial y}{\partial \dot{\gamma}_z} + \dot{\gamma}_z \frac{\partial z}{\partial \dot{\gamma}_z} \tag{E.3}$$

we can relate the first derivatives of ψ to the coordinates y and z

$$\frac{\partial \psi}{\partial \dot{\gamma}_y} = y \quad , \quad \frac{\partial \psi}{\partial \dot{\gamma}_z} = z. \tag{E.4}$$

Following *Rice* [1967][182] we rewrite the equation for mechanical equilibrium as

$$\frac{\partial y}{\partial \tau_{xy}} + \frac{\partial z}{\partial \tau_{xz}} = 0 \tag{E.5}$$

and define polar coordinates in the strain plane by

$$\dot{\gamma}_y = -\dot{\gamma}\sin\phi \quad , \quad \dot{\gamma}_z = \dot{\gamma}\cos\phi. \tag{E.6}$$

Note that in the hodograph plane, radius from the origin is equal to the equivalent engineering strain rate $\dot{\gamma}$. As shown in *Rice* [1967][182], the equation for mechanical equilibrium in the hodograph plane can be written as

$$\frac{\tau(\dot{\gamma})}{\dot{\gamma}\tau'(\dot{\gamma})}\frac{\partial^2\psi}{\partial\dot{\gamma}^2} + \frac{1}{\dot{\gamma}}\frac{\partial\psi}{\partial\dot{\gamma}} + \frac{1}{\dot{\gamma}^2}\frac{\partial^2\psi}{\partial\phi^2} = 0. \tag{E.7}$$

For the power law rheology defined in equation (7.3) this leads to

$$n\frac{\partial^2\psi}{\partial\dot{\gamma}^2} + \frac{1}{\dot{\gamma}}\frac{\partial\psi}{\partial\dot{\gamma}} + \frac{1}{\dot{\gamma}^2}\frac{\partial^2\psi}{\partial\phi^2} = 0. \tag{E.8}$$

Note that transforming from the physical plane to the hodograph plane has turned the nonlinear equation for u into a linear equation for ψ, which is the Legendre transform of u.

Having determined the equation that must be solved in the hodograph plane we next determine the boundary conditions. In the physical plane there are two boundary conditions. First, on the deforming bed we have a traction free boundary condition, which leads to

$$\dot{\gamma}_z = 0 \quad \text{on} \quad z = 0,\ y < 0. \tag{E.9}$$

Second, where the bed is undeforming we have the no slip condition

$$u = 0 \quad \text{on} \quad z = 0,\ y > 0. \tag{E.10}$$

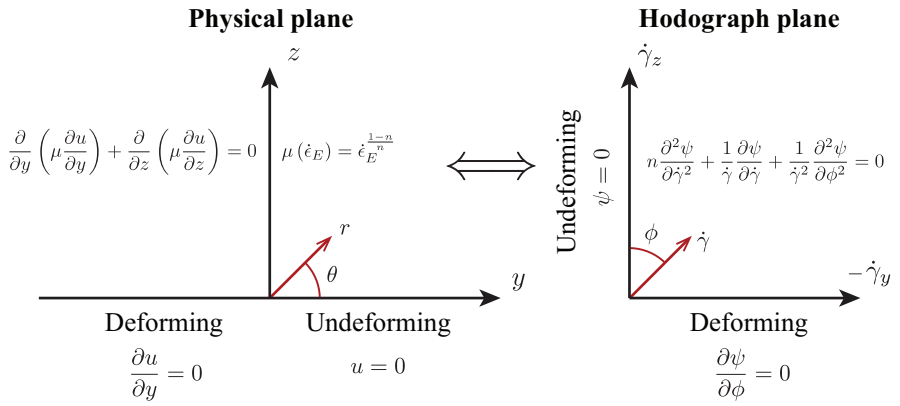

Figure E.1: A sketch of the physical plane and hodograph plane used in Appendix E.1 showing the equations solved, boundary conditions used, and coordinates in both planes.

We can determine where these two boundary conditions map to in the hodograph plane by noting that for the traction free condition $\dot{\gamma}_z = 0$ and $\dot{\gamma}_y < 0$, while for the no slip boundary condition $\dot{\gamma}_y = 0$ and $\dot{\gamma}_z > 0$. Thus the no slip condition maps to the positive $\dot{\gamma}_z$-axis and the traction free condition maps to the negative $\dot{\gamma}_y$-axis.

Having found where the boundary conditions are applied in the hodograph plane we next determine the form of the boundary conditions. We find that for the no slip condition all three terms in equation (E.1) vanish, leading to

$$\psi = 0 \quad \text{on} \quad \phi = 0. \tag{E.11}$$

In the physical plane the traction free boundary condition occurs on $z = 0$, and thus equation (E.4) tells us that along this boundary $\partial\psi/\partial\dot{\gamma}_z = 0$. This is equivalent to saying that

the normal derivative must vanish, which leads to

$$\frac{\partial \psi}{\partial \phi} = 0 \quad \text{on} \quad \phi = \pi/2. \tag{E.12}$$

Figure E.1 shows a sketch of the physical plane and hodograph highlighting the equations solved, boundary conditions used, and domain solved in.

The equation given in (E.8) and the boundary conditions given in (E.11) and (E.12) can be solved by the simple separable solution

$$\psi = -C\dot{\gamma}^{-1/n} \sin \phi, \tag{E.13}$$

where $C > 0$ is an arbitrary constant that will be determined later and the negative sign is required to ensure that when we map back to the physical plane our solution will lie in $z > 0$. Note that equation (E.13) is a much simplified case of the eigenfunction expansion given in the original solution of this problem from *Rice* [1967][182]. Using the solution for ψ given in equation (E.13) we can now determine the mapping that allows us to switch between $(\dot{\gamma}, \phi)$ in the hodograph plane and (r, θ) in the physical plane. To do this we use the identities relating the first derivates of ψ to the physical coordinates y and z given in (E.4). In the hodograph plane polar coordinates defined in equation (E.6) these identities become

$$y = -\sin \phi \frac{\partial \psi}{\partial \dot{\gamma}} - \frac{\cos \phi}{\dot{\gamma}} \frac{\partial \psi}{\partial \phi}, \tag{E.14}$$

$$z = \cos \phi \frac{\partial \psi}{\partial \dot{\gamma}} - \frac{\sin \phi}{\dot{\gamma}} \frac{\partial \psi}{\partial \phi}. \tag{E.15}$$

Inserting the solution from (E.13) we find,

$$y = -C\dot{\gamma}^{-(n+1)/n}\left(\left(\frac{n+1}{n}\right)\sin^2\phi - 1\right), \tag{E.16}$$

$$z = \frac{n+1}{n}C\dot{\gamma}^{-(n+1)/n}\sin\phi\cos\phi. \tag{E.17}$$

First we find the polar angle θ in the physical plane by dividing z by y to find

$$\tan\theta = \frac{(n+1)\tan\phi}{n - \tan^2\phi}. \tag{E.18}$$

This allows us to find θ as a function of ϕ, and noting that equation (E.18) defines a quadratic equation in $\tan\phi$ we can also solve to find

$$\tan\phi = -\frac{(n+1)\cot\theta}{2} + \sqrt{\frac{(n+1)^2\cot^2\theta}{4} + n}. \tag{E.19}$$

Next we find the radius r in the physical plane using $r^2 = y^2 + z^2$, leading to

$$r = C\dot{\gamma}^{-(n+1)/n}\sqrt{\left(\frac{1+n}{n}\right)\left(\frac{1-n}{n}\right)\sin^2\phi + 1}. \tag{E.20}$$

Equation (E.20) can be rearranged to give $\dot{\gamma}$ in terms of r

$$\dot{\gamma}^{(n+1)/n} = \frac{C}{r}\sqrt{\left(\frac{1+n}{n}\right)\left(\frac{1-n}{n}\right)\sin^2\phi + 1}, \tag{E.21}$$

where $\tan\phi$ is given by equation (E.19) and we use the trigonometric identity,

$$\sin^2\phi = \frac{\tan^2\phi}{1+\tan^2\phi}. \tag{E.22}$$

Now we solve for the constant C using the J-integral, which links the far-field loading to the asymptotic solution valid right at the transition from a deforming to an undeforming bed. This process is greatly simplified by comparing with the solution for the stress field around a sharp transition from *Suckale et al.* [2014][216]. Comparing our solution for z given in equation (E.15) with equation (B2) in *Suckale et al.* [2014][216] allows us to relate the function F defined in *Suckale et al.* [2014][216] to our solution through

$$F = \frac{n+1}{2n} C\dot{\gamma}^{-(n+1)/n}. \tag{E.23}$$

Using the definition of F given in equation (B4) of *Suckale et al.* [2014][216] allows us to find,

$$C = \frac{2n(2A)^{1/n} J_{tip}}{\pi(n+1)}. \tag{E.24}$$

Determining the constant C completes our solution for ψ.

Now that we have solved for ψ and can move between the hodograph and physical planes we invert for u using

$$u = y\dot{\gamma}_y + z\dot{\gamma}_z - \psi. \tag{E.25}$$

Using the polar coordinates defined in equations (E.4) we can show equation (E.25) is equivalent to

$$u = \dot{\gamma}\frac{\partial\psi}{\partial\dot{\gamma}} - \psi, \tag{E.26}$$

allowing us to find the velocity field around the transition point in terms of $\dot{\gamma}$ and ϕ

$$u = \frac{(n+1)C}{n}\dot{\gamma}^{-1/n}\sin\phi. \tag{E.27}$$

Using equations (E.19) and (E.21) we an rewrite this in terms of r and θ to find

$$u = \left(\frac{2A(n+1)}{n}\right)^{1/(n+1)}\left(\frac{2J_{tip}}{\pi}\right)^{n/(n+1)} r^{1/(n+1)}g(\theta), \tag{E.28}$$

where the shape of the velocity field is given by the function

$$g(\theta) = \left(\frac{n^2 f^{n+1}}{(n^2+f)(1+f)^n)}\right)^{1/(2n+2)} \tag{E.29}$$

and the function $f(\theta)$ is

$$f(\theta) = n + \frac{(n+1)^2}{2}\cot^2\theta - (n+1)\cot\theta\sqrt{\frac{(n+1)^2}{4}\cot^2\theta + n}. \tag{E.30}$$

E.2 Solution for circular channel and Newtonian rheology

In this appendix we develop an analytic solution for a circular channel in ice flowing with a Newtonian rheology. This solution uses complex variables, and thus cannot be extended to other stress exponents $n \neq 1$. To begin we assume that the basal resistance acting on the deforming bed is much smaller than the concentrated stresses associated with the transition from a deforming to an undeforming bed, allowing us to model the deforming bed as a stress free boundary. Following this we generalize the solution to account for the finite basal resistance that *Perol et al.* [2014][163] argued may occur due to the efficient drainage

associated with a channel.

E.2.1 Negligible basal resistance

To begin we define the complex coordinate $\xi = y + iz = re^{i\theta}$ and the holomorphic function G such that

$$u = 2AIm(G(\xi)), \tag{E.31}$$

where $Im(G)$ indicates the imaginary part of the complex function G. Differentiating G with respect to ξ we find

$$G'(\xi) = \tau_{xz} + i\tau_{xy}. \tag{E.32}$$

Based on the small scale yielding assumption validated in Section 7.3, we know that G must match the solution for a sharp transition as $\xi \to \infty$, leading to the boundary condition

$$G'(\xi) \to \left(\frac{J_{tip}}{2A\pi}\right)^{1/2} \xi^{-1/2} \quad \text{as} \quad \xi \to \infty. \tag{E.33}$$

We also have a traction free boundary condition at the channel face $r = R$

$$\tau_{zy}n_y + \tau_{xz}n_z = 0, \tag{E.34}$$

where n_y and n_z are the y and z components of the unit normal to the channel wall respectively. Using our definition of ξ and equation (E.32) this boundary condition can be written as

$$Im[e^{i\theta}G'(\xi)] = 0. \tag{E.35}$$

To match the stress free boundary condition at $r = R$ we look for a solution with

$$G'(\xi) = \left(\frac{J_{tip}}{2A\pi}\right)^{1/2} \xi^{-1/2} \left(1 + \sum_{k=1}^{\infty} \frac{C_k}{\xi^k}\right), \tag{E.36}$$

using the fact that all holomorphic functions are analytic to write $G'(\xi)$ as a series expansion in ξ. This series expansion naturally satisfies the no slip condition at $\theta = 0$ and the traction free boundary condition at $\theta = \pi$. Inserting (E.36) into (E.35) leads to

$$Im\left[e^{i\theta/2}\left(1 + \sum_{k=1}^{\infty} C_k R^{-k} e^{-ik\theta}\right)\right] = 0, \tag{E.37}$$

which can be solved by setting $C_1 = R$ and $C_k = 0$ for $k > 1$. Thus our final solution for $G'(\xi)$ is

$$G'(\xi) = \left(\frac{J_{tip}}{2A\pi}\right)^{1/2} \xi^{-1/2} \left(1 + \frac{R}{\xi}\right). \tag{E.38}$$

We can extract the shear stress along the undeforming portion of the bed by setting $\xi = y$, which leads to

$$\tau_{xz} = \left(\frac{J_{tip}}{2A\pi y}\right)^{1/2} \left(1 + \frac{R}{y}\right). \tag{E.39}$$

E.2.2 Finite basal resistance

The method used to calculate the maximum stress on the locked portion of the bed for a Newtonian rheology and a circular channel can be generalized to allow for a non-zero basal stress. When the deforming bed applies a non-zero shear stress τ_f to the ice the far-field

solution for a singular crack becomes

$$\tau_{xz} + i\tau_{xy} = \tau_f + \left(\frac{J_{tip}}{2A\pi}\right)^{1/2} \xi^{-1/2}, \tag{E.40}$$

which is equal to the linear superposition of a constant stress field $(\tau_{xy}, \tau_{xz}) = (0, \tau_f)$ and the solution for a sharp transition assuming that the bed provides no resistance. To find a solution that approaches the singular solution as $\xi \to \infty$ we again use a series expansion

$$\tau_{xz} + i\tau_{xy} = \tau_f + \left(\frac{J_{tip}}{2A\pi}\right)^{1/2} \xi^{-1/2} \left(1 + \sum_{k=1}^{\infty} \frac{C_k}{\xi^k}\right). \tag{E.41}$$

Inserting this expansion into the traction free boundary condition given in equation (E.35) we arrive at

$$\tau_f \sin\theta + \sqrt{\frac{J_{tip}}{2\pi AR}} \sum_{k=0}^{\infty} C_k \sin((1/2 - n)\,\theta)) = 0, \tag{E.42}$$

where we have set $C_0 = 1$. To find the coefficients C_k we use the series expansion

$$\sin\theta = \sum_{k=1}^{\infty} D_k \sin\left((n - 1/2)\theta\right) \quad , \quad -\pi \leq \theta < \pi, \tag{E.43}$$

which is equivalent to

$$\sin 2\psi = \sum_{k=1,3,5,\ldots}^{\infty} D_k \sin\left(n\psi\right) \quad , \quad -\frac{\pi}{2} \leq \psi < \frac{\pi}{2}. \tag{E.44}$$

To find the coefficients D_k we use the orthogonality condition

$$\int_{-\pi/2}^{\pi/2} \sin(n\psi)\sin(m\psi)\mathrm{d}\psi = \frac{\pi}{2}\delta_{mn}, \tag{E.45}$$

where δ_{mn} is the Kronecker delta and m, n are both odd. Using this we can calculate the formula for D_k

$$D_k = \frac{2}{\pi} \int_{-\pi/2}^{\pi/2} \sin(2\psi) \sin(k\psi) \mathrm{d}\psi \tag{E.46}$$

and evaluate this to find

$$D_k = \frac{8}{\pi(k^2-4)} (-1)^{\frac{(k+1)}{2}}. \tag{E.47}$$

Having found the values for D_k we can convert this to the coefficients C_k. We find that,

$$C_1 = 1 + \frac{8\tau_f}{3\pi} \sqrt{\frac{2\pi AR}{J_{tip}}}, \tag{E.48}$$

$$C_n = \sqrt{\frac{2\pi AR}{J_{tip}}} \frac{8\tau_f}{\pi(2n+1)(2n-3)} (-1)^n \quad , \quad n \geq 2. \tag{E.49}$$

These coefficients allow us to calculate the stress applied to the locked portion of the bed

$$\tau_{xz} = \tau_f + \sqrt{\frac{J_{tip}}{2\pi Ay}} \left(1 + \sum_{n=1}^{\infty} C_n \left(\frac{R}{y} \right)^n \right). \tag{E.50}$$

E.3 Generalization of locking radius to $n \neq 3$

In this appendix we generalize the analysis in section 7.6 to stress exponents $n \neq 3$. To do this we use the maximum stress on the bed given by equation (7.18),

$$\chi \left(\frac{n J_{tip}}{(n+1)\pi AR} \right)^{1/(n+1)} \tag{E.51}$$

This maximum stress is compared with the yield strength of the undeforming bed adjacent to the channel from equation (7.30),

$$2f\left(\frac{\rho_w g S Q_w}{\pi L \rho_i A R^2}\right)^{1/n} \tag{E.52}$$

Setting the stress less than or equal to the yield strength of the undeforming bed we now determine when locking occurs. This leads to the inequality,

$$\chi\left(\frac{nJ_{tip}}{(n+1)\pi AR}\right)^{1/(n+1)} < 2f\left(\frac{\rho_w g S Q_w}{\pi L \rho_i A R^2}\right)^{1/n}. \tag{E.53}$$

This inequality can be rearranged to find the critical locking radius that must no be exceeded by the channel radius for a stable margin configuration to occur

$$R < R_{lock} \tag{E.54}$$

where the locking radius is defined as

$$R_{lock} = \left(\frac{2f}{\chi}\right)^{\frac{n(n+1)}{n+2}} \left(\frac{\rho_w g S Q_w}{\pi L \rho_i A}\right)^{\frac{n+1}{n+2}} \left(\frac{\pi A(n+1)}{nJ_{tip}}\right)^{\frac{n}{n+2}}. \tag{E.55}$$

Recalling that for fixed material properties and loading conditions R and R_{lock} depend only on the water flux through the channel Q_w, we can rewrite the inequality $R < R_{lock}$ to find

$$Q_w > Q_{lock}, \tag{E.56}$$

where the critical water flux that must be exceeded for locking to occur is

$$Q_{lock} = 2^{\frac{5(n+2)}{5n+2}} \left(\frac{n_m}{\pi S^{1/2}}\right)^{\frac{3(n+2)}{5n+2}} \left(1+\frac{2}{\pi}\right)^{\frac{2(n+2)}{5n+2}} \left(\frac{\chi}{2f}\right)^{\frac{8n(n+1)}{n+2}} \left(\frac{\pi L \rho_i A}{\rho_w g S}\right)^{\frac{8(n+1)}{5n+2}} \left(\frac{n J_{tip}}{\pi A(n+1)}\right)^{\frac{8n}{5n+2}}. \tag{E.57}$$

The lead researcher on this project and primary author of the resulting manuscript was Brooks Proctor. I became involved in this project after the experiments were completed and worked closely with Brooks to construct the thermal models used to demonstrate that weakening occurs at a critical contact temperature and that the evolution of surface temperature can explain the hysteresis seen in the friction data. The work in this chapter has already been published and the relevant citation is: Proctor, B. P., T. M. Mitchell, G. Hirth, D. Goldsby, F. Zorzi, J. D. Platt, and G. Di Toro (2014), Dynamic weakening of serpentinite gouges and bare-surfaces at seismic slip rates, Journal of Geophysical Research, 119, 8107-8131.

F

Dynamic weakening of serpentinite gouges and bare-surfaces at seismic slip rates

F.0 Abstract

To investigate differences in the frictional behavior between initially bare-rock surfaces of serpentinite and powdered serpentinite ("gouge") at sub-seismic to seismic-slip rates,

we conducted single velocity-step and multiple velocity-step friction experiments on an antigorite-rich and lizardite-rich serpentinite at slip rates (V) from 0.003 m/s to 6.5 m/s, sliding displacements up to 1.6 m, and normal stresses (σ_n) up to 22 MPa for gouge and 97 MPa for bare surfaces. Nominal steady-state friction values (μ_{nss}) in gouge at $V = 1$ m/s are larger than in bare surfaces for all σ_n tested and demonstrate a strong σ_n dependence; μ_{nss} decreased from 0.51 at 4.0 MPa to 0.39 at 22.4 MPa. Conversely, μ_{nss} values for bare surfaces remained ~ 0.1 with increasing σ_n and V. Additionally, the velocity at the onset of frictional weakening and the amount of slip prior to weakening were orders of magnitude larger in gouge than in bare surfaces. Extrapolation of the normal stress dependence for μ_{nss} suggests that the behavior of antigorite gouge approaches that of bare surfaces at $\sigma_n \geq 60$ MPa. X-ray diffraction revealed dehydration reaction products in samples that frictionally weakened. Microstructural analysis revealed highly localized slip zones with melt-like textures in some gouge experiments and in all bare-surfaces experiments for $V \geq 1$ m/s. 1-D thermal modeling indicates that flash heating causes frictional weakening in both bare surfaces and gouge. Friction values for gouge decrease at higher velocities and after longer displacements than bare surfaces because strain is more distributed.

F.1 Introduction

Our understanding of the frictional behavior of faults at seismic slip velocities (>0.1 m/s) has significantly improved over the last 15 years with experiments performed on initially bare rock surfaces[58,93,97,107,223] and gouges[29,98,124,150,176]. In general, these studies of high-velocity friction (HVF) demonstrate that rock friction coefficients decrease dramatically from ~0.7 to as low as 0.1 as slip velocities approach seismic rates and (in most cases) increase rapidly

as velocities decelerate; this general behavior is nominally independent of rock composition[61,93]. Such dynamic fault-weakening behavior revealed in laboratory experiments is consistent with several earthquake-related observations retrieved from: 1) seismology: e.g., the large stress drops constrained from analysis of seismic radiation patterns of some earthquakes[111,141,232], or the (debated) breakdown of the scaling between radiated energy and seismic moment[1,122]; 2) geophysics: e.g., the lack of a pronounced heat flow anomaly along major fault zones[129,83] or the large seismic slip accommodated in fault patches in the Sumatra 2004 earthquake of moment magnitude (Mw) 9.3 (15 m of max slip, *Stein and Okal*, [2005][215] and the Tohoku 2011 Mw 9.0 (50 m of max slip, *Fujiwara et al.*, [2011][82]) event; 3) geology: e.g., estimates of coseismic frictional strength obtained from ancient exhumed faults (e.g., *Di Toro et al.*, [2006][59]; *Griffith et al.*, [2009][95]) or active deep-drilled seismic faults (*Chester et al.*, [2013][46]; *Hirono et al.*, [2007][104]).

A number of physical mechanisms have been proposed to explain the dynamic weakening behavior observed in experiments and postulated to occur on faults (see[61,154,187] for a summary). In particular, mechanical data and microstructural investigations of experimentally deformed bare rocks are consistent with flash heating of asperities[93,235], frictional melting[59,108,153,214], silica gel weakening[58,92] and superplasticity (grain boundary sliding accommodated by dislocation motion or diffusion)[94,109,200]. However, all faults generate a mm to cm thick layer of gouge during rupture and seismic slip[175], even within their deeper roots ($6-15$ km, e.g., *Sibson* [1977][206]; *Snoke et al.*, [1999][212]). This raises the questions: Which dynamic-weakening mechanisms occur in gouge-bearing faults? How might the presence of gouge modify the occurrence and/or efficacy of these weakening processes at seismic slip rates? Lubrication due to the presence of powders[98,176,221] is inconsistent with the rapid

recovery of frictional strength at the end of sliding. Moreover, in exposed fault zones it is commonly observed that slip tends to be localized along very thin surfaces within gouge (e.g., *Chester and Chester* [1998][42]; *Fondriest et al.* [2013][76]; *Sibson* [2003][207]), leading some workers to suggest that once strain is localized within gouge the system will emulate bare surface slip behavior (e.g., *Smith et al.* [2012][210]). But is it appropriate to extrapolate rock friction behavior obtained in rock-on-rock friction experiments to natural gouge-bearing faults? Furthermore, how does the effective normal stress affect this behavior? Interestingly, the results from *Smith et al.* [2013][211] on calcite gouge and *Han et al.* [2007][97] on (cohesive) calcite-bearing marble suggest that the shear stress or strength of calcite gouge is a factor of 2 or greater than marble bare surfaces at seismic slip velocities despite having localized strain.

Serpentinite is a common rock type in the oceanic lithosphere, and earthquakes may propagate into serpentinized mantle along mid-oceanic ridges, transform faults and subduction zones; the latter alone release about $85 - 90\%$ of the global seismic moment[197]. For this reason, the frictional behavior of serpentinite has been studied over a wide range of slip rates from plate rates to seismic slip rates[106,125,179]. Moreover, serpentine group minerals are expected to react to talc, olivine and enstatite due to frictional heating during rapid slip. These minerals are thought to be stable in the geologic record, and could therefore provide evidence for seismic slip[125]. Currently, the only widely accepted evidence for ancient seismic faulting is the presence of pseudotachylytes[205]. Other proposed geologic evidence for seismic slip includes thermally altered biomarkers in sedimentary rocks[169], peculiar crystal-plastic feature[16,211], injection of fluidized gouge[75,133,192] and the combination of mirror-like surfaces with truncated and exploded grains[76,208]. As a consequence, the occurrence of ser-

pentine breakdown minerals in slipping zones could be indicative of ancient seismicity in faults exhumed from seismogenic depths, outlining the importance for further field studies of exhumed fault zones hosted in oceanic rocks.

Employing a rotary-shear apparatus, we extend the study of the frictional behavior of serpentinite rocks to higher normal stresses (up to 96.6 MPa for bare surfaces and 22.4 MPa for gouges) and slip velocities (up to 4.3 m/s for bare surfaces and 6.5 m/s for gouges) than investigated previously. We also explore differences in dynamic frictional-weakening behavior observed on serpentine gouge and during tests on initially bare surfaces of serpentine by conducting relatively short displacement, high-velocity experiments while varying the normal stress between tests. Following each experiment the slip surfaces and wear material were analyzed with X-ray powder diffraction (XRPD) and several microstructural analysis techniques. These analyses, coupled with 1-D thermal modeling, allow us to constrain the effects of velocity, normal stress, shear heating, strain localization and dehydration reactions on dynamic frictional weakening of serpentine and, by extension, other materials.

F.2 Experimental procedures

F.2.1 Sample preparation and data acquisition

Twenty-seven frictional sliding experiments on initially bare-surfaces and powdered rock samples were performed with SHIVA (Slow- to HIgh-Velocity rotary-shear friction Apparatus) at the Istituto Nazionale di Geofisica e Vulcanologia (INGV) in Rome, Italy (for a description of SHIVA see *Di Toro et al.* [2010][60]; *Niemeijer et al.* [2011][153]). Two materials were tested: an antigorite-rich serpentinite (ATG) and a lizardite-rich serpentinite (LIZ). ATG samples contain 90% antigorite with minor magnesite and magnetite; LIZ samples

contain 80% lizardite, 14% clinochlore (chlorite) and minor magnetite and trace amounts of olivine and enstatite, as determined by petrographic and XRPD analyses (Table 1).

Bare surface samples were first cored into two ~50 mm long solid cylinders. The cylinders were pressed inside precut aluminum rings with an inner and outer diameter of 50 mm and 55 mm respectively and cemented within the rings with epoxy. Next, using a lathe, a depression was machined into the end face of each cylinder to yield an annulus with 50 and 30 mm outer and inner diameters, respectively. The sliding surface was ground with 320 grit sandpaper and samples were loaded into SHIVA using holders described in *Niemeijer et al.* [2011][153] (Figures F.1a and F.1b). Powdered ("gouge") samples were crushed and sieved between 37 and 105 μm, although some finer-grained material was also present in the starting material. The powder was evenly packed into a steel gouge holder (55 and 35 mm outer and inner diameters) and sheared between two roughened steel discs (Figures F.1c, F.1d, and F.1e) (for a description of the steel gouge holder and its calibration, see *Smith et al.* [2013][211]). Normal stress was applied from the non-rotary end with an air-actuated pneumatic piston cylinder and servo-controlled via an electro-valve in parallel with a digital pneumatic regulator. The regulator has a resolution of 0.02 bars and a response time of 0.2 s for a step of 50% of full scale [Di Toro et al., 2010].

In all gouge experiments, 4 g of powder was used, yielding a ~1.7 mm thick layer of compacted gouge. Slight variations in thickness occurred after initial loading of the gouge. This produced small fluctuations in the shear stress data with a wavelength of ~150 mm, consistent with the average circumference of the gouge holder (outer and inner circumferences of 173 and 111 mm). The normal stress also fluctuated in response to variations in thickness. These fluctuations were in some cases accentuated by the delayed servo-response of the reg-

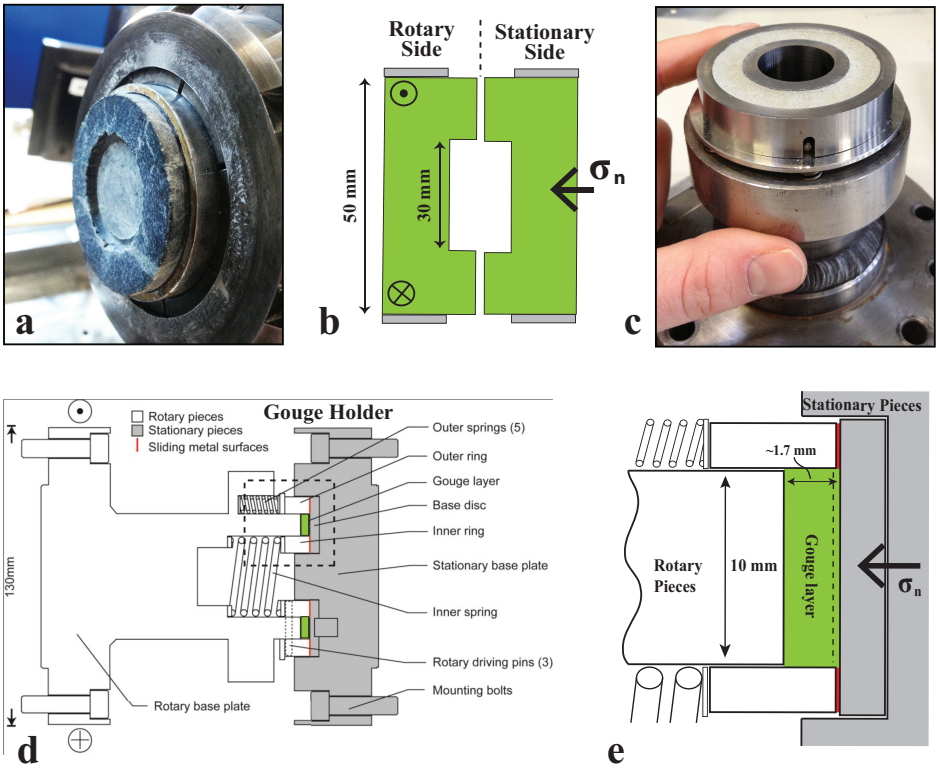

Figure F.1: Sample assembly for bare-surface and gouge experiments. (a) Photograph of rotary side of bare-surface sample holder with serpentinite sample prior to deformation. (b) Schematic of bare surface experimental assembly. (c) Photograph of gouge holder (rotary side) loaded with serpentinite powder. (d) Schematic of gouge holder (modified after *Smith et al.* [2013][211]). (e) Enlargement of (d) showing gouge sample compartment (green) and lubricated metal-metal rotary contacts (red). Dashed line indicates typical location of strain localization within the gouge.

ulator such that the stress was either over-or under-corrected causing variations as high as 5%; we report the average imposed normal stress during deformation in Table F.1. In most experiments the sample holder prevented extrusion of the gouge, but in Runs 705, 818, 825 and 826, as much as ∼0.2 g (∼85 μm of thickness) of the gouge leaked from the holder during deformation. In Runs 727 and 733 sliding displacement was not recorded; however we still report mechanical data assuming that the imposed velocity profile was similar to that

in other experiments with identical experimental parameters. Mechanical data (axial load, torque, axial displacement, and angular rotation) were acquired at a frequency of 25 Hz for samples deformed at velocities less than 0.1 m/s and 25 kHz for higher slip velocities. The total slip, slip rate, and shear stress were determined following methods discussed in *Di Toro et al.* [2010][60]. High-frequency noise in the data was reduced with a Fast-Fourier-Transform (FFT) smoothing filter (Appendix F.6).

Following each gouge experiment, a portion of the slip surface was collected for XRPD analysis. Similarly, following each bare surface experiment a portion of the wear material was collected for XRPD analysis. All but one XRPD analysis was conducted at Geosciences Dept. Padua, Italy (see Appendix F.7 for XRPD analysis details).

Micro-imaging was conducted with an Olympus SZX16 optical microscope fit with a digital camera, a JEOL 6500 and LEO 1500VP field-emission scanning electron microscope (SEM) with an accelerating voltage of $10 - 20$ kV and a Cameca SX100 electron microprobe.

F.2.2 Multiple velocity-step experiments

In each multiple velocity-step experiments we imposed the identical preset velocity function. Samples were first deformed at a sliding velocity of $\sim$3 mm/s to a displacement of 60 mm, then the velocity was stepped to $\sim$4.5 m/s then decelerated back to rest, resulting in a total displacement of $\sim$0.5 m. We imposed an acceleration and deceleration of $\sim$40 m/s^2, however, the servo-controlled response of the motor tends to overshoot this value and we observe initial peaks as high as 65 m/s^2 during acceleration and 70 m/s^2 during deceleration (see Table 1). In these experiments a constant normal stress (σ_n) was imposed, ranging

from 4.9 to 19.5 MPa in bare-surface experiments (Runs 734, 727, 735, and 733), and 7 to 8.5 MPa in ATG gouge experiments (Runs 824b and 818), and 8.5 MPa in one LIZ gouge experiment (Run 705).

F.2.3 Single velocity-step experiments

In single velocity-step experiments, samples were accelerated from rest to a set velocity then decelerated back to rest after a preset amount of displacement. In one suite of experiments the samples were slid at 1 m/s for ~1 m of displacement with an imposed acceleration and deceleration of ~20 m/s^2; actual accelerations and decelerations peaked as high as 65 m/s^2 (Table 1). In bare-surface experiments (Run 736) a constant σ_n was imposed, ranging from 5 to 97 MPa, which is the highest normal stress ever applied in high-velocity friction experiments on natural rocks: four times higher than in the study of *Hirose and Bystricky* [2007][106] (see Appendix F.8 for normal stress calculation of these runs). In ATG gouge experiments (Runs 820, 745, 821, 822, and 823), a constant σ_n was imposed, ranging from 4 to 22.4 MPa and in LIZ gouge experiments (Runs 747, 746, 748, 825, and 826) from 3.8 to 18.7 MPa. We were not able to deform gouge at higher normal stresses due to the torque limit of SHIVA. We also deformed ATG gouge at 0.1 m/s and 13.3 MPa for 1 m of slip (Run 835) and ~6.5 m/s and 10.9 MPa for 1.6 m of displacement (Run 834), respectively.

F.3 Results

F.3.1 Multiple velocity-step tests

Results from all multiple velocity-step tests are reported in Table F.1. Three representative experiments (Runs 705, 824b and 735) are shown in Figure F.2a. These tests illustrate dif-

ferences between the frictional behavior of serpentine bare surfaces and serpentine gouge at sub-seismic and seismic slip velocities.

During slip at 3 mm/s, ATG bare surfaces and LIZ and ATG gouge had similar nominal steady-state values of the friction coefficient (μ_{nss}) but differed in their frictional stability. μ_{nss} is the average of the relatively constant friction values generated during slip at these velocities. We use the term "nominal" to acknowledge that friction may evolve with continued displacement due to changes in the shear zone microstructure and/or thermal structure. Values of μ_{nss} for ATG were ~0.67 for bare surfaces (although slightly higher at lower normal stresses), ~0.7 for ATG gouge, and ~0.65 for LIZ gouge (Table F.1, labeled Slow μ_{nss}). Both LIZ and ATG gouge displayed stable sliding and slight strain hardening. Conversely, stick-slip instabilities occurred in all bare surface experiments at 3 mm/s. These events were audible and produced $0.1 - 0.25$ MPa stress drops, as reflected in the friction record (Figure F.2b).

After the velocity increased, friction of both bare surface and gouge samples first decreased (dynamically weakened) over a finite sliding displacement, reaching a minimum value. During deceleration, friction increased (recovered), resulting in a U-shaped friction versus displacement profile (e.g., Figure F.2a). In all runs there were sustained flat regions defining the minimum of the U-shaped profiles in which friction was relatively constant with changes in velocity. Similar to sliding at lower velocities, we define the average friction over these flat regions as μ_{nss} (labeled as Fast μ_{nss} in Table F.1). The μ_{nss} values for ATG bare surfaces were ~0.1 while those for ATG and LIZ gouge ranged from 0.35 to 0.38 (Table F.1).

To characterize the dynamic weakening, we report the amount of slip required to reach

Exp. #	Material	Exp. Conditions	Total Disp. (m)	Peak Vel. (m/s)	Peak Accel., Decel. (m/s^2)	Peak τ (MPa)	Avg. σ_n (MPa)	μ_{nss}; $^*\mu_{min}$	D_w (mm)	D_{th} (mm)	δ (mm)	V_f (m/s)	XRPD
736a	ATG_BS	SS_1	1.01	NA	41, 31	NA	5.4	0.14	NA	NA	NA	NA	Atg,En,Ol
736b	ATG_BS	SS_1	1.01	1.09	49, 30	5	12.4	0.14	27	4.6	0.4	0.2	Atg,En,Ol
736c	ATG_BS	SS_1	1.01	1.09	50, 30	8.1	20	0.12	82	4.8	0.4	0.2	Atg,En,Ol
736d	ATG_BS	SS_1	1.01	1.09	48, 29	11.4	32.1	0.11	15	2.3	0.4	0.2	Atg,En,Ol
736e	ATG_BS	SS_1	1.01	1.09	47, 30	16	49.8	0.11	21	1.9	0.4	0.2	Atg,En,Ol
736f	ATG_BS	SS_1	1.01	1.09	45, 29	26.2	65.1	0.11	24	1.6	0.4	0.2	Atg,En,Ol
736g	ATG_BS	SS_1	1.01	1.09	49, 30	31.1	75.7	0.11	22	1.6	0.3	0.2	Atg,En,Ol
736h	ATG_BS	SS_1	1.01	1.09	50, 29	35.2	96.6	0.11	9.3	1.5	0.3	0.22	Atg,En,Ol
820	ATG_G	SS_1	0.92	1	47, 49	2.5	4.0(0.2)	0.51(0.03)	200	130	NA	NA	Atg,Mgs,Mt
745	ATG_G	SS_1	0.92	1.2	60, 60	5.5	8.3(0.03)	0.48(0.02)	240	120	55	1	Atg,En,Mt,Ol
821	ATG_G	SS_1	0.91	1	41, 50	9	11.8(0.04)	0.52(0.01)	280	200	60	1	Atg,Mgs,Ol
822	ATG_G	SS_1	0.9	1	35, 46	12.4	17.8(0.08)	0.4(0.02)	175	67	40	0.85	Atg,Mgs,Ol
823	ATG_G	SS_1	0.9	1.1	24, 49	16.1	22.4(0.07)	0.39(0.02)	162	57	30	0.76	Atg,Mgs,Ol
747	LIZ_G	SS_1	0.92	1.2	65, 63	NA	3.8(0.06)	*0.5	NW	NW	NW	NW	Chl,En,Liz,Mt,Ol
746	LIZ_G	SS_1	0.92	1.2	60, 62	5.45	8.5(0.09)	*0.46	NA	NA	150	1	Chl,En,Liz,Mt,Ol
748	LIZ_G	SS_1	0.92	1.2	51, 60	8.3	11.5(0.6)	*0.52	NA	NA	100	1	Chl,En,Liz,Mt,Ol
825	LIZ_G	SS_1	0.9	1	40, 52	11.7	17.8(0.3)	*0.34	NA	NA	90	0.92	Aug,Chl,En,Liz,Mt,Ol
826	LIZ_G	SS_1	0.9	1.1	29, 48	14.3	18.7(0.4)	*0.31	NA	NA	70	0.87	Aug,Chl,En,Liz,Mt,Ol
834	ATG_G	SS_6.5	1.65	6.5	59, 30	8.9	10.9(0.08)	0.31(0.02)	180	70	20	1.4	Ol,Pyx
835	ATG_G	SS_0.1	0.89	0.14	4, 9	NA	23.3(0.07)	0.65(0.02)	NW	NW	NW	NW	Atg,Mgs,Mt
734	ATG_BS	MS_0.003_4.5	0.46	4.3	60, 70	4.4	4.9(0.04)	0.83(0.06); 0.12(0.03)	25	2.5	1	0.3	Atg,En,Mgs,Mt,Ol
727	ATG_BS	MS_0.003_4.5	0.46	4.3	NA	6.6	8.8(0.01)	0.67(0.01); 0.09(0.02)	NA	NA	NA	NA	Atg,En,Mgs,Mt,Ol
735	ATG_BS	MS_0.003_4.5	0.46	4.3	62, 70	10	14.9(0.4)	0.66(0.005); 0.09(0.01)	38	5.9	0.5	0.3	Atg,En,Mgs,Mt,Ol
733	ATG_BS	MS_0.003_4.5	0.46	4.3	NA	16	19.5(0.3)	0.68(0.05); 0.09(0.02)	25	NA	NA	NA	Atg,En,Mgs,Mt,Ol
824b	ATG_G	MS_0.003_4.5	0.51	4	65, 50	6.9	8.5(0.2)	0.72(0.002); 0.35(0.03)	68	44	33	2	Atg,Mgs,Ol
818	ATG_G	MS_0.003_4.5	0.51	4	63, 49	7.1	7(0.2)	0.73(0.002); 0.38(0.05)	197	183	70	2.6	NA
818	LIZ_G	MS_0.003_4.5	0.51	4.8	65, 75	5.9	8.5(0.2)	0.65(0.003); 0.38(0.02)	163	131	20	1.6	NA
Composition	LIZ												Chl,Liz,Mt(±Ol,En)
Composition	ATG												Atg,Mgs,Mt

Table F.1: Experimental conditions and mechanical data from 27 high-velocity friction experiments. Materials: ATG, antigorite-rich serpentinite; LIZ, lizardite-rich serpentinite; bare surface (BS) and gouge (G). Experimental conditions: SS_X, single velocity-step test at X m/s; MS_X_Y, multiple velocity-step test with initial velocity X m/s and stepped velocity Y m/s. NA, not applicable-indicates data was not recorded or measured. NW, experiment had no frictional weakening. Parentheses indicate standard deviation. X-ray powder diffraction (XRPD) data is reported in alphabetical order for observed mineral phases, antigorite (Atg), augite (Aug), clinochlore (chlorite, Chl), enstatite (En), lizardite (Liz), magnesite (Mgs), magnetite (Mt) and olivine (Ol).

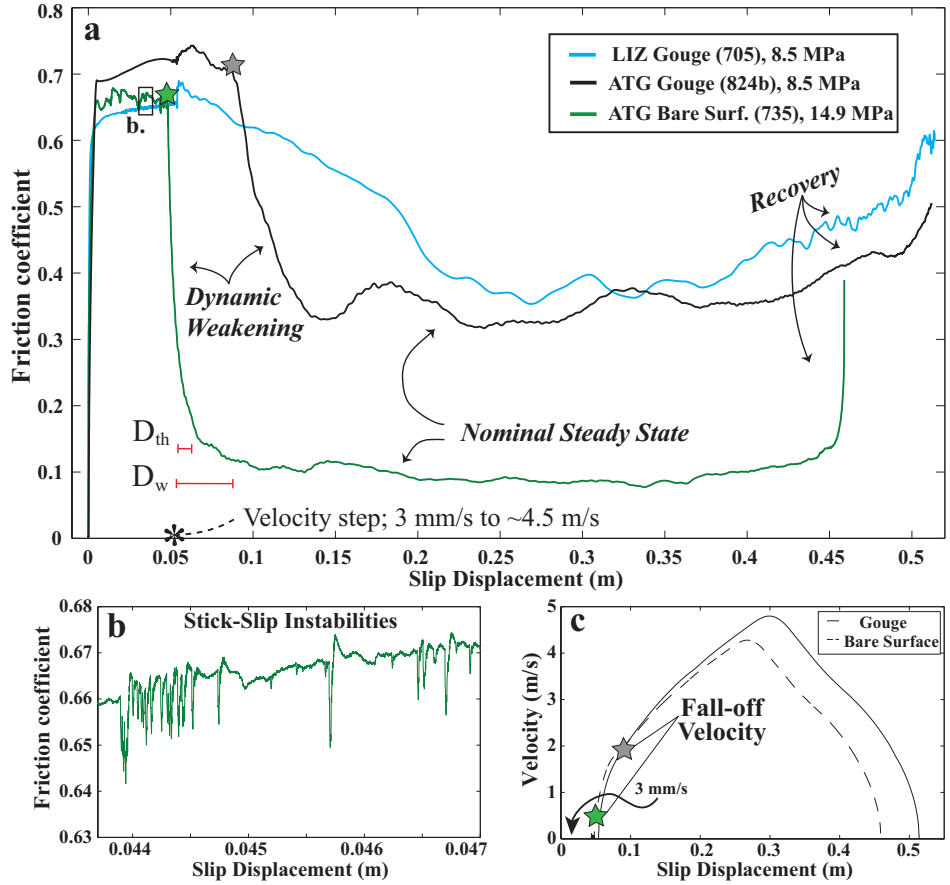

Figure F.2: (a) Results from three multiple velocity-step experiments; 3 mm/s for ∼6 cm of displacement, acceleration to ∼4.5 m/s and deceleration to rest. The approximate thermal- weakening distance (D_{th}) and slip-weakening distance (D_w) are indicated for Run 735 (see text for details). Stars indicate the displacement at which the friction rapidly decreases; the corresponding velocity (fall-off velocity) is shown in (b). (b) Frictional stick-slip instabilities observed in Run 735 at 3 mm/s. (c) The imposed velocity profiles for experiments shown in (a). Note that the acceleration is very similar in both gouge and bare surface experiments.

the new nominal steady-state friction value after the velocity step. Previous studies have defined this length-scale as either the slip-weakening distance (D_w), the distance over which the shear stress (or friction) drops by 95% of the total stress drop[108,150], or the thermal-weakening

distance (D_{th}), the distance over which stress falls to $1/e$ of the total stress drop[61]. We report both distances in Table F.1 for comparison with previous studies, however we discuss only D_{th} in this study. Values of D_{th} in bare surface experiments on ATG ranged from 3 to 8 mm. In contrast, for the same acceleration and normal stresses, D_{th} values in both the ATG and LIZ gouge experiments were over an order of magnitude larger, ranging from 40 to 180 mm.

To further quantify dynamic weakening, we report the velocity at the onset of frictional weakening, which we refer to as the fall-off velocity (V_f). Values of V_f were determined by first noting the displacement at which friction rapidly decreases (green and gray star in Figure F.2a), then finding the corresponding velocity for the given displacement (Figure F.2c). Values of V_f thus determined are simply a first-order observation dependent upon the imposed experimental conditions. For otherwise equivalent experimental conditions, V_f in gouge was as much as an order of magnitude larger than that in bare surface experiments (Table F.1).

F.3.2 Single velocity-step tests at 1 m/s

The results of all single velocity-step experiments are reported in Table F.1 and illustrated in Figure F.3. In general, these experiments demonstrated similar differences between the behavior of bare surfaces and gouge observed in the multiple velocity-step experiments. In addition, because the velocity was held constant and normal stress was varied we were able to explore the normal stress dependence on μ_{nss}, D_{th} and V_f (compiled in Figure F.4).

Values of μ_{nss} decreased with increasing normal stress in both gouge and bare surface experiments (Figures F.3a, F.3b and F.3c); the normal stress dependence is larger for gouge

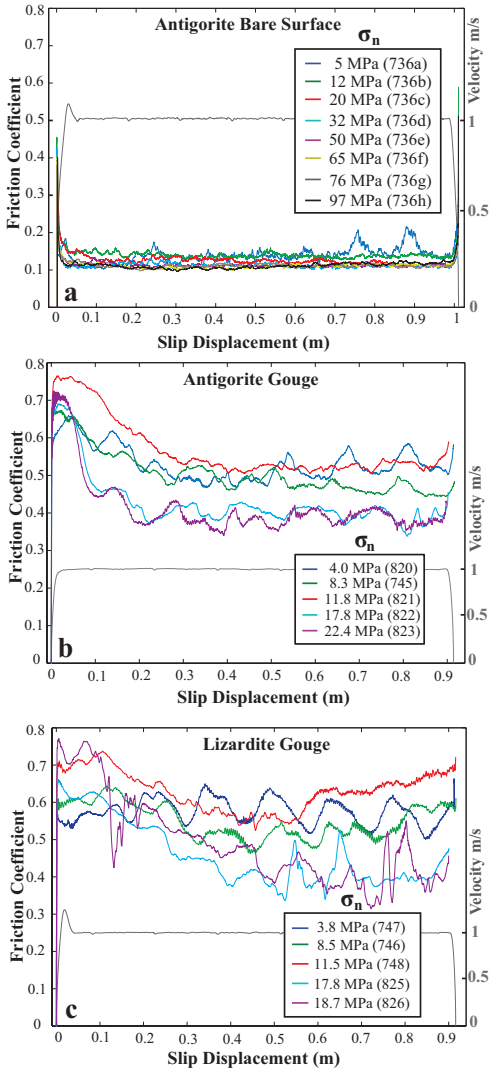

Figure F.3: Results from single velocity-step experiments with peak velocities of 1 m/s on (a) antigorite bare-surfaces, (b) ATG gouge, and (c) LIZ gouge. A representative velocity profile is shown for each suite of experiments (grey line). Large wavelength oscillations in gouge friction are caused by inconsistencies in gouge thickness (see Methods section).

than for bare surfaces (Figure F.4a). Values of μ_{nss} for bare surfaces decreased from 0.14 to 0.11 with an increase in σ_n from 5 to ~30 MPa and remained at a value of ~0.11 with ad-

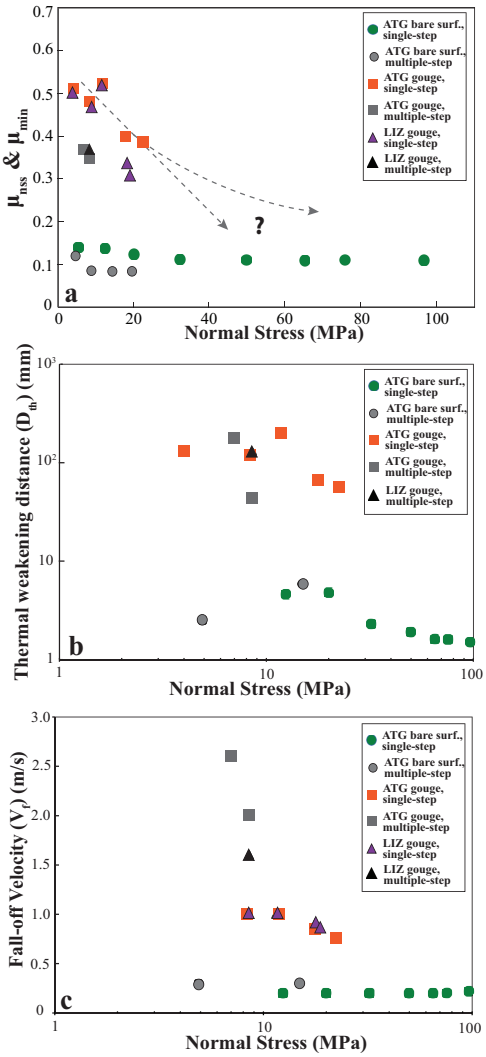

Figure F.4: Normal stress dependence on (a) nominal steady-state and minimum friction values (LIZ gouge), (b) thermal weakening distance, and (c) the fall-off velocity for multiple velocity-step and single velocity-step experiments.

ditional increase in σ_n from 30 to ~97 MPa (Figure F.4a). The friction data for gouge are more scattered than for bare surfaces. Interpretation of these experiments is complicated by (1) variations in sample thickness which caused sinusoidal oscillations in shear and nor-

mal stress, and (2) sample leaks, which caused spikes in the data. As such, the reported μ_{nss} values have larger standard deviations (Table F.1). Values of μ_{nss} for ATG gouge decreased from 0.51 to 0.39 with an increase in σ_n from 4 to 22.4 MPa (Figure F.4a). Friction for LIZ gouge did not appear to reach a steady-state value in any single-velocity experiment (Figure F.4a); for these experiments we report only a minimum friction value (μ_{min}). Values of μ_{min} for LIZ gouge decreased from 0.50 to 0.31 with an increase in σ_n from 3.8 to 18.7 MPa. The ATG and LIZ gouge samples deformed at σ_n ~12 MPa (Runs 821 and 748) deviate somewhat from this general trend. Values for μ_{nss} from multiple velocity-step experiments (with maximum slip rates of ~4.5 m/s) are generally consistent with single velocity-step results (with maximum slip rates of ~1 m/s) (Figure F.4a). Values of D_{th} for both ATG bare surfaces and gouge decreased with increasing normal stress, though there is scatter for the gouge samples (Figure F.4b). We did not calculate D_{th} values for LIZ gouge because steady-state friction was not reached. Values of D_{th} for ATG bare surfaces decreased from 0.46 to 0.15 mm with an increase in σ_n from ~11 to 97 MPa. Values of D_{th} for ATG gouge are more than an order of magnitude greater than for ATG bare surfaces and decreased from 130 to 57 mm with an increase in σ_n from 4 to 22.4 MPa. Values of D_{th} from multiple velocity-step experiments are similar to those observed from single velocity-step experiments on both bare surface and gouge samples (Figure F.4b).

Values of V_f are independent of normal stress in bare-surface experiments and decrease modestly with increasing normal stress in gouge experiments; V_f is much smaller for bare surface samples than gouge samples deformed at the same conditions. Figure F.4c shows that values of V_f for all ATG bare surface experiments were ~0.2 m/s. In contrast, for approximately the same velocity profile, V_f decreased from 1 to 0.76 m/s for LIZ gouge and

from 1 to 0.87 m/s for ATG gouge with increasing normal stress. These trends in V_f for gouge also reflect a decrease in the amount of slip that occurred prior to frictional weakening with increasing normal stress; at low σ_n, the gouge experiments reached the peak velocity (1 m/s) and continued to slip for tens of millimeters before frictional weakening occurred, while at higher σ_n, the gouge weakened during acceleration before the peak velocity was attained. For bare surfaces, values of V_f in multiple velocity-step experiments are similar to those observed from single velocity-step experiments (Figure F.4c). In contrast, for gouge samples, values for V_f are significantly higher in the multiple velocity-step experiments (Figure F.4c).

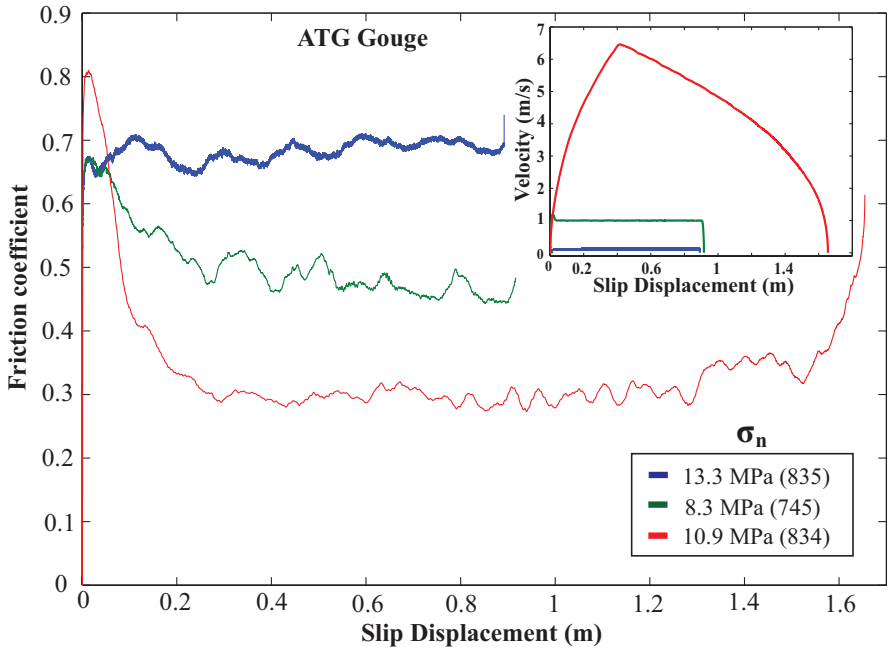

Figure F.5: Velocity dependence of antigorite gouge; inset shows velocity profile for corresponding experiments. Run numbers are indicated in parentheses.

F.3.3 Additional single velocity-step tests

To better constrain the velocity and displacement dependence of friction for the ATG gouge samples, we conducted two single velocity-step experiments at 0.1 m/s and ∼6.5 m/s (Runs 835 and 834, Figure F.5). These experiments were conducted at normal stresses of 13.3 and 10.9 MPa, respectively. No frictional weakening was observed at 0.1 m/s (Run 835, blue trace in Figure F.5); the value of μ_{nss} remained ∼0.65 throughout the duration of the 0.9 m slip cycle. In contrast, the sample deformed at a peak velocity of 6.5 m/s (Run 834, red trace in Figure F.5) yielded a value of the friction coefficient of 0.31. This sample was also deformed to a larger amount of slip, ∼1.6 m, than in the other single-velocity tests (slip ∼1 m) and velocity-stepping tests (slip ∼0.45 m). As is shown in Figure F.5, the friction coefficient was independent of velocity and achieved a steady value (∼0.3) during the acceleration stage for $V > 4$ m/s (after 0.2 m of slip) and began to increase during the deceleration stage for $V < 2.5$ m/s (after 1.5 m of slip).

F.3.4 Velocity dependence and frictional hysteresis

In all of the high-velocity experiments, we observe hysteresis in plots of friction versus velocity, with greater velocity dependence and higher friction values during acceleration than deceleration (e.g., Figures F.2a, F.3a, F.3b, F.3c and F.5). In Figure F.6a we plot unfiltered data for two multiple velocity-step experiments on ATG bare surfaces (Runs 734 and 735; blue and green traces). In this figure the value of friction traces a clockwise "path" in log velocity space. During acceleration from 3 mm/s to ∼0.1 m/s, the friction remains nominally constant; friction then begins to decrease at a velocity of ∼0.1 m/s, and decreases more rapidly at velocities above ∼0.3 m/s. In Figure F.6b we plot the friction data for ATG

gouge during one single velocity-step experiment (Run 834, red trace in Figure F.6b). In this run, there was no initial period of slow slip at 3 mm/s; the sample was accelerated from rest to the target slip rate of 6.5 m/s. We also plot the data from a multiple velocity-step gouge experiment (Run 824b, black trace in Figure F.6b); in this test, the sample was slid for 60 mm at 3 mm/s and then accelerated to 4.5 m/s.

During acceleration, the gouge experiments show behavior similar to that for the bare surface experiments, except that for the gouge, the onset of weakening is shifted to higher velocities ($\sim$1 m/s) producing a larger hysteresis (Figure F.6b). During deceleration, friction during both ATG bare surface and ATG gouge experiments increases to values somewhat lower than those determined during the initial low-velocity portion of the experiments; friction for the gouge recovers at a higher velocity ($\sim$0.2 m/s) than for the bare surfaces (< 0.02 m/s) (Figures F.6a and F.6b).

In Figure F.6 we superimpose μ_{nss} data on the friction path data for experiments on bare surfaces (green circles) and gouge (green squares). In both diagrams, black numbers correspond to the run number. For velocities below $\sim$0.1 m/s, values of μ_{nss} are similar to the transient values observed during acceleration. In contrast, at higher velocities, values of μ_{nss} are similar to the transient values observed during deceleration.

F.3.5 Microstructural and mineralogical analysis

E.3.5.1 Bare surface experiments

All bare-surface samples deformed at velocities of 1 m/s and higher developed grooved striations and exhibit glass-like material on the slip surface. The glass-like material was observed in two textural forms. The first was a dark-green veneer with glassy sheen that occurred in

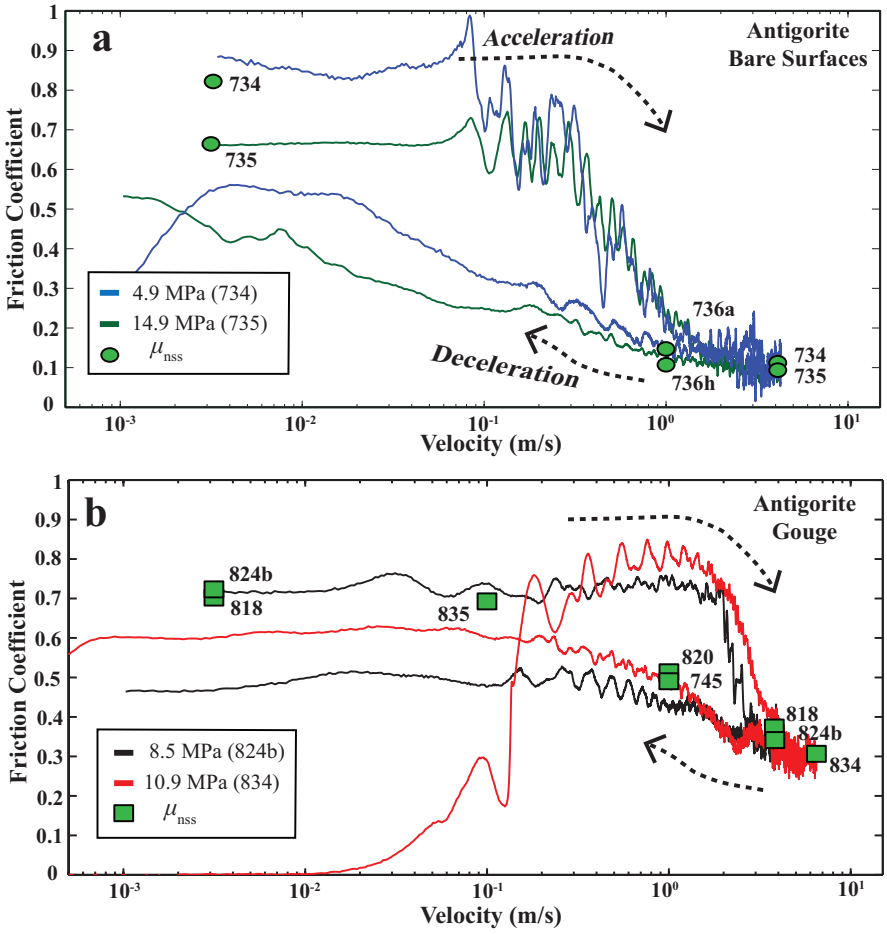

Figure F.6: Hysteresis and velocity dependence of (a) ATG bare surfaces and (b) ATG gouge. Lines trace the evolution of friction from the onset of acceleration to the completion of deceleration. Run numbers are indicated in parentheses. In Runs 734, 735, and 824b, the velocity was accelerated from 3 mm/s from which they were sheared for 6 cm. Experiment 834 was accelerated from rest with no prior deformation. Symbols indicate nominal steady state values (μ_{nss}); corresponding Run number is noted in black.

bands along topographically higher ridges on the slip surface (Figure F.7a). This material was observed in all bare-surface experiments. An SEM micrograph of one of these surfaces shows finger-like tendrils and bulbous structures (Figure F.7b), similar to glass fibers de-

scribed in *Friedman et al.* [1974][80]. The second textural form of glass-like material was $10 - 20$ μm thick glassy patches of light-green and translucent material observed on the slip surface (Figures F.7c and F.7d) of samples deformed at $\sigma_n > 20$ MPa. The glassy material is composed of a nominally homogenous ultra-fine grained matrix (i.e., the matrix grain-size is either too small to resolve with an SEM (<10 nm) or amorphous) with larger magnetite inclusions as suggested by backscattered electron SEM micrographs (Figure F.7e and F.7f) and exploratory micro-chemical analyses. These glassy patches occurred as bands oriented parallel to striations on the slip surface (similar to the "melt welts" described by *Brown and Fialko* [2012][36]) and are more numerous in samples deformed at higher normal stresses. At the highest normal stress the entire slip surface appeared to be covered with the glass-like material.

X-ray powder diffraction analysis of wear material collected after bare surface experiments showed evidence of serpentine dehydration products, olivine and enstatite (Table F.1), in all samples tested (all of which were deformed at high enough slip velocity to cause frictional weakening). In several ATG bare surface experiments (e.g., Runs 733, 734, and 735) magnesite was detected, but never in the LIZ experiments where carbonates were not present in the starting material. A comparison of XRPD profiles shows a systematic increase in the peak heights of olivine with increasing applied normal stress (Figure F.8), suggesting a relative increase in the mass of the reaction products. None of the bare surface samples showed XRPD evidence for talc.

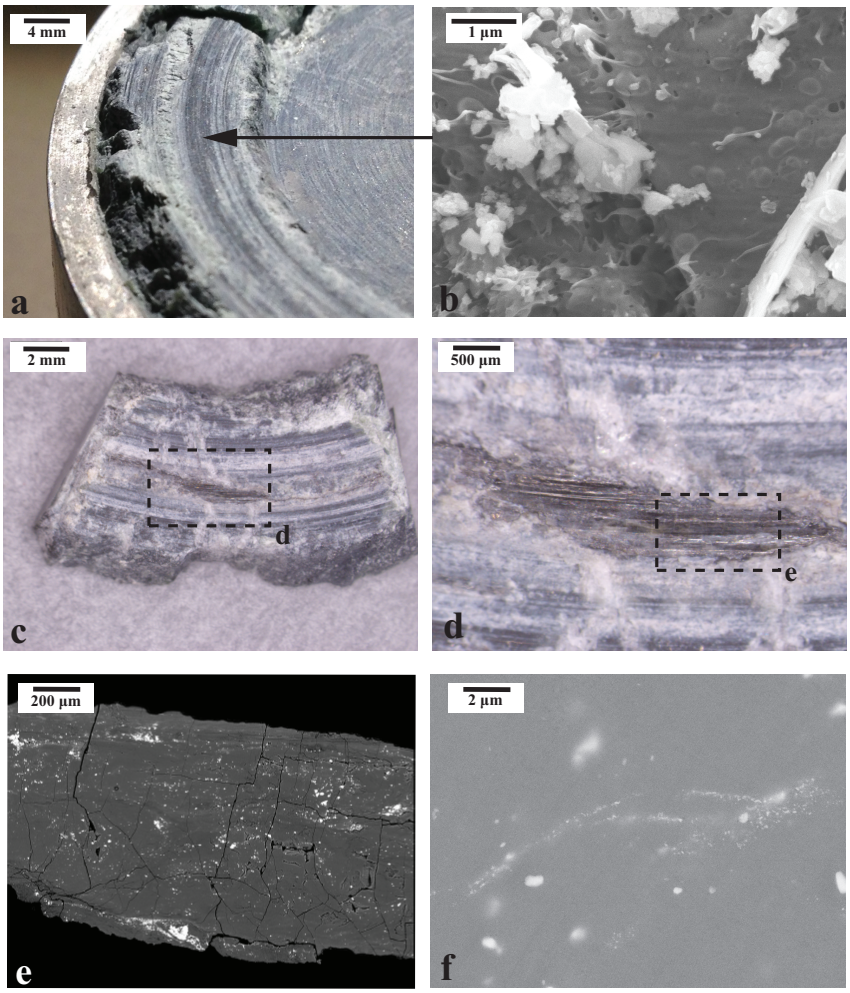

Figure F.7: Microstructures of antigorite bare-surfaces. (a) Photomicrograph showing dark striations on slip surface at low normal stress; Run 727, $\sigma_n = 8.8$ MPa. (b) SEM micrograph of dark band from sample from Run 727 showing melt-like tendrils and bulbous features on the slip surface. (c) Photomicrograph showing glass-like band on cut section of the slip surface at higher normal stress; Run 733, $\sigma_n = 19.5$ MPa. (d) Magnified region from F.6c showing glassy luster and transparent nature of the material. (e) SEM micrograph from polished glassy surface shown in (d). (f) Enlargement from 7e showing gray ultra-fine grained matrix with bands of nm-scale iron-rich minerals that are too fine-grained to resolve.

E.3.5.1 Gouge experiments

In all gouge samples some degree of strain localization and grain-size reduction was observed. The ATG gouge sample tested at $V = 0.1$ m/s was poorly consolidated after deformation and developed a $400 - 500$ μm-thick zone of reduced grain size where strain was apparently localized (Figure F.9a). The localized zone was composed of a matrix of $50 - 500$ nm rounded antigorite grains (Figure F.9b). This sample did not develop a well-defined slip surface or slickenlines.

ATG and LIZ gouge samples deformed at $V \geq 1$ m/s developed $100 - 200$ μm thick fine-grained localized zones consisting of an ultra-fine-grained matrix hosting clasts ranging from $<$ 1 to 20 μm in diameter (Figures F.9c and F.9e). The fine-grained zones tend to be welded in all samples (e.g., Figures F.9d and F.9f). In some cases, microstructures indicate that the welded zones were brecciated after welding. The inspection of the localized zone from Run 746 (LIZ) illustrates clasts that are welded aggregates of fine-grained material (Figure F.9f), suggesting a welded zone formed first then became brecciated and comminuted. In instances where the localized slip surface was exposed during sample recovery, we observed dark glassy striated patches (Figure F.10g). These thin zones appeared translucent and became more abundant in samples deformed at higher normal stresses. An SEM image shows the cross-sectional profile of the dark glassy material (Figure F.10h). At higher normal stresses and at the highest slip velocities (Run 834) we observed whitish (e.g., Figure F.10g) and brownish streaks along the slip surface in addition to the dark glassy material. Brownish streaks are composed of micron- to submicron-in size granular clasts; spot XRPD analysis of one of these streaks revealed strong peaks for olivine and weak peaks for enstatite (Run 834, Table F.1). A cross-section through a whitish streak in an ATG sample (Run 823,

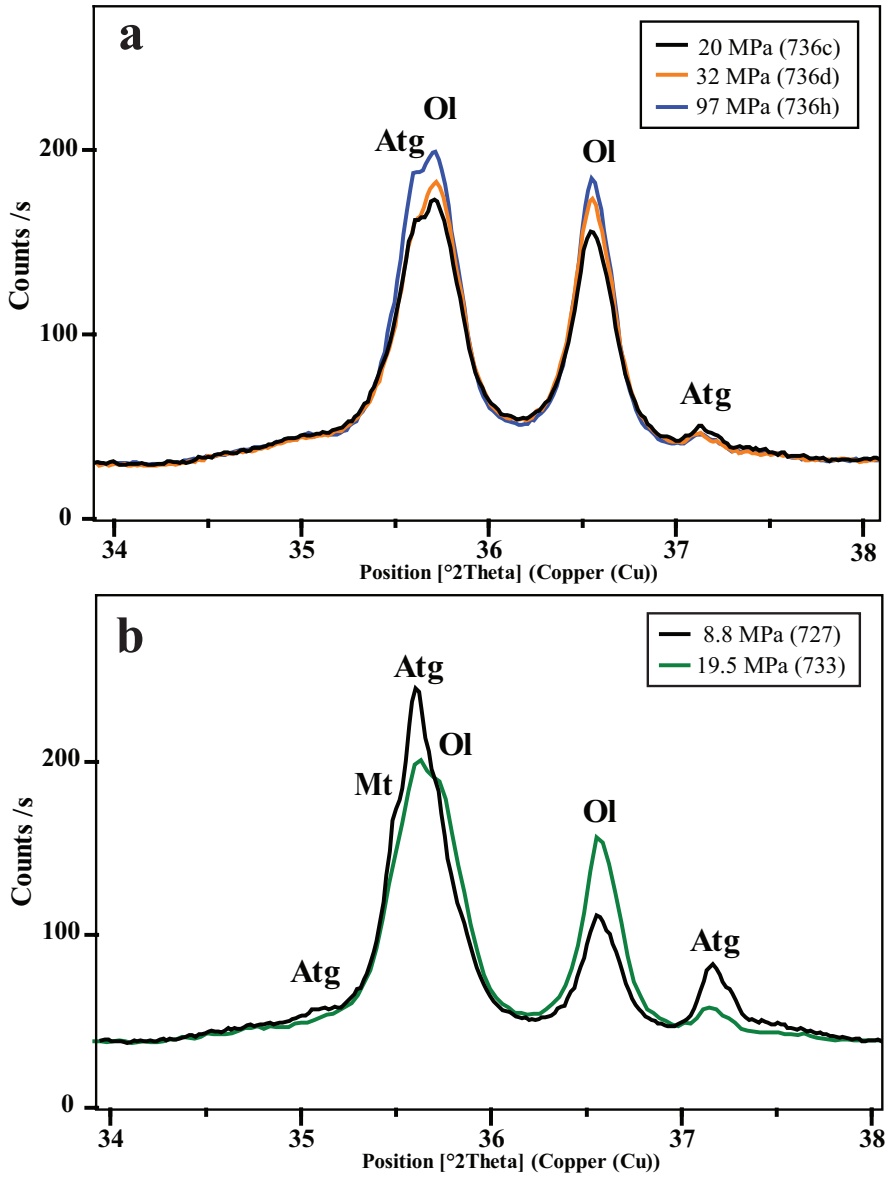

Figure F.8: Comparison of XRPD results from 3 single velocity-step experiments (a) and 2 multiple velocity-step experiments (b); the applied normal stress for each experiment and run number is noted in the key.

Figure F.10i and F.10j) shows an ultra-fine-grained matrix with amoeboid-shaped vesicles. The vesicles are dispersed in a glass-like matrix probably resulting from quenching of the friction melt. The vesicles become smaller with increasing distance from the slip surface; next to the latter they become interconnected defining a shear-parallel fabric (Figure F.10j). Similar glass-like material and degassing related textures were observed in LIZ samples. Figures F.10k and F.10l show an ultra- fine-grained zone that appears to have been injected into the brecciated zone. In this sample we note a high density of vesicles near the top of this apparently once-molten layer.

In both LIZ and ATG gouge samples strain localized within the gouge layer near the interface between the gouge holder and the stationary side of the shearing rotary disk (dashed line, Figure F.1e). In all ATG samples deformed at $V \geq 1$ m/s we observed little textural evidence for deformation outside of the $100 - 200$ μm thick localized zone. This is also true of LIZ gouge samples at lower normal stresses (<10 MPa), however, in samples from Runs 825 and 826 deformed at a normal stress of 18 and 19 MPa, respectively, we observed localized zones containing ultra-fine-grained (glassy) material adjacent to both the stationary and rotary-side of the sheared layer. Further microstructural inspection of these samples revealed a varying degree of deformation throughout the shearing gouge layer.

X-ray powder diffraction revealed a general trend that gouge samples that underwent frictional weakening showed evidence for serpentine dehydration products (Table F.1). In contrast, Run 835 (which was conducted at 0.1 m/s and showed no frictional weakening) did not show XRPD peaks for olivine or enstatite (Table F.1). Two samples did not fit this trend. One LIZ sample (Run 747) did not demonstrate frictional weakening, yet contained trace amounts of olivine and enstatite; we suspect these phases were inherited

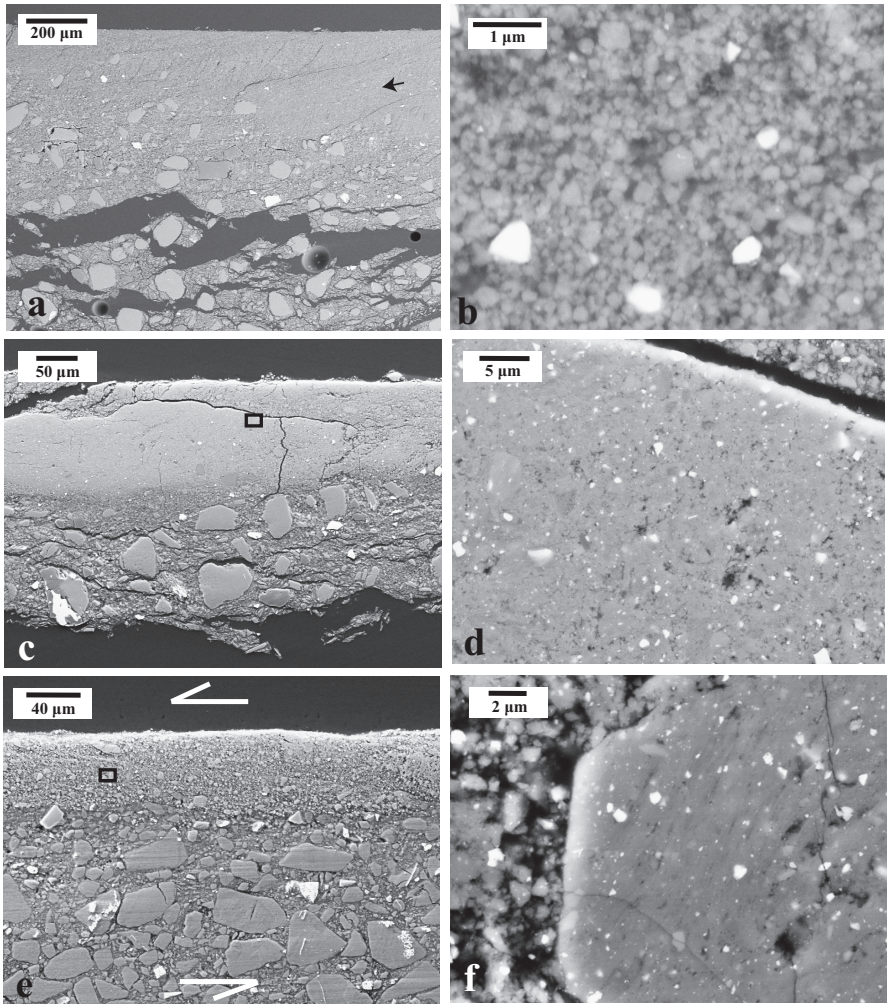

Figure F.9: Microstructures of antigorite and lizardite gouges, all BSE-SEM micrographs with exception of Fig. (g). The SEM micrographs show cross-sectional profiles; samples are oriented such that top surface was adjacent to non-rotary disk, however in all cases the section of the gouge zone closest to the stationary side was not recovered. (a) Run 835 (ATG) deformed at 0.1 m/s; orientation of shearing is not known, $\sigma_n = 13.3$ MPa. (b) Enlargement of granular fine-grained material within localized zone from 9a (black arrow). (c) Run 821 (ATG) deformed at 1 m/s; sample is cut perpendicular to shearing direction, $\sigma_n = 11.8$ MPa. (d) Enlargement of ultra fine-grained material in (c) (black frame box). (e) Run 746 (LIZ) deformed at 1 m/s; sample is cut parallel to shearing direction, $\sigma_n = 8.5$ MPa. (f) Enlargement of brecciated clast within localized zone in (e).

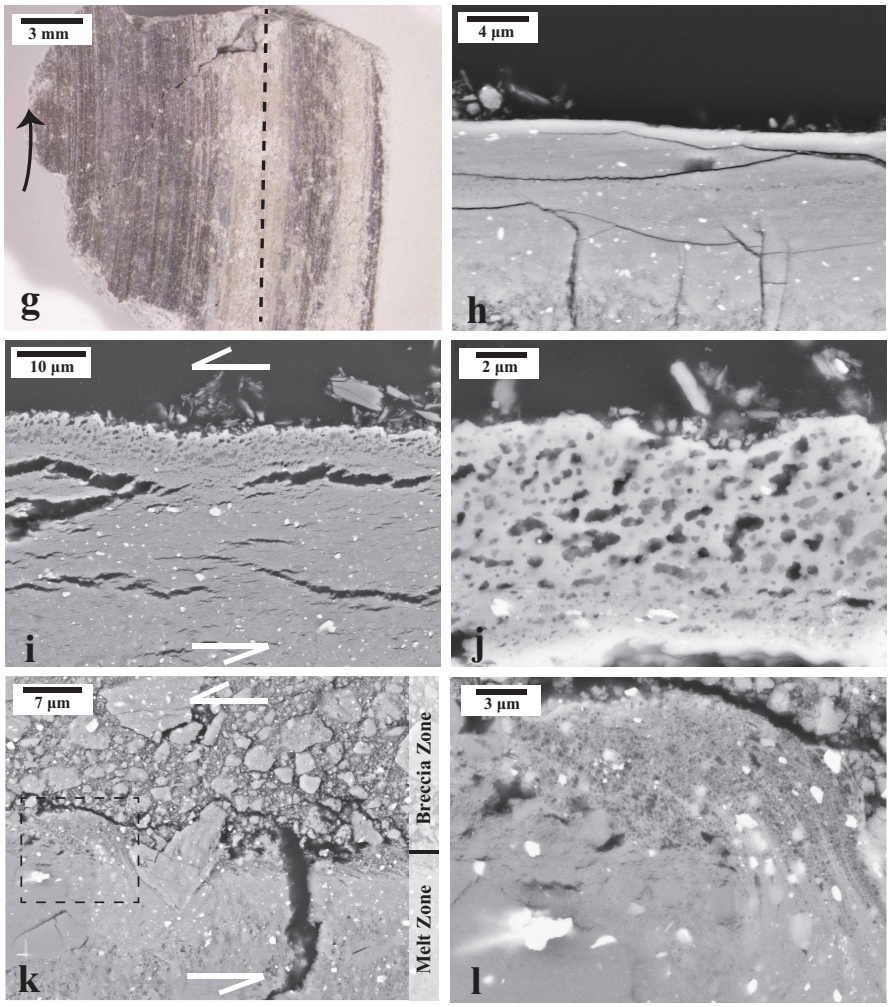

Figure F.10: (g) Photomicrograph of slip surface from Run 823 deformed at 1 m/s showing vitreous and striated dark material and whitish streaks; rotary direction is indicated with black arrow, $\sigma_n = 22.4$ MPa. (h) Enlargement of dark glassy material shown in (g); sample is cut perpendicular to shearing direction. (i) Enlargement of whitish streak in (g) showing vesicular ultra-fine-grained material along the slip surface; sample is cut along black dashed line. (j) Enlargement of (i) showing irregular-shaped vesicles. (k) Run 826 deformed at 1 m/s showing an ultra-fine-grained zone "flowing" into the brecciated zone; sample is cut parallel to shearing direction, $\sigma_n = 19$ MPa. (l) Enlargement of (k) (dashed box) showing flow structure.

from the starting material. One ATG sample (Run 820) demonstrated frictional weakening, yet contained no XRPD evidence for dehydration; since this sample was deformed at 4 MPa we suspect the amount of reaction products may have been too small to resolve with XRPD. Diffraction peaks for talc were not found in any samples.

F.4 Discussion

Our experiments show that serpentine bare surfaces and gouge undergo frictional weakening during high-velocity shear experiments. However, friction evolves differently in each material with changes in slip displacement, velocity and normal stress. These differences can be reconciled by exploring the underlying processes that promote dynamic weakening: strain localization and shear heating. In the following discussion we first compare our bare surface data to previous high-velocity friction studies on similar materials. This comparison allows us to develop a conceptual model to better understand experimental observations on serpentine bare surfaces. We then use 1-D thermal models to explore how measured friction values are affected by frictional heating at the surface-scale (mm) and asperity-scale (μm) in both bare-surface and gouge experiments.

Figure F.11: Interpretation of friction hysteresis in high speed experiments on serpentinites. (a) Comparison of ATG bare-surface friction data from this study with results from short displacement experiments from *Kohli et al.* [2011][125] (see text for discussion). Parentheses indicate the Run number. (b) Schematic model illustrating friction hysteresis during an earthquake slip event (EQ) for serpentinite bare-surfaces (solid lines) and dry gouge (dashed lines) (see text for discussion). (c) Predicted friction profile (black curve) using flash weakening model[186] for bare surface sample (Run 735); equation (F.1) is used to model surface temperature increase during slip, which is then inserted into the formula for V_w from *Rice*[2006][186]. Model shows that the deceleration friction path will be offset to lower velocities and the measured friction data (green trace) only partially fits the model during deceleration. (d) Predicted friction profile (black curve) during acceleration using flash weakening model[186] for gouge sample (Run 834); the temperature of the deforming zone is assumed constant.

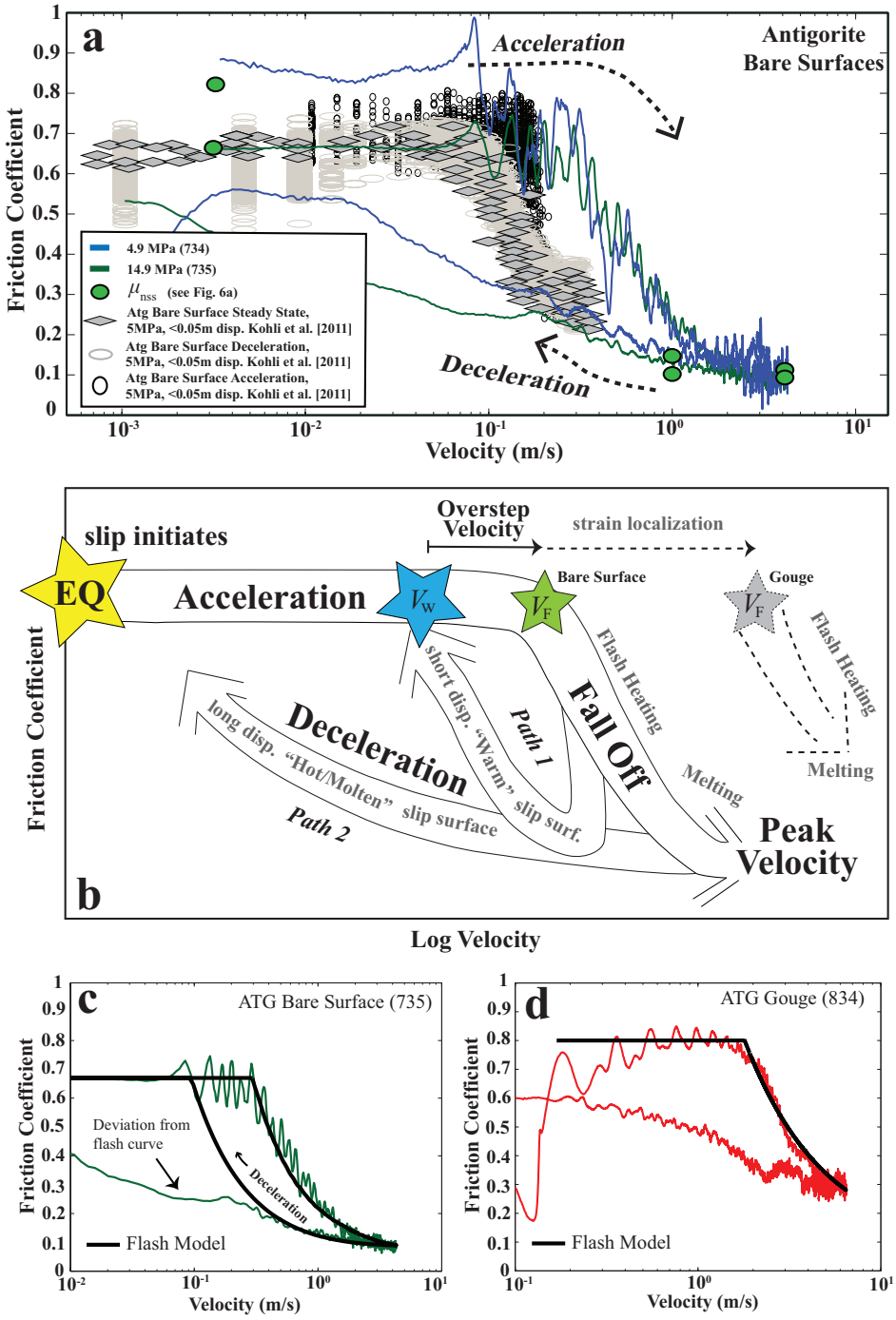

Figure F.11: (continued)

F.4.1 Displacement- and velocity-dependent hysteresis of friction on bare surfaces

Values of macroscopic friction for a given sliding surface are a manifestation of frictional heating and temperature evolution on both the macro- (slip-surface) scale and the asperity-scale (μm). These relationships are qualitatively demonstrated via variations in hysteresis loops between short and long displacement experiments shown in Figure F.11a. In Figure F.11a we plot results from our ATG bare-surface experiments together with results of 50 experiments from *Kohli et al.* [2011][125] on ATG bare surfaces conducted at a normal stress of 5 MPa, a maximum velocity of 0.3 m/s, and a maximum acceleration of 10 m/s^2. This data set can be subdivided into two friction paths shown schematically in Figure F.11b. Path 1 is modeled after the friction data from small displacement experiments (<0.05 m) from *Kohli et al.* [2011][125] shown in Figure F.11a. *Kohli et al.* [2011][125] concluded that weakening occurred via flash heating of asperities above a critical weakening velocity (V_w) of ~0.1 m/s for samples deformed at room temperature, based on the coincidence of the steady-state friction data (grey diamonds in Figure F.11a) with the deceleration-path data, the observation of talc in XRPD analyses from the wear material of high velocity samples, and the general agreement between the data and theoretical descriptions for flash weakening[8,186].

Flash weakening theory predicts that values of friction should decrease when the asperity velocity exceeds the weakening velocity V_w[186]. However in all experiments in which the slip rate was accelerated above V_w friction remained transiently high before decreasing to steady-state values (black ovals, Figure F.11a) resulting in a modest hysteresis. This velocity overstepping represents a deviation from theoretical predictions and is characterized using the difference between the fall-off velocity (V_f) and the critical weakening velocity (V_w), defining an overstep velocity ($V_f - V_w$) (Figure F.11b). Following *Kohli et al.* [2011][125] and

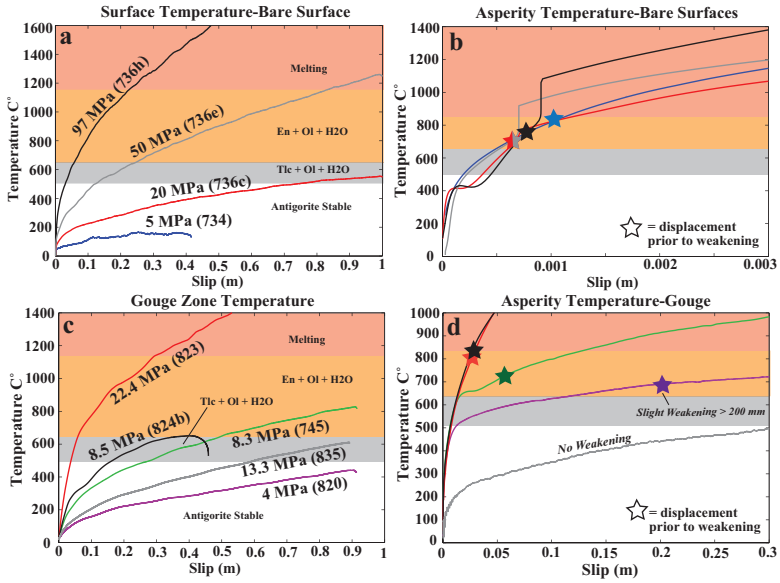

Figure F.12: Results from 1-D thermal modeling with projected antigorite phase diagram (see text details). (a) Sliding surface temperatures in four ATG bare-surface experiments; the applied normal stress and run number are noted by the corresponding temperature profile. (b) Asperity contact temperatures for bare surface samples modeled in (a); line colors correspond with (a). (c) Shear zone temperatures in five ATG gouge experiments assuming a 150 μm-wide shear zones. (d) Asperity contact temperatures within deforming gouge; line colors correspond with (c).

Goldsby and Tullis [2011][93], we posit that the overstepping results from the displacement required for strain localization and subsequent shear heating to occur within the thin gouge layer generated by wear between the bare surfaces. The displacement that occurs during acceleration between V_f and V_w is defined as an overstep displacement (δ) following *Kohli et al.* [2011][125] (labeled δ_w therein). All δ values are reported in Table F.1 assuming V_w = 0.1 m/s. In this study δ was ~0.4 mm for single step velocity-step tests and ranged from 0.5 to 1 mm in multiple-velocity step tests, consistent with δ values observed by *Kohli et al.* [2011][125].

Path 2 is defined by experiments conducted in this study (green and blue traces in Fig-

ure F.11a) that have higher total displacement, peak velocities and normal stresses than the *Kohli et al.* [2011][125] experiments. In our experiments the friction during acceleration is similar to that observed in the short displacement (Path 1) experiments of *Kohli et al.* [2011][125]; the somewhat higher value for V_f in the Path 2 experiments arises from greater acceleration (50 m/s^2 compared to 10 m/s^2). Nonetheless, δ remains approximately the same (Table F.1), indicating that the initial weakening results from flash heating in both suites of experiments. At peak velocities, the Path 2 steady-state friction values are lower than the Path 1 values, but are consistent with the overall weakening trend and the results of *Hirose and Bystricky* [2007][106] on serpentine bare surfaces slid at 1 m/s. During deceleration frictional recovery is delayed to lower velocities than observed in Path 1 experiments, resulting in a larger hysteresis loop (Figure F.11b). We suggest that the difference between Path 1 and Path 2 experiments is in part due to the sensitive dependence of V_w on the fault surface temperature (T_{surf}), where $V_w \propto (T_w - T_{surf})^2$; if the difference between the surface temperature and the weakening temperature (T_w) is reduced by a factor of two, a typical value seen in our thermal models, then V_w decreases by a factor of 4[186]. The higher displacements, slip rates and normal stresses used in Path 2 experiments generate higher surface temperatures, leading to lower values of V_w during deceleration than seen in Path 1 experiments. This is consistent with the observation that in Run 734 performed at 4.9 MPa normal stress, the recovery of the friction coefficient occurs at a higher velocity than in Run 735 performed at 14.9 MPa (Figure F.11a). Small patches of melt produced on the slip surface may further delay Path 2 recovery. Conversely, in Path 1 experiments there is not enough time for the surface temperature to significantly increase, thus V_w remains constant, resulting in rapid friction recovery at velocities higher than in Path 2 experiments. In the following section we

use 1-D thermal modeling to further explore this hypothesis.

F.4.2 1-D Thermal Modeling: Bare Surfaces

To quantitatively explore differences in temperature evolution between the slip surface and asperity contacts in bare surface experiments we employ 1-D thermal models. These models do not consider the latent heat of reaction; nonetheless they allow for a first-order exploration of the processes governing dynamic weakening and frictional recovery. For the bare surface experiments we calculate the surface temperature using the following model (see Appendix F.9 for derivation)

$$T_{surf} = T_0 + \int_0^t \frac{\tau(t')V(t')}{\rho c} \frac{1}{\sqrt{4\pi\alpha_{th}(t-t')}} \mathrm{d}t', \tag{F.1}$$

where T_0 is the initial temperature (21 °C), $\tau(t')$ is time dependent shear stress, $V(t')$ is time dependent velocity, ρc is the effective heat capacity per unit volume, and α_{th} is the thermal diffusivity. The heat capacity and thermal diffusivity for antigorite are 2700 kJ (K m^3)$^{-1}$ and 0.90 mm^2 s^{-1} respectively[160]. For a given experiment the integral is evaluated numerically using measured values for τ and V. In Figure F.12a we plot T_{surf} for three single velocity-step tests and one multiple velocity-step test together with a projection of the MgO-SiO_2-H_2O phase diagram[164] and the wet solidus for ultramafic rocks[220] (see discussion below). Figure F.12a shows that peak surface temperatures increase with increasing normal stress from ∼200 °C at 5 MPa to $>$ 1600 °C at 97 MPa which is generally consistent with the microstructural observation of glassy material on samples deformed at the highest normal stresses. However, recall that olivine and enstatite were observed in the wear material in all bare-surface experiments (Table F.1), even those at the lowest normal stress

(e.g., Run 734). The presence of these dehydration products is inconsistent with the 1-D thermal model for the surface temperature. To reconcile this observation with the thermal model, we consider the temperature evolution at the asperity contacts (T_{asp}) with the following flash-heating model (see Appendix F.9)

$$T_{asp} = T_{surf} + \frac{\tau_c}{\rho c}\left(\frac{Vd}{\pi\alpha_{th}}\right)^{1/2}, \tag{F.2}$$

where τ_c is the contact shear stress and d is the contact diameter. Here we have assumed that a contact ceases to exist after it has slipped a distance equal to the contact diameter, and thus the contact lifetime is equal to d/V. Following *Kohli et al.* [2011][125] τ_c is approximated as 3 GPa (based on indentation hardness measurements[91] and plasticity data for antigorite[103]) and d is estimated to be 5 μm (based on the critical slip distance observed during velocity changes at low slip velocities on identical samples of similar roughness[178]). Figure F.12b shows that T_{asp} in all experiments quickly increased above antigorite thermal stability over slip displacements $<$ 1 mm. The total displacements at which the onset of weakening was observed (stars in Figure F.12b) is coincident with predicted antigorite dehydration reactions and generally consistent with the flash weakening temperature inferred by *Kohli et al.* [2011][125] ($\sim$600 $^\circ C$). Recall that δ is the displacement that occurs during acceleration between V_f and V_w, where V_w is 0.1 m/s. So the total displacement prior to weakening is simply δ plus the slip that occurs from the onset of acceleration to 0.1 m/s which is on the order of 200 to 300 μm. Furthermore, using experimental parameters from *Kohli et al.* [2011][125], equation (F.2) predicts temperatures consistent with their observation of talc in the wear material. In contrast, our experiments have over an order of magnitude larger velocity, which promotes asperity temperatures significantly above the talc stability field,

into the olivine and enstatite field, and eventually above the wet solidus, consistent with the observation of olivine and enstatite in the wear material and the glass-like textures and materials on the slip surface (e.g., Figure F.7b). The modeled asperity temperature is only valid before the onset of weakening, since we have neglected changes to the contact shear stress and possible latent heat effects that accompany the onset of weakening.

These models also suggest that flash heating is likely causing the initial weakening observed in Path 2 experiments, similar to the Path 1 (Figure F.12b); moreover, the fact that both samples from Runs 734 and 735 (performed at normal stresses of 4.9 MPa and 14.9 MPa, respectively), weaken at about the same slip rate of 0.1 m/s (Figure F.6a), suggest that the initial weakening is independent of normal stress, consistent with the flash heating mechanism[186]. However, with increasing displacement/deformation time the T_{surf} increases at a rate dependent on the shear stress and velocity. For high enough slip and velocity, weakening due to flash heating will be associated with asperity melting, which will lead to the generation of melt patches with increasing power dissipation and eventually lead to bulk melting of the entire fault surface[223,108]. A first order fit of the friction data from Run 735 (ATG) with the flash weakening model given in *Rice* [2006][186], such that T_{surf} is allowed to increase using equation F.1 (Figure F.12c), demonstrates that an increase in surface temperature alone cannot explain the delayed recovery during deceleration. We therefore conclude that the delayed frictional recovery shown in Path 2 is in part a manifestation of this transition from flash weakening to bulk melting.

F.4.3 1-D Thermal Modeling: Gouge

To quantitatively explore differences in temperature evolution between a uniformly shearing gouge zone and asperity contacts between clasts within the zone we modify the 1-D thermal modeling to account for the thickness of the deforming zone. Similar to bare surface models we do not consider the latent heat of reaction; nonetheless these models allow for a first-order exploration of the processes governing dynamic weakening in gouge. To calculate the temperature within the gouge samples (T_{goug}) we set $y = 0$ in equation (F.9) to find

$$T_{goug} = T_0 + \int_0^t \frac{\tau(t')V(t')}{\rho c\sqrt{2\pi}} \frac{1}{\sqrt{W^2 + 2\alpha_{th}(t-t')}} \mathrm{d}t', \tag{F.3}$$

where W is the half width of the deforming zone. T_{goug} is the maximum temperature in the deforming zone (at $y = 0$), where shearing is most intense; repeating the analysis using the average temperature in the deforming zone did not significantly alter our results. Figure F.12c shows the predicted temperatures for three single velocity-step experiments with a peak velocity of 1 m/s (Runs 820, 745 and 823), one single velocity-step experiment with a peak velocity of 0.1 m/s (Run 835) and one multiple velocity-step experiment with a peak velocity of 4 m/s (Run 824b). We use a deforming zone thickness of 150 μm (i.e., $W = 75$ μm), based on our microstructural observations (see Figures F.9 and F.10). Repeating the analysis for thicknesses ranging from 50 to 500 μm resulted in negligible differences ($\sim$25 °C). The model predicts that gouge temperatures may become high enough to dehydrate serpentine for all experiments at $\sigma_n > 5$ MPa, which is consistent with XRPD data, except for Run 835 that did not contain dehydration products. Additionally, the model predicts temperatures high enough to produce melt in Run 823, consistent with the melt textures

along the slip surface. However, if dynamic weakening occurs for $T > 600$ °C, the model is inconsistent with the observed total weakening distances in the all experiments. For example, Runs 820 and 745 dynamically weakened after 200 mm and 5 mm of slip respectively whereas the model predicts that the temperatures in both runs should be ~200 °C for the given slip, far below the critical temperature.

To reconcile this inconsistency we explore the role of flash heating within the gouge zone using the relationship suggested by *Beeler et al.* [2008][8], which accounts for the width of the deforming zone. In this case, the flash-heating model (F.11) is modified to

$$T_{asp} = T_{goug} + \frac{\tau_c}{\rho c}\left(\frac{V(g/w)d}{\pi\alpha_{th}}\right)^{1/2}, \tag{F.4}$$

where g is the grain size and w is the thickness of the deforming gouge layer. Again, we assume the deforming gouge layer thickness is ~150 μm (i.e., $w = 2W = 150$ μm) based on the width of ultra-fine grained zones in our experiments. The initial grain size (g) within this deforming zone is less obvious. The grain size prior to deformation (i.e., the grain size of the starting material) will undoubtedly be somewhat comminuted during initial slip as strain becomes more concentrated into the ~150 μm shear zone. As demonstrated by *Di Toro et al.* [2013][62], once strain becomes highly localized very little additional deformation occurs outside the localized zone, thus the material adjacent to the localized zone should preserve the grain size at the onset of localization. In our experiments the grain size of the material adjacent to the ultra-fine grained zones was ~15 μm suggesting a g/w ratio of ~0.1. In equation (F.4) we assume $(g/w) = 0.1$ while all other physical constants remain the same as previously assumed in equation (F.2). Figure F.12d shows that the asperity-scale temperature increase varies dramatically with varying normal stress and velocity, and that

the magnitude of the temperature rise for a given displacement is significantly lower than in equivalent bare- surface experiments (Figure F.12b). Similar to bare surface experiments, there is a strong correlation between the onset of dynamic weakening (stars, Figure F.12b) and model temperatures $> 600\,^{\circ}\mathrm{C}$, suggesting that dynamic weakening is caused by flash heating in gouge. However the dynamic weakening in gouge occurs after larger displacements and at higher velocities than bare surfaces because strain is more distributed. Remarkably, the gouge flash heating model predicts that Run 824b and 823 should have similar asperity-scale temperatures with slip despite having different imposed normal stresses and velocity profiles, consistent with the total weakening distances observed in both runs (Figure F.12d). Our conclusion that dynamic weakening in the gouge is promoted by flash heating is also supported by comparison of the friction data (during acceleration) with the model illustrated in Figure F.12d.

Flash heating has also been observed in HVF experiments on carbonate gouge. In experiments conducted at $\leq$ 2 MPa, *De Paola et al.* [2011][56] and more recently *Mitchell et al.* [2013][148] showed CO_2 degassing after only a few hundred microns of slip suggesting that flash heating was occurring. In higher normal-stress experiments (8.5 MPa), *Smith et al.* [2013][211] demonstrate that dynamic weakening in carbonate gouge initiates at sliding displacements of $(100 - 150$ mm), similar to the behavior seen in our experiments.

The application of phase equilibria to high-velocity frictional processes remains a challenge due to short reaction times, high energy input rates and dynamic nature of the physical parameters under which reactions occur. Based on the identification of crystalline reaction products in wear material, in conjunction with the thermal models, we conclude that reaction kinetics must be rapid enough for phase transformations to occur within the life-

time of an asperity (few milliseconds). In the short-displacement experiments of *Kohli et al.* [2011][125], the consistency between the modeled asperity temperatures, XRPD observation of talc and the predicted reaction temperature suggests near-equilibrium phase relationships at pressures similar to the asperity normal stress are applicable in HVF systems. For material not in contact at asperities, the reaction pressure will be set by the pore fluid pressure (which is lower than the asperity pressure), thus generally reducing the reaction temperature in these zones. Following this logic, in Figure F.12 we projected phase boundaries through ambient pressures for T_{surf} and T_{goug} plots and through $5 - 6$ GPa for asperity temperature plots (based on our assumption that the contact shear stress is 3 GPa and friction is ~0.6 prior to weakening). Nonetheless, we acknowledge that considerable uncertainty remains regarding the magnitude, spatiotemporal variability of pressure at the asperity scale.

Other textural observations suggest the application of equilibrium phase boundaries is more complicated in HVF systems. Recall that in antigorite bare surface and gouge experiments we observed melt-like textures directly on the slip surfaces (e.g., Figures F.7b, F.7d and F.10j). These textures suggest the reaction Atg →melt + H_2O, which is not consistent with equilibrium thermodynamics. Thus, rapid heating apparently promotes reaction overstepping.

F.4.4 Comparisons of gouge and bare surfaces at higher normal stress

With increasing normal stress the high-velocity friction behavior of gouge approaches that of bare surfaces. This trend is demonstrated by both δ and μ_{nss} values. As discussed above, values of δ characterize the onset of dynamic weakening. In gouge, values of δ decrease with

increasing normal stress while values for bare surfaces remain approximately constant (e.g., Figure F.12d and Table F.1). Similarly, values of μ_{nss} for gouge decrease with increasing normal stress while values for bare surfaces remain approximately constant (e.g., Figure F.4a). A linear approximation to the μ_{nss} data for gouge predicts that both gouge and bare surfaces would have the same values of μ_{nss} at normal stresses $\sim$60 MPa or larger (as shown by dashed line in Figure F.4a) and data for both would be nominally independent of normal stress. A normal stress of 60 MPa corresponds to a depth of $\sim$5 km along an Andersonian normal fault at hydrostatic conditions[52]. It remains unclear if bare-surface samples would actually strengthen if wear material was allowed to accumulate during slip; in our experimental assembly, wear products are flung out of the assembly, leaving a minimal thickness of wear debris.

F.4.5 Geophysical Implications

The results of this study have potential implication for earthquakes in geologic locations that contain serpentine, such as within oceanic transform faults[78], oceanic detachment faults[140] and some locations along the San Andreas fault[151]. However, all natural faults contain a layer of gouge material produced during a seismic rupture propagation even in initially cohesive fault rocks[175]. Thus, some of the first-order observations found in this study may be applicable for all nominally dry faults as those reproduced in our experiments (room-humidity).

For serpentine-rich fault zones at low normal stresses ($<$60 MPa) under nominally dry conditions, dynamic frictional-weakening will be delayed to longer slip by the presence of unconsolidated material possibly resulting in smaller slips during earthquakes. For rup-

tures that propagate into shallow unconsolidated fault-patches, less seismic energy will be emitted due to smaller static- and dynamic-stress drops. These interpretations complement hypotheses derived from slow velocity experiments on gouge, which have been interpreted to promote the lack of shallow seismicity in some fault zones[142]. For large slip events (>5 m) gouge likely has no ability to subdue radiated seismic energy; previous studies have demonstrated for long displacements ($5 - 25$ m) under room-humidity conditions, friction values will decay to ∼0.1 for phyllosilicate-rich gouges[124,149]. We suspect these friction trends are also applicable in highly permeable fluid-saturated faults, with the added complication that water cools the asperity contacts rendering the flash-heating weakening mechanism less efficient than in room-humidity[235]. In water saturated faults with low permeability, thermal pressurization may occur adding further complication[155]. In such cases it is not clear how the presence of gouge may affect dynamic weakening during seismic slip; no machine to date can simulate these conditions. At normal stresses $>$ 60 MPa the presence of unconsolidated serpentine within the fault may have no direct effect on the onset of dynamic weakening or steady state friction values.

F.5 Conclusions

Our work finds significant frictional differences between the serpentinite bare surfaces and gouge at low normal stresses (<22 MPa). We demonstrate that the frictional behavior is strongly normal stress dependent in gouge while relatively normal stress invariant in bare surfaces. Extrapolation of our data suggests that the behavior of antigorite gouge will approach that of bare surfaces at normal stresses ≥60 MPa (∼5 km depth). We thus infer the presence of gouge will alter the weakening properties of shallow sections of serpentine-rich

faults, but have little effect at greater depths. Using 1-D thermal modeling, X-ray diffraction and microstructural analysis, we constrain the effects of velocity, normal stress, shear heating, strain localization and dehydration reactions on frictional weakening. We show that the evolution of friction for a given slip event on either bare surfaces or gouge zones is dependent on the evolution of temperature at both the asperity-scale and surface-scale and we show that both scales need to be modeled in order to reconcile experimental data. We conclude that flash heating is the primary process causing initial weakening in bare surfaces. Flash heating also occurs in gouge, however because strain is more distributed, dynamic weakening occurs at higher velocities and after larger displacements than in bare surfaces experiments. We find values of friction in LIZ gouge have longer weakening distances than ATG gouge but generally have similar dynamic weakening trends. Finally, we observe slip-generated dehydration products and melt textures in both bare-surface and gouge samples. These mineral and textural signatures likely form in natural serpentine-rich faults, the presence of which would indicate seismic slip.

F.6 Appendix A: Smoothing data

High frequency noise was removed from all data using a fast-fourier-transform (FFT) smoothing filter. Figure F.13 shows filtered or smoothed friction data from three representative experiments (black, green and blue lines) and corresponding unsmoothed (raw) data (gray lines).

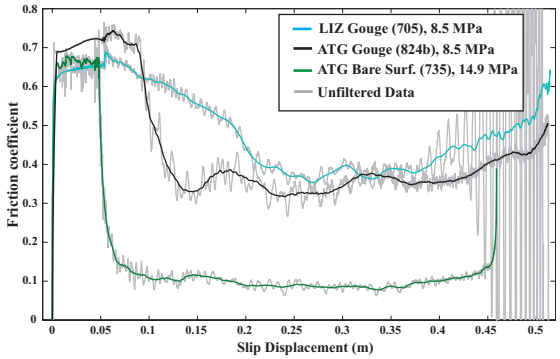

Figure F.13: Results from high-frequency noise filtering in three characteristic friction experiments. Parentheses indicate experimental Run number.

F.7 Appendix B: X-ray powder diffraction methods

Twenty-six X-ray powder diffraction analyses were conducted at the Geosciences Department at the University of Padua used a Panalytical θ-θ diffractometer (Cu radiation) equipped with a long, fine-focus Cu X-ray tube (operating at 40kV and 40mA), sample spinner, Ni filter and a solid-state detector (X'Celerator). The system optics consist of a fixed 1/2° divergent slit and 1° antiscatter slit on the incident beam path and soller slits (0.04 rad) on incident and diffracted beam paths. The powders were mounted on a 32-mm (internal diameter) circular sample holder. Scans were performed over the 2θ range $3 - 80°$ with a virtual step size of 0.017° in 2θ and a counting time of 100 s/step. Phase identification and semi-quantitative analysis were performed using the software package X'Pert HighScore Plus; the phase identification was confirmed by comparison with the reference pattern database Panalytical-ICSD (Inorganic Crystal Structure Database). One additional XRPD analysis was conducted at Brown University on sample 834 using a Bruker D-8 Advance diffractometer with DaVinci system, a Cu X-ray tube operating at 40 kV and 40 mA and a Bruker

Vantec-500 (Xe-CO_2 gas filled) detector with a 13.5 cm diameter window set at 20 cm from the goniometer center and Ni filter. The scans were performed over the 2θ range $25 - 80^\circ$ with a virtual step size of 0.25° in 2θ and a counting time of 60s /step. The phase identification was performed using the software package Diffrac.Eva by Bruker and confirmed by comparison with the ICDD (The International Centre for Diffraction Data).

F.8 Appendix C: Area correction for single velocity-step bare-surface experiments

In the suite of 1 m/s experiments on ATG bare surfaces (Runs 736a to 736h), one sample was used for eight consecutive slip cycles, with 1 m of slip per cycle. The applied normal force was increased after each cycle from 6.2 kN during the first cycle up to 53 kN during the last cycle. This force correlates with an increase in nominal normal stress from ~5 to 40 MPa assuming the initial nominal area of the slip surface (~12.5 cm^2) remained constant. However, during each slip cycle the area progressively decreased because the sample on the stationary side became progressively wedge shaped due to wear during sliding (Figure F.14a). Wear of the sample on the opposing rotary side resulted in significant loss of material normal to the fault, but the surface area remained approximately constant. The final slip surface area (dashed orange region in Figure F.14c) was determined via imaging software to be 5.38 cm^2, indicating that the actual normal stress was 96.6 MPa during the last cycle.

Figure F.14: Photographs of deformed bare-surface sample (Run 736) after eight consecutive deformation cycles: (a) the stationary surface and (b) rotary surface. (c) Sequential mechanical erosion reduced the surface area of the non-rotary side by ∼57%; yellow lines indicate initial surface area and orange dashed lines outline final slip surface area. (d) Mass of wear material collected after each deformation cycle with the corresponding applied normal force and axial shortening for the given slip cycle. (e) Cross-sectional diagram modeling the final sample shape (green) and material lost to erosion (white). The initial shape is indicated with bold black lines (see text for description of model). (f) Cumulative collected wear (blue diamonds) and the estimated total mass of wear material (black line), assuming 60% of wear material was captured. The modeled volume of wear material (purple circles) was fit to the estimated wear and the corresponding surface area parameter (lambda, green triangles). (g) Modeled surface area after each deformation cycle (Runs 736a to 736h) and the calculated normal stress (applied normal force/surface area). The measured initial and final surface areas are indicated with black stars.

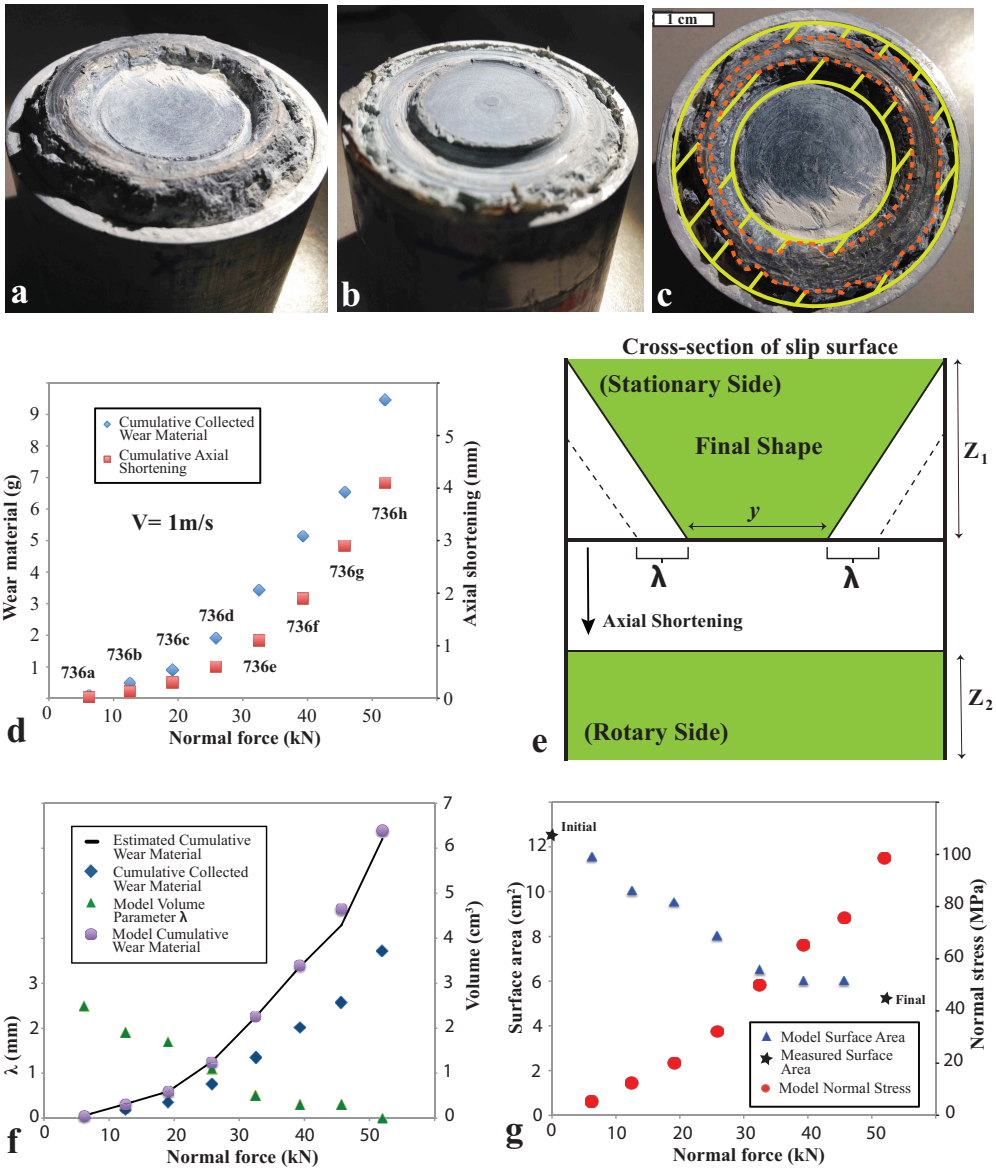

Figure F.14: (continued)

We constructed a simple model to estimate the area of the slip surface after each slip cycle. The model is constrained by the final slip surface outline in plane view, the initial and final area of the slip surface, the mass of wear material collected after each slip cycle and the axial shortening. The axial shortening was monitored with a linear variable differential transformer (LVDT) and the wear material was collected in a foil tray located under the sample. In Figure F.14d the cumulative mass of collected wear material and cumulative axial shortening are plotted for all eight slip cycles; both data sets show a similar non-linear increase with increasing normal force. The final shape of the slip surface is modeled as a wedge-shaped quadrilateral (in cross-section) on one side (Figure F.14e) and as a migrating flat surface on the other side (Figure F.14e). The effective annular width of the slip surface (y) is calculated from the final measured surface area (Figure F.14c). The thickness of the stationary sample (Z1) remained approximately constant, while the thickness of the rotary sample (Z2) decreased in accord with axial shortening. The evolution of the cross-sectional area of the top sample is calculated using mass balance and the change in the annular width (λ); values of λ are estimated by assuming that the eroded angle remains constant. The total volume of wear calculated from this model is $\sim$6.5 cm^3 (purple circle in Figure F.14f). The total volume of collected wear (collected mass/density of antigorite) was somewhat less than the value determined by mass balance (blue diamond in Figure F.14f), indicating that $\sim$60% of the total wear material was recovered. We ignore changes in mass due to frictional-heating-induced metamorphism. The black line in Figure C1f shows cumulative wear by assuming that 60% of the total wear material was collected after each slip pulse. This assumption is reasonable because the collection tray did not capture all particles expelled from the sample. We then use the cumulative collected wear in conjunction with the

LVDT displacement to calculate the value of λ that is consistent with the estimated volume of wear material produced after each slip cycle (green triangles in Figure F.14f). Finally, we use λ to calculate the surface area. The modeled surface area values were used to correct the recorded normal stress and shear stress values for each slip cycle (Figure F.14g)

F.9 Appendix D: Thermal Model

To model the temperature evolution within the deforming zone we use the one- dimensional heat equation

$$\frac{\partial T}{\partial t} = \frac{\tau \dot{\gamma}}{\rho c} + \alpha_{th} \frac{\partial^2 T}{\partial y^2}, \tag{F.5}$$

where t is the time since slip began, y is the distance from the center of the deforming zone, τ is the shear stress, $\dot{\gamma}$is the strain rate, α_{th} is the thermal diffusivity, and ρc is the effective heat capacity per unit volume. The initial conditions are $T = T_0$ at $t = 0$, which models the ambient laboratory conditions before deformation begins. For the boundary conditions we choose $T \to T_0$ as $y \to \infty$. These boundary conditions ignore the presence of the metal gouge holder, which will have a higher thermal diffusivity than the gouge. However, for the typical experiment durations of about one second it is likely that thermal diffusion through the gouge holder has a small effect, justifying our choice of boundary conditions.

The frictional heating in the deforming zone is controlled by the shear stress and strain rate. *Rice* [2006][186] argued that unrealistically high accelerations are required to make inertial effects important within the gouge layer, and thus the shear stress should be constant throughout the deforming zone. *Platt et al.* [2014][166] used numerical simulations to show that this assumption is valid for the normal stresses considered here. We assume that the

deforming zone has a gaussian shape

$$\dot{\gamma} = \frac{V}{W\sqrt{2\pi}} \exp\left(-\frac{y^2}{2W^2}\right), \tag{F.6}$$

where W is the half-width of the deforming zone. A better approach would be to model the physical processes driving strain localization within the gouge, but this is beyond the scope of this paper.

For the shear stress and strain rate profiles justified in the previous paragraph we can solve equation (F.5) using a Green's function approach, leading to the solution

$$T(y,t) = T_0 + \int_0^t \int_{-\infty}^{+\infty} \frac{\tau(t')V(t')}{\rho c W\sqrt{2\pi}} \exp\left(-\frac{y'^2}{2W^2}\right) G(y-y', t-t'; \alpha_{th}) \mathrm{d}y' \mathrm{d}t', \tag{F.7}$$

where the Green's function is

$$G(y-y', t-t'; \alpha_{th}) = \frac{1}{\sqrt{4\pi\alpha_{th}(t-t')}} \exp\left(-\frac{(y-y')^2}{4\alpha_{th}(t-t')}\right). \tag{F.8}$$

The integral over y' can be done exactly leading to

$$T(y,t) = T_0 + \int_0^t \frac{\tau(t')V(t')}{\rho c\sqrt{2\pi}} \frac{1}{\sqrt{W^2 + 2\alpha_{th}(t-t')}} \exp\left(-\frac{y^2}{2W^2 + 4\alpha_{th}(t-t')}\right) \mathrm{d}t'. \tag{F.9}$$

This expression was previously derived in *Andrews* [2002][4] and was used to model thermal pressurization during seismic shear.

To find the temperature evolution of the sliding surface for the bare surface experiments we set the deforming zone thickness equal to zero in equation (F.9). This is equivalent to

solving using a Green's function for a half-space heated by a flux at the boundary, and leads to the solution for the surface temperature

$$T_{surf} = T_0 + \int_0^t \frac{\tau(t')V(t')}{\rho c} \frac{1}{\sqrt{4\pi\alpha_{th}(t-t')}} \mathrm{d}t'. \tag{F.10}$$

Equation (F.10) can be repurposed to calculate the asperity temperature using the typical flash heating model by setting the shear stress equal to the contact shear stress τ_c, the slip velocity equal to the current value from the experiment, and the initial temperature T_0 equal to the current temperature on the sliding surface. The assumptions of constant velocity and shear stress allow us to evaluate the integral in equation (F.10) to find the maximum asperity temperature

$$T_{asp} = T_{surf} + \frac{\tau_c}{\rho c} \left(\frac{Vd}{\pi\alpha_{th}} \right)^{1/2}, \tag{F.11}$$

where d is the contact (i.e., asperity) diameter.

References

[1] Abercrombie, R. E. (1995), Earthquake source scaling relationships from– 1 to 5 ML using seismograms recorded at 2.5-km depth, *Journal of Geophysical Research*, 100(B12), 24015-24036.

[2] Abercrombie, R. E., and J. R. Rice (2005), Can observations of earthquake scaling constrain slip weakening?, *Geophysical Journal International*, 162(2), 406-424.

[3] Alley, R. B., D. D. Blankenship, C. R. Bentley, and S. T. Rooney (1986), Deformation of till beneath ice stream B, West Antartica, *Nature*, 322, 57-59.

[4] Andrews, D. J. (2002), A fault constitutive relation accounting for thermal pressurization of pore fluid, *Journal of Geophysical Research*, 107, B12, 2363.

[5] Bamber, J. L., D. G. Vaughan, and I. Joughin (2000), Widespread complex flow in the interior of the Antarctic ice sheet, *Science*, 287, 1248-1250.

[6] Barenblatt, G. I. (1959), On the equilibrium cracks formed in brittle failure, *Journal of Applied Mathematics and Mechanics*, 23 (3), 893-900.

[7] Beeler N. M., T. E. Tullis, M. L. Blanpied, and J. D. Weeks (1996), Frictional behavior of large displacement experimental faults, *Journal of Geophysical research*, 101, 8,697-8,715.

[8] Beeler, N. M., T. E. Tullis, and D. L. Goldsby (2008), Constitutive relationships and physical basis of fault strength due to flash heating, *Journal of Geophysical Research*, 113, B01401.

[9] Beem, L., K. Jezek, and C. Van der Veen (2010), Basal melt rates beneath Whillans Ice Stream, West Antarctica, *Journal of Glaciology*, 56(198), 647–654.

[10] Ben Amar, M., and J. R. Rice (2002), Exacts results with the J-integral applied to free-boundary flows, *Journal of Fluid Mechanics*, 461, 321–341.

[11] Benallal, A., and C. Comi (2003), Perturbation growth and localization in fluid-saturated inelastic porous media under quasi-static loadings, *Journal of the Mechanics and Physics of Solids*, 51, 851-899.

[12] Benallal, A. (2005), On localization modes in coupled thermo-hydro-mechanical problems, *Comptes Rendus Mécanique*, 333, 7, 557-564.

[13] Bender, C. M., and S. A. Orszag (1999), Advanced mathematical methods for scientists and engineers: Asymptotic methods and perturbation theory, Springer, New York.

[14] Berman, R. G., Thermobarometry using multi-equilibrium calculations: a new technique, with petrological applications, *Can. Mineral.*, *29*(4), 833–855.

[15] Berrut, J.-P., and L. N. Trefethen (2004), Barycentric Lagrange Interpolation, *SIAM Review*, 46(3), 501-517.

[16] Bestmann, M., G. Pennacchioni, S. Nielsen, M. Göken, and H. De Wall (2012), Deformation and ultrafine dynamic recrystallization of quartz in pseudotachylyte-bearing brittle faults: A matter of a few seconds, *Journal of Structural Geology*, 38, 21-38.

[17] Bilby, B., and J. Eshelby (1968), Dislocations and the theory of fracture, in *Fracture, an Advanced Treatise*, vol. II, edited by H. Liebowitz, chap. 3, pp. 191–311, Academic, New York.

[18] Bindschadler, R. A., and P. L. Vornberger (1990), A VHRR imagery reveals Antarctic ice dynamics, *Eos*, 71(23).

[19] Bindschadler, R. A., and P. L. Vornberger (1998), Changes in the West Antarctic ice sheet since 1963 from declassified satellite photography, *Science*, 279, 689-692.

[20] Bizzarri, A., and M. Cocco (2006), A thermal pressurization model for the spontaneous dynamic rupture propagation on a three-dimensional fault: 2. Traction evolution and dynamic parameters, *Journal of Geophysical Research*, 111, B05304.

[21] Blankenship, D. D., C. R. Bentley, S. T. Rooney, and R. B. Alley (1986), Seismic measurements reveal a porous layer beneath an active Antarctic ice stream, *Nature*, 322, 54-57.

[22] Blankenship, D. D., C. R. Bentley, S. T. Rooney, and R. B. Alley (1987), Till beneath ice stream B 1. Properties derived from seismic travel times, *Journal of Geophysical Research*, 92, 8,903-8,911.

[23] Blanpied, M. L., D. A. Lockner, and J. D. Byerlee (1995), Frictional slip of granite at hydrothermal conditions, *Journal of Geophysical Research*, 100, 13045-13064.

[24] Blanpied, M. L., C. J. Marone, D. A. Lockner, J. D. Byerlee, and D. P. King (1998), Quantitative measure of the variation in fault rheology due to fluid-rock interactions, *Journal of Geophysical Research*, 103, 9691-9712.

[25] Boettcher, M. S., G. Hirth, and B. Evans (2007), Olivine friction at the base of oceanic seismogenic zones, *Journal of Geophysical Research*, 112, B01205.

[26] Bose, K. and J. Ganguly, Thermogravimetric study of the dehydration kinetics of talc, *Am. Min.,79*, 692–699, 1994.

[27] Boullier, A.-M., E.-C. Yeh, S. Boutareaud, S.-R. Song, and C.-H. Tsai (2009), Microscale anatomy of the 1999 Chi-Chi earthquake fault zone, *Geochemistry, Geophysics, Geosystems*, 10, Q03016.

[28] Boutareaud, S., D.-G. Calugaru, R. Han, O. Fabbri, K. Mizoguchi, A. Tsutsumi, and T. Shimamoto (2008), Clay-clast aggregates: A new textural evidence for seismic fault sliding?, *Geophysical Research Letters*, 35, L05302.

[29] Brantut, N., A. Schubnel, J.-N. Rouzaud, F. Brunet, and T. Shimamoto (2008), High-velocity frictional properties of a clay-bearing fault gouge and implications for earthquake mechanics, *Journal of Geophysical Research*, 113, B10401.

[30] Brantut, N., A. Schubnel, J. Corvisier, and J. Sarout (2010), Thermochemical pressurization of faults during coseismic slip, *Journal of Geophysical Research*, 115.

[31] Brantut, N., and J. R. Rice (2011), Decomposition-induced overpressures and fault zone dilation during earthquake slip, *AGU Fall Meeting 2011*, Abstract T23G-06.

[32] Brantut, N., R. Han, T. Shimamoto, N. Findling, and A. Schubnel, Fast slip with inhibited temperature rise due to mineral dehydration: Evidence from experiments on gypsum, *Geology*, *39*(1), 59–62, 2011.

[33] Brantut, N., and J. Sulem (2012), Strain localization and slip instability in a strain-rate hardening, chemically weakening material, *Journal of Applied Mechanics*, 79(3).

[34] Briggs, W. L., V. E. Henson, and S. F. McCormick (2000), A Multigrid Tutorial, vol. 72, Siam Monograph, Philadelphia, Pa., U.S.A.

[35] Broberg, K. B. (1978), On transient sliding motion, *Geophysical Journal International*, *52*(3), 397-432

[36] Brown, K. M., and Y. Fialko (2012), "Melt welt" mechanism of extreme weakening of gabbro at seismic slip rates, *Nature*, 488(7413), 638-641.

[37] Bullock, R. J., N. De Paola, R. E. Holdsworth, and J. Trabucho-Alexandre (2014), Lithological controls on the deformation mechanisms operating within carbonate-hosted faults during the seismic cycle, *Journal of Structural Geology*, 58, 22-42.

[38] Byerlee, J. (1978), Friction of rocks, *Pure and Applied Geophysics*, 116, 4-5, 615-626.

[39] Chester, F. M., J. Evans, and R. Biegel (1993), Internal structure and weakening mechanisms of the San Andreas fault, *Journal of Geophysical Research*, 98, 771-786.

[40] Cherepanov, G. (1968), Cracks in solids, *International Journal of Solids and Structures*, 4(8), 811–831.

[41] Chester, F. M. (1994), Effects of temperature on friction: Constitutive equations and experiments with quartz gouge, *Journal of Geophysical Research*, 99, 7247-7261.

[42] Chester, F. M., and J. S. Chester (1998), Ultracataclasite structure and friction processes of the Punchbowl Fault, San Andreas System, California, *Tectonophysics*, 295, 199-221.

[43] Chester, J. S., A. K. Kronenberg, F. M. Chester, and R. N. Guillemette (2003), Characterization of natural slip surfaces relevant to earthquake mechanics, *Eos Tans. AGU*, 84 (46), Fall Meet Suppl., Abstract S42C-0185.

[44] Chester, F. M., J. S. Chester, D. L. Kirschner, S. E. Schulz, and J. P. Evans (2004), Structure of large-displacement, strike-slip faults in the brittle continental crust, in *Rheology and Deformation in the Lithosphere at Continental Margins*, edited by G. D. Kamer et al., 223-260, Columbia Univ. Press, New York.

[45] Chester, J.S., F. M. Chester, and A. K. Kronenberg (2005), Fracture surface energy of the Punchbowl Fault, San Andreas System, *Nature*, 437, 133-136.

[46] Chester, F. M., C. Rowe, K. Ujiie, J. Kirkpatrick, C. Regalla, F. Remitti, J. C. Moore, V. Toy, M. Wolfson-Schwehr, and S. Bose (2013), Structure and Composition of the Plate- Boundary Slip Zone for the 2011 Tohoku-Oki Earthquake, *Science*, 342(6163), 1208- 1211.

[47] Clarke, T. S., C. Liu, N. E. Lord, and C. R. Bentley (2000), Evidence for a recently abandoned shear margin adjacent to ice stream B2, Antarctica, from ice-penetrating radar measurements, *Journal of Geophysical research*, 105, 13,409-13,422.

[48] Coker, D., G. Lykotrafitis, A. Needleman, and A. J. Rosakis (2005), Frictional sliding modes along an interface between identical elastic plates subject to shear impact loading., *Journal of the Mechanics and Physics of Solids*, 53, 884-922.

[49] Collettini, C., C. Viti, T. Tesei, and S. Mollo (2013), Thermal decomposition along natural carbonate faults during earthquakes, *Geology*, 41, 927-930.

[50] Cooper, R. F., and D. L. Kohlstedt (1986), Rheology and structure of olivine-basalt partial melts, *Journal of Geophysical research*, 91, 9315-9323.

[51] Coussy, O. (1995), Mechanics of Porous Continua, Wiley, New York.

[52] Cowie, P.A.,C.H. Scholz, M. Edwards, and A. Malinverno (1993), Fault strain and seismic coupling on mid-ocean ridges, *Journal of Geophysical Research*, 98(B10).

[53] Cuffey, K., and W. S. Paterson (2010), *The physics of glaciers (fourth edition)*, Butterworth-Heinemann.

[54] Da Cruz, F., S. Emam, M. Prochnow, J.-N. Roux, and F. Chevoir (2005), Rheophysics of dense granular materials: Discrete simulation of plane shear flows, *Physical Review E*, 72, 021309.

[55] De Paola, N., C. Collettini, D.R. Faulkner, and F. Trippetta (2008), Fault zone architecture and deformation processes within evaporitic rocks in the upper crust, *Tectonics*, 27, TC4017.

[56] De Paola, N., T. Hirose, T. Mitchell, G. Di Toro, C. Viti, and T. Shimamoto, Fault lubrication and earthquake propagation in thermally unstable rocks, *Geology*, *39*(1), 35–38.

[57] Dieterich, J. H. (1979), Modeling of rock friction 1. Experimental results and constitutive equations, *Journal of Geophysical Research*, 84, 2161-2168.

[58] Di Toro, G., D. L. Goldsby, and T. E. Tullis (2004), Friction falls towards zero in quartz rock as slip velocity approaches seismic rates, *Nature*, 427(6973), 436-439.

[59] Di Toro, G., T. Hirose, S. Nielsen, G. Pennacchioni, and T. Shimamoto (2006), Natural and experimental evidence of melt lubrication of faults during earthquakes, *Science*, 311(5761), 647-649,.

[60] Di Toro, G., A. Niemeijer, A. Tripoli, S. Nielsen, F. Di Felice, P. Scarlato, G. Spada, R. Alessandroni, G. Romeo, and G. Di Stefano (2010), From field geology to earthquake simulation: a new state-of-the-art tool to investigate rock friction during the seismic cycle (SHIVA), *Rendiconti Lincei*, 21(1), 95-114.

[61] Di Toro, G., R. Han, T. Hirose, N. De Paola, S. Nielsen, K. Mizoguchi, F. Ferri, M. Cocco, and T. Shimamoto (2011), Fault lubrication during earthquakes, *Nature*, 471, 494-498.

[62] Di Toro, G., M. Rempe, S. A. Smith, and T. M. Mitchell (2013), Strain localization in experimentally sheared gouge layers, *AGU Fall Meeting*, Abstract MR13A- 2225.

[63] Dollimore, D., P. Tong, and K. S. Alexander, The kinetic interpretation of the decomposition of calcium carbonate by use of relationships other than the Arrhenius equation, *Thermochim. Acta*, 282/283, 13–27.

[64] Dreimanis, A. (1988), Tills: Their genetic terminology and classification, in *Genetic Classification of Glacigenic Deposits*, edited by R. P. Goldthwait and C. L. Matsch, pp. 17–83, A. A. Balkema, Rotterdam.

[65] Dugdale, D. S. (1960), Yielding of steel sheets containing slits, *Journal of the Mechanics and Physics of Solids*, 8, 100-104.

[66] Durham, W. B., S. H. Kirby, and L. A. Stern (1997), Creep of water ices at planetary conditions: A compilation, *Journal of Geophysical Research*, 102, 16,293-16302.

[67] Duval, P. (1977), The role of the water content on the creep rate of polycrystalline ice, in *Isotopes and impurities in Snow and Ice*, IAHS Publications, 118, 29-33.

[68] Echelmeyer, K. A., W. D. Harrison, C. Larsen, and J. E. Mitchell (1994), The role of the margins in the dynamics of an active ice stream, *Journal of Glaciology*, 40 (136), 527-538.

[69] Echelmeyer, K. A., and W. D. Harrison (1999), Ongoing margin migration of Ice Stream B, Antarctica, *Journal of Glaciology*, 45 (150), 361-369.

[70] Engelhardt, H., N. Humphrey, B. Kamb, and M. Fahnestock (1990), Physical conditions at the base of a fast moving Antarctic ice stream, *Science*, 248, 57–59.

[71] Erdogan, F., and G. D. Gupta (1972), On the numerical solution of singular integral equations, *Quarterly of Applied Mathematics*, 525-534.

[72] Erdogan, F., G. D. Gupta, and T. S. Cook (1973), Numerical solution of singular integral equations, in *Mechanics of Fracture*, vol. 1, edited by G. C. Sih, chap. 7, pp. 368–425, Noordhoff Int., Leyden, Netherlands.

[73] Fahnestock, M., T. Scambos, R. Bindschadler, and G. Kvaran (2000), A millennium of variable ice flow recorded by the Ross Ice Shelf, Antarctica, *Journal of Glaciology*, 46(155), 652–664.

[74] Fine, R. A., and F. J. Millero (1973), Compressibility of water as a function of temperature and pressure, *The Journal of Chemical Physics*, 59(10), 5529-5536.

[75] Fondriest, M., S. A. F. Smith, G. Di Toro, D. Zampieri, and S. Mittempergher (2012), Fault zone structure and seismic slip localization in dolostones, an example from the Southern Alps, Italy, *Journal of Structural Geology*, 45, 52-67.

[76] Fondriest, M., S. A. F. Smith, T. Candela, S. B. Nielsen, K. Mair, and G. Di Toro (2013), Mirror-like faults and power dissipation during earthquakes, *Geology*, 41(11), 1175- 1178.

[77] Forterre, F., and O. Pouliquen (2008), Flows of dense granular media, *Annual Reviews of Fluid Mechanics*, 40, 1-24.

[78] Francis, T. J. G. (1981), Serpentinization faults and their role in the tectonics of slow spreading ridges, *Journal of Geophysical Research*, 86, 11616-11622.

[79] Freund, L. B. (1979), The mechanics of dynamic shear crack propagation, *Journal of Geophysical Research*, 84, 2199–2209.

[80] Friedman, M., J. M. Logan, and J.A. Rigert (1974), Glass-indurated quartz gouge in sliding-friction experiments on sandstone, *Geological Society of America Bulletin*, 85(6), 937-942.

[81] Frost, H., and M. Ashby (1982), *Deformation Mechanism Maps: The Plasticity and Creep of Metals and Ceramics*, Pergamon Press, Oxford, New York, Sydney.

[82] Fujiwara, T., S. Kondaira, T. No, Y. Kaiho, N. Takahashi, and Y. Kaneda (2011), The 2011 Tohoku-Oki earthquake: Displacement reaching the trench axis, *Science*, 334(6060), 1240.

[83] Fulton, P. M., E. E. Brodsky, Y. Kano, J. Mori, F. Chester, T. Ishikawa, R. N. Harris, W. Lin, N. Eguchi, S. Toczko, and the Exp. 343/343T & KR13-08 Scientists (2013), Low coseismic friction on the Tohoku-Oki fault determined from temperature measurements, *Science*, 342, 1214-1217.

[84] Gabriel, A.-A., J.-P. Ampuero, L. A. Dalguer, and P. M. Mai (2012), The transition of dynamic rupture styles in elastic media under velocity-weakening friction, *Journal of Geophysical Research*, 117, B09311.

[85] Garagash, D. I., and J. W. Rudnicki (2003), Shear heating of a fluid-saturated slip-weakening dilatant fault zone 1: Limiting regimes, *Journal of Geophysical Research*, 108, 2121-2139.

[86] Garagash, D.I. (2012), Seismic and aseismic slip pulses driven by thermal pressurization of pore fluid, *Journal of Geophysical Research*, 117, B04314.

[87] Giovinetto, M. B., and H. J. Zwally (2000), Spatial distribution of net surface accumulation on the Antarctic Ice Sheet, *Annals of Glaciology*, 31(1), 171–178.

[88] Goldman, N. L., and J. W. Hutchinson (1975), Fully plastic crack problems: The center-cracked strip under plane strain, *International Journal of Solids and Structures*, 11(5), 575–591.

[89] Goldsby, D. L., and D. L. Kohlstedt (2001), Superplastic deformation of ice: Experimental observations, *Journal of Geophysical research*, 106, 11,017-11,030.

[90] Goldsby, D. L. (2006), Superplastic flow of ice relevant to glacier and ice-sheet mechanics, in *Glacier Science and Environmental Change*, edited by P. G. Knight, Blackwell Publishing.

[91] Goldsby, D. L., and G. Hirth (2006), Frictional behavior of serpentine at high sliding velocity: Implications for seismic coupling at oceanic transform faults, *AGU Fall Meeting*, Abstract T11C-0458.

[92] Goldsby, D. L., and T. E. Tullis (2002), Low frictional strength of quartz rocks at subseismic slip rates, *Geophysical Research Letters*, 29(17), 1844.

[93] Goldsby, D. L., and T. E. Tullis (2011), Flash heating leads to low frictional strength of crustal rocks at earthquake slip rates, *Science*, 334, 216-218.

[94] Green, H., D. Lockner, K. Bozhilov, A. Maddon, N. Beeler, and Z. Reches (2010), Nanometric gouge in high-speed shearing experiments: superplasticity?, *AGU Fall Meeting*, Abstract T31D-08.

[95] Griffith, W. A., G. Di Toro, G. Pennacchioni, D. D. Pollard, and S. Nielsen (2009), Static stress drop associated with brittle slip events on exhumed faults, *Journal of Geophysical Research*,114.

[96] Han, R., T. Shimamoto, J. Ando, and J. Ree, Seismic slip record in carbonate-bearing fault zones: an insight from high-velocity friction experiments on siderite gouge, *Geology*, *35*(12), 1131–1134, 2007.

[97] Han, R., T. Shimamoto, T. Hirose, J. Ree, and J. Ando, Ultra-low friction of carbonate faults caused by thermal decomposition, *Science*, *316*(5826), 878–881, 2007.

[98] Han, R., T. Hirose, and T. Shimamoto (2010), Strong velocity weakening and powder lubrication of simulated carbonate faults at seismic slip rates, *Jouranl of Geophysical Research*, 115, B03412.

[99] Harrison, W. D., K. A. Echelmeyer, and C. Larsen (1998), Measurements of temperature in a margin of Ice Stream B, Antarctica: implications for margin migration and lateral drag, *Journal of Glaciology*, 44 (148), 615-624.

[100] Heaton, T. H. (1990), Evidence for an implications of self-healing pulses of slip in earthquake rupture, *Physics of the Earth and Planetary Interiors*, 64, 1-20.

[101] Heermance, R., Z. K. Shipton, and J. P. Evans (2003), Fault structure control on fault slip and ground motion during the 1999 rupture of the Chelungpu Fault, Taiwan, *Bulletin of the Seismological Society of America*, 93, 1034-1050.

[102] Hewitt, I. J. (2011), Modelling distributed and channelized subglacial drainage: the spacing of channels, *Journal of Glaciology*, 57 (202), 302-314.

[103] Hilairet, N., I. Daniel, and B. Reynard (2006), Equation of state of antigorite, stability field of serpentines, and seismicity in subduction zones, *Geophysical Research Letters*, 33(2).

[104] Hirono, T., T. Yokoyama, Y. Hamada, W. Tanikawa, T. Mishima, M. Ikehara, V. Famin, M. Tanimizu, W. Lin, and W. Soh (2007), A chemical kinetic approach to estimate dynamic shear stress during the 1999 Taiwan Chi-Chi earthquake, *Geophysical Research Letters*, 34, L19308.

[105] Hirono, T., and W. Tanikawa, Implications of the thermal properties and kinetic parameters of dehydroxylation of mica minerals for fault weakening, frictional heating, and earthquake energetics, *Earth and Planetary Science Letters*, *307*, 161–172, 2011.

[106] Hirose, T., and M. Bystricky, Extreme dynamic weakening of faults during dehydration by coseismic shear heating, *Geophysical Research Letters*, *34*, L14311, 2007.

[107] Hirose, T., and T. Shimamoto (2003), Fractal dimension of molten surfaces as a possible parameter to infer the slip-weakening distance of faults from natural pseudotachylytes, *Journal of Structural Geology*, 25(10), 1569-1574.

[108] Hirose, T., and T. Shimamoto (2005), Slip-weakening distance of faults during frictional melting as inferred from experimental and natural pseudotachylytes, *Bulletin of the Seismological Society of America*, 95(5), 1666-1673,

[109] Holdsworth, R., N. De Paola, I. Faoro, R. Bullock, C. Viti, and C. Collettini (2013), Nano-scale diffusion-accommodated weakening triggered by frictional sliding during earthquakes in carbonate rocks, Geological Society of America *Abstracts with Programs*, 45, 679.

[110] Ikari, M. J., D. M. Saffer, and C. J. Marone (2009), Frictional and hydrologic properties of clay-rich fault gouge, *Journal of Geophysical Research*, 114, B05409.

[111] Imanishi, K., and W. L. Ellsworth (2006), Source scaling relationships of microearthquakes at Parkfield, CA, determined using the SAFOD pilot hole seismic array, *Geophysical Monograph Series*, 170, 81-90.

[112] Iverson, N. R., T. S. Hooyer, and R. W. Baker (1998), Ring-shear studies of till deformation: Coulomb-plastic behavior and distributed strain in glacier beds, *Journal of Glaciology*, 44 (148), 634-642.

[113] Jackson, M., and B. Kamb (1997), The marginal shear stress of Ice Stream B, West Antarctica, *Journal of Glaciology*, 43 (145), 415-426.

[114] Jacobel, R., T. Scambos, C. Raymond, and A. Gades (1996), Changes in the configuration of ice stream flow from the West Antarctic Ice Sheet, *Journal of Geophysical Research*, 101(B3), 5499–5504.

[115] Jacobel, R., T. Scambos, N. Nereson, and C. Raymond (2000), Changes in the margin of Ice Stream C, Antarctica, *Journal of Glaciology*, 46(152), 102–110.

[116] Jacobson, H. P., and C. F. Raymond (1998), Thermal effects on the location of ice stream margins, *Journal of Geophysical research*, 103, 12,111-12,122.

[117] Jordan, R., and J. Stark (2001), Capillary tension in rotting ice layers, Technical Report ERDC/CRREL TR-01-13, US Army Corps of Engineers, Cold Regions Research and Engineering Laboratory.

[118] Joughin, I., S. Tulaczyk, R. Bindschadler, and S. F. Price (2002), Changes in west Antarctic ice stream velocities: Observation and analysis, *Journal of Geophysical research*, 107.

[119] Joughin, I., D. R. MacAyeal, and S. Tulaczyk (2004), Basal shear stress of the Ross ice streams from control method inversions, *Journal of Geophysical Research*, 109(B9).

[120] Kamb, B. (1991), Rheological nonlinearity and flow instability in the deforming bed mechanism of ice stream motion, *Journal of Geophysical Research*, 96, 16,585-16,595.

[121] Kamb, B. (2001), Basal zone of the West Antarctic ice streams and its role in lubrication of their rapid motion, in *The West Antarctic Ice Sheet: Behavior and Environment*, vol. 77, edited by R. B. Alley and R. A. Bindschadler, pp. 157–199, AGU, Washington, D. C.

[122] Kanamori, H., and T. H. Heaton (2000), Microscopic and macroscopic physics of earthquakes, *Geophysical Monograph Series*, 120, 147-163.

[123] King, D.L., and T.E. Tullis, Flash heating leads to low frictional strength of crustal rocks at earthquake slip rates, *Science*, *334*, 2011.

[124] Kitajima, H., J. S. Chester, F. M. Chester, and T. Shimamoto (2010), Flash weakening of serpentinite at near-seismic slip rates, *Journal of Geophysical Research*, 116, B03202.

[125] Kohli, A. H., D. L. Goldsby, G. Hirth, and T. Tullis (2011), High-speed friction of disaggregated ultracataclasite in rotary shear: Characterization of frictional heating, mechanical behavior, and microstructure evolution, *Journal of Geophysical Research*, 115, B08408.

[126] Kubo, S., K. Ohji, and K. Ogura (1979), Analysis of creep crack-propagation on the basis of the plastic singular stress-field, *Eng. Fract. Mech.*, 11(2), 315–329.

[127] Lachenbruch, A. H. (1980), Frictional heating, fluid pressure, and the resistance to fault motion, *Journal of Geophysical Research*, 85, 6097-6112.

[128] Lachenbruch, A. H., and J. H. Sass (1980), Heat flow and energetics of the San Andreas fault zone, *Journal of Geophysical Research*, 85.

[129] Lachenbruch, A. H., and J. H. Sass (1992), Heat flow from Cajon Pass, fault strength, and tectonic implications, *Journal of Geophysical Research*, 97(B4), 4995-5015.

[130] Landes, J., and J. Begley (1976), A fracture mechanics approach to creep crack growth, in *Mechanics of Crack Growth*, edited by J. R. Rice and P. C. Paris, pp. 128–148, Amer. Soc. for Testing and Materials (ASTM), Special Technical Publication (STP) 590, Philadelphia.

[131] Lapusta, N. (2005), Modes of dynamic rupture on interfaces with nonlinear rate and state friction laws, *Proceedings of the 11th International Conference on Fracture*, Turin, Italy.

[132] Likhachev, E. R. (2003), Dependence of water viscosity on temperature and pressure, *Technical Physics*, 48(4), 514-515.

[133] Lin, A. (2011), Seismic slip recorded by fluidized ultracataclastic veins formed in a coseismic shear zone during the 2008 Mw 7.9 Wenchuan earthquake, *Geology*, 39(6), 547-550.

[134] Linker, M. F., and J. H. Dieterich (1992), Effects of variable normal stress on rock friction: Observations and constitutive equations, *Journal of Geophysical Research*, 97, 4923-4940.

[135] Llana-Fúnez, S., K. H. Brodie, E. H. Rutter and J. C. Arkwright, Experimental dehydration kinetics of serpentinite using pore volumometry, *J. Metamorphic Geol.*, *25*, 423–438, 2007.

[136] Lliboutry, L. A., and P. Duval (1985), Various isotropic and anisotropic ices found in glaciers and polar ice caps and their corresponding rheologies, *Annales Geophysicae*, 3 (2), 207-224.

[137] Lliboutry, L. (1996), Temperate ice permeability, stability of water veins and percolation of internal meltwater, *Journal of Glaciology*, 42(141), 201–211.

[138] L'vov, B. V., Mechanism and kinetics of thermal decomposition of carbonates, *Thermochim. Acta*, *386*, 1–16, 2002.

[139] MacAyeal, D. R. (1989), Large-scale ice flow over a viscous basal sediment: Theory and application to Ice Stream B, Antarctica, *Journal of Geophysical Research*, 94(B4), 4071–4087.

[140] MacLeod, C. J., J. Escartin, D. Banerji, G. J. Banks, M. Gleeson, D. H. B. Irving, R. M. Lilly, A. M. McCaig, Y. Niu, and S. Allerton (2002), Direct geological evidence for oceanic detachment faulting: The Mid-Atlantic Ridge, 15 45′ N, *Geology*, 30(10), 879-882.

[141] Malagnini, L., S. Nielsen, K. Mayeda, and E. Boschi (2010), Energy radiation from intermediate-to large-magnitude earthquakes: Implications for dynamic fault weakening, *Journal of Geophysical Research*, 115, B06319.

[142] Marone, C., and C. H. Scholz (1988), The depth of seismic faulting and the upper transition from stable to unstable slip regimes, *Geophysical Research Letters*, 15(6), 621-624.

[143] Marone, C., C. B. Raleigh, and C. H. Scholz (1990), Frictional behavior and constitutive modeling of simulated fault gouge, *Journal of Geophysical Research*, 95, 7007-7025.

[144] Mase, C. W., and L. Smith (1985), Pore-fluid pressures and frictional heating on a fault surface, *Pure and Applied Geophysics*, 122, 583-607.

[145] Mase, C. W., and L. Smith (1987), Effects of frictional heating on the thermal, hydrologic, and mechanical response of a fault, *Journal of Geophysical Research*, 92, 6249-6272.

[146] McMeeking, R., and R. Johnson (1986), On the mechanics of surging glaciers, *Journal of Glaciology*, 32(110), 120–132.

[147] McTigue, D. F. (1986), Thermoelastic response of fluid-saturated porous rock, *Journal of Geophysical Research*, 91, 9533-9542.

[148] Mitchell, T. M., S. A. Smith, M. H. Anders, and G. Di Toro (2013), Catastrophic emplacement of giant landslides aided by thermal decomposition, Geological Society of America *Abstracts with Programs*, 45(7), 679.

[149] Mizoguchi, K., T. Hirose, T. Shimamoto, and E. Fukuyama (2007), Reconstruction of seismic faulting by high-velocity friction experiments: An example of the 1995 Kobe earthquake, *Geophysical Research Letters*, 34, L01308.

[150] Mizoguchi, K., T. Hirose, T. Shimamoto, and E. Fukuyama (2009), High-velocity frictional behavior and microstructure evolution of fault gouge, obtained from Nojima fault, southwest Japan *Tectonophysics*, 471, 285-296.

[151] Moore, D. E., and M. J. Rymer (2007), Talc-bearing serpentinite and the creeping section of the San Andreas fault, *Nature*, 448(7155), 795-797.

[152] Muir-Wood, D. (1990), Soil Behaviour and Critical State Soil Mechanics, Cambridge University Press, Cambridge, United Kingdom.

[153] Niemeijer, A., G. Di Toro, S. Nielsen, and F. Di Felice (2011), Frictional melting of gabbro under extreme experimental conditions of normal stress, acceleration, and sliding velocity, *Journal of Geophysical Research*, 116, B07404.

[154] Niemeijer, A., G. Di Toro, W. A. Griffith, A. Bistacchi, S. A. F. Smith, and S. Nielsen (2012), Inferring earthquake physics and chemistry using an integrated field and laboratory approach, *Journal of Structural Geology*, 39, 2-36.

[155] Noda, H., E. M. Dunham, and J. R. Rice (2009), Earthquake ruptures with thermal weakening and the operation of major faults at low overall stress levels, *Journal of Geophysical Research*, 114, B07302.

[156] Noda, H., and N. Lapusta (2010), 3D earthquake sequence simulations with evolving temperature and pore pressure due to shear heating: Effect of heterogeneous hydraulic diffusivity, *Journal of Geophysical Research*, 115, B12314.

[157] Noda, H., and N. Lapusta (2010), Stable creeping fault segments can become destructive as a result of dynamic weakening, *Nature*, 493, 518-521.

[158] Nye, J. F. (1953), The flow law of ice from measurements in glacier tunnels, laboratory experiments and the Jungfraufirn borehole experiment, *Proceedings of the Royal Society A*, 219, 477-489.

[159] Nye, J. F. (1976), Water flow in glaciers: Jökulhluaps, tunnels and veins, *Journal of Glaciology*, 17 (76), 181-207.

[160] Osako, M., A. Yoneda, and E. Ito (2010), Thermal diffusivity, thermal conductivity and heat capacity of serpentine (antigorite) under high pressure, *Physics of the Earth and Planetary Interiors*, 183(1), 229-233.

[161] Perol, T., and J. R. Rice (2011), Control of the width of West Antarctic ice streams by internal melting in the ice sheet near the margins, *AGU Fall Meeting*, Abstract C11B-0677.

[162] Perol, T., J. D. Platt, J. Suckale, and J. R. Rice (2012), Stressing, Hydraulic and Locking Processes at Ice Stream Margins, *AGU Fall Meeting*, C34A-07

[163] Perol, T., J. R. Rice, J. Suckale, and J. D. Platt, Stabilizing mechanism for migration of Western Antarctic ice streams, *in preparation*.

[164] Perrillat J. P., I. Daniel, K. T. Koga, B. Reynard, H. Cardon, and W. A. Crichton (2005), Kinetics of antigorite dehydration: a real-time X-ray diffraction study, *Earth and Planetary Science Letters*, 236(3), 899-913.

[165] Perrin, G., J. R. Rice, and G. Zheng (1995), Self-healing slip pulse on a frictional surface, *Journal of the Mechanics and Physics of Solids*, 43, 1461–1495.

[166] Platt, J. D., J. W. Rudnicki, and J. R. Rice (2014), Stability and localization of rapid shear in fluid-saturated fault gouge, 2. Localized zone width and strength evolution, *Journal of Geophysical Research*, 119, 4334-4359.

[167] Platt, J. D., N. Brantut, and J. R. Rice, Strain localization driven by thermal decomposition during seismic shear, *Submitted to Journal of Geophysical Research*.

[168] Poliakov, A. N. B., R. Dmowska, and J. R. Rice (2002), Dynamic shear rupture interactions with fault bends and off-axis secondary faulting, *Journal of Geophysical Research*, 107.

[169] Polissar, P. J., H. M. Savage, and E. E. Brodsky (2011), Extractable organic material in fault zones as a tool to investigate frictional stress, *Earth and Planetary Science Letters*, 439-447.

[170] Poulet, T., E. Veveakis, K. Regenauer-Lieb, and D. A. Yuen (2014), Thermo-poro-mechanics of chemically active creeping faults: 3. The role of serpentinite in episodic tremor and slip sequences, and transition to chaos, *Journal of Geophysical Research*, 119, 4606-4625.

[171] Proctor, B. P., T. M. Mitchell, G. Hirth, D. Goldsby, F. Zorzi, J. D. Platt, and G. Di Toro (2014), Dynamic weakening of serpentinite gouges and bare-surfaces at seismic slip rates, *Journal of Geophysical Research*, 119, 8107-8131.

[172] Rathbun, A., C. Marone, R. Alley, and S. Anandakrishnan (2008), Laboratory study of the frictional rheology of sheared till, *Journal of Geophysical Research*,113, F02020.

[173] Raymond, C. (1996), Shear margins in glaciers and ice sheets, *Journal of Glaciology*, 42(140), 90–102.

[174] Raymond, C. (2000), Energy balance of ice streams, *Journal of Glaciology*, 46(155), 665–674.

[175] Reches, Z., and T. A. Dewers (2005), Gouge formation by dynamic pulverization during earthquake rupture, *Earth and Planetary Science Letters*, 235(1), 361-374.

[176] Reches, Z., and D. A. Lockner (2010), Fault weakening and earthquake instability by powder lubrication, *Nature*, *467*, 452-455.

[177] Reches, Z., A. S. Madden, and X. Chen (2012), Fault gouge rheology under confined, high-velocity conditions, Abstract T21C-2590 presented at 2012 Fall Meeting, AGU, San Francisco, Calif. 3-7 Dec.

[178] Reinen, L. A., J. D. Weeks, and T. E. Tullis (1991), The frictional behavior of serpentinite: Implications for aseismic creep on shallow crustal faults, *Geophysical Research Letters*, 18(10), 1921-1924.

[179] Reinen, L. A., T. E. Tullis, and J. D. Weeks (1992), Two-mechanism model for frictional sliding of serpentinite, *Geophysical Research Letters*, 19(15), 1535-1538.

[180] Rempel, A. W., and J. R. Rice (2006), Thermal pressurization and onset of melting in fault zones, *Journal of Geophysical Research*, 111, B09314.

[181] Rempel, A. W. (2009), Effective stress profiles and seepage flows beneath glaciers and ice sheets, *Journal of Glaciology*, 55 (191), 431-443.

[182] Rice, J. R. (1967), Stresses due to a sharp notch in a work-hardening elastic-plastic material loaded by longitudinal shear, *Journal of Applied Mechanics*, 34, 287-298.

[183] Rice, J. R. (1968), Mathematical analysis in the mechanics of fracture, in *Fracture, an Advanced Treatise*, vol. II, edited by H. Liebowitz, chap. 3, pp. 191–311, Academic, New York.

[184] Rice, J. R. (1968), A Path Independent Integral and the Approximate Analysis of Strain Concentration by Notches and Cracks, *Journal of Applied Mechanics*, 35, 379-386.

[185] Rice, J. R. (1999), Flash heating at asperity contacts and rate-dependent friction, *EOS, Trans. AGU*, 80 (46), Fall Meet. Suppl., F681.

[186] Rice, J. R. (2006), Heating and weakening of faults during earthquake slip, *Journal of Geophysical Research*, 111, B05311.

[187] Rice, J. R., and M. Cocco (2007), Seismic fault rheology and earthquake dynamics, *Tectonic Faults: Agents of Change on a Dynamic Earth*, edited by M.R. Handy, G. Hirth, and N. Hovius, 99-137, MIT Press, Cambridge, MA.

[188] Rice, J. R., C. G. Sammis, and R. Parsons (2005), Off-fault secondary failure induced by a dynamic slip-pulse, *Bulletin of the Seismological Society of America*, 95 (1), 109–134.

[189] Rice, J.R, J.W. Rudnicki, and J. D. Platt (2014), Stability and localization of rapid shear in fluid-saturated gouge, 1. Linearized stability analysis, *Journal of Geophysical Research*, 119, 4311-4333.

[190] Rose, K. (1979), Characteristics of ice flow in Marie Byrd Land, Antarctica, *Journal of Glaciology*, 24, 63–75.

[191] Röthlisberger, H. (1972), Water pressure in intra- and subglacial channels, *Journal of Glaciology*, 11 (62), 177-203.

[192] Rowe, C. D. (2013), Do faults preserve records of the seismic cycle? 14 years of advancements from field observations and laboratory experiments, Geological Society of America *Abstracts with Programs*, 45(7), 519.

[193] Ruina, A. (1983), Slip instability and state variable friction laws, *Journal of Geophysical Research*, 88, 10,359-10,370.

[194] Saxena, S. K., and Y. Fei, Fluids at crustal pressures and temperatures 1. Pure species, *Contributions to Mineralogy and Petrology*, 95, 370-375, 1987.

[195] Scambos, T. A., K. A. Echelmeyer, M. A. Fahnestock, and R. A. Bindschadler (1994), Development of enhanced ice flow at the southern margin of Ice Stream D, Antarctica, *Annals of Glaciology*, 20, 313-318.

[196] Schofield, A. N. and P. Wroth (1968), Critical State Soil Mechanics, McGraw-Hill, New York.

[197] Scholz, C. H. (2002), The mechanics of earthquakes and faulting, *Cambridge University Press*.

[198] Schoof, C. (2004), On the mechanics of ice-stream shear margins, *Journal of Glaciology*, 50, 169, 208-218.

[199] Schoof, C. (2012), Thermally driven migration of ice-stream shear margins, *Journal of Fluid Mechanics*, 712, 552-578.

[200] Schubnel, A., F. Brunet, N. Hilairet, J. Gasc, Y. Wang, and H. W. Green (2013), Deep-Focus Earthquake Analogs Recorded at High Pressure and Temperature in the Laboratory, *Science*, 341(6152), 1377-1380.

[201] Segall, P., and J. R. Rice (1995), Dilatancy, compaction, and slip instability of a fluid-infiltrated fault, *Journal of Geophysical Research*, 100, 22,155-22,171.

[202] Shabtaie, S., and C. R. Bentley (1987), West Antarctic ice streams draining into the Ross ice shelf: Configuration and mass balance, *Journal of Geophysical research*, 92, 1311-1336.

[203] Shabtaie, S., and C. R. Bentley (1988), Ice-thickness map of the West Antarctic ice streams by radar sounding, *Annals of Glaciology*, 11, 126-136.

[204] Shreve, R. L. (1972), Movement of water in glaciers, *Journal of Glaciology*, 11 (62), 205-214.

[205] Sibson, R. H. (1975), Generation of pseudotachylyte by ancient seismic faulting, Geophysical Journal International, 43(3), 775-794.

[206] Sibson, R. H. (1977), Fault rocks and fault mechanisms, *Journal of the Geological Society*, 133, 191-213.

[207] Sibson, R. H. (2003), Thickness of the seismic slip zone, *Bulletin of the Seismological Society of America*, 93(3), 1169-1178.

[208] Siman-Tov, S., E. Aharonov, A. Sagy, and S. Emmanuel (2013), Nanograins form carbonate fault mirrors, *Geology*, 41(6), 703-706,

[209] Shi, Z., Y. Ben-Zion, and A. Needleman (2008), Properties of dynamic rupture and energy partition in a solid with a frictional interface, *Journal of the Mechanics and Physics of Solids*, 56, 5-24.

[210] Smith, S. A., G. Di Toro, S. Nielsen, and M. Fondriest (2012), Field and experimental constraints on seismic localization in granular fault gouge, *AGU Fall Meeting*, Abstract S11A-06.

[211] Smith, S. A. F., G. Di Toro, S. Kim, J.-H. Ree, S. Nielsen, A. Billi, and R. Spiess (2013), Coseismic recrystallization during shallow earthquake slip, *Geology*, 41, 63-66.

[212] Snoke, A. W., T. J. Kalakay, J. E. Quick, and S. Sinigoi (1999), Development of a deep- crustal shear zone in response to syntectonic intrusion of mafic magma into the lower crust, Ivrea–Verbano zone, Italy, *Earth and Planetary Science Letters*, 166(1), 31-45.

[213] Spikes, V. B., G. S. Hamilton, S. A. Arcone, S. Kaspari, and P. A. Mayewski (2004), Variability in accumulation rates from GPR profiling on the West Antarctic Plateau, *Annals of Glaciology*, 39(1), 238–244.

[214] Spray, J. G. (2005), Evidence for melt lubrication during large earthquakes, *Geophysical Research Letters*, 32, L07301.

[215] Stein, S., and E. A. Okal (2005), Seismology: Speed and size of the Sumatra earthquake, *Nature*, 434(7033), 581-582.

[216] Suckale J., J. D. Platt, T. Perol, and J. R. Rice (2014), Deformation-induced melting in the margins of the West Antarctic ice streams, *Journal of Geophysical research*, 119, 1004-1025.

[217] Sulem, J., and V. Famin (2009), Thermal decomposition of carbonates in fault zones: Slip-weakening and temperature-limiting effects, *Journal of Geophysical Research*, 114, B03309.

[218] Sulem, J., V. Famin, and H. Noda, Correction to "Thermal decomposition of carbonates in fault zones: Slip-weakening and temperature-limiting effects", *Journal of Geophysical Research*, 114, 2009.

[219] Sulem, J., I. Stefanou, and E. Veveakis (2011), Stability analysis of undrained adiabatic shearing of a rock layer with Cosserat microstructure, *Granular Matter*, 13, 261-268.

[220] Till, C. B., T. L. Grove, and A. C. Withers (2012), The beginnings of hydrous mantle wedge melting, *Contributions to Mineralogy and Petrology*, 163(4), 669-688.

[221] Tisato, N., G. Di Toro, N. De Rossi, M. Quaresimin, and T. Candela (2012), Experimental investigation of flash weakening in limestone, *Journal of Structural Geology*, 38, 183-199.

[222] Townend, J., and M. D. Zoback (2004), Regional tectonic stress near the San Andreas fault in central and southern California, *Journal of Geophysical Research*, 113.

[223] Tsutsumi, A., and T. Shimamoto (1997), High-velocity frictional properties of gabbro, *Geophysical Research Letters*, 24, 699-702.

[224] Tulaczyk, S., B. Kamb, R. P. Scherer, and H. F. Engelhardt (1998), Sedimentary processes at the base of a West Antarctic ice stream; constraints from textural and compositional properties of subglacial debris, *Journal of Sedimentary Research*, 68(3), 487–496.

[225] Tulaczyk, S. (1999), Ice sliding over weak, fine-grained tills: Dependence of ice-till interactions on till granulometry, *Geol. S. Am. S.*, 337, 159–177.

[226] Tulaczyk, S., W. B. Kamb, and H. F. Engelhardt (2000), Basal mechanics of Ice Stream B, West Antarctica 1. Till mechanics, *Journal of Geophysical research*, 105, 463-481.

[227] Tullis, T. E., and J. D. Weeks (1986), Constitutive behavior and stability of frictional sliding of granite, *Pure and Applied Geophysics*, 124, 383-414.

[228] Urata, Y., K. Kuge, and Y. Kase (2012), Spontaneous dynamic rupture propagation beyond fault discontinuities: Effect of thermal pressurization, *Bulletin of the Seismological Society of America*, 102, 53-63.

[229] Urata, Y., S. Hok, E. Fukuyama, and R. Madariaga (2014), The effect of thermal pressurization on dynamic fault branching, *Geophysical Journal International*, 196, 1237-1246.

[230] Vardoulakis, I. (2002), Dynamic thermo-poro-mechanical analysis of catastrophic landslides, *Géotechnique*, 52, 157-171.

[231] van der Veen, C. J., and I. M. Whillans (1996), Model experiments on the evolution and stability of ice streams, *Annals of Glaciology*, 23, 129-137.

[232] Viegas, G. M., L. G. Baise, and R. E. Abercrombie (2010), Regional Wave Propagation in New England and New York, *Bulletin of the Seismological Society of America*, 100(5A), 2196-2218.

[233] Viesca, R. C, and D. Garagash (2012), Steady slip pulses on faults with rate- and state-dependent friction and multiple thermal weakening mechanisms, *AGU Fall Meeting 2012*, S21B-2435.

[234] Viesca, R. C, and D. Garagash, Fracture energy of dynamic fault weakening processes, *in preparation*.

[235] Violay, M., S. Nielsen, B. Gibert, E. Spagnuolo, A. Cavallo, P. Azais, S. Vinciguerra, and G. Di Toro (2014), Effect of water on the frictional behavior of cohesive rocks during earthquakes, *Geology*, 42(1), 27-30.

[236] Vogel, S. W., S. Tulaczyk, B. Kamb, H. Engelhardt, F. D. Carsey, A. E. Behar, A. L. Lane, and I. Joughin (2005), Subglacial conditions during and after stoppage of an Antarctic ice stream: Is reactivation imminent?, *Geophysical Research Letters*, 32, L14502.

[237] Vornberger, P. L., and I. M. Whillans (1990), Crevasse deformation and examples from Ice Stream B, Antarctica, *Journal of Glaciology*, 36(122), 3–10.

[238] Weertman, J. (1972), General theory of water flow at the base of a glacier or ice sheet, *Reviews of Geophysics and Space Physics*, 10, 287-333.

[239] Weertman, J. (1980), Unstable slippage across a fault that separates elastic media of different elastic constants, *Journal of Geophysical Research*, 85, 1455-1461.

[240] Wegner, W. W., and W. G. Ernst, Experimentally determined hydration and dehydration reaction rate in the system MgO-SiO_2-H_20, *American Journal of Science*, 283-A, 151-180, 1983.

[241] Whillans, I. M., and C. J. Van Der Veen (1993), New and improved determinations of velocity of Ice Streams B and C, West Antarctica, *Journal of Glaciology*, 39, 483–490.

[242] Whillans, I. M., and C. J. Van der Veen (2001), Transmission of stress between an ice stream and interstream ridge, *Journal of Glaciology*, 47(158), 433–440.

[243] Wibberley, C. A. J., and T. Shimamoto (2003), Internal structure and permeability of major strike-slip fault zones: The Median Tectonic Line in Mie Prefecture, southwest Japan, *Journal of Structural Geology*, 25, 59-78.

[244] Yund, R. A., M. L. Blanpied, T. E. Tullis, and J. D. Weeks (1990), Amorphous material in high strain experimental faults gouges, *Journal of Geophysical research*, 95, 15,589-15,602.

[245] Zheng, G., and J. R. Rice (1998), Conditions under which velocity-weakening friction allows a self-healing versus a cracklike mode of rupture, *Bulletin of the Seismological Society of America*, 88(6), 1466–1483.

[246] Zotikov, I. (1986), *The Thermophysics Of Glaciers*, D. Reidel Mass, Dordrecht, Holland.